UCLA
UCLA Electronic Theses and Dissertations

Title
Pediatric Mechanical Circulatory Support Applications for Frequency-Leveraged Piezoelectric Hydraulic Pumps

Permalink
https://escholarship.org/uc/item/34b4t1zg

Author
Valdovinos, John

Publication Date
2014

Peer reviewed|Thesis/dissertation

eScholarship.org Powered by the California Digital Library
University of California

UNIVERSITY OF CALIFORNIA

Los Angeles

Pediatric Mechanical Circulatory Support Applications for Frequency-Leveraged Piezoelectric Hydraulic Pumps

A dissertation submitted in partial satisfaction of the

requirements for the degree Doctor of Philosophy

in Biomedical Engineering

by

John Valdovinos

2014

© Copyright by

John Valdovinos

2014

ABSTRACT OF DISSERTATION

Pediatric Mechanical Circulatory Support Applications

for Frequency-Leveraged Piezoelectric Hydraulic Pumps

By

John Valdovinos

Doctor of Philosophy in Biomedical Engineering

University of California, Los Angeles, 2014

Professor Gregory P. Carman, Co-Chair

Professor Daniel S. Levi, Co-Chair

While the development of ventricular assist devices for the pediatric population has grown and helped these patients in bridge-to-transplantation, the motors used for these devices have remained electromagnetic. Because the physical space requirements for pediatric ventricular assist devices (PVADs) implantation are smaller in children, these motors are susceptible to decreased power output and efficiency as they are scaled down. Piezoelectric actuators, which scale down favorably in terms of power output and efficiency, have yielded novel compact piezoelectric hydraulic pumps in the aerospace industry. The focus of this research is on the development of a ventricular assist driver powered by a miniature piezoelectric hydraulic pump (PHP). This driver is designed to drive a working fluid to an extracorporeal ventricular assist

device, also called a blood pump, which has been fabricated at UCLA for bridge-to-transplantation mechanical support. The majority of the focus for this dissertation was on developing a fundamental understanding of the factors that affect the transduction of power from a small scale piezoelectric to the human circulation. Two piezoelectric pumps were developed and mechanically tested. An 8.1 W/kg pump with 3% efficient pump was fabricated. In-vitro studies were carried out to show that the piezoelectric pump could produce physiological pressure and flow rate waveforms for pediatric patients. While the driver could only provide 1 L/min flow to the mock circulation, these studies have laid the groundwork to optimize piezoelectric pump technology for mechanical support applications in the pediatric community.

The dissertation of John Valdovinos is approved.

Christopher S. Lynch

Jacob J. Schmidt

Daniel S. Levi, Committee Co-Chair

Gregory P. Carman, Committee Co-Chair

University of California, Los Angeles

2014

To my parents, Juan and Esther, my sister, Marissa, and my fiancée, Irene.

Table of Contents

List of Figures

List of Tables

Acknowledgements

First and foremost, I want to thank my two advisors, Dr. Gregory Carman and Dr. Daniel S. Levi. Thank you for taking me in and allowing me to bring to life a vision you both had before I arrived at UCLA. Thank you for giving me the opportunity to conduct research in the Active Materials Laboratory and for fostering in me a grant-writing mentality that I know will serve me well in the future as an academic. Without your support and encouragement, this achievement would not have come to fruition. For that, I am deeply indebted to you both.

To my committee members: Thank you for the support and flexibility. I have heard horror stories about trying to set a time for the prospectus and defense. Fortunately, because of you, I have not had to experience such events. Thank you also for the research insight.

To the members of the Active Materials Laboratory: Thanks for all the fun memories that made this journey personally rewarding. I will truly miss the random discussions we had in the lab that made the entire PhD experience tolerable.

Lastly, I want to thank my family. Thank you Esperanza Campos, Guillermo Campos, and Guillermo Campos Jr. for all the support you have showed me throughout this process. I am one lucky guy to have future in-laws that support me like my biological parents do. For that I am forever grateful to you all. To my beautiful fiancée, Irene: Thank you for all the love and support you have given me and continue to give. This is our accomplishment! Thank you for putting up with my complaints and listening to all my presentations. I am sure you have heard enough about piezohydraulic pumps by now! I love you with all my heart. Thanks for everything. And of course, to my Mom, Dad, and beautiful sister: Words cannot describe the love and appreciation I have for you all. Without you, this would not have been possible. You inspire me to be the most intelligent and caring person I can be. This is also our achievement! Thank you for everything

you have sacrificed to help me get to this point and continue to do to keep me moving forward. All I can hope is that this achievement makes all your hard work worthwhile. I love you all and I cannot wait to see what the future brings us. Fight on! (I had to get a USC reference in there for you Dad).

VITA

2009	B.S. Biomedical Engineering (Electrical Engineering Emphasis) University of Southern California, Los Angeles, CA
2008-2009	Implantable Sensor Research and Development Intern Medtronic Diabetes, Northridge, CA
2009	UCLA Graduate Opportunity Research Fellowship University of California Los Angeles, Los Angeles, CA
2010-2014	Graduate Student Researcher Active Materials Laboratory University of California Los Angeles, Los Angeles, CA
2010	M.S. Biomedical Engineering University of California Los Angeles, Los Angeles, CA
2011	Ford Foundation Predoctoral Fellowship Honorable Mention
2013	ASAIOfyi Fellowship Recipient
2014	Ford Foundation Postdoctoral Fellowship Alternate

Selected Publications

Journals:

Valdovinos J, Levi DS, Williams RJ, Carman GP. "Evaluating Piezoelectric Hydraulic Pumps as Drivers for Pulsatile Pediatric Ventricular Assist Devices". Journal of Intelligent Material Systems and Structures, 2013, DOI:10.1177/1045389X13504476

Valdovinos J, Shkolyar E, Carman GP, Levi DS. "Evaluation of an External Compression Device for Fontan Mechanical Assistance: In vitro Study". Artificial Organs, 2013, DOI: 10.1111/aor.12152

Derk G, Laks H., Biniwale R, Patel S, De LaCruz K, Mazor E, Williams RJ, **Valdovinos J**, Levi DS, Reardon L, Aboulhosn J. "Use of a Ventricular Assist Device to Restore Cardiac Output in an Animal Model of a Failing Fontan". Journal of Heart and Lung Transplantation, (submitted)

Valdovinos J. "Book Review. Mechanical Circulatory Support: Principles and Applications (1st Edition). Edited by David L. Joyce, Lyle D. Joyce, and Matthias Loebe". Cardiovascular Engineering and Technology, 2013, DOI: 10.1007/s13239-013-0147-5

Conference Proceedings:

Valdovinos J, Levi DS, Williams RJ, Carman GP. Feasbility of using Piezohydraulic Pumps as Motors for Pediatric Ventricular Assist Devices. 34th Annual International Conference of the IEEE Engineering in Medicine and Biology Society (EMBC'12), August 28th, San Diego,CA

Presentations

Conference:

Valdovinos J, Levi DS, Williams RJ, Carman GP. Feasbility of using Piezohydraulic Pumps as Motors for Pediatric Ventricular Assist Devices. 3rd International Conference on Engineering Frontiers in Pediatric and Congenital Heart Disease, May 1-2, Stanford, CA.

Valdovinos J, Levi DS, Shkolyar E, Carman GP. In Vitro Evaluation of an External Compression Device for Fontan Mechanical Assistance. ASAIO 59th Annual Conference, June 12-15, Chicago, IL.

Invited:

Valdovinos J, Levi DS, Carman GP. Miniaturizing Pulsatile Pediatric Ventricular Assist Drivers with Piezohydraulic Pumps. California State University Northridge Engineer's Week. February 20th, Northridge, CA.

Chapter 1: Introduction

1.1Motivation and Background

Cardiomyopathy, a disease in which the heart muscle functions abnormally, has an annual incidence of 1.13 in 100,000 children in the United States [1]. While the gold standard treatment for these patients is heart transplantation, the shortage of pediatric heart donors results in long waiting lists for these patients. Pediatric patients with cardiomyopathy thus rely on short-term mechanical support from pediatric ventricular assist devices (VADs) while they await a heart transplant. Even though small continuous flow VADs exist for adult patients, pulsatile pediatric VADs are the only currently FDA approved devices for pediatric heart failure in small children with body surface areas less than 0.7 m^2 [2]–[4]. Pulsatile VADs are pneumatically driven blood pumps that consist of polymer valves and an extendable diaphragm to mimic the ventricle. While pulsatile VADs have decreased patient mortality, the drivers to power these VADs have limited patient mobility. Patient mobility has been shown to be important to patient recovery and survival rate after cardiac surgery [5]. The presently available electro-pneumatic driver units, which rely on multiple electric motor-driven air compressors, weigh between 13-125 kg [6]. Compact piston-type versions of these drivers are available but their use is restricted to adult blood pumps (> 60 mL) [7]. Therefore, new motor approaches for pulsatile VADs need to be pursued to reduce the size of the drivers for the pediatric community.

Piezoelectric frequency leveraged actuators have been used in standing and traveling wave ultrasonic motors [8] and inchworm motors [9]. These solid-state devices utilize a piezoelectric operated at high frequency to convert small stroke and low work output to large displacement and high power output [10]. Unlike electromagnetic motors, power output per unit volume scales favorably with decreasing size in piezoelectric materials. In addition, Uchino (2008) found that

for power outputs less than 30W, piezoelectric driven devices perform better in terms of efficiency than their electromagnetic counterparts. Thus, researchers have demonstrated that these actuators can theoretically be miniaturized without sacrificing power density and efficiency [11], [12]. While these motors have produced significant power outputs for their size, the mechanical translation through friction has limited power output. Tieck *et al.* (2007) measured the intrinsic piezoelectric material power densities and compared them to the ultrasonic motor that utilized them. The intrinsic piezoelectric power densities ranged from 6.53 W/kg to 4500 W/kg while the actual power densities of the motors spanned 0.82 W/kg to 85.73 W/kg. This discrepancy is partially attributed to the use of friction to transfer mechanical loads.

Piezohydraulic pumps, unlike ultrasonic and inchworm motors, do not utilize friction to transfer mechanical loads. These pumps consist of a piezoelectric actuators working with valves to generate hydraulic power in the form of a pressurized continuous flow [13]. For instance, Mauk and Lynch (2000) utilized a piezohydraulic pump with a hydraulic cylinder to produce an actuator with a blocking force of 271 N and 72.5 mm/s no-load velocity (4.9 W maximum power output). However, power density was limited since the piezoelectric stack was operated at sub-kilohertz frequencies. In contrast, O'Neill and Burchfield (2007) developed a piezohydraulic pump operating in the kilohertz regime that yielded power densities as high as 157 W/kg and total power on the order of 46 W [14]. While these pumps produced large power outputs, the pump valve resonant frequency (<1 kHz) limited further increases in power output [15]. Future piezohydraulic pumps are anticipated to use high frequency valves (~10 kHz) but they are presently unavailable (O'Neill, 2012). Nonetheless, it is important to begin evaluating the feasibility of existing piezohydraulic pumps for use in VAD motors to encourage more research and development efforts in the area of biomedical applications of these motors.

Piezoelectric actuators have previously been studied for use in artificial hearts. Loehr (1964) used piezoelectric disc bimorph actuators to drive a working fluid into a blood pump to provide circulatory support [16]. Similarly, Smiley and O'Neill (1969) utilized a piezoelectric stack actuator coupled with a volume amplification system to produce 7 L/min of flow against a 16kPa for a VAD [17]. While successful, the low operating frequencies of these actuators (~ 1 Hz) resulted in low power densities and relatively large devices which prevented further developmental efforts. To date, researchers have not yet studied frequency leveraged piezohydraulic pumps operating in the kilohertz regime for potential use in VAD applications.

1.2Hypothesis

The hypothesis of this dissertation is that frequency leveraged piezohydraulic technology represents a new and potentially superior approach to construct miniaturized drivers to power pediatric ventricular assist devices. *The goal is to demonstrate that a compact piezohydraulic pump can be used as a small power source to re-energize the blood flow of children that are awaiting heart transplantation while allowing increased mobility and thus increased rehabilitation.* This could potentially shift the paradigm of research in pulsatile circulatory support to piezoelectric based drivers rather than the conventional electro-magnetic based approaches. The application of piezohydraulic technology also has implications to other fields, such as medical robotics, where efficient, high power density, and compact motors are needed. The vision for this dissertation is shown in Figure 1-1.

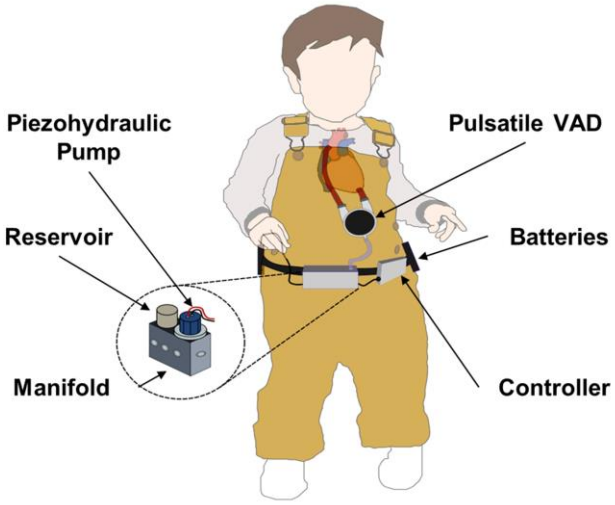

Figure 1-1. Development of a piezohydraulic driven pediatric ventricular assist device driver proposed in this dissertation

Summary of Chapters

Chapter 2

Chapter 2 of this dissertation covers the history and state of the art of mechanical circulatory support for adults and pediatric patients. The chapter starts with an introduction of the important characteristics of the human circulation, cardiovascular anatomy and cardiac physiology. A brief description of cardiovascular disease is covered before presenting the history of adult mechanical circulatory support. The state of the art and design of pulsatile ventricular assist device drivers and the limitations of this technology are also summarized. Lastly, the various methods of in vitro and in vivo testing are briefly discussed. Part of this literature review is published in *Cardiovascular Engineering and Technology Journal* (DOI: 10.1007/s13239-013-0147-5).

Chapter 3

Chapter 3 gives a condensed literature review of the phenomena of piezoelectricity, the development of piezoelectric actuators and motors, and piezohydraulic pumps. First, the physical

mechanisms that distinguish piezoelectric materials from non-piezoelectric materials are described. The constitutive relations describing the strain and charge output of piezoelectric materials are covered and from those relationships some simplified actuator equations are derived. An overview of piezoelectric actuators, motors and the concept of frequency-leveraged devices are presented. Lastly, the development and history of piezohydraulic pumps is covered. The basic principles of operation, design, development, and modeling research conducted by various researchers within the past few decades are presented.

Chapter 4

A feasibility study of using a commercially available piezoelectric pump as a pediatric ventricular assist device driver is presented in Chapter 4. A theoretical analysis is carried out to predict the minimum size of the piezohydraulic pump needed to output the necessary pressures and flows for a pediatric ventricular assist device. Some experimentally experiments were carried out to measure the pressure and flow outputs from the Kinetic Ceramics piezohydraulic pump. The device was then integrated into a driver that supplied pressurized air to a 30 mL stroke volume pediatric blood pump. The findings in this research are published in the *Journal of Intelligent Material Systems and Structures* (DOI: 10.1177/1045389X13504476)

Chapter 5

The design, development, and testing of the first miniature (non MEMs) piezohydraulic pump prototypes designed for medical applications is presented in Chapter 5. The design requirements for utilizing this type of hydraulic pump as a blood pump driver are detailed in more depth than in Chapter 4. The components that make the device are sized and shown. Utilizing a combination of one-dimensional quasi-static modeling and three dimensional finite element modeling, the performance of the pump was predicted and the effect of each components design on power

transmission was also investigated. The experimental results delineating pressure flow and power outputs of these various prototypes are also presented. The results and information from this chapter are part of a pending publication that will be submitted to the journal of *Smart Materials and Structures.*

Chapter 6

The use of the miniature piezohydraulic pump prototype, described in Chapter 5, in a compact pediatric blood pump driver is presented in Chapter 6. First, the design of a pediatric blood pump that can take hydraulic power and covert it to useful circulator stroke work is described. The blood pump driver components and fabrication are also described. A one-dimensional model, modeled on MATLAB Simulink® and Simscape®, is developed to predict the dynamics and control of the driver. In vitro testing of the driver in mock circulation is also presented and the plans for an in vivo animal study are discussed. The results presented in this chapter are part of a submitted publication to the *The Journal of Heart and Lung Transplantation*.

Chapter 7

Chapter 7 covers additional research conducted in the field of mechanical circulatory support under this dissertation. The use of a commercially available minimally invasive implantable left ventricular assist device (Sunshine C-Pulse) as a right heart assist device for patients with one functioning ventricle is presented. An in vitro experimental setup shows that this type of device can help augment the flow to the lungs in Fontan patients who suffer from increased venous pressures. The research paves the way for the use of this device and similar technologies in helping augment the blood flow to patients suffering from what is termed failing Fontans. The research in this chapter is published in an article in *Artificial Organs* (DOI: 10.1111/aor.12152).

Chapter 2: Mechanical Circulatory Support Literature Review

In this chapter a summary of the anatomy and physiology of a heart is presented to give a foundation for the mechanisms behind cardiac pumping. This background is then extended to various diseased states of the heart that result in pediatric heart failure. The history and design of pulsatile and continuous flow mechanical circulatory support (MCS) devices used for adults and pediatric patients with heart failure are also presented.

2.1 Human Cardiovascular Physiology and Heart Failure

The cardiovascular system is responsible for the transportation of hormones, oxygen, carbon dioxide, and nutrients over long distances between various organs, tissue and cells. This transportation is crucial in maintaining homeostasis in the body and is achieved with the cardiovascular system's basic components. These components consist of blood, the transport medium, blood vessels, the structures that mediate blood flow, and the heart, the pump that provides energy for blood transportation. Homeostasis is achieved by utilizing the heart, which consists of two pumps, the right and left ventricle, connected in series as seen in Figure 2-1a. The right ventricle propels blood to the lungs for oxygen uptake and carbon dioxide removal (pulmonary circulation). Once the blood is oxygenated, the blood enters the left ventricle to be distributed to the rest of the body so oxygen can be delivered to organs, muscle, and tissue (systemic circulation). When the function of the heart is compromised by disease, homeostasis cannot be achieved and can lead to deleterious outcomes affecting organ function.

The heart, located in the center thoracic cavity, is a muscular pump that utilizes four chambers and four valves to effectively impart energy into the pulmonary and systemic circulations. The heart, shown in Figure 2-1b, consists of two atria and two ventricles. In a normal circulation, de-oxygenated blood from the systemic circulation (organs and tissues)

enters the right atrium via the tricuspid valve and is pumped it to the right ventricle. The right ventricle, the energy source for the pulmonary circulation, pumps this de-oxygenated blood to the lungs via the pulmonary valve and pulmonary arteries for oxygen uptake and carbon dioxide removal. Oxygenated blood is then returned to the left side of the circulation to the left atrium where it is pumped to the left ventricle via the mitral valve. The left ventricle then pumps the oxygenated blood through the aortic valve to the tissue and organs in the systemic circulation. Unidirectional flow through the heart is achieved with four valves (tricuspid, pulmonary, mitral, and aortic valves). These valves open passively with the pressure gradient produced between the atrial and ventricular chambers during the cardiac cycle.

The pressure produced by the ventricles is developed by electrically-triggered contracting cardiac myocytes (muscle cells). These cells are triggered cyclically and synchronously by the cardiac conduction system. Figure 2-2a shows the ventricular pressure and volume during one cardiac cycle versus time (known as the Wigger's diagram). The cycle starts with ventricular diastolic filling (section A Figure 2-2a), in which the mitral valve is open and the aortic valve is closed resulting from a pressure gradient from the left atrium to the ventricle. This results in filling of the ventricle with a minimal increase in intraventricular pressure. The final volume of the ventricle before ventricular contraction is the end diastolic volume (EDV).

The contraction of the ventricular myocytes causes an increase in ventricular pressure without a change in ventricular volume because both the mitral and aortic valves are closed (Section C of Figure 2-2a) and this is known as isovolumetric contraction. When ventricular pressure of the ventricle exceeds the aortic pressure, the aortic valve (pulmonary valves in the right heart) opens and the mitral valve (tricuspid valve on the right heart) closes which results in fluid ejection from the ventricle and an increased flow through the aorta to the systemic

circulation. This is part of the cardiac cycle is known as ventricular systole and the final volume is the end systolic volume (ESV).

When the cardiac myocytes relax ventricular pressure falls and the aortic valve closes, while the mitral valve remains closed (Section E of Figure 2-2a). This is known as isovolumetric relaxation. When the ventricular pressure falls below the atrial pressure (when atrium contracts), ventricular filling begins again and the cycle continues. Typically, the peak systolic pressure produced by the left ventricle (~ 120 mmHg, 16 kPa) is larger than the pressure produced by the right ventricle (~ 25 mmHg, 3.3 kPa). This is because the systemic circulation offers a larger resistance to the left ventricle than the compliant lungs to the right ventricle.

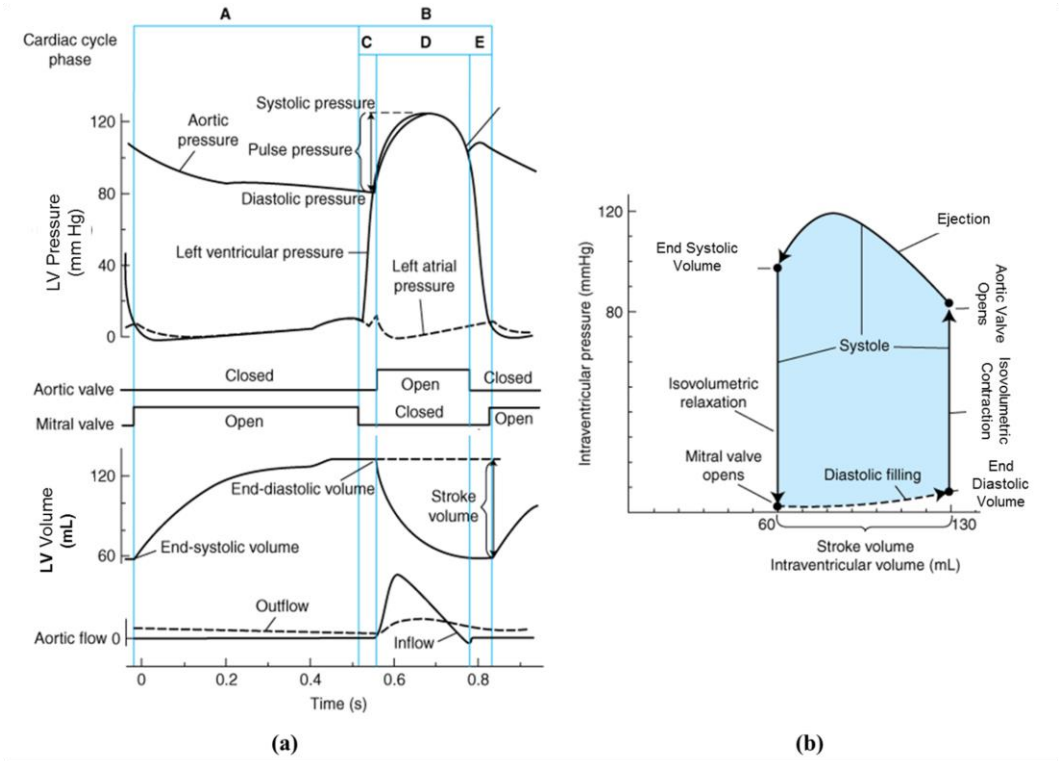

Figure 2-1. (a) Left atrial and ventricular pressure and ventricular volume produced by the left heart during the cardiac cycle and (b) the corresponding left ventricular pressure-volume curve [1]

Plotting the intraventricular pressure as a function of ventricular volume, as shown in Figure 2-2b, shows the ventricular stroke work. The area (in light blue) under the curves

represent the amount of work the ventricle performs to eject fluid into the aorta (or into the pulmonary arteries in the right heart).Assuming the curve is a rectangle with 120 mm Hg (~16 kPa) height (from peak systolic ventricular pressure) and a width of 70 mL (from the stroke volume defined by ESV-EDV), approximately 1.12 Joules of work are performed. There are various factors that can influence the stroke work imparted to the circulation. Cardiac preload, the amount of ventricular filling, can increase the stroke volume by increasing the end diastolic volume (Figure 2-3a). In addition, increased afterload, systemic arterial pressure, can increase the peak systolic pressure and decreased stroke volume. Thus, the cardiac output (CO), the amount of blood ejected by the ventricles per minute, is a function of vascular resistance seen by the ventricles and the contractility of the cardiac muscle. Thus, any disease affecting stroke volume, heart rate, vascular resistance (afterload), ventricular filling (preload) and ventricular contractility can affect the effectiveness of nutrient transport and can potentially disturb homeostasis.

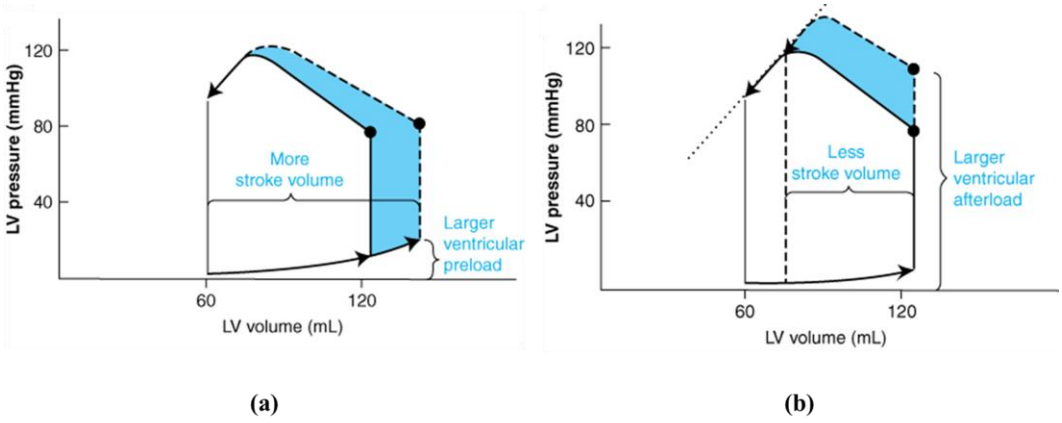

Figure 2-2. (a) Effect of increased ventricular preload (filling) on the ventricular pressure-volume curve and (b) the effect of increased ventricular afterload (back pressure) on the ventricular pressure-volume curve [1]

Some classes of disease that affect the hearts of children at birth or at a young age are cardiomyopathies and congenital heart disease. Cardiomyopathies are diseases of the myocardium, heart muscle, that result in cardiac pumping dysfunction [18]. There are different

categorizations of cardiomyopathies that consist of dilated, hypertrophic, and restrictive cardiomyopathies. Dilated cardiomyopathies are the most common form of heart muscle disease in children. It is typically characterized by dilation of the ventricle (Figure 2-4) and results in impaired systolic function of the one or both ventricles which can lead to heart failure. Dilated cardiomyopathies have an annual incidence of 1.13 in 100,000 children in the United States [1]. Depending on the severity of the heart failure, treatment of this disease in adults and in children varies. Heart failure can be managed pharmacologically (ie. diuretics, digitalis, or β blockers) or surgically with heart transplantation. However, if heart transplantation is needed there is usually a long waitlist for donor hearts and the long wait for a transplant has historically lead to increased patient mortality [19].

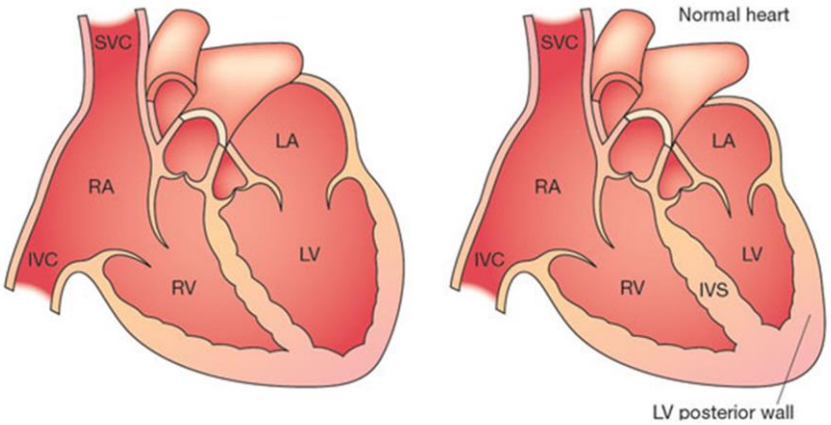

Figure 2-3. Comparison of a normal heart with normal and a heart with dilated cardiomyopathy [5]

Congenital heart defects, also known as congenital heart disease, are a class of anatomical cardiac malformations that can compromise the function of the heart. Some examples of congenital heart defects include: atrial septal defects (hole in the atrial septum), hypoplastic left heart syndrome (underdeveloped left ventricle), and Tetralogy of Fallot (consists of ventricular septal defect, pulmonary stenosis, right ventricular hypertrophy, and an overriding aorta) [20].

The majority of these diseases necessitate some form of surgical intervention to encourage adequate perfusion of the organs. In severe cases, children the most deadly diseases must undergo heart transplantation. The development of circulatory support devices in the form of blood pumps has ushered in a new era of heart failure therapy for children and adult patients waiting for viable heart transplants.

2.2 Overview of Mechanical Circulatory Support

The use of mechanical circulatory support started when Dr. John Gibbon used a roller pump in the first clinically successful cardiopulmonary bypass on a patient with an atrial septal defect [7]. As a result, the National Institutes of Health (NIH) established the U.S. Artificial Heart Program in 1964 to fund the development of total artificial hearts (TAH) for adults suffering from heart failure. While the ambitious goal of replacing the entire heart with a mechanical blood pump ultimately failed in the 1960's through the 1980's, the program led to the growth of the mechanical circulatory support field and the development of key clinical devices like the intra-aortic blood pump [21], [22], the extracorporeal membrane oxygenation (ECMO) system [23], and the first implantable pneumatic ventricular assist device (VAD) [24]. In the late 1990's a multicenter study supported by the NIH National Heart, Lung, and Blood Institute, known as the Randomized Trial of Mechanical Circulatory Support for the Treatment of Heart Failure (REMATCH), demonstrated that ventricular assist devices were superior for long-term implantation and palliation for patients with end-stage heart failure when compared to optimal medical management [25]. As a result, today there are currently 7 VADs (4 pulsatile and 3 continuous flow) and 1 TAH FDA approved for use in adults [7]. The design of these devices has also evolved over the past decades from large pulsatile positive displacement pumps to implantable turbine devices that provide non-pulsatile flow.

There are two types of adult VADs: pulsatile pumps (1st generation blood pumps) and continuous flow pumps (2nd and 3rd generation blood pumps). Pulsatile pumps were the first developed blood pumps for adults with heart failure. The first clinically approved pulsatile ventricular assist device was the Pierce-Donachy VAD, which consists of a pneumatic chamber, flexible diaphragm, blood sac, pneumatic driveline, and inlet and outlet valves (Figure 2-5a) to mimic the ventricle. These pumps are positive displacement pumps that are placed outside of the patient's body. The mechanism by which these devices eject blood varies. However, the most common method is the use of pneumatics. During systole, pressurized air fills the pneumatic chamber via the driveline to compress the diaphragm and allow blood to be ejected from the blood sac through the outlet valve. During diastole, negative pressure is applied to the pneumatic chamber which opens the inlet valve (closes outlet valve) and fills the blood sac. The valves, which are typically tilting disc valves or tri-leaflet polymer valves, ensure unidirectional blood flow. The inlet of these devices is connected to the failing ventricle via cannula while the outlet is connected to the corresponding systemic circulation. The majority of research on pulsatile VADs has been geared towards reducing the incidences of blood clotting, thrombosis, and increasing biocompatibility of blood contacting surfaces [26]. As a result, the pneumatic drivers that supply pressurized air have not decreased in size significantly. The use of continuous flow pumps in adults has also provided an alternative to the large pulsatile VAD drivers needed for 1st generation blood pumps.

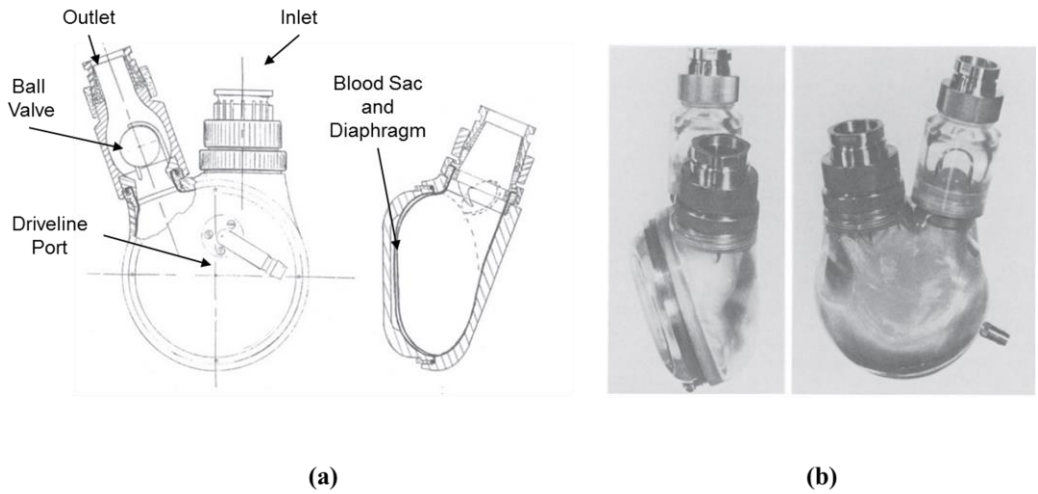

Figure 2-4. (a) Drawings of the first clinically used paracorporeal pneumatically actuated pulsatile VAD from Thoratec (PVAD) (b) images of the developed device [14]

Continuous flow pumps eliminated the need for large external pneumatic drivers and valves. They also consume less power which has resulted in a reduction in battery size [7]. The 2nd generation devices consist of a magnet-impregnated vaned impeller resting on sapphire bearings. An electromagnet, contained in the pump housing, induces impeller rotation. Third generation VADs build on 2nd generation technology utilize magnetic bearings to levitate the impeller to eliminate the need for blood-contacting sapphire bearings [27]–[31]. Two types of blood pumps that use this technology are axial flow pumps (Figure 2-6a) and centrifugal pumps (Figure 2-6b). Centrifugal pumps require lower impeller speed [7]. While continuous flow pumps have miniaturized entire VAD systems for adults, they are associated with increased bleeding [32], blood cavitation, and ventricular septum collapse due to suction [33]. Nonetheless, over the past 50 years the development of adult mechanical circulatory support has improved the lives of countless of patients with heart failure.

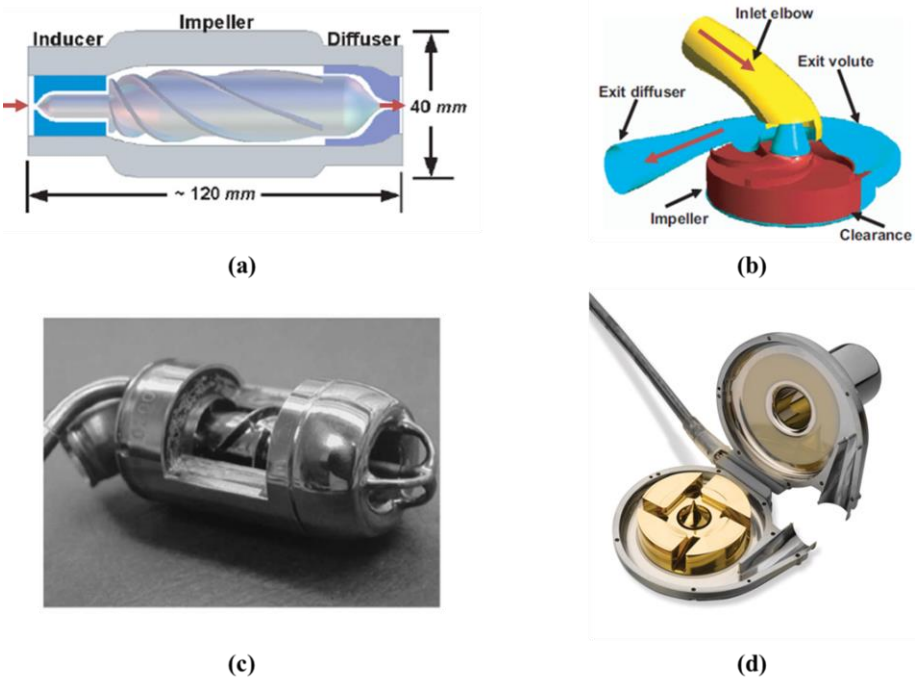

Figure 2-5. (a) Cross-sectional view of an axial continuous flow VAD (b) centrifugal continuous flow VAD [17], (c) the Jarvik 2000 axial flow VAD [16], and (d) the Heart-Ware HVAD centrifugal pump [7]

The majority of ventricular assist device research to date has centered on designing blood pumps that are biocompatible, cause minimal blood damage, and minimize thrombus formation (references). Researchers have concluded that the local flow profiles of blood entering and leaving ventricular assist devices, pulsatile or continuous, are important factors contributing to hemolysis (blood damage) and clot formation. The first extensive study on the flow profile of blood through pulsatile blood pumps was by Baldwin (1990's). Baldwin showed that pulsatile blood pumps, specifically the 70cc stroke volume Penn State pulsatile LVAD, when designed correctly, do not have high wall shear stresses and no areas of stagnant flow [34]. Two key variables with pulsatile pumps are inlet valve design and the angle of outflow and outflow [35]. Similarly, research with continuous flow blood pumps have utilized computational fluid dynamics (CFD) to ensure blood contacting surfaces, impeller speed, and pump clearances do not lead to high shear stress that can cause hemolysis, cavitation or stagnant flow that can

encourage thrombus deposits [36], [37]. Nonetheless, the majority of research has centered on eliminating hemolysis and thrombus formation regardless of the mechanism by which pulsatile and continuous flow pumps operate.

The performance of continuous and pulsatile VADs differ significantly because of the mechanisms each of these designs utilizes to impart energy into the circulation. Continuous flow VADs are classified as dynamic pumps. These types of pumps continuously impart energy into the fluid by increasing the fluid velocity within the pump to values greater than at the discharge port [38]. This has the effect of producing a pressure differential (head pressure) across the pump that results in a volumetric flow rate. Pulsatile VADs are categorized as positive displacement pumps that impart energy into a fluid (usually enclosed) by applying a force via a movable boundary. This movable boundary directly increases the pressure on the fluid until it discharged through the outlet, usually through a valve. The actuating mechanism used in these type of devices vary from pneumatic actuation to electric motor drives. Nonetheless, the performances of dynamic and positive displacement pumps differ significantly and have a significant effect on the efficiency of these devices.

Figure 2-7(a-b) show the performance curves for a dynamic pump and a positive displacement pump. The graphs also show the typical curves for hydraulic systems with resistance. Typically, as the flow rate through a hydraulic system (with losses) increases the pressure losses across that system increase. This resistive loss is typically nonlinear and increases parabolically as a function of flow rate. When a dynamic pump, like a continuous flow VAD is attached to the hydraulic system, the performance curve of the pump intersects hydraulic system curve to yield the pump operating point. Dynamic pumps are characterized by a parabolic head-flow rate curve. As the head or differential pressure across the pump is decreased the flow rate

increased. In other words, as the outlet pressure increases (for a constant inlet pressure and impeller rotation) the flow rate decreases (Figure 2-7a). As a consequence, the pressure produced by dynamic pumps is highly dependent on the load or pressure in the hydraulic system.

Conversely, the pressure produced by positive displacement pumps is only dependent on the stroke volume (and any leakages across the seals and ports). As a result, the performance curves for positive displacement pumps are vertical lines, which suggest that flow rate is constant regardless of the pressure in the hydraulic system. While this may seem to indicate that positive displacement pumps are superior, it is important to note the dynamic pumps are typically more reliable [38].

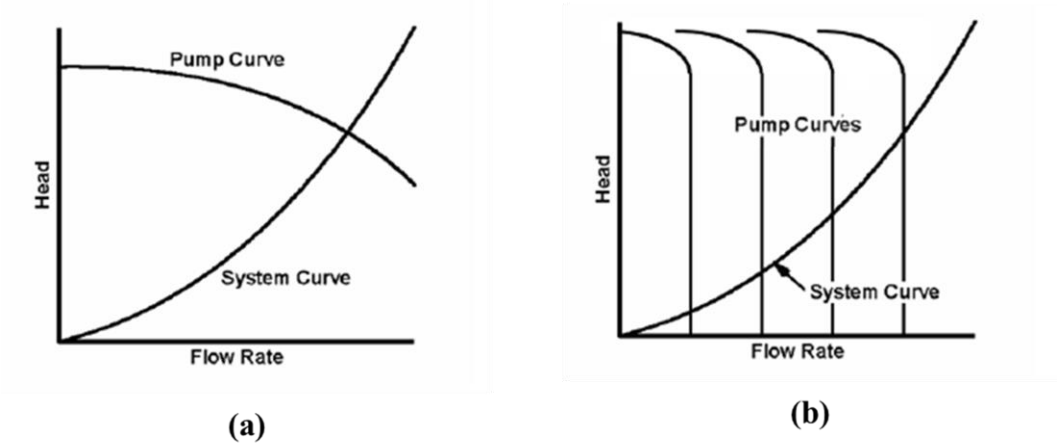

Figure 2-6. (a) Performance curve for a dynamic type pump and (b) performance curves for a positive displacement type pump

2.3 Pediatric MCS Devices

The last 50 years have yielded numerous successful adult mechanical support devices (both pulsatile and continuous flow devices). Unfortunately, the technology has not translated to a Food and Drug Administration (FDA) approved device for pediatric patients with heart failure. Design of pediatric specific assist devices can be challenging because of the small size of children and continuous physical of these patients [39]. It was not until 2004 that the National

Heart Lung and Blood Institute at the National Institutes of Health established a program to provide VADs specifically designed for pediatric patients. Under this program, five contracts were awarded for the development of ventricular assist devices designed for patients with BSAs less than 0.7 m^2 [4]. One of these contracts was awarded to Pennsylvania State University for the development of a pulsatile pediatric VAD (Figure 2-8a). This blood pump uses a seamless blood sac which has led to improved flow profiles and potentially reduced risk of thrombosis and blood clotting [40]. Another contract was awarded to the University of Pittsburgh for the development of a continuous flow PediaFlow pump which uses magnetic bearings to levitate the rotating impeller [41] (Figure 2-8b).

The Berlin Heart EXCOR, similar to the Penn-State pulsatile VAD, is a pneumatically driven pulsatile pump that comes in sizes ranging from 10 mL stroke volumes to 80 mL stroke volumes [42]. It is the only FDA approved VAD for children with a body surface area (BSA) less than 0.7 m^2 [7]. Thus, while trends in adult mechanical circulatory support have shifted towards continuous flow devices, pulsatile VADs are still crucial to pediatric patient survival. Even though the portable drivers for adult pulsatile VADs have been developed they are not rated for the high resistance presented by pediatric inlet and outlet cannula [7]. In addition, they are not able to supply the high pressures needed at high pulse rates. Rating these drivers for pediatric pulsatile VADs would increase their size.

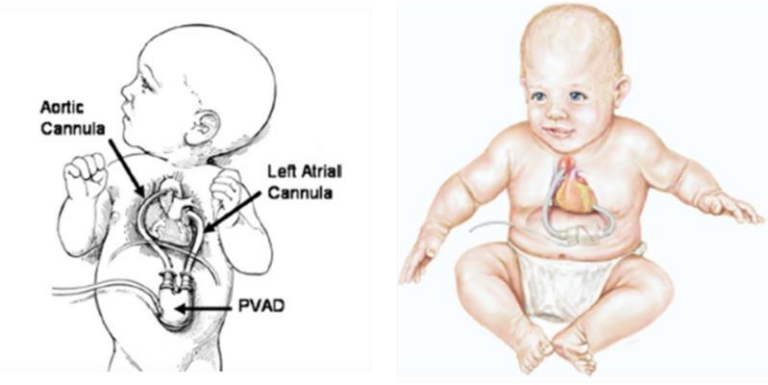

Figure 2-7. (a) Progressive miniaturization of pulsatile VAD drivers [32] and (b) design of the smallest pulsatile drivers to date [33]

2.4 Pulsatile Blood Pump Driver Design

The progressive miniaturization of ventricular assist devices and their drivers has improved patient mortality and mobility. Mobility has been shown to be important to recovery after cardiac surgery [5]. As mentioned previously, the drivers for continuous flow pumps are inherently small because of the limited number of moving parts and their lower power requirements. However the drivers for pulsatile VADs have also undergone a significant decrease in size. One of the first commercially available pulsatile drivers was the CardioWest circulatory support system (CCS) or "Big Blue" (Figure 2-9a) [43]. The driver, which weighs a little under 150 kg [6], is used to provide pneumatic pressure to the CardioWest Total artificial Heart and consists of two pneumatic drivers (one for redundancy), air tanks, alarm, and computer monitor [43]. Development of more compact air compressors, has led to more portable VAD driving systems. Thoratec's TLC-II, for example, was the first commercially available portable electro-pneumatic driver capable of powering two pulsatile ventricular assist devices [44]. The device consisted of four electric motor-driven air compressors, directional proportional valves, and a microcontroller. Typically these driving systems regulate the amount of air volume delivered to the pulsatile VAD plenum during systole (ventricular ejection) and how much vacuum is applied

during diastole (VAD filling). The heart rate and the amount of time the driver applies pressure/vacuum during systole and diastole are typically adjustable.

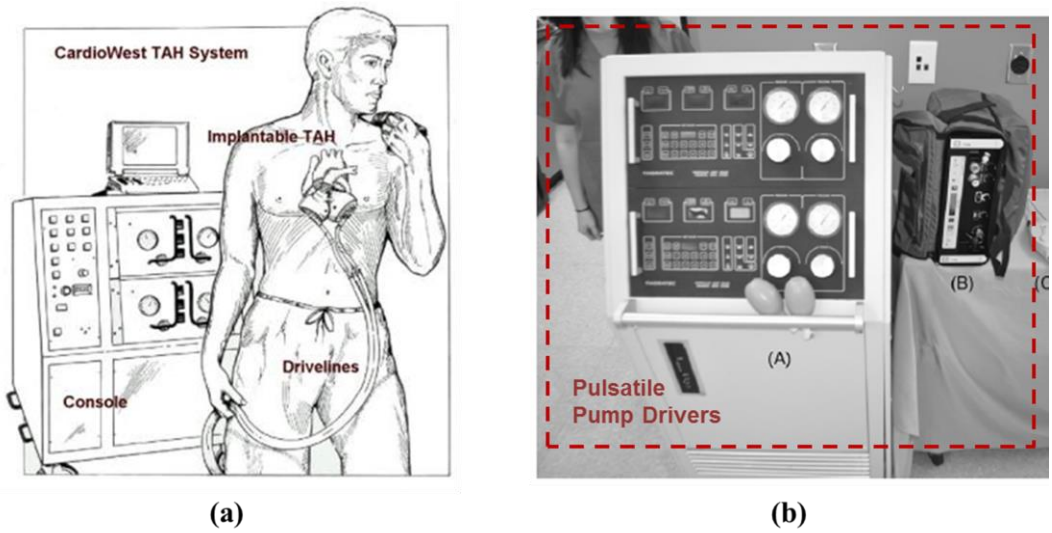

Figure 2-8. (a) Drive console for pulsatile VADs and the CardiWest TAH [35] (b) hospital stationary pneumatic driver and the TLC II [32]

The most common type of air compressor used in portable VAD driving consoles is the reciprocating-piston air compressor. Nishinaka *et al*. developed a 20 cm x 8.5 cm x 20 cm and 1.8 kg pneumatic driver that utilized a brushless DC motor with gears and a crankshaft-piston to drive a 70 mL stroke pulsatile VAD at 100 beats per minute (BPM) against a 120 mm Hg back pressure [45]. The driver also consumed 12 W of power during animal tests, which is on par with some of the continuous flow VADs. In 1992, Sipin *et* al. developed a 2.5 kg portable pneumatic drive console that utilized a rotary air compressor to provide pressurized air to a TAH and pneumatic VADs [46]. Syncardia Systems Inc. has developed a 5 kg driver [47]. The drive unit consists of two motors and two pistons housed in the same cylinder (Figure 2-10a). The motors actuate the pistons to provide a sweeping volume for a right VAD and left VAD [48]. For these reciprocating drivers, the pressure applied to the VAD pump chamber is a function of the sweeping volume the dead air volume contained in the actuation system. More recently,

Syncardia has utilized a scroll type air compressor to further miniaturize the driver and eliminate excessive noise that is produced by reciprocating-type pneumatic consoles.

To ensure adequate filling of the VAD blood chamber, a negative pressure (typically -5 to -20 mm Hg) is applied to the VAD pneumatic chamber for 60-70% of the heart rate cycle. During 30% of the cycle, the cylinders of the drivers provide a sweeping volume that result in pressures between 200-300 mm Hg for LVADs and 50-100 mm Hg for RVADs. These drive pressures, as seen in Figure 2-10b, are characterized by increase in pressure due to the initial resistance of the VAD diaphragm. As the diaphragm extends, the drive pressure levels off until it is fully extended and ejects the blood from the blood chamber (see blip in pressure waveform of Figure 2-10b). Because of the compressibility of gas used in these pneumatic drivers, some researchers have utilized various electromechanical and hydraulic drives to integrate the drivers into the VAD pump to make the device totally implantable.

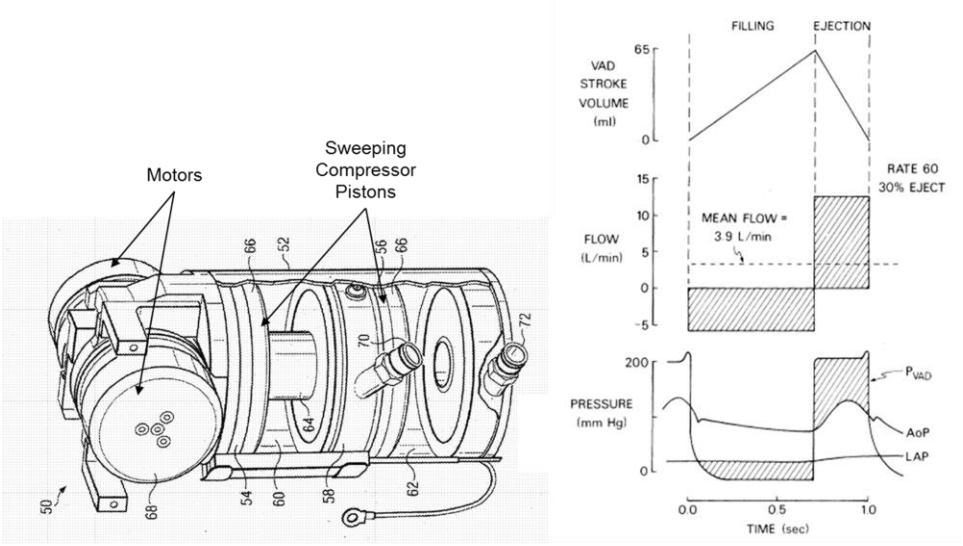

Figure 2-9. (a) Compact reciprocating-piston pulsatile VAD driver [39] and (b) pressure waveforms for an ideal pneumatic pulsatile VAD driver [40]

In an effort to integrate the driving mechanism into the VAD pump, for total implantability, researchers have utilized electromechanical actuators in pulsatile VADs. The

HeartMate VE (vented electric) ventricular assist device, for instance, contains an internal low torque direct current (DC) motor that actuates a pusher plate and textured diaphragm to pressurize the blood chamber and eject blood from the VAD outlet [49], [50]. The motor runs on 12 volts and is powered via a percutaneous driveline. Arrow International developed a similar pulsatile VAD, the Lion Heart LVD-2000, that utilized a transcutaneous powered brushless DC motor that actuates a linear screw mechanism to drive a pusher plate that provides direct blood chamber pressure [51]. In order to eliminate the use of linkages and bearings common in the electromechanical pulsatile VADs, Novacor Corp developed a pulsatile VAD, Novacor II (Figure 2-11a), that uses a magnetically levitated pusher plate as the driving mechanism [52]. The force of the pusher plate on the blood chamber is proportional to the current drawn by the motor which allowed precise control of the drive pressure. Researchers have also looked into the use of DC motors with hydraulics to better impedance match the actuator and failing patient circulation.

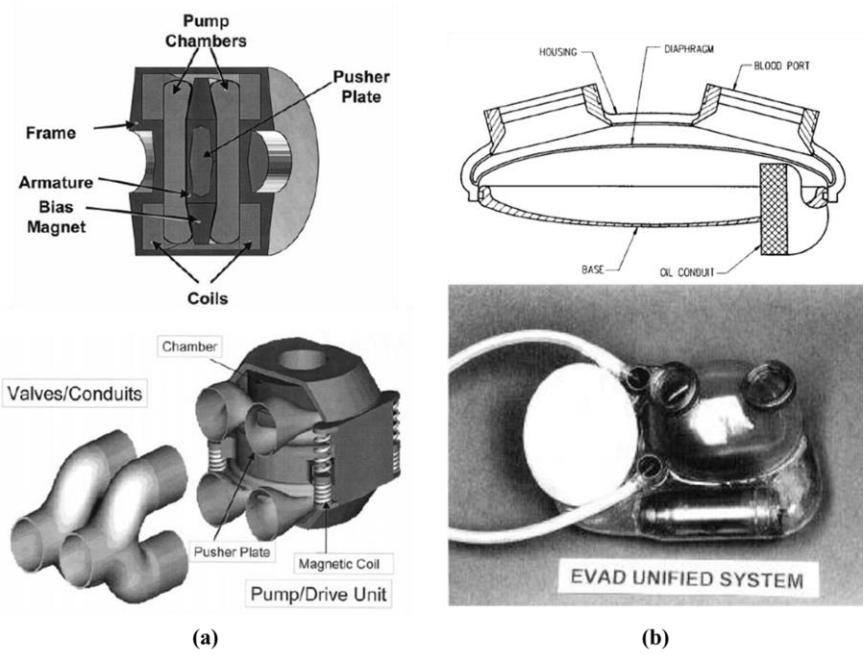

Figure 2-10. (a) The Novacor II pulsatile VAD that utilizes a magnetically suspended pusher plate and (b) electrohydraulic pulsatile VAD

Researchers have also used hydraulic actuation to bypass the compressibility of pneumatic actuation and the need for large pneumatic drivers. Researchers at the University of Utah Artificial Heart Laboratory and the Cardiovascular Devices Division of the University of Ottawa heart Institute developed a permanent implantable electrohydraulic ventricular assist device [53]. The VAD, shown in Figure 2-11b, consists of a blood chamber, oil chamber, oil reservoir (called the video displacement chamber) and a flexible diaphragm that separates the two plenum. During systole, the energy converter drives oil from the video displacement chamber to the oil chamber to deflect the flexible diaphragm. This causes blood to be ejected from the blood chamber. During diastole, the energy converter pushes oil from the oil chamber back to the video displacement chamber causing suction in the oil chamber and subsequent diaphragm restoration for blood chamber filling. The energy converter is an axial flow pump driven by a brushless DC motor [54]. While the device was able to provide 5.7 L/min against 100 mm Hg *in vivo*, the entire device was 18 cm x 12 cm x 4 cm in size and consumed up to 60

W of power. While all these pulsatile drivers have been successful in providing the necessary pressure and flow rate, their size has be constrained by the DC motors they utilize.

2.5 MCS *In Vitro* and *In Vivo* Testing

Before reviewing the fundamentals of piezoelectric transducers and how the can be used in VAD drivers, a brief overview of the testing methods for MCS systems is presented. In order to validate the performance of a mechanical circulatory support device, like an artificial heart, extensive in lab tests must be carried out. Before the device can be used in humans, the device must undergo two types of testing: *in vitro* ("in glass") and *in vivo* ("within the living") testing. *In vitro* testing involves the development of a bench-top system that mimics the physiological state which the medical device in question is designed to assist. In the case of MCS pumps, the bench-top system needs to mimic the cardiovascular hemodynamic state of the human circulation. This involves designing a test rig that will accurately simulate the pressure and flow amplitudes, waves, and response of a human circulatory system. *In vivo* testing involves the use of an animal to create an accurate clinical situation. Again, in the case of MCS devices, researchers must alter an animal's anatomical and physiological state (via surgical or pharmacological methods) to simulate a disease state seen in clinical settings. The device is then used on the animal to test its efficacy in reversing the problems associated with the particular disease in question.

In vitro testing of MCS devices involves the design of hydraulic loops known as mock circulations. These bench-top systems use hydraulic accumulators to mimic the compliance of the vessels in the systemic and pulmonary branch circulations. Needle valves or pincher valves are used to mimic the resistance of the blood vessels. To mimic the viscosity of blood, water and glycerin are mixed. One of the first mock circulations developed for total artificial heart testing

was by Donovan in 1975 [55] (Figure 12a). The mock circulatory system was built from 1/2" in thick acrylic sheets with hermetically sealed compliance chambers separated by the acrylic walls. The compliance of each chamber, which simulated the arterial and venous branches, is set by modulating the amount of entrapped gas above the fluid. In general, because the elasticity of the veins is much higher than that of the arteries, the compliance chambers are larger. Similar to Donavan, Lui *et al*. constructed a mock circulation for testing ventricular assist devices in parallel to a failing ventricle [56] (Figure 12b). The hydraulic loop consisted of two cardiac simulators to act as the left and right atrium. The cardiac simulators consisted of rubber diaphragms encased in transparent sealed air chamber with check valves simulating the cardiac valves. Airtight tanks mimicked the systemic arterial, systemic venous and pulmonary compliances. Various researchers have develop more sophisticated mock circulations that mimic the hemodynamics of pediatric patients and congenital heart disease patients [57]–[59].

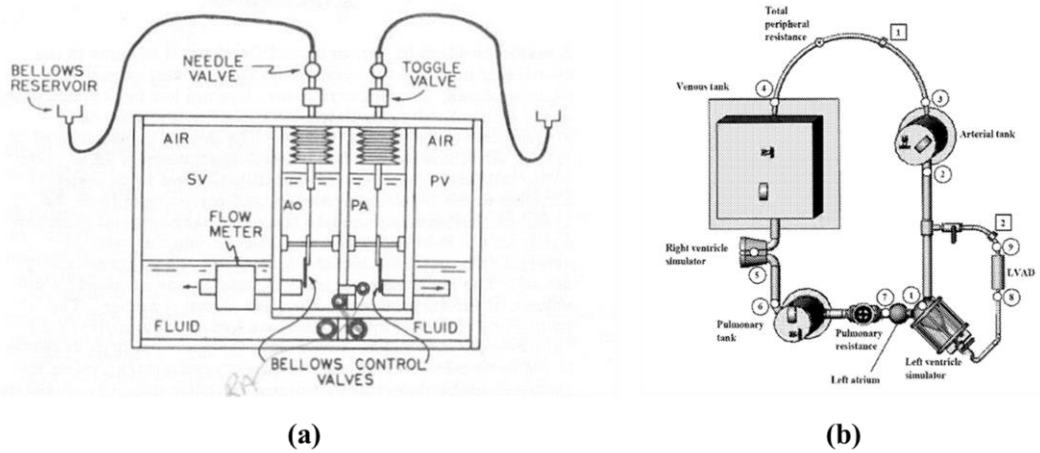

Figure 2-11. In vitro mock circulation for testing artificial hearts [47] and ventricular assist devices [48]

While *in vitro* mock circulations are invaluable to testing newly developed mechanical circulatory devices, they do have their limitations. For instance, the Frank-Starling mechanism (ventricles output adjusts to preload) is not easily simulated in *in vitro* mock circulations. In

addition, device biocompatibility, ventricular structure, ventricular function and neurohormonal response to device implantation and therapy cannot be studied in the lab. As a result, animal models of heart disease are needed to accurately predict the efficacy of therapeutic medical devices. The choice of animal used to mimic the desired disease state is important and anatomical and physiological considerations must be taken into account. With regards to animal models for general heart disease, swine, dog, and sheep are typically used [60] because of the close anatomical and physiologic similarity to human hearts.

In order to test the effectiveness of mechanical circulatory support devices in recovering hemodynamic outcomes, animal models simulating heart failure are crucial. The majority of animal models used to test ventricular assist devices are dilated cardiomyopathy induced heart failure. This disease state can be achieved a few ways in swine, dogs, or sheep. The most common method to induce ventricular failure via cardiomyopathy is by pacemaker-induced tachycardia [61]. With this method, a pacemaker disrupts the electrical activity of the heart resulting in ventricular tachycardia. This pacing induces ventricular systolic function and myocyte contractile dysfunction which are both present during heart failure. A ventricular assist device inlet is attached to the ventricular apex and the outlet is attached to the ascending aorta (for LVAD configuration) for mechanical support. Another method to induce dilated cardiomyopathy in animals is to ligate a coronary artery (which induces a myocardial infarction and subsequent myocyte dysfunction) or place microspheres to block the coronary circulation [62].

2.6 Summary

In this chapter a summary of the anatomy and physiology of a heart was presented to give a foundation for the mechanisms behind cardiac pumping. The background was extended to

understand the mechanisms leading to heart failure. A history mechanical circulatory support (MCS) devices used for adults and pediatric patients with heart failure was also covered. The various types of driving mechanisms for pulsatile and continuous flow MCS devices were discussed. Finally, a review of *in vitro* and *in vivo* MCS testing methods was presented.

Chapter 3: Piezoelectric Hydraulic Pump Literature Review

In this chapter a summary of piezoelectric transducers is presented. The crystallographic origins of piezoelectric phenomenon are discussed and the resulting constitutive relations for these devices are also reviewed. Lastly, an overview of piezoelectric actuators and frequency-leveraged piezoelectric motors and pumps are discussed to lay the groundwork for their use in mechanical circulatory support.

3.1 Piezoelectric Transducer Background

In this section the phenomena of piezoelectricity is presented. The crystallographic origin of piezoelectricity is explained and the constitutive relations for piezoelectric materials are discussed. The use of frequency rectification to produce high power density piezoelectric motors is then presented. Lastly, the advantages of piezohydraulic pumps over ultrasonic piezoelectric motors are discussed.

Piezoelectricity History

In 1880 Jacques and Pierre Curie discovered that certain crystalline materials develop a macroscopic polarization, in the form of a surface charge, when subjected to a mechanical stress. This relationship between applied mechanical stress and induced charge became known as the direct piezoelectric effect. Soon after, in 1881, Gabriel Lippman mathematically predicted the converse effect, a mechanical strain in response to an applied electric field, from thermodynamic principles. The Curie brothers confirmed the converse, also called in-direct, piezoelectric effect later that year [63].

Piezoelectric Crystallographic Properties

Piezoelectric materials are a class of dielectric (electrically insulating) materials that can be polarized with the application of an electric field and/or the application of an external mechanical

stress. Traditional piezoelectric ceramics have a perovskite crystal structure (ABO_3), shown in Figure 3-1a. The crystal structure, shown as a simple unit cell, consists of large cations on the corners (A), a smaller cation in the middle (B), and oxygen (O_2^-) at the center of the faces (O) [64]. The large cations are usually divalent metal ions like Barium or Lead. The small center cation is usually a small metal tetravalent ion like Titanium or Zirconium. For a crystal perovskite crystal with cubic symmetry, the top and bottom oxygen anions are in plane (in all three directions) with the corner large cations and the side oxygen anions are in plane with the center small cation. This centrosymmetric configuration means that there is no uneven spatial distribution of charge and as a result there is no net polarization. This means that there is no electric dipole moment associated with the crystal. Above a critical temperature, known as the Curie temperature, the perovskite crystal structure typically exhibits this cubic structure because the oxygen anions fit in a centrosymmetic position. Two important characteristics of cubic crystal structures are that the three crystal axis are perpendicular and have the same length. As a result, the mechanical and electrical properties are the same in all three directions (isotropic).

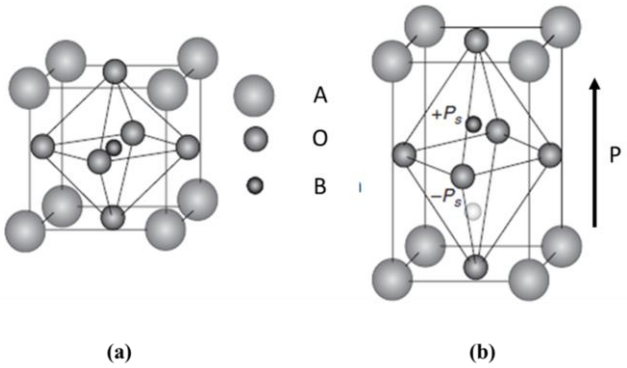

Figure 3-1. (a) Perovskite crystal structure with cubic symmetry (above Curie temperature) (b) Tetragonal perovskite crystal structure with a net dipole moment [3]

Below the Curie temperature, the crystals are either tetragonal or rhombohedral depending on the composition. Tetragonal and rhombohedral structures are characterized by a dimensional offset between the cations and the anions, which results in an uneven spatial

distribution of charge (polarization). A tetragonal crystal for instance, shown in Figure 3-1b, has an offset between the top plane A cations and the top center oxygen anion. There is also an offset between the central B cation and the center plane oxygen anions. This gives rise to a net polarization and dipole moment in the crystal because the bottom of the crystal is charged more negative and top is more positive. It is important to note that the polarization direction can have six stable directions. This means that the oxygen cations can "pop" out from the top, bottom, or sides without a preferred direction. Because of this distortion in the placement of the cations and anions, the length of the unit cell is elongated in one direction (along the direction of the polarization). For a tetragonal crystal structure, all three crystal axis are perpendicular with only two sides of the same length. Crystal structures that are tetragonal are said to be transversely isotropic because the two axis with the same lengths have identical mechanical and electrical properties. However, the mechanical and electrical material properties along the polarization direction of the crystal differ from the other two directions.

Piezoelectric Poling and Switching

Some piezoelectric materials constitute a subset of materials known as ferroelectrics. Ferroelectric materials are materials that exhibit spontaneous polarization. However, not all piezoelectrics are ferroelectric (even though all ferroelectric materials are piezoelectric). Piezoelectric materials typically operate along a linear region where ferroelectrics can exhibit nonlinear behavior. Typically, the spontaneous polarization direction within a ferroelectric material is not uniform throughout the material. Because there are six possible directions of polarization (including the negative directions), the spontaneous polarization throughout the material will vary. In fact, there are regions within the bulk material where polarization is uniform, and these are called domains (Figure 3-2). The boundary connecting these domains of

uniform polarization directions is called a domain wall. Domain walls that lie between domains in which the polarizations are oriented in opposite directions are called 180˚ walls (Figure 3-2). Similarly, walls that lie between domains in which the polarizations are oriented perpendicular to each other are called 90˚ walls (Figure 3-2). The orientation of the polarizations within these domains can be manipulated by applying electric energy (in the form of an electric field) or mechanical energy (in the form of an applied stress).

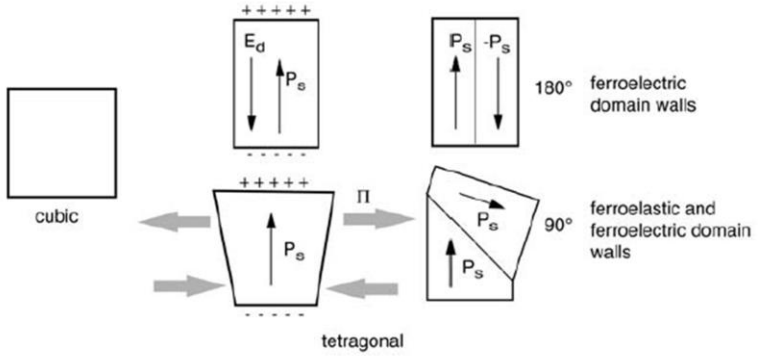

Figure 3-2. Ferroelectric domains and domain walls (180˚ and 90˚ domain walls) [4]

The net polarization of a ferroelectric can be manipulated by the application of an electric field. Consider a ferroelectric material with no net polarization (has regions of uniform polarization but no net polarization direction). On Figure 3-3a, the material starts off at point A. Upon the application of a positive electric field, the ferroelectric domains begin to align in the direction of the applied field. When a large enough positive field is applied (points A-D), the majority of the ferroelectric domains are aligned in the direction of the electric field. An increase in the electric field after a certain electric field level will not increase the polarization. The point at which this occurs is called the saturation field strength (usually 2-3 MV/m). When the electric field is removed the polarization of the material begins to decrease. When the electric field reaches zero, a net remnant polarization still exists. When the electric field is driven into the

negative regime (points E-G), some domains start to switch back (antiparallel to electric field) until half of the polarizations are aligned against the field (point F). A further decrease in the electric field eventually leads to the majority of the domains to align in the negative direction until the polarization saturates (point G). When the electric field is increased (points G- C) some domains switch in alignment with the electric field while others remain (leaving a remnant negative polarization). As the electric field enters the positive regime, the domains begin to align in the positive direction. The cycle then repeats. The electric field necessary to bring the polarization to zero is called the coercive field. The energetic loss during this cycle is equal to the area under the P-E loop. Cycling this process at high frequency can lead to significant loss in energy in the form of heat.

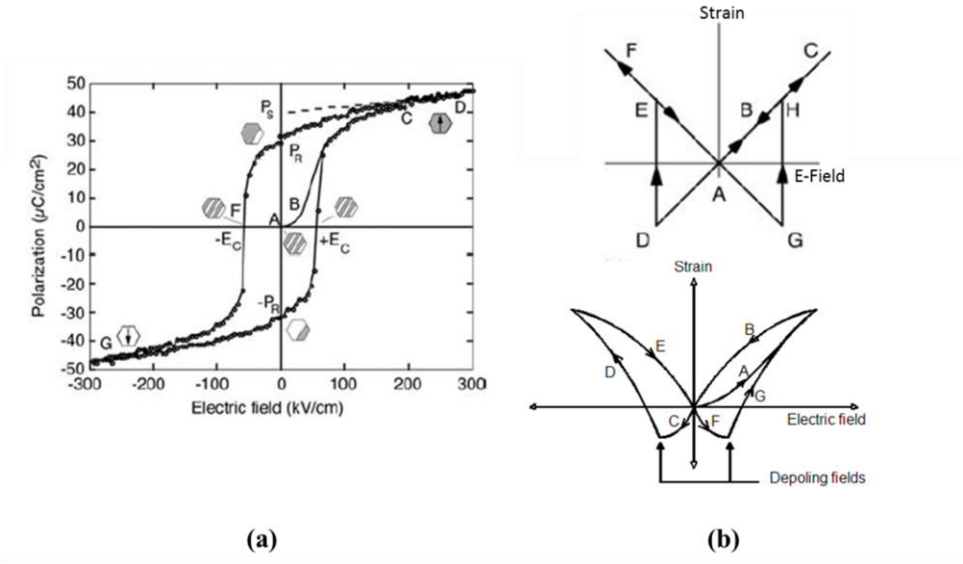

Figure 3-3. (a) Polarization versus electric field plot of a ferroelectric material with no net polarization (b) strain versus electric field of ferroelectric material without an initial net polarization [4]

The application of an electric field also induces a change in the ferroelectric dimension (or strain). This is important in actuators that utilize ferroelectric and piezoelectric materials. Consider a ferroelectric with no net polarization. When a positive electric field is applied in the

direction of the polarization, the crystal expands linearly along the direction of the applied electric field (which constitutes a piezoelectric regime). When the electric field is decreased the strain moves back to zero. As the electric field turns negative, the ferroelectric material contracts in a linear fashion. When the electric field is sufficiently negative, the polarization switches to align with the electric field which causes the material to expand (positive strain). As the electric field is increased again into the positive regime, the material starts to contract again until the electric field is sufficiently positive to cause the polarization to switch. This causes the material to expand (positive strain). This is the ideal strain versus electric field curve for a ferroelectric material. This plot is typically known as the butterfly curve.

The butterfly curve of real ferroelectric materials is usually more complicated. For example, the linear piezoelectric regime is not entirely linear and does exhibit some hysteresis. In addition, the negative strain (contraction) for these materials is not as large as the positive strains that can be produced. In this dissertation, we are concerned about the linear strain behavior of piezoelectric materials. This means that we are restricted to points ABC in the bottom plot of Figure 3-3b.

Piezoelectric Constitutive Equations and Induced Strain

Piezoelectric ceramic transducers can be used as sensors (direct piezoelectric effect) or as actuators (indirect piezoelectric effect). The set of mathematical formulations that describe the electromechanical coupling exhibited by piezoelectrics are the piezoelectric constitutive relations. These equations of state relate the elastic variables, electric field and electric displacement, to the elastic variables, stress and strain [64]. The compact strain-charge form, as seen in equations 3-1 and 3-2, relate the mechanical strain and electric displacement as functions of applied stress and electric field.

$$S_i = s_{ij}^{E} T_j + d_{ik} E_k \qquad (3\text{-}1)$$

$$D_m = d_{mj} T_j + \varepsilon^T_{mk} E_n \qquad (3\text{-}2)$$

S_i is a 6x1 strain vector, s^E_{ij} is the 6x6 compliance matrix at constant electric field, T_j is the 6x1 stress vector, d_{ik} is the 3x6 piezoelectric coupling coefficient matrix, ε^T_{mk} is the 3x3 electric permittivity matrix, and E_k is the 3x1 electric field vector. In expanded form of these equations are shown in (3-3 and 3-4).

$$\begin{Bmatrix} S_1 \\ S_2 \\ S_3 \\ S_4 \\ S_5 \\ S_6 \end{Bmatrix} = \begin{bmatrix} s^E_{11} & s^E_{12} & s^E_{13} & s^E_{14} & s^E_{15} & s^E_{16} \\ s^E_{21} & s^E_{22} & s^E_{23} & s^E_{24} & s^E_{25} & s^E_{26} \\ s^E_{31} & s^E_{32} & s^E_{33} & s^E_{34} & s^E_{35} & s^E_{36} \\ s^E_{41} & s^E_{42} & s^E_{43} & s^E_{44} & s^E_{45} & s^E_{46} \\ s^E_{51} & s^E_{52} & s^E_{53} & s^E_{54} & s^E_{55} & s^E_{56} \\ s^E_{61} & s^E_{62} & s^E_{63} & s^E_{64} & s^E_{65} & s^E_{66} \end{bmatrix} \begin{Bmatrix} T_1 \\ T_2 \\ T_3 \\ T_4 \\ T_5 \\ T_6 \end{Bmatrix} + \begin{bmatrix} d_{11} & d_{12} & d_{13} \\ d_{21} & d_{22} & d_{23} \\ d_{21} & d_{32} & d_{33} \\ d_{41} & d_{42} & d_{43} \\ d_{51} & d_{52} & d_{53} \\ d_{61} & d_{62} & d_{63} \end{bmatrix} \begin{Bmatrix} E_1 \\ E_2 \\ E_3 \end{Bmatrix} \qquad (3\text{-}3)$$

$$\begin{Bmatrix} D_1 \\ D_2 \\ D_3 \end{Bmatrix} = \begin{bmatrix} d_{11} & d_{12} & d_{13} & d_{14} & d_{15} & d_{16} \\ d_{21} & d_{22} & d_{23} & d_{24} & d_{25} & d_{26} \\ d_{21} & d_{32} & d_{33} & d_{34} & d_{35} & d_{36} \end{bmatrix} \begin{Bmatrix} T_1 \\ T_2 \\ T_3 \\ T_4 \\ T_5 \\ T_6 \end{Bmatrix} + \begin{bmatrix} \varepsilon^T_{11} & \varepsilon^T_{12} & \varepsilon^T_{13} \\ \varepsilon^T_{21} & \varepsilon^T_{22} & \varepsilon^T_{23} \\ \varepsilon^T_{31} & \varepsilon^T_{32} & \varepsilon^T_{33} \end{bmatrix} \begin{Bmatrix} E_1 \\ E_2 \\ E_3 \end{Bmatrix} \qquad (3\text{-}4)$$

Because most piezoelectrics are orthotropic materials (mechanical properties are unique and direction dependent) and because of symmetry in the crystal structure the constitutive relations in 3-3 and 3-4 are reduced to the following:

$$\begin{Bmatrix} S_1 \\ S_2 \\ S_3 \\ S_4 \\ S_5 \\ S_6 \end{Bmatrix} = \begin{bmatrix} s^E_{11} & s^E_{12} & s^E_{13} & 0 & 0 & 0 \\ s^E_{21} & s^E_{22} & s^E_{23} & 0 & 0 & 0 \\ s^E_{31} & s^E_{32} & s^E_{33} & 0 & 0 & 0 \\ 0 & 0 & 0 & s^E_{44} & 0 & 0 \\ 0 & 0 & 0 & 0 & s^E_{55} & 0 \\ 0 & 0 & 0 & 0 & 0 & s^E_{66} \end{bmatrix} \begin{Bmatrix} T_1 \\ T_2 \\ T_3 \\ T_4 \\ T_5 \\ T_6 \end{Bmatrix} + \begin{bmatrix} 0 & 0 & d_{13} \\ 0 & 0 & d_{23} \\ 0 & 0 & d_{33} \\ 0 & d_{24} & 0 \\ d_{15} & 0 & 0 \\ 0 & 0 & 0 \end{bmatrix} \begin{Bmatrix} E_1 \\ E_2 \\ E_3 \end{Bmatrix} \qquad (3\text{-}5)$$

$$\begin{Bmatrix} D_1 \\ D_2 \\ D_3 \end{Bmatrix} = \begin{bmatrix} 0 & 0 & 0 & 0 & d_{15} & 0 \\ 0 & 0 & 0 & d_{24} & 0 & 0 \\ d_{13} & d_{23} & d_{33} & 0 & 0 & 0 \end{bmatrix} \begin{Bmatrix} T_1 \\ T_2 \\ T_3 \\ T_4 \\ T_5 \\ T_6 \end{Bmatrix} + \begin{bmatrix} \varepsilon_{11}^T & 0 & 0 \\ 0 & \varepsilon_{22}^T & 0 \\ 0 & 0 & \varepsilon_{33}^T \end{bmatrix} \begin{Bmatrix} E_1 \\ E_2 \\ E_3 \end{Bmatrix} \qquad (3\text{-}6)$$

3.2 Piezoelectric Actuators and Motors

There are typically two modes of operation of piezoelectric transducers, the 33-mode and 31-mode operating mode. When used as actuators, piezoelectric ceramics operated in the 33-mode require an electric field in the same direction as the polarization (3-direction or z-direction) to produce a strain in that direction. Piezoelectric ceramics operated in the 31-mode produce strains in the 1-direction (x-direction) when an electric field is applied in the same direction as the polarization (3-direction). The most common 31-mode actuators are piezoelectric extensional and benders shown in Figure 3-4. These multilayer composite actuators contain two layers of piezoelectric ceramics that sandwich a non-active layer (such as aluminum, steel, or brass). Typically the polarization direction is in the 3-direction with strain produced in the 1-direction when an electric field is applied in the direction of polarization. For extensional actuators, the electric field is applied in the same direction as the crystal polarization for both piezoelectric layers, resulting in a net displacement in the 1-direction (Figure 3-4a). For benders, the electric field is applied antiparallel to the polarization of one piezoelectric layer, which causes a contraction in the 1-direction for that layer. The net displacement for benders is in the 3-direction (Figure 3-4b).

When utilizing piezoelectric transducers in the 31 operating mode, the following assumptions are made to simplify the constitutive equations 2-5 and 2-6.

$$E_1 = 0,\ T_3 = 0,\ T_2 = E_2 = 0,\ T_4 = 0,\ T_5 = 0,\ T_6 = 0 \qquad (3\text{-}7)$$

As a result, the strain (in the 1-direction) and electrical displacement (in the 3-direction) are reduced to the following:

$$S_1 = s_{11}^E T_1 + d_{13} E_3 \qquad (3\text{-}8)$$

$$D_3 = d_{13} T_1 + \varepsilon_{33}^T E_3 \qquad (3\text{-}9)$$

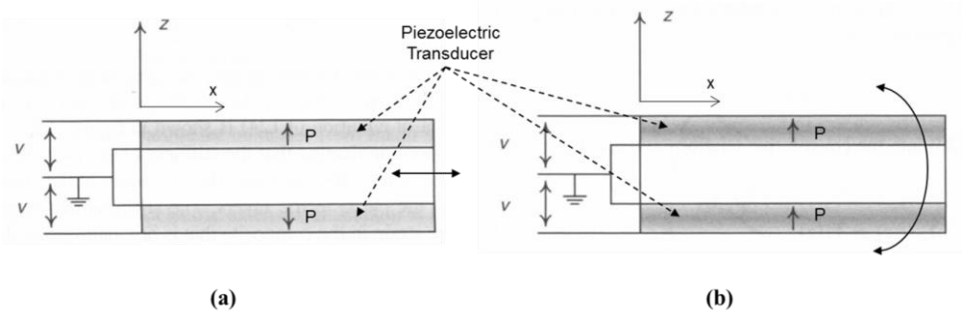

Figure 3-4. (a) Cross-sectional view of a piezoelectric extensional actuator (b) Cross-sectional view of a piezoelectric bender actuator [5]

When utilizing piezoelectric transducers in the 33 operating mode, the following assumptions are made to simplify the constitutive equations 3-5 and 3-6.

$$E_1 = 0,\ T_2 = 0,\ T_1 = E_2 = 0,\ T_4 = 0,\ T_5 = 0,\ T_6 = 0 \qquad (3\text{-}10)$$

As a result, the strain (in the 3-direction) and electrical displacement (in the 3-direction) are reduced to the following:

$$S_3 = s_{33}^E T_3 + d_{33} E_3 \qquad (3\text{-}11)$$

$$D_3 = d_{33} T_3 + \varepsilon_{33}^T E_3 \qquad (3\text{-}12)$$

In this dissertation, we will only consider 1-D piezoelectric transducers operated in the 33-mode. One of the limitations of piezoelectric transducers is the displacement (strain) they can produce. While the stress they can output can be on the order of mega Pascals (large force depending on the geometry of the actuator), the strains that result are at most 1% (or at most a few micrometers

depending on the actuator dimensions). In order to overcome this, engineers have designed different type of actuators, piezoelectric stacks and piezoelectric benders, to produce large displacement.

Piezoelectric benders operated in the 33-mode, typically consist of a passive element like aluminum and a piezoelectric layer. The composite is clamped on one end and left free on the other end. When an electric field is applied to the piezoelectric element, the atrain produced is resisted by the passive layer which results in a bending moment in the composite. This results in a net displacement perpendicular to the plane of the fixed constraint. Piezoelectric benders produce large displacements (100-1000 μm) but with low output forces (>10 N) as seen in Figure 3-5b.

Another common type of 33-mode piezoelectric actuator is the piezoelectric stack. The piezoelectric stack consists of multiple thin layers of piezoelectric ceramics polarized in the 3-direction (Figure 3-5a). Stacking multiple layers of piezoelectric ceramics in series produces an amplification of displacement and force output along the 3-directon. Piezoelectric stack actuators can produce a large amount of force (100-10000 N) and can produce relatively larger displacements (> 100 μm). However, maximum displacement is a function of actuator length and the number of piezoelectric layers. Thus, if a large displacement is needed, a long stack needs to be manufactured. Because the aspect ratio (ratio of length dimension to width dimension) of an actuator should exceed 10, this also puts a constraint on the minimum force output. Researchers have studied mechanisms by which to increase overall displacement from piezoelectric actuators using mechanical leveraging.

Mechanically leverage can amplify displacement multifold. One of the simplest examples is attaching a lever arm to the piezoelectric actuator. In this configuration, the lever is attached to

the piezoelectric stack actuator to amplify the strain output of the device. While this method of mechanical amplification s effective, Guirgiutiu *et* al. showed that the stiffness of the support system (ie. actuator housing) an amplification mechanism can adversely affect the displacement output [65]. They found that the stiffness of the support system should be at least ten times the stiffness of the actuator to limit the compliance losses into the housing. In addition, mechanical amplification reduces the maximum force output of the actuator by the same displacement amplification factor. Thus, in order to increase displacement, another method should be used. On method used by researchers is to utilize the fast response of piezoelectric transducers can help to amplify mechanical displacement without theoretically affecting force output. This not only can increase displacement while maintaining force output, but it can lead to high power actuator systems.

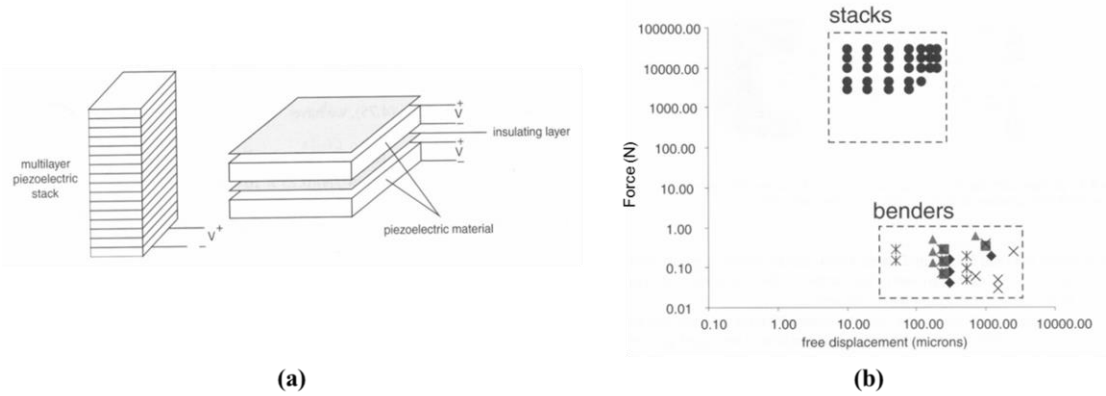

Figure 3-5. (a) Geometry and construction of a multilayer piezoelectric stack actuator (b) Comparison of force and displacements produced by piezoelectric stacks and piezoelectric benders [5]

Frequency-Leveraged Piezoelectric Motors

As mentioned previously, another method researchers have used to increase piezoelectric displacement is to utilize the fast response of piezoelectric transducers. This method is called frequency leveraging [66]. This method involves the "accumulation" of small displacements produced by the piezoelectric transducer by operating it oscillating at high frequency (<1000

Hz). This has two advantages over mechanical leveraging. It can amplify the displacement of the piezoelectric transducer without affecting force output. As a result the moderate work output (force x displacement) of the piezoelectric actuator can be converted to a high power output. This has important implications for the size of devices using these piezoelectric actuators when used at high frequency. Theoretically, piezoelectric transducers can be miniaturized without loss in power output when utilized at high frequencies. Frequency leveraging has yielded high power density piezoelectric ultrasonic motors and piezoelectric pumps.

The power of high frequency operated piezoelectric crystals was not observed until French physicist Paul Langevin developed a submarine detector that sandwiched a quartz crystal between two steel plates [67]. Researchers working on these quartz resonators observed that "quartz winds" emanated from both sides of the device and that these devices could atomize water and sear skin when touched [68]. However, it wasn't until six decades later that high frequency piezoelectrics would be used as motor technology. In 1973, Barth described the first ultrasonic rotary motor utilizing two piezoelectric transducers attached to two horns (Figure 3-6a). When one of the piezoelectric ceramics vibrated at ultrasonic frequencies, the horn would impact a rotor unit and cause the rotor to turn [69]. This sparked the development of many rotary and linear ultrasonic motors, devices that used vibrating piezoelectrics to produce mechanical movement (Figure 3-6b), over the next three decades [8]. For example, in 1982 Sashida developed a wedge-type ultrasonic motor that utilized a piezoelectric Langevin vibrator. The vibrating piece was placed off center from the rotor, which was angled 6º from the vertical axis (Figure 3-6b). When the Langevin vibrator collided with the angled rotor, it would deflect upward, causing the rotor to spin. Sashida was able to achieve a maximum of 60% efficiency, a

maximum power output of 45W with approximately 95W input power (47% efficiency at this point) [70].

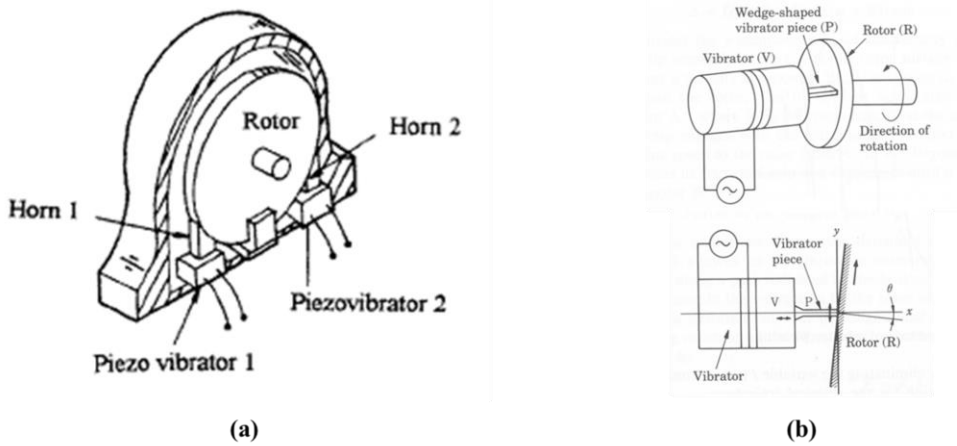

Figure 3-6. (a) First frequency-leveraged piezoelectric rotary motor developed by Barth in 1973 (b) Efficient and powerful wedge-type ultrasonic motor developed by Sashida in 1982 [11]

Since the development of Sashida's motor, many researchers have published manuscripts detailing the design of various miniaturized frequency-leveraged linear and rotary motors. Galante (1998) developed a compact (6x6x2cm) inchworm motor capable of a producing a large holding force (~200 N) and producing amplified displacements (~1 cm). The inchworm configuration uses two piezoelectric stacks as clamps and a third piezoelectric stack as a pusher (Figure 3-7a). The clamps are used to engage or disengage the moving linear element while the pusher provides the linear displacement. Even though the piezoelectric displacement of the pusher is in the micrometer range, high frequency repetition leads to a centimeter net displacement. The smallest ultrasonic motor to date was produced by Cagatay *et al*. (2003). These researchers developed a 1.6mm diameter and 6mm long ultrasonic rotary motor (Figure 3-7b) operating at 130 kHz. The motor produced 0.5mNm torque at a maximum power output of 45mW with a speed of 45 rad/sec and 16% efficiency. While these motors have produced significant power outputs for their size, the mechanical translation through friction has limited

power output. Tieck et al. (2007) measured the intrinsic piezoelectric material power densities and compared them to the ultrasonic motor that utilized them. The intrinsic piezoelectric power densities ranged from 6.53 W/kg to 4500 W/kg while the actual power densities of the motors spanned 0.82 W/kg to 85.73 W/kg. This discrepancy is partially attributed to the use of friction to transfer mechanical loads.

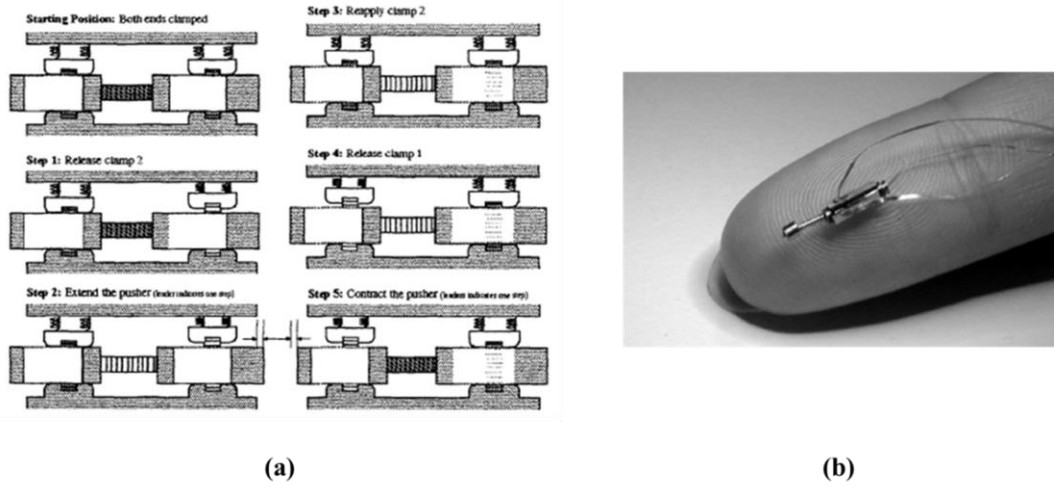

Figure 3-7. (a) Inchworm motor concept by Galante in 1998 [12] (b) miniature ultrasonic rotary motor [13]

3.3 Piezoelectric Hydraulic Pumps

Piezohydraulic pumps, unlike ultrasonic and inchworm motors, do not utilize friction to transfer mechanical loads. These devices combine the effective power transmission of hydraulics with the high power density of piezoelectric stacks to generate high power output from moderate work output of the stack. Typically, piezohydraulic pumps consist of a piezoelectric stack, diaphragm, hydraulic chamber, and inlet and outlet valves to rectify the stroke of the piezoelectric stack to a continuous flow (Figure 3-8a). These pumps are then typically coupled to a hydraulic cylinder, to convert the generated pressure and flow to force and displacement for mechanical work. This configuration, combining piezohydraulic pump and hydraulic cylinder, is known as a

electrohydraulic hybrid actuator (Figure 3-8b) [71]. These hybrid actuators also use external directional valves to create bidirectional motion of the hydraulic cylinder piston they drive.

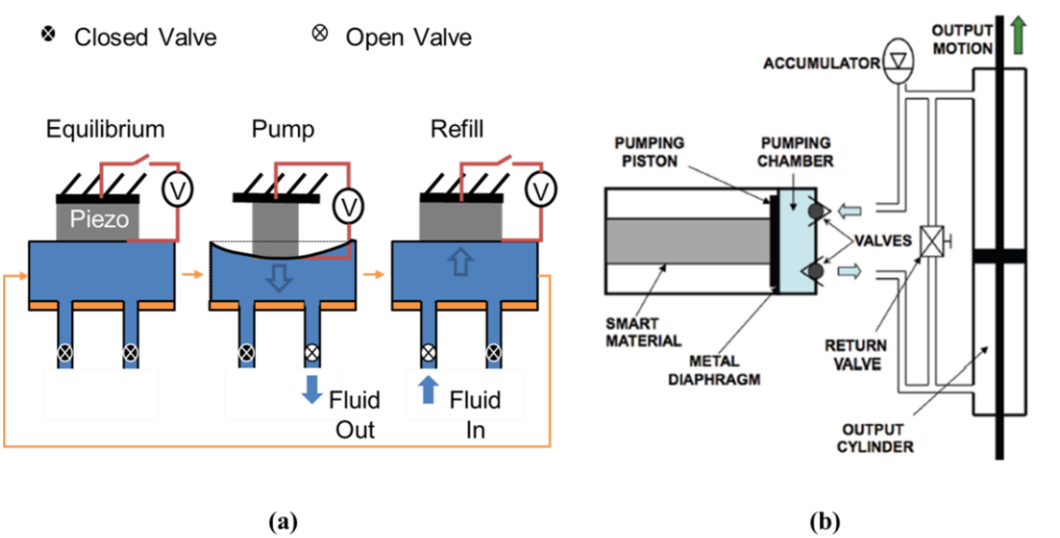

Figure 3-8. (a) Operation of a piezohydraulic pump (b) use of a piezohydraulic pump in an electrohydraulic hybrid actuator to convert pressure and flow to a force and displacement

The basic work output of a piezoelectric pump can be approximated by some simple approximations using the piezoelectric constitutive relations and an understanding of how these actuators interact with different loads. The simplest case, shown in Figure 3-9(a) is the case in which a piezoelectric actuator compresses a linear elastic load. The piezoelectric actuator has an intrinsic stiffness which is related to the material properties of piezoelectric and the geometry of the actuator. Typically this stiffness value, assuming a 1D model, can be found by taking the maximum force that is generated by the actuator, also known as the blocking force F_b, (ie. with an infinitely stiff load attached) and divide it by the maximum displacement it can output, called the free displacement δ_{free}, (ie. when it is free to extend without the presence of a load). This stiffness comes is also defined as the load line of the actuator. The amount of work performed on the spring by the actuator can be calculated as the area under the curve where the spring stiffness line meets the piezoelectric actuator load line. From Figure 3-9(a) it can be seen that when the

stiffness of the spring (slope of the spring line) equals the stiffness of the actuator, the total amount of work transferred by the actuator is maximized. This is known as impedance matching. In the case where an impedance matched spring is attached to the piezoelectric actuator, the maximum work that can be transferred to the spring is:

$$\text{Work}=\frac{1}{2}\left(\frac{F_b}{2}\right)\left(\frac{\delta_{free}}{2}\right)=\frac{F_b\delta_{free}}{8} \quad (3\text{-}13)$$

As a result, only $1/8^{th}$ of the available energy from the piezoelectric stack is used. The use of an incompressible fluid and rectifying valves can lead to an increase in the work output.

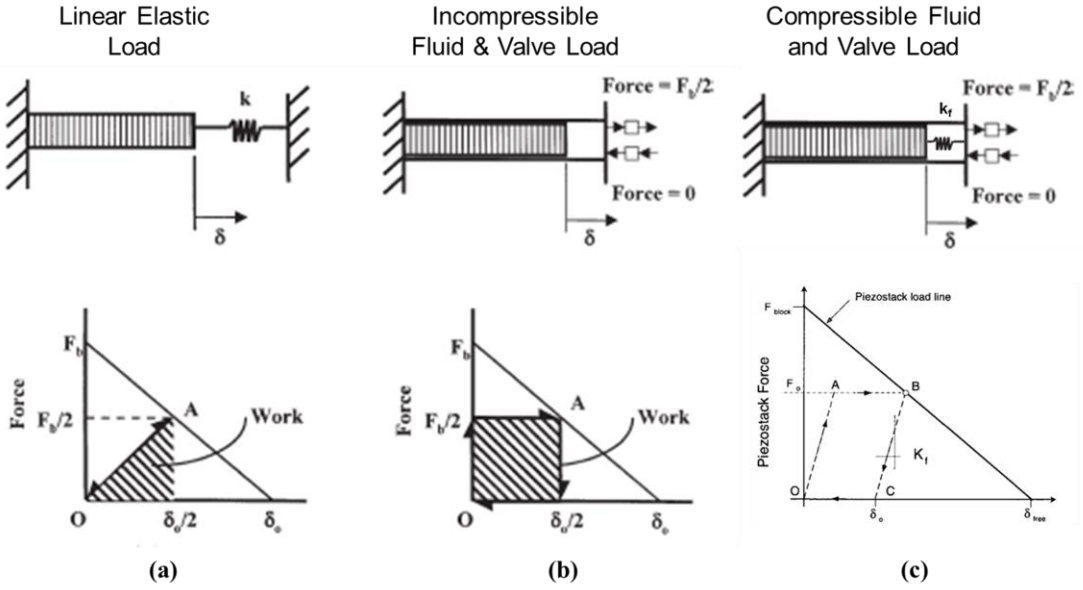

Figure 3-9. (a) Piezoelectric actuator working against a linear elastic load and (b) against an incompressible load with valves and (c) a compressible fluid with valves

In a piezoelectric pump, the load is an incompressible fluid. When an incompressible fluid is used, as shown in Figure 3-9(b), the amount of work that can be transferred by the piezoelectric actuator follows the closed working cycle shown in Figure 3-9(b). Starting at **O**, the piezoelectric actuator is not energized. When a voltage is applied to the actuator the actuator prefers to extend. However, because it is working against a theoretically incompressible fluid,

there is no displacement and the piezoelectric outputs a force (with no displacement, from **O** to $F_b/2$). This force is associated with a pressure increase in the pumping chamber and the closure of the inlet valve. When the pumping chamber pressure increases to a value higher than the pressure at the outside of the outlet valve, the outlet valves opens and the piezoelectric actuator displaces (point $F_b/2$ to **A**). The voltage applied to the piezoelectric is then decreased which causes a decrease in the force output of the piezoelectric (with no displacement). This force decrease is associated with a decrease in pumping chamber pressure and when the pressure in the chamber follows below the pressure outside the inlet, fluid flows into the chamber and the cycle returns to point **O**. In this cycle the maximum amount of work transferred by the actuator is calculated as the area under the force displacement cycle which is:

$$\text{Work}=\left(\frac{F_b}{2}\right)\left(\frac{\delta_{free}}{2}\right)=\frac{F_b\delta_{free}}{4} \qquad (3\text{-}14)$$

The work output is twice the work output when a linear elastic load is attached. Realistically, fluid cannot be considered incompressible, especially when compared to the stiffness of piezoelectric actuators. This finite stiffness, labeled as K_f on Figure 3-9(c), affects the slope of the first and third legs of the piezoelectric pump work cycle. As a result, the maximum work output of a piezoelectric pump is reduced. This means that the effective stiffness of the fluid in the pumping chamber must be as high as possible to ensure the maximum amount fo work is transferred to the load.

The first piezohydraulic pump was developed by O'Neill and Smiley in 1973 [72]. The pump consisted of a piezoelectric stack, operated at 50 Hz, piston with an O-ring, inlet and outlet check valves, and an external control valve. Potential applications of this pump were fluid injectors and a heart assist device. In the late 1990's, Mauck and Lynch developed a piezohydraulic pump utilizing check valves capable of outputting 300 mL/min flow rate and 500 psi maximum stall

pressure when operated at 60 Hz [73]. This corresponded to a maximum power output of 4.3 W. Konoshi *et al*. developed a series of piezoelectric pumps with high power output and efficiency. The first prototype piezoelectric pump they designed consisted of a 22mm diameter and 55mm long piezoelectric stack, diaphragm, and pumping chamber with passive reed valves. This prototype was driven at 300 Hz (the fluidic resonance of the hydraulic circuit) and produced 34 W of power at 27% efficiency [74]. A subsequent prototype utilized this hydraulic resonance and improved the pump by decreasing the pumping chamber. This resulted in a power output of 62 W at 35% efficiency [75].

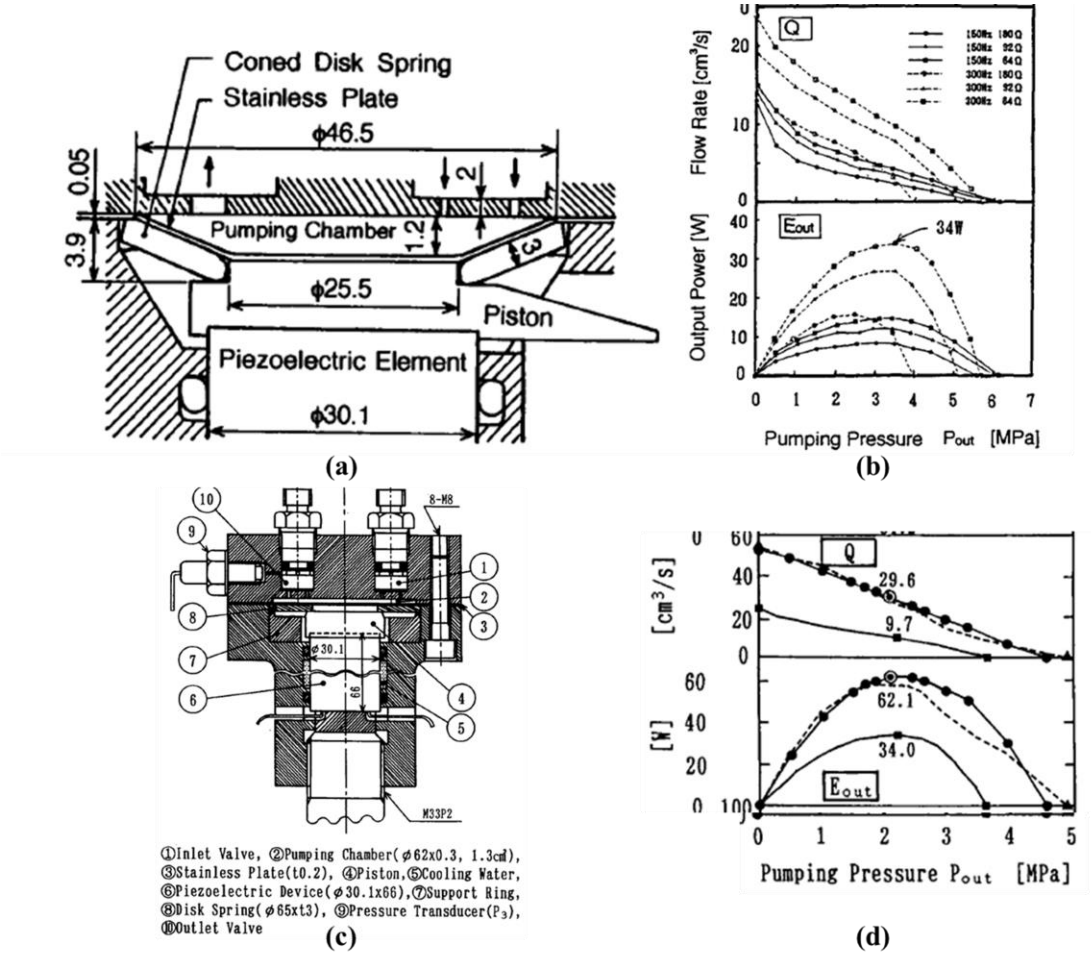

Figure 3-10. (a) First prototype by Konoshi *et al.* which produced (b) 34 W of power at 27% efficiency and (c) second prototype that produced (d) 64 W of power at 35% efficiency

The power output and potential efficiency of piezohydraulic technology over electromagnetic motors led many researchers to design and develop piezohydraulic pumps for wing morphing structures on unmanned air vehicles [76]. Sirohi and Chopra developed a piezohdraulic driven hybrid actuator that had a stall force of 156 N and free velocity of 30mm/s which corresponded to a 1 W maximum output [77]. The piezoelectric stacks used were two 18mm long 10x10mm actuators connected in series. In 2003, Lindler and Anderson, developed a hybrid actuator that utilized a piezoelectric stack that produced a 42 W output [78]. Kinetic Ceramics has developed the best piezoelectric hydraulic pumps. They have reported the development of 0.5 kg pumps that output 160 W of power (320 W/kg power density) [72]. However, researchers have utilized other solid-state induced strain actuators in hydraulic pump technology.

Researchers have also utilized other smart material actuators like magnetostrictive and electrostrictive actuators in hydraulic pumps [71], [79]. Electroctrictive materials, much like piezoelectric materials, strain under the presence of an electric field. However the strain increases quadratically with electric field and is only positive. Magnetostrictive materials strain under the presence of a magnetic field. Chaudhuri and Wereley, developed a electrostrictive pump that utilized a single crystal PMN-PT stack. The pump had a power output of 4 W with 5.5% efficiency when operated at 600 Hz [80]. In 2004, Bridger *et al*. developed a magnetostrictive pump that had a maximum pressure output of 21 MPa and maximum flow rate of 3.4 L/min. While solid state strain-induced hydraulic pumps have shown potential, they have been bandwidth limited. Most of the pumps to date have only been operated below the kilohertz regime. In theory, the amount of fluid flow that these pumps can produce is proportional to frequency at which the active material is actuated. Because pump power output is defined as the

amount of fluid flow multiplied by the amount of head pressure, the power output should also increase with frequency. Unfortunately, with the exception of the Kinetic Ceramics pumps (which operate at 1.5 kHz), the majority of piezoelectric pumps have been limited to operation below 1 kHz. This has limited the size and power density of these devices.

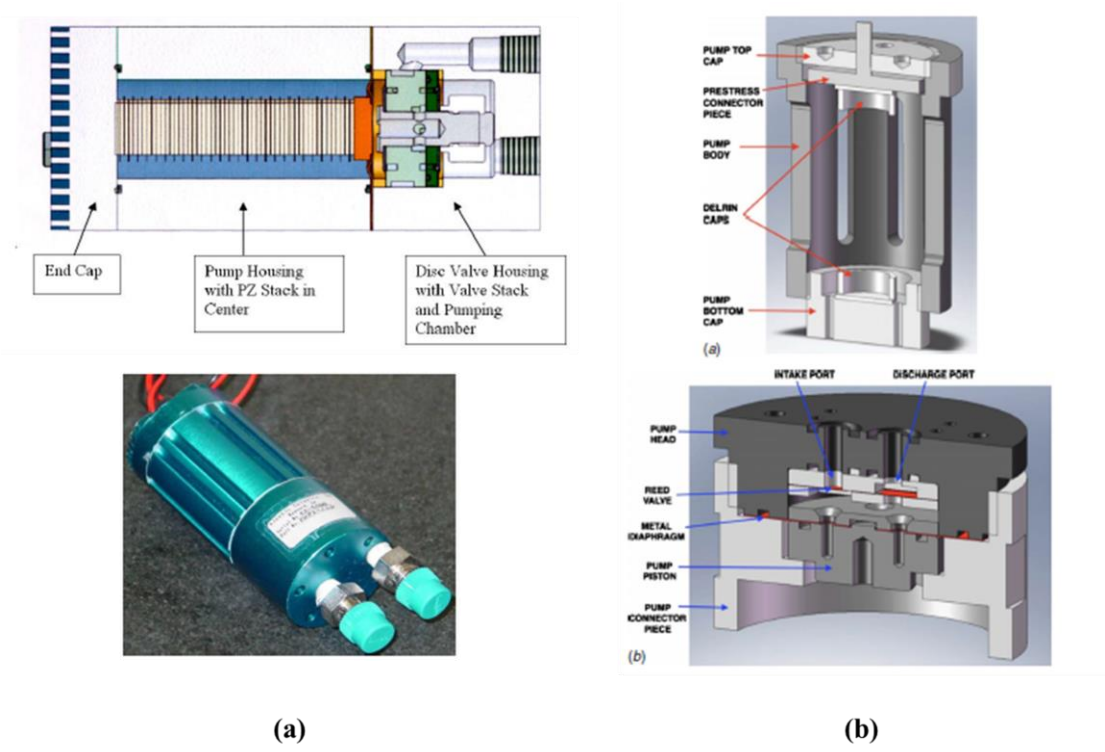

Figure 3-11. (a) Kinetic Ceramics piezoelectric pump schematic and final design (b) Chaudhuri and Wereley electrostrictive pump

One of the major limiting factors affecting piezoelectric pump bandwidth is the resonance frequency of the piezoelectric pump valves. Passive check valves, such as ball valves and poppet valves, are associated with low resonance frequencies. As a result, these rectifying components cannot keep up with high frequency-operated piezoelectric stacks. As a result, the flow rates and power outputs of these early pumps were constrained above a few hundred hertz. To circumvent this problem researchers have designed reed valves and miniature valves that have high resonant frequencies. Reed valves can be designed for the appropriate resonance frequency and deflection

[81], [82]. With reed valves, Chapman *et al.* developed a piezohydraulic pump that could operate as high as 450 Hz with a maximum flow rate of 350 mL/min [83]. As mentioned previously, Kinetic Ceramics has been able to develop piezoelectric pumps that operate in the kilohertz regime with flow rates up to 1800 mL/min and 2500 psi stall pressures [84]. Kinetic ceramics pumps have yielded maximum power outputs of 160 W and up to a 400 W/kg power density. Lee *et al* designed an array of micromachined valves (Figure 3-12a) with resonant frequencies up to 50 kHz that could withstand 0.14 MPa pressure and allowed 35 mL/s of fluid flow [82]. While these valves were promising, they had inferior back-flow characteristics and failed at high back pressures [14]. Larson and Dapino manufactured more robust laser cut miniature reed valves [81].

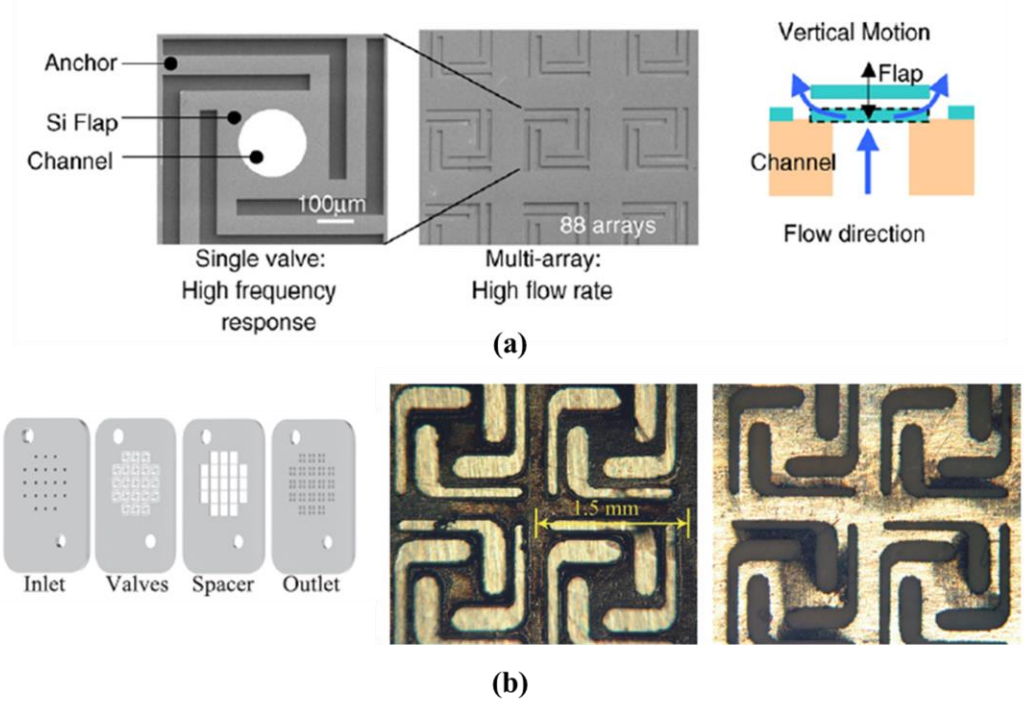

Figure 3-12. (a) Nickel-titanium micro-valve array manufactured by Lee *et al.* (b) Laser cut miniature reed valves designed by Larson and Dapino

Another method to get around the frequency limited response of passive valves is to utilize active valves, like piezoelectrically actuated flaps [85], [86]. For example, Lee *et al*. developed a piezohydraulic pump that utilized two piezoelectric unimorph valves which increased the pump bandwidth to 15 kHz. Similarly, Wen *et al.* developed circular piezoelectric bimorph valves that allowed a maximum flow rate of 540 mL/min [87]. While the use of active valves has showed improvement in pump bandwidth, the additional control and input power needed for these configurations complicates piezoelectric pump design and reduces overall pump efficiency. Thus, the use of high frequency passive valves remains the best option to develop high power density piezohydraulic pumps. Even though the inlet and outlet valve design is important for increasing pump bandwidth, the properties of the driving fluid are also important in understanding and improving the frequency response of piezohydraulic pumps.

While piezohydraulic pumps have the potential to lead to high power density motors for aerospace and medical applications, their performance is highly dependent on other factors such as valve dynamics and fluid properties. For instance, because piezoelectric stacks produce small displacements, the compliance penalties in the form of fluid and housing compliance can have a tremendous impact on pump performance. This, in turn, affects the frequency response of the piezoelectric pump, which limits their use above a few hundred hertz. Researchers, such as Kim and Wang, have shown that the size of pipe fittings and hydraulic cylinder can have a dramatic impact on pump volumetric efficiency [88]. They showed that the addition of fluid compliance and fluid inertia can influence the flow rate of the piezoelectric pump as a function of frequency.

Several researchers have attempted to understand the dynamic behavior of piezoelectric pumps operated at higher frequencies by developing theoretical models of the systems that utilize these piezoelectric pumps. Oates and Lynch developed a system dynamic model, using the state space

method, to predict piezohydraulic pump output based on check valve resistance, pipe resistance, fluid compliance, fluid inertia and piezoelectric dynamics (ie. stiffness, coupling coefficient) [89]. Nasser and Leo (2000) created a model predicting the efficiency of piezohydraulic actuation versus piezo-pneumatic actuation [90] using state space methods and taking into account fluid compressibility, inertia, ad viscous losses. Using steady state assumptions, they predicted that the upper bound efficiency for piezohydraulic actuation was 29%. Ullmann and Fono, developed a dynamic model, based on the momentum equations, that took into account the dynamics of the fluid lines connected to the piezoelectric pump. The found that the resonance and nonlinear behavior of piezoelectric pump flow rates is a function of the piping lines connected to the device [91]. Lastly, Kan *et al* showed that the thickness of the diaphragm and the radius of the piston relative to chamber radius can affect piezoelectric pump performance [92]. This, in effect, can affect the volumetric output and pressure out of the pump. They showed, analytically, that pump flow rate and pressure output can be increased b simultaneously decreasing pump diaphragm thickness and increasing the piston-chamber radius ratio. While these models have given accurate approximations of the dynamic behavior of piezoelectric pumps, the complex interaction of the valves and fluid resonances has not been fully captured. Thus, while many factors can affect the performance of piezoelectric pumps at high frequencies, the potential of these devices outweighs the technical complexities. Some of these intricacies will be covered in more detail in Chapter 5.

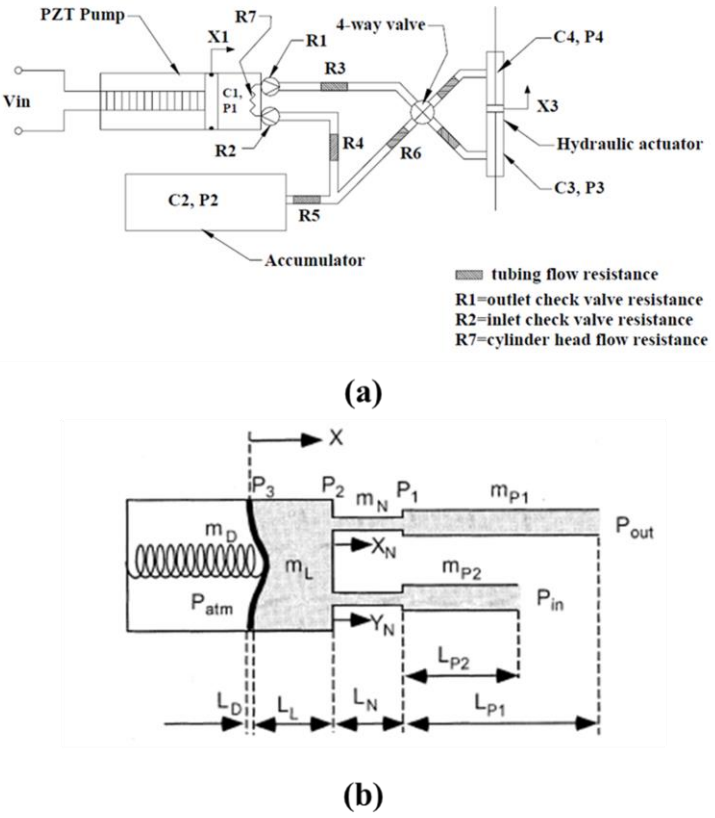

Figure 3-13. (a) Oates and Lynch system dynamic model of a piezoelectric hybrid actuator (b) Ullmann dynamic piezoelectric model taking into consideration the fluid lines

3.4 Summary

This chapter covered the fundamental mechanisms of piezoelectricity and the constitutive relations that govern the strain and charge output of these devices. From these constitutive relations the generalized equations of 31-mode and 33-mode piezoelectric actuators were introduced. The strain output limitations of these actuators were discussed and various methods to circumvent this limitation were covered. These methods included, but were not limited to mechanical amplification and frequency leveraging. From frequeny leveraging, we summarized the state of the art of high frequency inertial piezoelectric motors. The use of frequency leveraging was discussed in the context of piezohydraulic pumps. Finally, the bandwidth

limitations of these devices were summarized. The rest of this dissertation covers the research done in the Active Materials Laboratory concerned with utilizing piezohydraulic pumps in mechanical circulatory support blood pumps for pediatric patients.

Chapter 4: Piezohydraulic Pump Ventricular Assist Device Driver: Feasibility Study

In this chapter, the feasibility of using PHPs in pulsatile pediatric ventricular assist devices (VADs) is presented in this chapter. A theoretical analysis is presented to calculate the preliminary PHP dimensions needed to meet flow and pressure requirements. In addition, an existing PHP was incorporated into a VAD driver to drive a pulsatile pediatric 30 mL stroke VAD as proof of concept. The driver was tested at heart rates ranging from 50-110 beats per minute (BPM) in a mock circulation to characterize its performance. The maximum drive pressure was 33 kPa with a peak flow rate of 6 L/min against a 10 kPa back pressure. The maximum mean flow rate from the VAD outlet was 3 L/min at 100 BPM operation. These results compare well to commercially available systems that output between 25-40 kPa drive pressure and flows between 0-10 L/min against 10-16 kPa pressures.

4.1 Theoretical Analysis for Design Requirements

First the amount of power output and power consumption of a pediatric heart will be discussed. From this analysis we can get a first approximation of the size of piezoelectric stack and pump components needed to drive a pediatric ventricular assist device. Then an experimental setup using a commercially available piezohydraulic pump to drive a pulsatile blood pump is presented. This chapter demonstrates the feasibility of using piezohydraulic pumps as drivers for pediatric pulsatile blood pumps.

Pediatric Cardiac Power

The power output of a heart with functional ventricles varies with age, body surface area, and physical demands. For a patient with heart failure, a VAD needs overcome the back pressure from the circulation (pressure work) and needs to accelerate blood through the VAD outlet

(kinetic work), known as the cannula. Madihally (2010) derived an output power expression for a VAD as [93]:

$$P_o = p_V Q_V = p_c Q_c + \frac{1}{2}\frac{Q_c^3 \rho_b}{A_c^2} \qquad (4\text{-}1)$$

Where P_o is the VAD power, p_V is the VAD output pressure, Q_V is the VAD output flow rate, p_c circulatory pressure outside the VAD cannula, Q_c is the required circulatory flow, ρ_b is the density of blood, and A_c is the cannula cross-sectional area. The flow rate from the VAD also needs to match that of a healthy ventricle (ie. $Q_V = Q_c$). Using Equation (4-1), the VAD output pressure reduces to:

$$p_V = p_c + \frac{1}{2}\frac{Q_c^2 \rho_b}{A_c^2} \qquad (4\text{-}2)$$

Healthy pediatric patients typically output a maximum flow of 5 L/min (Q_V) against a 16 kPa circulatory pressure (p_c). They also require cannula diameters on the order of 6 mm to interface the VAD with their vasculature [7]. Based on these requirements, Equation (4-2) indicates a 21 kPa VAD pressure (p_V) and 1.7 W VAD power output (P_o) is needed. In this power regime, piezoelectric motors are reported to be superior to electromagnetic motors [94].

Preliminary Piezohydraulic Pump Sizing

Figure 4-1a shows a representative PHP driving a pediatric VAD. The PHP consists of a piezoelectric stack and diaphragm coupled with an incompressible fluid that actuates a VAD pusher plate. The 1-D piezoelectric constitutive relation for the strain output is:

$$\frac{\delta}{L_s} = \frac{1}{Y_3^E}\frac{F}{A_p} + d_{33}\frac{V}{t_p} \qquad (4\text{-}3)$$

Where δ is the piezoelectric stack displacement, L_s is the length, Y_3^E is the young's modulus at constant electric field, F is the force output, A_p is the stack cross-sectional area, d_{33} is the

piezoelectric strain coefficient, V is the applied voltage and t_p is the thickness of each piezoelectric layer. The blocking force, F_b, and maximum stack displacement, δ_{max}, can be derived from Equation (4-3) as:

$$\delta_{max} = \frac{d_{33} L_s}{t_p} V \qquad (4\text{-}4)$$

$$F_b = \frac{d_{33} Y_3^E A_p}{t_p} V \qquad (4\text{-}5)$$

Figure 4-1 (b) shows a representative piezoelectric stack force output versus displacement during the pumping cycle of an impedance matched PHP [95]. The area **ABCD** represents the work done on the hydraulic fluid by the piezoelectric stack in one cycle. Based on geometric considerations of Figure 4-1 (a) and the PHP cycle in Figure 4-1 (b), the pressure and flow from the VAD is approximated as:

$$p_V \cong \frac{A_{Hc}}{2 A_V A_d} F_b \qquad (4\text{-}6)$$

$$Q_V \cong \frac{A_V A_d}{2 A_{HC}} f \delta_{max} \qquad (4\text{-}7)$$

Where A_{HC} is the hydraulic cylinder piston cross sectional area, A_V is the VAD pusher plate area, and A_d is the PHP diaphragm area. This relation states that the ventricular assist device pressure can be reduced by choosing the appropriate hydraulic cylinder and pusher plate dimensions as long as the free displacement and blocking force are known.

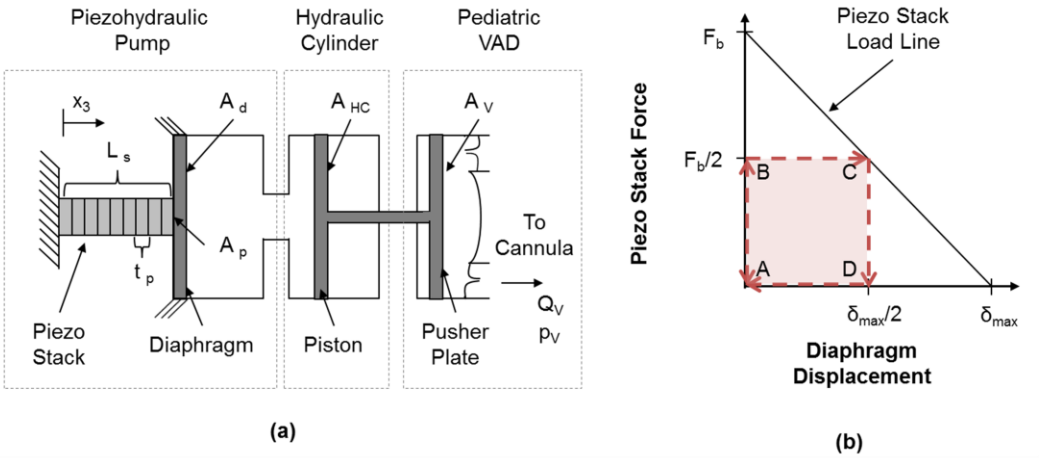

Figure 4-1. (a) Theoretical schematic of a piezohydraulic pump driving a pediatric VAD with hydraulic transmission, (b) PHP cycle when piezoelectric stack is impedance matched to the hydraulic load adapted from Mauk and Lynch (2000)

Using Equations 4-5 and a 0.2 x 0.2 x 2 cm NCE51 PZT stack (NAC2001-H20, Noliac North America, Inc.) with 20 µm thick piezoelectric layer (t_p), and properties listed in Table 4-1, the F_b and δ_{max} are 95 N and 9 µm respectively with a 20 V excitation (1 MV/m electric field). Using Equation 4-5 and assuming$A_{HC} = {}^{1}/_{2}\, A_V$, a 3.8 cm diameter diaphragm produces a 21 kPa VAD pressure. From Equation 4-6, a piezoelectric stack operating at 8.1 kHz produces 5 L/min and 1.7 W required by Equation 4-2. Thus, a 0.2 x 0.2 x 2 cm piezoelectric stack with 20 V applied voltage, operating at 8.1 kHz and 3.8 cm diaphragm can power a pediatric VAD. Further size can be achieved by increasing the piezoelectric operational frequency. This PHP volume can be substantially smaller than portable electro-pneumatic adult VAD drivers which are approximately 10.4 × 28.2 × 8.3 cm [96]. More sophisticated models that account for hydraulic losses, valve frequency response [77], [97] and the electronic drive size [98] would more accurately predict the size of the entire PHP system. Nonetheless, this analysis demonstrates the promise PHPs offer pediatric VADs. While hydraulic fluid provides improved

power transmission, current VADs are pneumatically driven. As proof of concept, we use a PHP to drive pneumatic pediatric VADs.

Table 4-1. Properties of NCE51 PZT

Property	Unit	Symbol	Value
Piezoelectric strain Coefficient	10^{-12} C/N	d_{33}	460
Young's Modulus	GPa	Y_3^E	52
Density	kg/m^3	ρ	7800

Electronic Drive Considerations

While the use of high frequency piezoelectric actuators in conjunction with a working fluid and rectifying valves offers a high power density driving device, the power consumption and driving electronics can represent a limiting design factor in using these systems as compact motors. In order to predict if using piezohydraulic pumps for mechanical circulatory support applications is feasible, the average electrical power consumption and maximum current draw must be understood. Fortunately, the electrical power requirements of piezoelectric actuators are well understood.

As mentioned in Chapter 3, piezoelectric actuators are electrically reactive elements which store electrical energy. At operational frequencies below electromechanical resonance, the majority of piezoelectric materials behave like electrical capacitors. More specifically, when a voltage, or electric field, is applied to the piezoelectric material, the device builds up charge. When the device is shorted, the piezoelectric element discharges. As a result, the ideal capacitor, does not consume current but returns it to the power supply providing the charging voltage. Let's assume the piezoelectric actuator can be modeled as an ideal capacitor. The electric field applied to the piezoelectric actuators in this dissertation are biased about a specific voltage level, V_{off}.

Thus, knowing the sinusoidal voltage, with amplitude V_s, applied to the piezoelectric actuator and the current-voltage relation for an ideal capacitor (both shown by equation 4-7), the maximum current drawn, power output, and average power consumption can be predicted.

$$v(t) = V_{off} - V_s \sin(2\pi ft) \qquad (4\text{-}8)$$

$$i(t) = C\frac{dv}{dt} \qquad (4\text{-}9)$$

$$i(t) = -2\pi CfV_s \cos(2\pi ft) \qquad (4\text{-}10)$$

$$p(t) = -2\pi CV_{off} fV_s \cos(2\pi ft) + 2\pi CfV_s^2 \sin(2\pi ft)\cos(2\pi ft) \qquad (4\text{-}11)$$

v(t) is the sinusoidal voltage applied to the piezoelectric, f is the operational frequency, t is time, i(t) is the instantaneous current drawn from the capacitor/piezoelectric, and p(t) is the instantaneous power consumed. The maximum current drawn occurs when $\cos(2\pi ft) = -1$ and has a magnitude of $2\pi CfV_s$. Thus the maximum instantaneous current draw from the piezoelectric actuator is proportional to the frequency of operation. The current can also be negative and this represents current that is returned to the power source. Most power sources dissipate the returned current and power in the form of heat. Similarly, the instantaneous power consumed by the capacitive element is proportional to the frequency and the square of the applied voltage. The average power consumption can be calculated by integrating the instantaneous power consumption over one cycle of charging and discharging. For ideal capacitive loads, the average power consumed is zero.

$$\langle P_{avg} \rangle = \int_{-T}^{T} p(t)dt = 0$$

This is not surprising since ideal reactive elements, like some capacitors and inductors, have bidirectional power flow. This means that they store energy and can discharge that energy

to a dissipative load. In reality, piezoelectric materials act as lossy capacitors, which are reactive elements that dissipate power, usually in the form of heat. These losses are a function of conduction currents through the material and the molecular friction between the atoms in the piezoelectric crystal structure. Researchers typically model piezoelectric materials as ideal transformers that convert energy in the electrical domain to the mechanical domain as shown in Figure 4-2.

Typically, the electrical portion of the piezoelectric is modeled as a capacitor with capacitance C_e shunted with a resistance R_L. The physical characteristics of the piezoelectric are modeled with mechanical compliance, C_m, and a device mass M_m. The electromechanical conversion factor is defined by N. An ideal capacitor has an infinitely large shunt resistance (open circuit) and thus does not dissipate any power. However, real piezoelectrics have finite shunt resistances and dissipate power in the form of heat. A useful metric for defining the "lossiness" of a piezoelectric material is the dissipation factor known as tanδ. The tanδ is dependent on frequency of and is essentially a measure of the power consumption of the actuator. Single crystal piezoelectric actuators typically have tanδ values ranging from 1-2% and polycrystalline materials (PZT-5H) have tanδ values ranging from 10-150%. While single crystal piezoelectric devices have superior power consumption characteristics, they produce strain much smaller than polycrystalline materials.

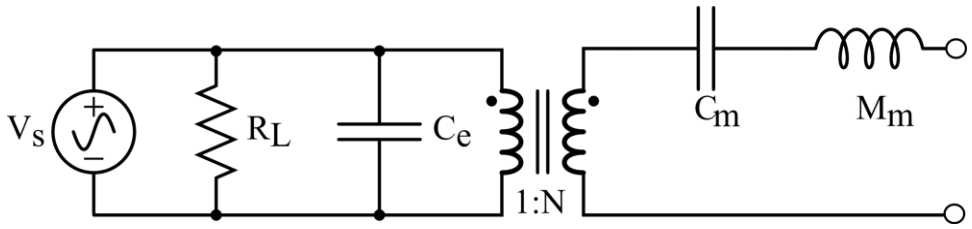

Figure 4-2. Equivalent circuit representation of a piezoelectric actuator modeled as an ideal transformer with a shunt resistance to represent the losses in the reactive element

From the above analysis, it is apparent that the power consumed by the piezoelectric material is dependent on material properties (tanδ), the frequency of operation, and most importantly, the applied electric field (voltage). Typically the tanδ value of piezoelectric materials are fixed and difficult to change without changing the material as a whole. The electric field can be reduced but that affects the amount of strain that can be produced and affects the power output of the device utilizing the piezoelectric actuator. Operation frequency can be reduced with reduction in power density. Thus, methods to reduce intrinsic loss in piezoelectric actuators are limited. However, these losses are actually very small. This biggest engineering challenge in piezoelectric electronic drives is designing drive circuitry that can supply the current needed to drive piezoelectric actuators and handle the returned current when the device is discharged.

The electronic drivers that deliver this electrical power can be optimized to provide efficient power transfer from source to actuator. Researchers have developed drive circuits that are efficient and compact ($< 3in^2$) [77] utilizing pulse width modulated circuitry[99], [100]. Others have developed driver circuitry that re-use the re-circulated charge from the reactive actuator [101]. Both methods have led to compact energy efficient drive circuits that can supply the necessary voltage and currents to piezoelectric actuator systems. The next section details the

testing of a commercially available piezohydraulic pump to be used as a ventricular assist device driver.

4.2 Experimental Setup

The PHP (Kinetic Ceramics; PHP3-1.6) used in this study, shown in Figure 4-3a, is a 0.5 kg, 14 cm long, and 3.8 cm diameter pump. The PHP consists of a PZWT100 piezoelectric stack actuator, pump chamber, and passive inlet valve to convert the mechanical stroke of the stack actuator to a continuous flow of hydraulic fluid [14]. The PHP uses Dexron IV hydraulic oil as the working fluid which does not come into contact with blood in the potential application. The stack actuator is operated at 1.5 kHz with electric field oscillation from -0.5 to 2 MV/m in all tests. This operational frequency produces audible noise. However, future devices would be designed to operate at higher frequencies to both boost power output and eliminate noise (outside the frequencies audible to the human ear). In this study, the PHP is used to drive a pulsatile VAD.

The VAD (Berlin Heart; EXCOR) used in this study, shown in Figure 4-3b, is a pulsatile VAD that consists of a rigid outer casing with inflow and outflow connectors that interface with the vascular system. A flexible diaphragm, located inside the VAD, separates a pneumatic chamber from the blood chamber and forces blood through the outflow connector during compression and allows blood to refill the blood chamber through the inflow connector. One-way polymer valves, located inside the inlet and outlet connectors, ensure unidirectional blood flow through the VAD. This commercially available VAD is typically driven by a large electro-pneumatic driver that consists of multiple electric motor-driven air compressors. As proof of concept, we evaluate the PHP as a ventricular assist device driver.

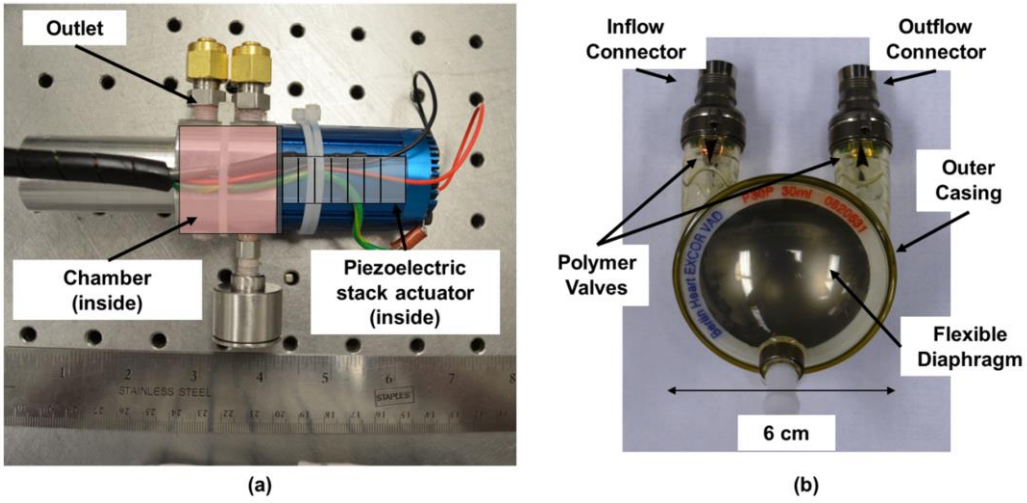

Figure 4-3. (a) Piezohydraulic pump used in this study, (b) The VAD (Berlin Heart EXCOR 30 mL stroke volume) used in this study to be driven by the PHP

Mechanical Testing

To utilize the PHP as a driver, a 40m L diaphragm-style hydraulic accumulator (Hawe Hydraulics Inc., AC-40), a 1.9 cm diameter hydraulic cylinder (Mack Corporation), a 4-way solenoid directional valve (Hydraforce Inc.; SV08-40), and a 10 cm pneumatic cylinder were attached to the PHP as shown schematically and pictorially in Figure 4-4a and 4-4b respectively. The accumulator provides a bias pressure of 2.2 MPa to the hydraulic system. The hydraulic cylinder converts the PHP flow to a linear mechanical stroke while the 4-way solenoid valve produces bidirectional actuation. The size of the hydraulic cylinder was dictated by the smallest commercially available high pressure hydraulic cylinder and does not represent an ideal impedance matched system. Equations 4-6 and 4-7 indicate that flow rate can be increased and pressure can be decreased by choosing a smaller bore hydraulic cylinder than used in this study. The pneumatic cylinder attached to the hydraulic cylinder rod provides a sweeping volume of air to the VAD per stroke. The size of the pneumatic piston was determined by using Boyle's Law

to determine the sweeping volume needed to achieve VAD drive pressure. The driver, without electronics, can be contained in a non-optimized 30 x 23 x 33 cm volume which is comparable to portable adult piston-type electro-pneumatic driver which are approximately 10.4 × 28.2 × 8.3 cm [96]. However, it is important to note that this is proof of concept and not an optimization study. The Theoretical Analysis suggests additional size reductions are possible. Before feasibility testing, the PHP was mechanically characterized for flow rate, pressure, and power output.

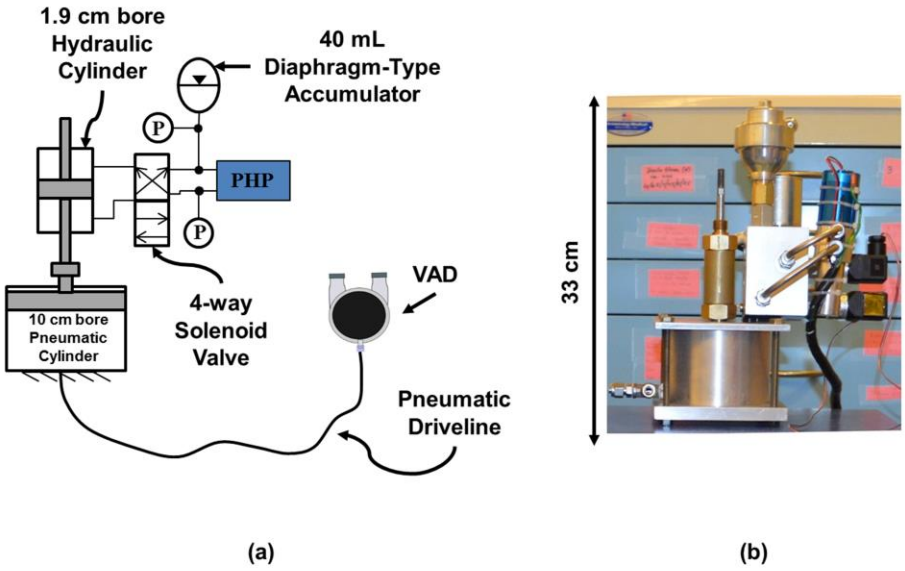

Figure 4-4. (a) Schematic of the ventricular assist device driver consisting of a hydraulic cylinder, 4-way solenoid valve, and pneumatic cylinder that supplies air to the VAD, (b) picture of the driver setup

The PHP flow rate, pressure, and power were measured by attaching it to a hydraulic cylinder and running the PHP with and without an applied load (Figure 4-5a). For operation with a load, a 27 kN/m die spring was attached to the hydraulic cylinder rod. Pressures were measured near the PHP inlet and outlet with 4-20mA pressure transducers (Wika Instrument Corp.; A-10). PHP flow rate was calculated via the rate of spring compression measured by an LVDT (Omega

Engineering; LD620). PHP instantaneous power output was determined from flow rate measurements and the pressure difference between the PHP inlet and outlet (ΔP). The VAD and driver were then tested in a mock circulation that mimics a pediatric circulation.

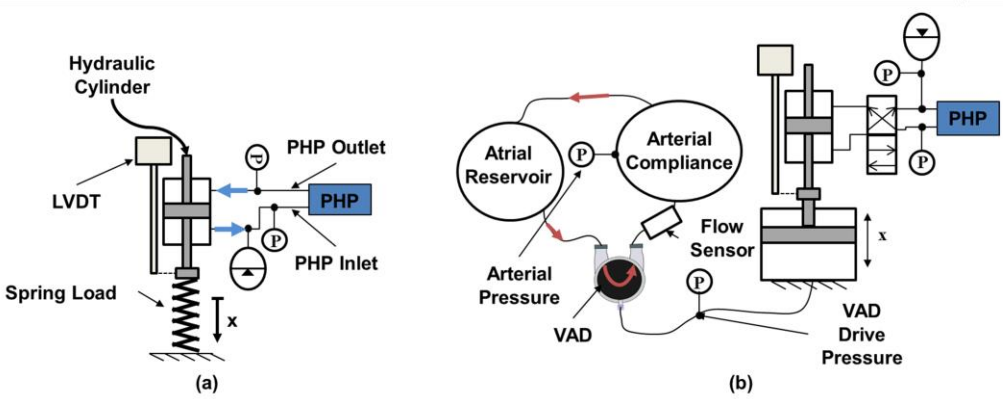

Figure 4-5. (a) Schematic of the mechanical test used to measure the PHP flow rate, pressure, and power (b) Schematic of the *in-vitro* mock circulation test setup

In-vitro Testing

To create a scenario as close as possible to the pediatric cardiovascular system, the mock circulation (Figure 4-5b) consisted of an atrial reservoir, arterial compliance chamber, and 3/8" ID Tygon tubing [102]. Glycerin (40%) and water (60%) solution was used in the mock circulation to mimic blood viscosity. To simulate ventricular blood ejection, known as systole, the PHP supplied pressurized fluid to produce forward actuation of the hydraulic cylinder rod to pressurize the VAD pneumatic chamber. To simulate ventricular refilling, known as diastole, the hydraulic cylinder rod was retracted and removed air from the VAD. The driver was operated at heart rates ranging from 50-110 BPM in 10 BPM increments to measure the mean flow imparted to the mock circulation. Arterial pressure and VAD drive pressure were recorded with pressure transducers (Utah Medical; Deltran). Ultrasonic flow probes and flow meter (Transonic Systems

Inc., ME12PXL) measured instantaneous flow rate. Mean flow was determined from integrating the instantaneous flow measurements over time.

4.3 Results and Discussion

Figure 4-6 shows the pressure difference, ΔP, across the PHP (left ordinate) and the flow rate from the PHP (right ordinate) versus time for the unloaded PHP mechanical test (Figure 4-5a without spring). The flow rate ramps up quickly (<250 ms) to 10.2 cm^3/s upon turning on the PHP and drops back to zero flow when the hydraulic cylinder rod reaches its full stroke. The fast flow rate ramp is desirable since the PHP needs to actuate and provide power to the circulation in a short time interval per heart beat (<500 ms). Figure 4-6 shows the ΔP increases to a steady state value of 0.3 MPa and ramps to a maximum of 2.2 MPa, when the hydraulic cylinder rod reaches its full stroke. In comparison, a healthy pediatric ventricle, which includes patients as small as infants to young children, is able to eject up to 85 cm^3/s flow with a pressure output between 10-16 kPa. Thus the unmodified PHP produces substantially higher output pressures at flow rates approaching pediatric requirements. The iterations in the following chapters will address the issue of reducing the pressure output of the piezohydraulic pump.

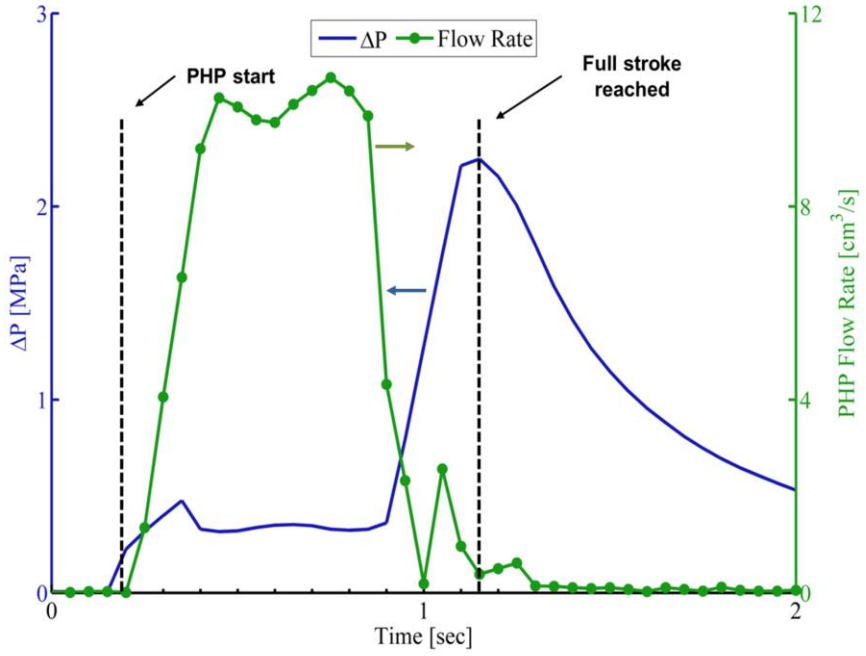

Figure 4-6. No load PHP ΔP and PHP flow rate

Figure 4-7 plots the ΔP across the PHP (left ordinate) and PHP power output (right ordinate) versus the PHP flow rate for the spring-loaded PHP mechanical test (shown in Figure 4-5a). The solid lines in the figure represent a least squares fit to the data. The PHP pressure (ΔP) decreases linearly with increasing PHP flow rate and power output increases parabolically with increasing flow rate. The peak power output is 5.4 W and occurs at 4.75 cm^3/s flow rate which is close to half of the maximum flow rate (10.2 cm^3/s) reported in Figure 5. Previous reports indicate that this pump outputs up to 28 W of power (O'Neill, 2012); differences in power output may be attributed to varying test setups. Nonetheless, the 5.4 W power output exceeds the power requirement for the normal pediatric left ventricle (1.7 W), which suggests that a well-designed pump could be 3x's smaller than tested in this study.

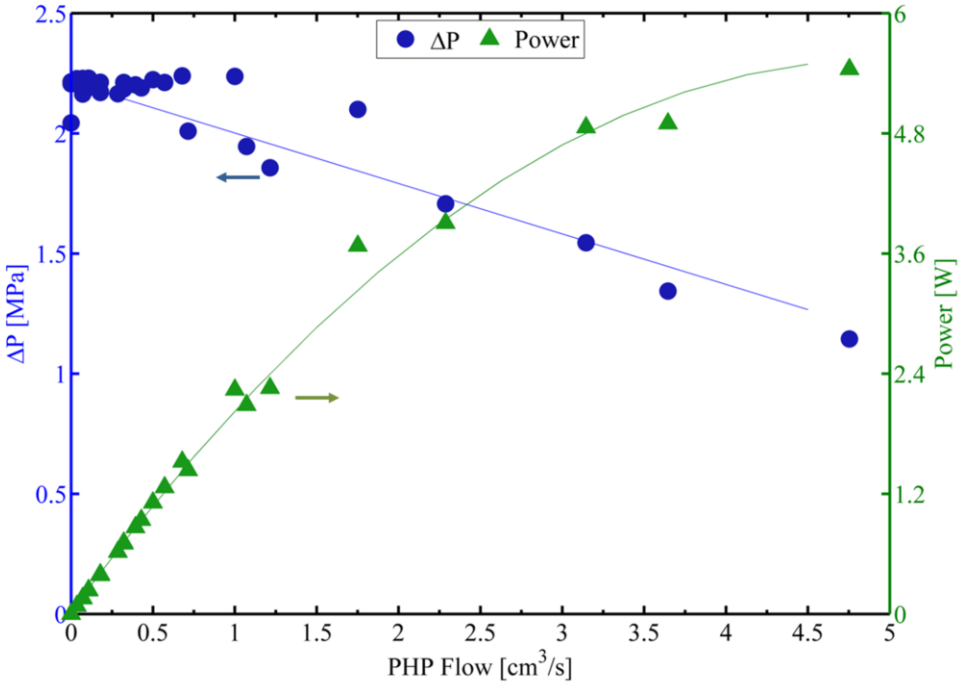

Figure 4-7. PHP outlet and inlet pressure difference (left ordinate) versus flow rate and PHP power output (right ordinate) versus flow rate in the presence of an external load

The load force, left ordinate, as a function of hydraulic cylinder rod velocity is shown in Figure 4-8. Force and velocity data were fitted using least squares fitting. The shaft velocity of the hybrid actuator decreases linearly as the applied external load increases. The blocking force is 180 N. The right ordinate shows the power output of the overall hybrid actuator (ie. the product of spring force and velocity) as a function of velocity. The maximum power output in the forward direction is 1.6 W at a 1.75 cm/s shaft velocity. Comparing the maximum power output of the hybrid actuator to the PHP shows that there was a significant loss in power from the pump to the hybrid actuator. This loss in power can be attributed to the pressure drop across the solenoid valve, the hoses connecting the hydraulic components together, and entrapped air in the working fluid (Dexron VI).

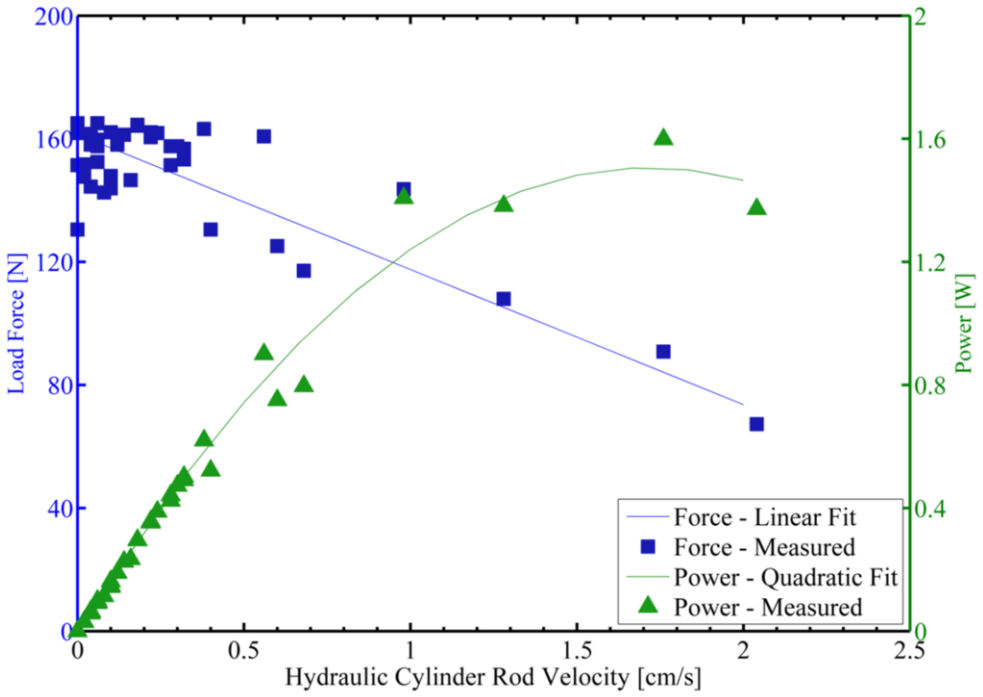

Figure 4-8. Hybrid actuator output force (left ordinate) versus velocity and hybrid actuator power output (right ordinate) versus velocity in the presence of an external load

Figure 4-9 shows the pressure difference, ΔP, across the PHP (left ordinate) and PHP flow rate (right ordinate) versus time for the in-vitro test (Figure 4-5b) at 60 BPM. Note this is for a modified PHP pump driver shown in Figure 4-5b. As seen in Figure 4-9, PHP flow rate and ΔP oscillate periodically twice a second. During systole, the maximum PHP flow rate reaches 7.1 cm^3/s, while the ΔP increases from approximately 0.8-1.3 MPa to extend the hydraulic cylinder rod (A) and eject fluid from the VAD. During diastole, ΔP increases from approximately 0.15-2.4 MPa with a maximum flow reaching 8.7 cm^3/s to retract the hydraulic cylinder rod (B) and refill the VAD. The difference in flow between the two phases is attributed to the fact that the PHP faces the circulatory load during systole and not during diastole. A comparison of the modified PHP flow rate profile to that of the PHP flow rate under no load (Figure 4-5) shows that the PHP is performing work in the high flow and low pressure regime

when a circulatory load is attached. This represents an impedance mismatch between the PHP and mock circulation. Nonetheless, even with this impedance mismatched system, the PHP supplies sufficient power to drive the VAD.

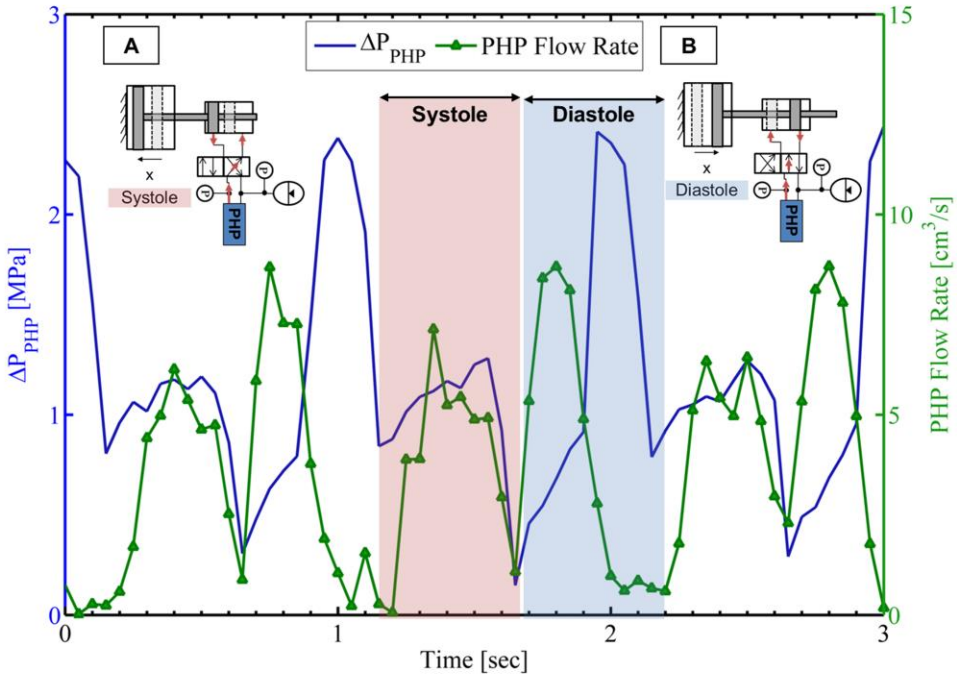

Figure 4-9. Three second window of PHP ΔP versus time (left ordinate) and PHP flow rate versus time (right ordinate) during the 60 BPM mock circulation test

Hydraulic cylinder rod displacement and velocity are plotted in Figure 4-10. The maximum rod stroke length under the 60 BPM control is 1 cm and the magnitude of the forward and backward velocity was 4 cm/s. This shows that the actuator operates at a velocity close to the no-load velocity of the hybrid actuator (5.7 cm/s) when subjected to a circulatory load. This corresponds to a small force output to the VAD and an impedance mismatched system. To correct this, a newly designed pump with the appropriate pressure output and flow rate needs to be developed.

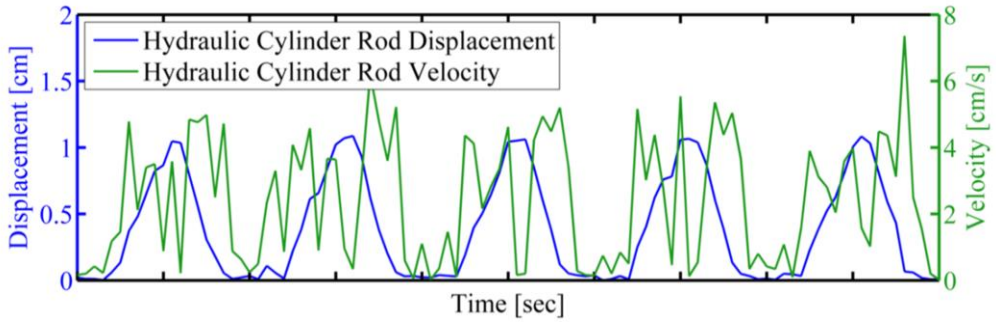

Figure 4-10 Hybrid actuator output force (left ordinate) versus velocity and hybrid actuator power output (right ordinate) versus velocity in the presence of an external load

Figure 4-11 shows the VAD drive pressure, arterial pressure, and flow rate waveforms versus time for the in-vitro test at 60 BPM (see Figure 4-5b). As can be seen, the VAD drive pressure, arterial pressure and flow rate oscillate once a second. During systole, the VAD drive pressure increases to its maximum at approximately 33 kPa and causes the VAD diaphragm to eject fluid from the VAD outlet port which causes the flow rate in the mock circulation to increase to approximately 6 L/min. This increases the pressure in the arterial compliance chamber to 10.5 kPa. The maximum VAD drive pressure compares well to commercial electro-pneumatic drivers which output between 25-40 kPa. The peak flow rate of 6 L/min against a 10 kPa arterial pressure also compares well to traditional drivers that can output between 0-10 L/min instantaneous flows against arterial pressures ranging from 10-16 kPa. Therefore, the initial driver prototype (i.e. modified PHP) confirms that it is feasible for a PHP to output pressures and flow rates that are comparable to traditional electro-pneumatic drivers.

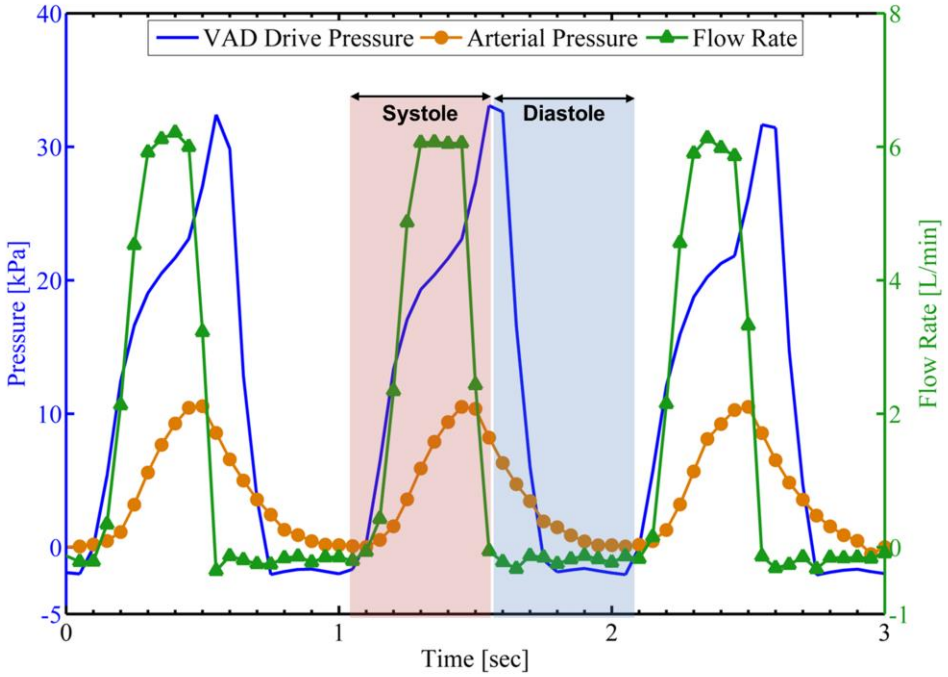

Figure 4-11. VAD drive pressure, arterial pressure wave forms (left ordinate) and flow rate (right ordinate) during the 60 BPM mock circulation test

Figure 4-12 plots the mean flow rate from the VAD versus heart rate for the *in vitro* experiment (shown in Figure 4-5b) at different heart rates ranging from 50-110 BPM in 10 BPM increments. The mean flow rate increases linearly with heart rate up until 100 BPM. This linear relationship is expected since the mean flow from a pulsatile VAD is the product of its stroke volume and heart rate at which it is actuated. These results indicate that the driver was capable of fully ejecting the VAD stroke volume within the allotted time when operating at 100 BPM. Mean flow falls off at heart rates larger than 100 BPM because the sweeping volume from the pneumatic cylinder is not sufficient to fully eject the fluid from the VAD. Pediatric pumps are typically run between 80-150 BPM [7]. This output is independent of the PHP output and can be fixed with a larger pneumatic cylinder. Nonetheless, these results show proof of concept that a PHP can be used for this application.

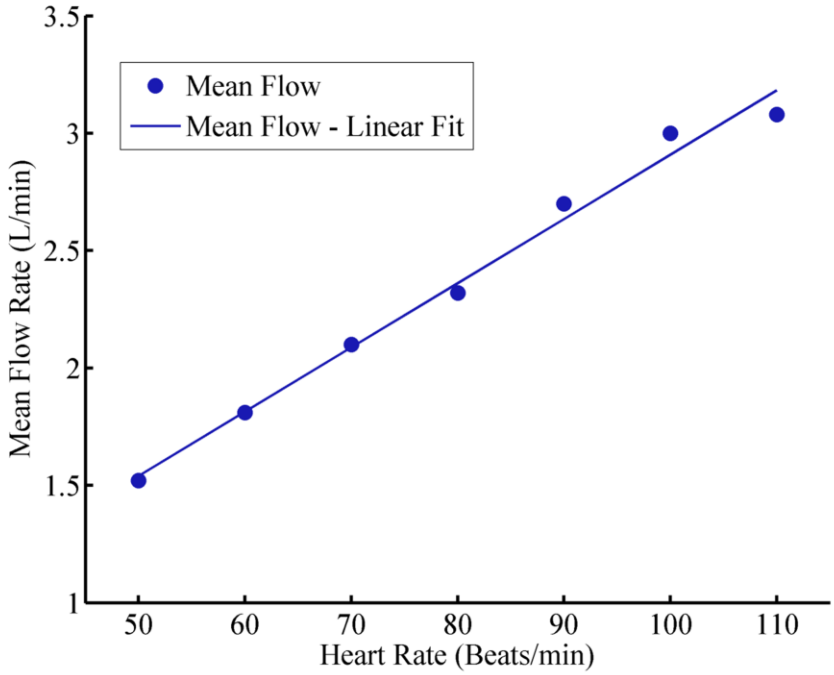

Figure 4-12. Mean flow rate of VAD driven by the driver versus heart rate

4.4 Summary

The feasibility of using a piezohydraulic actuated ventricular assist device driver has been demonstrated. A theoretical analysis has been presented that shows for a given piezoelectric frequency operation and piezoelectric stack, a compact PHP can be developed to match the power requirements of a Pediatric VAD. In addition, Tests were performed to characterize the maximum PHP flow and the maximum power output. For this PHP, 10.2 cm^3/s flow rates were recorded. In addition, a maximum PHP power output of 5.4 W was recorded and is higher than the 1 W that is typically output by the healthy pediatric heart. A hydraulic cylinder, 4-way solenoid valve, and pneumatic cylinder were attached to the PHP to use it as a driver and tested it in a mock circulation. At 60 BPM, the driver provided sufficient VAD drive pressure at approximately 33 kPa to provide flow in the mock circulation. The driver was also able to operate at 100 BPM to generate an output of 3 L/min of mean flow. These results indicate that it

is not only feasible to use PHPs in pediatric VAD applications but they can potentially lead to smaller drivers when operated at high frequencies.

Chapter 5: Miniature Piezohydraulic Pump Design, Modeling, and Mechanical Testing

5.1Piezohydraulic Pump Design and Components

Ventricular assist device systems are power transmission structures that deliver energy to the circulation hindered by a failing ventricle. As a result, the design of a mechanical circulatory support system consists of multiple stages of energy transfer. These stages, illustrated in Figure 5-1, consist of an energy source, power circuitry, energy converter, human interface stage and the load. Like all power transmission systems, an energy source, like a battery of power supply, provides the electrical power from which mechanical work will be transformed. This power, voltage and current, are then converted and regulated to the appropriate levels by the power circuitry to be delivered to the energy converter. The energy converter then converts the regulated electrical power from the power circuitry into mechanical power to be transferred to the human interface. The human interface converts the mechanical power into useful work for the circulation, which is the load.

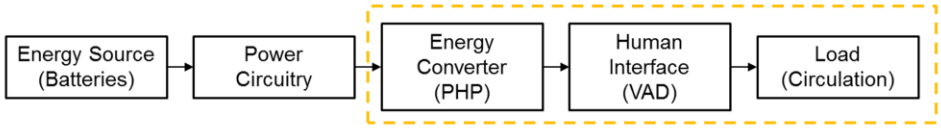

Figure 5-1. The system level components that make up a ventricular assist device system (the boxes highlighted in yellow indicate the topic of this dissertation)

The heart ventricular assist device systems, highlighted in the yellow dashed line, are the energy converter and human interface. As mentioned in Chapter 2, traditionally, the energy converter used in pulsatile ventricular assist device systems consists of an electro-pneumatic driver with supplies pressurized air to the human interface (blood pump). For continuous flow devices, the energy converter consists of permanent magnet, active electromagnetic bearings, and

driving coils and the human interface consists of the rotating impeller and pump housing. In this dissertation, the use of piezohydraulic technology as an energy converting mechanism for pediatric pulsatile blood pumps is studied. The aim of this research is to demonstrate that piezohydraulic pumps, when operated at high frequency, can provide sufficient power to pediatric pulsatile blood pumps while maintaining small form factor. In demonstrating this advantage, the different components that effect the conversion of electrical to mechanical energy will be discussed. The overarching goal is to design the pump such that its components allow the maximum amount of energy transfer from piezoelectric material to the human circulation. This chapter focuses on the piezohydraulic pump design while Chapter 6 focuses on the blood pump design (human interface).

Ventricular Assist Device Driver Design Revisited

In Chapter 4, the pressure and flow rate requirements from a pediatric pulsatile blood pump were discussed. Using these requirements and using a simplified power transmission train (seen in Figure 4-1), the flow rate and pressure output needed from a piezoelectric pump were calculated. In this section we will take a closer look into these requirements. Specifically, the pressure, flow, and power output requirements of a pulsatile blood pump for the left and right heart will be discussed. The same 1-D quasi-static model of a piezoelectric pump driver is used again to calculate final piezoelectric pump component dimensions. First we will look closer at the components of a pediatric pulsatile blood pump.

Consider a typical pulsatile blood pump seen in Figure 5-2(a). Pulsatile blood pumps, as mentioned in Chapter 2, consist of a blood chamber, valves (that mimic the valves in a native heart), drive chamber, and cannula to interface the blood pump with the circulation. For pediatric blood pumps, the circulation pressure (back pressure seen by the blood pump), flow

rate, and cannula diameter dictate the power output required from the ventricular assist driver. In Chapter 2, the assumptions were that a 6mm cannula and 5 L/min flow rate is needed to help the systemic circulations of pediatric patients with heart failure. For smaller children, specifically toddlers, these parameters are different. Thus for the remainder of this dissertation, the pressure and flow requirements used to design the piezohydraulic pump ventricular assist device driver are derived from the following assumptions.

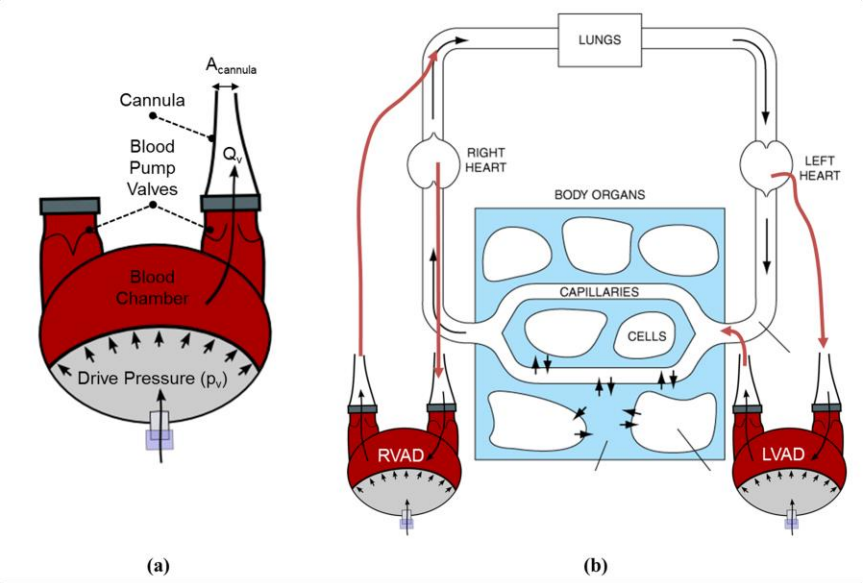

Figure 5-2. (a) Important components and drive variables for a pediatric blood pump (b) Blood pump used as a left ventricular assist device (LVAD) and a right ventricular assist device (RVAD)

Ventricular assist blood pumps can act as both right ventricular assist devices (RVADs) and left ventricular assist devices (LVADs) (Figure 5-2b). Recall from Chapter 2 that the pressure output of a healthy native left ventricle differs in magnitude from that of a healthy right ventricle. Because the left ventricle has a larger load, the necessary output pressure is larger than that of the right ventricle. As a result, the back pressure seen by a blood pump installed in the left and right side will be different. The average circulation pressures, P_{circ}, seen by the blood pump on the left and right side are 16 kPa and 2.5 kPa respectively. The required mean flow rate at that pressure

for both sides is 3 L/min. This flow output has to be achieved against the said back pressures and against the large resistance provided by the blood pump cannula, which are as small as 4mm in diameter. Thus, from equation 4-2, the drive pressure, p_v, needed to drive blood through a 4mm diameter cannula against the appropriate back pressures are 25 kPa and 11 kPa for a left heart assist and right heart assist blood pump respectively. The pressure and flow requirements for left and right heart assist device are summarized in Table 5-1.

Table 5-1. Requirements for Left and Right Heart Assist Pumps

Parameter	Left Heart Assist	Right Heart Assist
P_{circ} [kPa]	16 (2.3 psi)	2.5 (0.4 psi)
Q_{circ} [L/min]	3 (@ Pcirc)	3 (@ Pcirc)
ρ_{blood} [kg/m^3]	1063	1063
$A_{cannula}$ [mm^2]	12	12
p_v [kPa]	25.2 (3.7 psi)	11.3 (1.6 psi)
Q_v [L/min]	3 (@Pcirc)	3 (@Pcirc)

The resulting power output needed from the blood pump for left and right heart assist is 1.3 W and 0.6 W respectively. Now that the flow rate and pressure output from a left and right assist pediatric VAD have been specified, the piezoelectric hydraulic pump components can be sized. The components that make up a piezoelectric pump will be discussed next.

Piezoelectric Pump

The piezoelectric pump in this dissertation consists of multiple components that work together to convert the oscillatory displacement of a high energy density piezoelectric actuator to useful fluidic work. The cut-away schematic of the piezohydraulic pump designed for this research is shown in Figure 5-3. The final schematic drawings are included in the Appendix. The piezohydraulic pump consists of a piezoelectric stack, end cap, housing, stiffener, diaphragm, chamber spacer, valve (not shown), valve seat, and port end. The piezoelectric stack is the main

component in the piezoelectric pump. It is responsible for converting electrical energy to mechanical work. The housing and end cap provide a fixed reference for the piezoelectric actuator. The piezoelectric stack is bonded to a steel stiffener which is also bonded to a spring steel diaphragm. The stiffener constrains the shape of the diaphragm to a flat surface to increase the effective stroke volume of the device. The diaphragm has two functions. It is used as a seal for the pumping chamber and to increase the effective stiffness of the stiffener and piezoelectric stack combination. A chamber spacer is clamped between the diaphragm-stiffener assembly and the valve seat. This chamber spacer defines the pump chamber height and area. The valve seat, machined out of aluminum, consists of the inlet and outlet valve orifices. The valves are clamped to the valve seat by screwing in small screws into threaded holes of the valve seat. The port end consists of threaded ports that interface the piezoelectric pump to the hydraulic lines used in the rest of the driving system. A more in depth analysis and discussion of the piezoelectric stack, stiffener-diaphragm, chamber spacer, valve and valve seat will be presented.

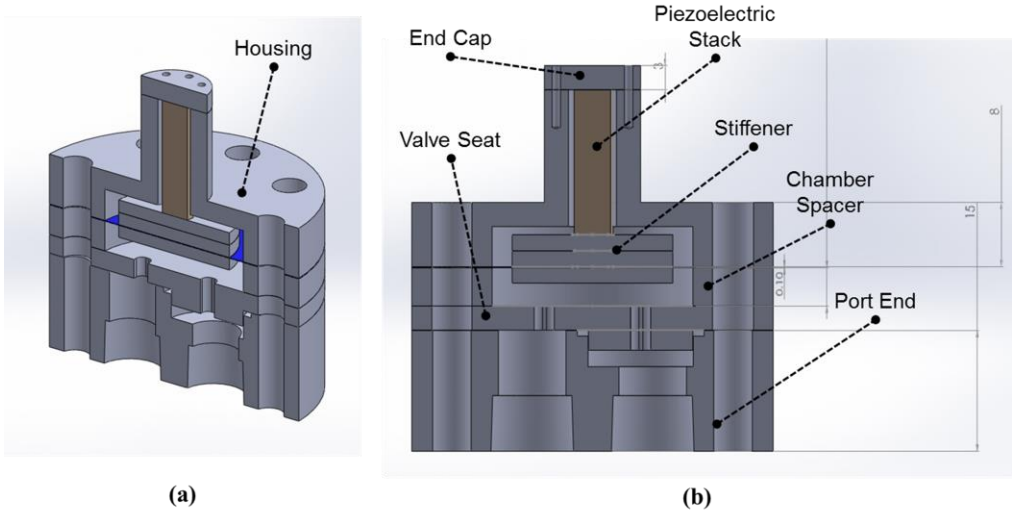

Figure 5-3. (a) Isometric center-cut view of the miniature piezohydraulic pump (b) front-cut view of the inside components of the pump

In this section, we will revisit the 1D quasi-static model of a piezohydraulic VAD driver discussed in Chapter 4. It is important to note that this analysis differs from that of Chapter 4 in the compliance of the hydraulic fluid, housing stiffness, and diaphragm stiffness will be considered. The stiffness of these components has a significant effect on the work transmitted to the VAD from the piezoelectric actuator. Using the work output cycle of a piezoelectric hydraulic pump, discussed by Sirohi and Chopra [77], [103], the relationship between the pump diaphragm, hydraulic cylinder, pediatric blood pump dimensions and stroke work can be calculated. The goal of the following section is to maximize the stroke work of the pediatric VAD while meeting the pressure and flow rate requirements of the patient's circulation.

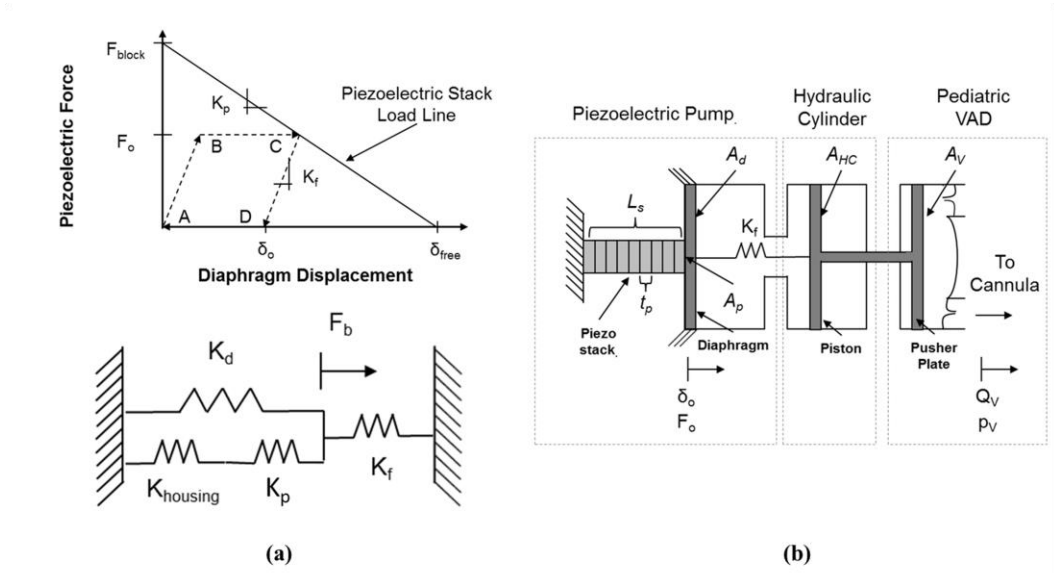

Figure 5-4. (a) 1D schematic of piezoelectric VAD driver (b) work cycle of the piezohydraulic pump and simplified system model of piezoelectric actuator, housing, and diaphragm

The plot in Figure 5-4(a) represents the realistic work cycle of a piezoelectric hydraulic pump with fluid compliance (fluid is not assumed incompressible). The cycle is enclosed by the parallelogram **ABCD**. In Chapter 2, this analysis was carried out assuming fluid is incompressible and the diaphragm, housing, and actuator were infinitely stiff. As will be seen

later in the experimental section of this chapter, these assumptions are not the true and as a result, the amount of work that can be transferred from the piezoelectric actuator to the working fluid is reduced. When a voltage is applied to the piezoelectric stack, the diaphragm is displaced and the chamber is pressurized. Unlike in the analysis in Chapter 4, where the chamber pressure increases instantaneously, the displacement produced by the piezoelectric contributes to the compression of the chamber fluid and this compression follows the line **AB** on Figure 5-4(a). The slope of this line corresponds to the effective stiffness of the fluid in the chamber. When the crack pressure from the outlet valve is reached, at F_o, the diaphragm displaces fluid at a constant force and follows the path **BC**. When the voltage is removed, the pressure in the pumping chamber drops along line **CD** until the diaphragm is displaced δ_o and the outlet valve is closed. The pressure drops low enough to open the inlet valve and restore the diaphragm to the original displacement (along **DA**). The area within this cyclic curve represents the total amount of work done on the working fluid in the hydraulic system connected to the piezoelectric pump.

The pumping cycle for a piezohydraulic pump allows us to calculate the size of pump needed to drive a pediatric ventricular assist device blood pump. Figure 5-4(b) shows the use of a piezoelectric hydraulic pump coupled with a hydraulic cylinder used to drive a pediatric VAD (as previously shown in Chapter 4). The piezohydraulic pump uses a piezoelectric stack and diaphragm to send pressurized fluid to the hydraulic cylinder which subsequently drives a pusher plate in the ventricular assist device. The piezohydraulic pump has a chamber with height h, which contains a working fluid with bulk modulus β. The amount of work that can be transferred from the piezoelectric pump is constrained by the operating range of the piezoelectric stack, which is defined by the piezoelectric load line (refer to Chapter 3) shown in Figure 5-4(a). The piezoelectric displacement can be written in terms of the force output.

$$\delta_o = \delta_{free}\left(1 - \frac{F_o}{F_{block}}\right) = \delta_{free} - \frac{F_o}{K_p} \qquad (5\text{-}1)$$

$$K_p = \frac{F_{block}}{\delta_{free}} \qquad (5\text{-}2)$$

Where δ_{free} is the free displacement of the piezoelectric stack actuator, F_{block} is the piezoelectric blocking force, and K_p is the piezoelectric actuator stiffness. Continuing with the quasi-static assumption and ignoring inertial terms in this analysis, the actuator, diaphragm (K_d), and hosing ($K_{housing}$) components can be modeled as a set of elastic springs connected in series and parallel. The housing and the piezoelectric share the same stress and thus are connected in series, so the effective stiffness of this structure is given by K_1.

$$K_1 = \frac{K_p K_{housing}}{K_p + K_{housing}} \cong K_p \text{ when } K_p \ll K_{housing} \qquad (5\text{-}3)$$

If the stiffness of the housing is comparable to the stiffness of the piezoelectric actuator, some of the force output of the actuator goes into straining the housing. This is undesirable and is the reason the housing should be made much stiffer than the actuator. In addition, the diaphragm shares the same displacement of the piezoelectric actuator and housing and is connected in parallel to this structure. The effective stiffness of this combination (housing, piezoelectric actuator and diaphragm) becomes K_2.

$$K_2 = K_p + K_d \cong K_p \text{ when } K_d \ll K_p \qquad (5\text{-}4)$$

Equation 5-3 states that the effective stiffness of the pump structure simplifies to the stiffness of the actuator when the housing is made much stiffer than the piezoelectric stack and the diaphragm (which constitutes the diaphragm stiffener combination) stiffness is much lower than the actuator. Finally, the fluid in the chamber is the last major compliance connecting the actuator to the ventricular assist device. The effective stiffness of the entire fluid filled pump becomes K_{eff}.

$$K_{eff} = \left(\frac{1}{K_f} + \frac{1}{K_p}\right)^{-1} \qquad (5\text{-}5)$$

$$K_f = \frac{\beta A_d}{h} \qquad (5\text{-}6)$$

Where K_f is the effective stiffness of the piezoelectric pump chamber fluid, β is the fluid bulk modulus, A_d is the diaphragm area, and h is the chamber height. The displacement of the piezoelectric actuator becomes:

$$\delta_o = \delta_{free} - F_o \left(\frac{1}{K_p} + \frac{1}{K_f}\right) \qquad (5\text{-}7)$$

Assuming the hydraulic cylinder and ventricular assist device pusher plate are perfect transformers, we can calculate the pressure generated by the ventricular assist device blood pump as a function of the force output.

$$P_V = \frac{A_{Hc}}{A_V A_d} F_o \qquad (5\text{-}8)$$

Where A_{HC} is the cross sectional area of the hydraulic cylinder piston, A_V is the area of the ventricular assist device pusher plate, and $A_{d.}$ is the area of the diaphragm in the PHP. The work output of the VAD blood pump can be written as a function of the piezoelectric force, displacement, hydraulic cylinder area, and pusher plate area. The work output of the piezoelectric pump can be written as seen in equation 5-9 by using equation 5-7.

$$W_{cycle} = \delta_o F_o = F_o \left[\delta_{free} - F_o \left(\frac{1}{K_p} + \frac{1}{K_f}\right)\right] \qquad (5\text{-}9)$$

Equation 5-9 can be separated into three separate terms and the work output can be written in terms of the ventricular assist device pressure P_V and the hydraulic cylinder and ventricular assist device pusher plate dimensions assuming these components act as ideal transformers.

$$W_{cycle} = \frac{A_d A_v}{A_{HC}} \delta_{free} P_V - \frac{A_d^2 A_v^2}{A_{HC}^2} \frac{\delta_{free}}{F_{block}} P_v^2 - \frac{A_d A_v^2}{A_{HC}^2 \beta} P_v^2 h \qquad (5\text{-}10)$$

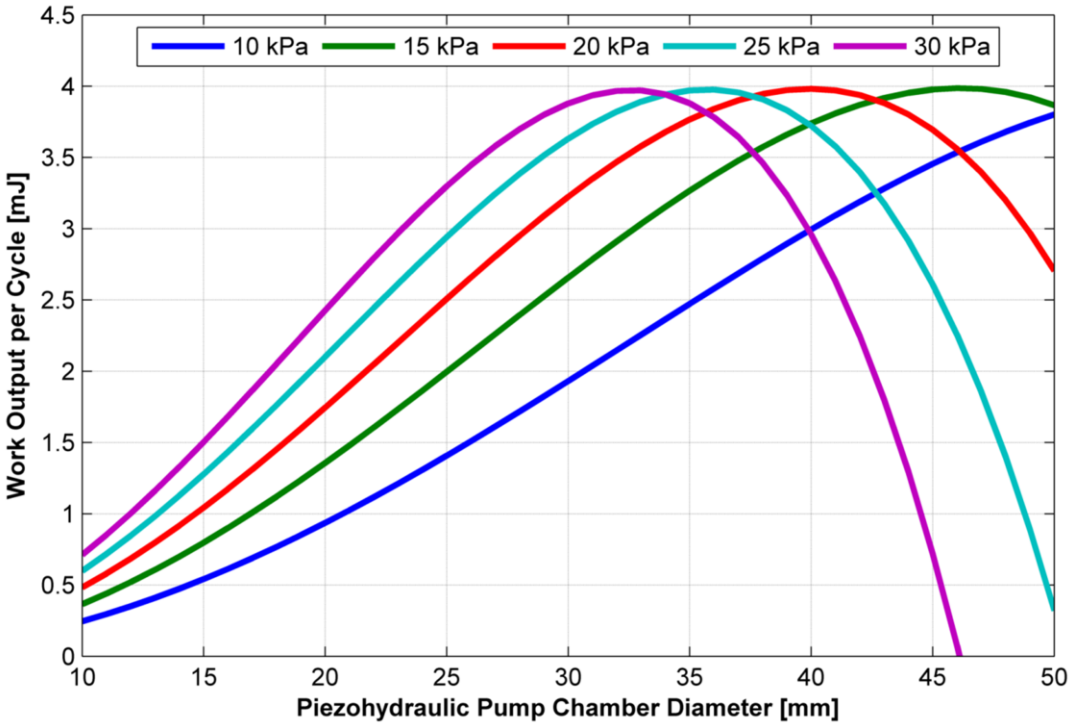

Figure 5-5. Graphical representation of the work output per cycle for various pump chamber diameters, ventricular assist device pressure output, pusher plate diameter (38mm) and hydraulic cylinder size (5/8" bore with ¼" rod)

Figure 5-5 shows the graphical representation of equation 5-10. Because the piezoelectric stack and hydraulic cylinder and pusher plate dimensions are typically fixed and based off dimensional analysis presented in Chapter 6, the work output per cycle of the entire driver system (shown in Figure 5-4) is dependent on the piezohydraulic pump chamber diameter. In this work output approximation, a 800 N block force and 20µm free displacement actuator is assumed (similar to the stack used in these experimental setups). A 5/8" bore hydraulic cylinder (with ¼" diameter rod) and 38 mm diameter pusher plate were also assumed (these represent the actual dimensions used in experimental tests). The work output per cycle can be optimized by choosing the appropriate chamber diameter. For this piezoelectric stack and hydraulic cylinder and pusher

plate dimensions, the maximum 4 mJ per cycle when working against a 30 kPa load. This analysis confirms that in order to optimize the amount of work transferred from a piezoelectric to the circulation; the load needs to be impedance matched to the stack actuator by choosing the appropriate hydraulic cylinder and ventricular assist device dimensions. Thus, for larger ventricular assist device pressures, a smaller chamber diameter is needed to match the high pressure requirement to the high force output of the actuator. Similarly, smaller VAD pressures necessitate larger chamber diameters to amplify down the force output from the piezoelectric stack. This impedance matching can also be achieved by modulating the hydraulic cylinder bore or the ventricular assist device pusher plate diameter. As a result, his analysis can be repeated for different cylinder and blood pump pusher plate geometries. Depending on if a 30 cc or 60 cc ventricular assist device is needed, the piezoelectric pump dimensions can be optimized to output the maximum amount of work per cycle.

While the work output is important, the flow rate and pressure output from the blood pump are also important driving requirements. The VAD blood pump pressure is shown derived in equation 5-11. Continuing with the quasi-static behavior and assuming that the valves from the PHP have a larger frequency bandwidth than the frequency of operation of the piezoelectric stack, we can approximate the flow rate from the PHP as:

$$Q_{PHP} \cong \delta_o A_d f = A_d f \left(\delta_{free} - F_o \left[\frac{1}{K_p} + \frac{1}{K_f} \right] \right) \qquad (5\text{-}11)$$

Where, *f* is the frequency of operation of the piezoelectric stack. Because we have assumed the hydraulic cylinder and pusher plate are perfect transformers, we get the flow from the VAD as:

$$Q_V \cong \frac{A_V A_d}{A_{HC}} f \left(\delta_{free} - F_o \left[\frac{1}{K_p} + \frac{1}{K_f} \right] \right) \qquad (5\text{-}12)$$

Thus, the unloaded maximum flow from the VAD is just equal to:

$$Q_{V,unloaded} \cong \frac{A_V A_d}{A_{HC}} f\delta_{free} \qquad (5\text{-}13)$$

Hydraulic Cylinder

The size of the hydraulic cylinder is important in sizing the piezohdraulic pump components. The hydraulic cylinder used in this study has a small bore and short stroke. This is to minimize the amount of fluid required to fulfill a forward pusher plate stroke. In this study, a ⅝" bore, ½" stroke double acting hydraulic cylinder (Clippard, AF-TDD-10-1/2) is used. The hydraulic cylinder has a ¼" diameter rod and thus has an effective area, A_{HC}, of 1.7 cm^2 and 2.11 cm^3 stroke volume. This cylinder stroke volume dictates the highest flow rate needed from the piezohydraulic pump. The typical electro-pneumatic driver must supply pressurized air at pumping rates as high as 100 beats per minute (BPM) [104]. This means that one pumping cycle (which consists of blood pump ejection and filling takes 0.6 seconds, 30% of which is dedicated to systole or blood ejection. Thus the 2.1 cm^3 from the hydraulic cylinder must be output within 0.18 seconds (700 cm^3/s flow rate). This flow rate must be achieved against a 16 kPa circulation pressure (for left heart assist) and 2.5 kPa circulation pressure (for right heart assist).

Piezoelectric Stack Actuator

Five types of piezoelectric actuators were used in this study. The size of the actuator was limited for two reasons: to keep the dimensions of the piezoelectric pump compact and to limit the capacitance of the piezoelectric to reduce the peak current drawn from the electronic power amplifier and power supply. With the exception of one piezoelectric stack, the heights of these piezoelectric stacks were 20 mm or less. The two smallest piezoelectric stacks used were the 2 mm x 2 mm x 20 mm NAC2011 (Noliac Group) and the 2 mm x 3 mm x 20 mm AE0203D16 (NEC Tokin) piezoelectric stacks. These stacks were chosen based on the initial design analysis carried on in Chapter 4. Two larger area stacks were also chosen to increase the pressure and

flow rate outputs of the pump. As will be discussed later in this chapter, the smaller stacks could not provide sufficient power output for the desired mechanical circulatory support requirements. A 3.5 mm x 3.5 mm x 20 mm Pst150/3.5x3.5/20 (APC International), 5 mm x 5 mm x 30 mm NAC2013 (Noliac Group) and 6.7 mm x 6.7 mm x 30 mm EPCOS piezoelectric stack were also tested. The EPCOS piezoelectric stack, typically used in fuel injector systems, represents the highest energy density actuator used in this research. The free displacements and blocking forces for these five actuators, summarized in Table 5-2, range from 17 μm to 42 μm and 168 N to 2500 N respectively.

Table 5-2. Five Types of Piezoelectric Stacks

Piezoelectric Stack Manufacturer	Catalog Name	Dimensions (lxwxh)mm	Free Displacement [μm]	Blocking Force [N]	Operating Voltage [V]
Noliac Group	NAC2011-H20-A02	2x2x20	20	168	0-150
NEC Tokin	AE0203D16	2x3x20	17	200	0-150
APC International	Pst150/3.5x3.5/20	3.5x3.5x20	20 (28)	800	0-150 (-30-150)
Noliac Group	NAC2013-H30-A02	5x5x30	42	1050	0-150
EPCOS International	----------	6.7x6.7x30	40	2500	0-160

All of the actuators in this study, shown in Figure 5-6, are low voltage unipolar piezoelectric stacks. The voltage range for these devices is limited to 0-160V. The relatively low voltage supplied to these actuators is a result of the thin (> 100 μm) piezoelectric plates making up the stack. Depending on the thickness of these plates (which can range from 50-100μm for these devices), the voltage range of these devices corresponds to electric fields between 0-2 MV/m. In addition, all of these stacks, excluding the Noliac Group actuators, are coated with insulating resin to prevent electrode shorting. A comparison of the different sizes of the piezoelectric stack actuators is shown in Figure 5-6.

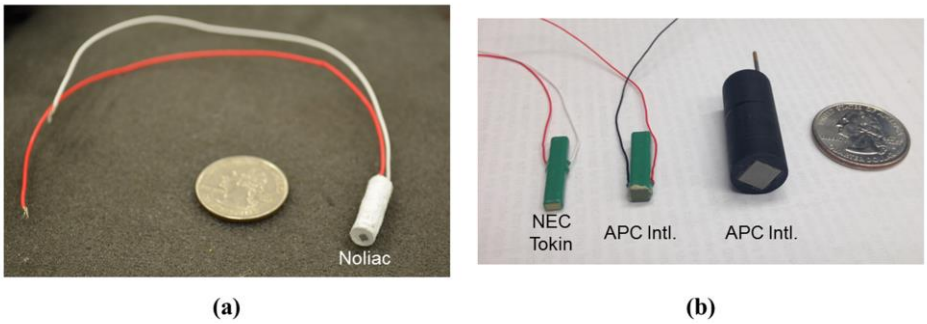

Figure 5-6. (a) Noliac 2x2x20mm piezoelectric stack and (b) from left to right: NEC Tokin 2x3x20mm, APC 3.5x3.5x20mm, and EPCOS 6.7x6.7x30mm piezoelectric stacks

Diaphragm and Stiffener

The diaphragm, shown in Figure 5-7a, is made of 0.004" (101µm) thin spring steel. The diaphragm provides a seal in between the pump chamber spacer and the pump housing. It also acts as a spring connected in parallel to the piezoelectric stack and actuator to effectively stiffen the piezoelectric-stiffener-diaphragm combination. Most importantly it provides a returning force to aid the piezoelectric pump chamber in refilling when the electric field to the piezoelectric stack is reduced to zero in the second half of the actuation cycle. It is important that the diaphragm be stiff enough to aid in pump refilling but not so stiff as to limit the displacement of the piezoelectric stack.

The stiffener, shown in Figure 5-7b, is a stainless steel cylinder that is attached to the diaphragm. Because the cross-sectional area of the piezoelectric stack is limited to the manufacturer dimensions (and in some cases rectangular) an additional component is needed to evenly distribute the stress applied to the diaphragm from the piezoelectric stack. The diaphragm-stiffener combination can be modeled as an annular flat plate with a central boss, outer edge clamped, and load on the boss [105] (shown in Figure 5-7c). The maximum deflection of the diaphragm, which occurs at the center, can be calculated from equation 5-1.

$$x_d = k_d \frac{PR_{chamber}^4}{Yt^3} \quad (5\text{-}14)$$

$$k_d = \frac{3(1-\upsilon^2)}{16}\left(1 - \left(\frac{R_{stiffener}}{R_{chamber}}\right)^4 - 4\left(\frac{R_{stiffener}}{R_{chamber}}\right)^2 \log\left(\frac{R_{chamber}}{R_{stiffener}}\right)\right) \quad (5\text{-}15)$$

Where x_d is the maximum diaphragm deflection, P is the pressure applied to the stiffener, $R_{chamber}$ is the radius of the chamber, $R_{stiffener}$ is the radius of the stiffener, υ is the poisson ratio, Y is the elastic modulus, and t is the thickness. From equations 5-14 and 5-15, the ratio of the stiffener radius to the chamber radius constrains the maximum possible deflection for a given applied force. This has important implications on the stroke volume of the piezoelectric pump. Various diaphragm-stiffener combinations were fabricated and are shown in Figure 5-7d. As will be seen in the 3D modeling section, there is an optimal stiffener to chamber radius ratio in terms of piezoelectric pump stroke volume. This optimum ratio is especially important when the pumping chamber and entire hydraulic system must be pressurized to increase the effective bulk modulus of the working fluid and prevent cavitation in the system.

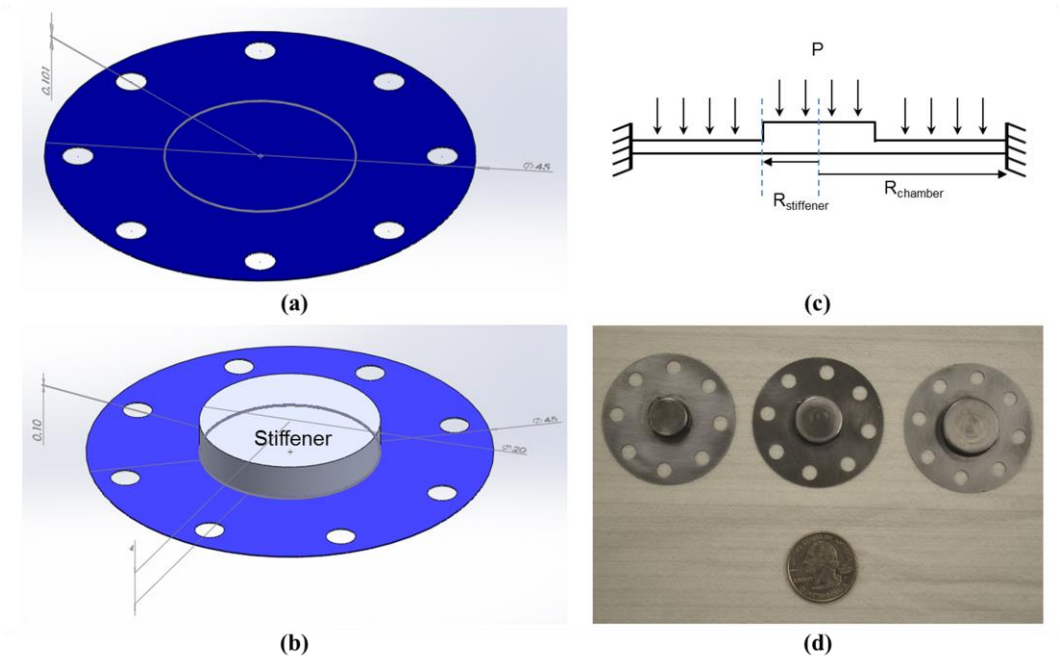

Figure 5-7. (a) Diaphragm computer aided design (CAD) structure, (b) diaphragm-stiffener structure, (c) schematic of a diaphragm with a central boss, and (d) different diaphragm-stiffener structures with varying stiffener radii

Chamber Spacer

Two types of chamber spacers were fabricated. The first chamber spacer, which was the spacer used in the majority of the research in this chapter, was fabricated from aluminum and had an inner diameter of 25 mm and height of 2 mm (Figure 5-8a and 5-8c). From the discussion above, we know that by decreasing the height of the chamber or by increasing the area of the chamber, the power can be more efficiently transmitted from the piezoelectric actuator to the hydraulic lines. Since the area is constrained by the desired size of the pump and the pressure requirement of the pediatric ventricular assist device, the height of the chamber was reduced. A second chamber spacer, 0.004" (101 μm) in height, was fabricated from steel and was chemically etched to get a thin profile (Figure 5-8b and 5-8d). The valves and valve seat were designed to give enough clearance to avoid contact between the diaphragm and the valves.

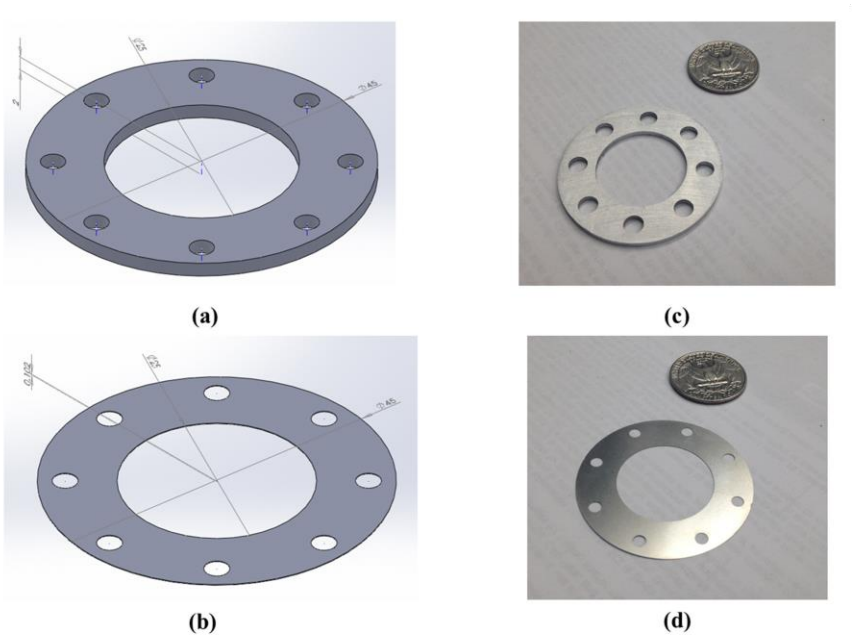

Figure 5-8. Computer aided design of the (a) 2 mm tall chamber spacer and (b) the 0.101 mm tall spacer, and the images for these components (c-d)

Valve and Valve Seat

The valves are one of the most important components in the piezohydraulic pump design. The valves are responsible for rectifying the high frequency strain oscillations into unidirectional flow and pressure output. Three different valves were designed and fabricated. All of the valves were cantilever reed valve designs. This design consists of a thin beam clamped at one end with the unclamped beam covering an orifice (Figure 5-9). There are two important characteristics of the reed valves that affect the performance of the piezohydraulic pump: the displacement of the valve upon pressurization and the resonant frequency. The reed valve, assuming a rectangular cross-sectional area, can be modeled as a one dimensional structure of length L clamped at one end undergoing a uniform applied load. The displacement at any position along the length of the beam is given by Equation 5-16.

$$y_{reed}(x)= \frac{qx^2}{24YI}\left(6L^2-4Lx+x^2\right) \qquad (5\text{-}16)$$

$$I = \frac{wt^3}{12} \qquad (5\text{-}17)$$

Where y_{reed} is the displacement of the cantilever beam at position x, q is the applied force per unit length, Y is the modulus of elasticity, I is the area moment of inertia (calculated in Equation 5-17), w is the beam width, and t is the beam thickness. The maximum deflection occurs at x = L. Knowing the maximum reed valve deflection, an approximate relationship between flow rate and pressure drop across the valve can be determined. This relationship is given by equation 5-18.

$$Q_{valve} = k_c N A \sqrt{\frac{2\Delta P}{\rho}}, \quad A = 2\pi R_{orifice} y_{reed}(L) \qquad (5\text{-}18)$$

Where Q_{valve} is the flow rate through the valve, k_c is the contraction coefficient of the valve orifice, N is the number of orifices, A is the effective flow area (diameter of orifice multiplied by the valve displacement), ΔP is the pressure difference across the valve, ρ is the density of the fluid, and $R_{orifice}$ is the radius of the orifice. As can be seen in this equation, a larger displacement in the reed valve can result in an increase in flow rate through the valve with a constant pressure difference across the valve. While a large reed valve deflection is important in ensuring the valve does not limit flow rate, the valve resonant frequency must be higher than the piezoelectric operation frequency.

The natural resonant frequency (first mode) of a rectangular cross-sectional area cantilever valve clamped at one end can be calculated from equation 5-19.

$$f_{natural} = \frac{1.875^2}{2\pi} \sqrt{\frac{Yt^2}{12\rho L^4}} \qquad (5\text{-}19)$$

Where $f_{natural}$ is the 1st natural frequency of the reed valve and ρ is the density of the cantilever structure. From equation 5-19, the best method to increase the natural frequency is to shorten the reed valve length. However, from equation 5-16, shortening the reed valve length also constrains

the maximum valve deflection. As a result, there is a tradeoff between the valve resonant frequency and the maximum deflection that can be achieved for a given reed valve length.

The first reed valve design was laser cut from 0.004" thick 1095 spring steel (blue tempered) and had a four-leaf structure with the center clamped (Figure 5-9a,d,g). The purpose of this first design was to develop a valve with multiple structures and orifices (increase the effective flow area) and short valve lengths (for high resonant frequency). The valve has an approximate dimension of 3 mm x 5.4 mm x 0.1 mm (L x W x t). The calculated resonant frequency for this first design is 9.4 kHz and the maximum deflection (with 100 N/m load per unit length) is 10.2 μm. The orifices are 5/64" (1.98 mm) holes offset 3.5 mm from the center. While the resonant frequency is in the kilohertz regime, the deflection of the valves is small. In addition, because there are no alignment marks or stoppers, it is difficult to align the valve flaps with the orifices on the valve seat. This leaves an uneven coverage of the valve flap over the orifices.

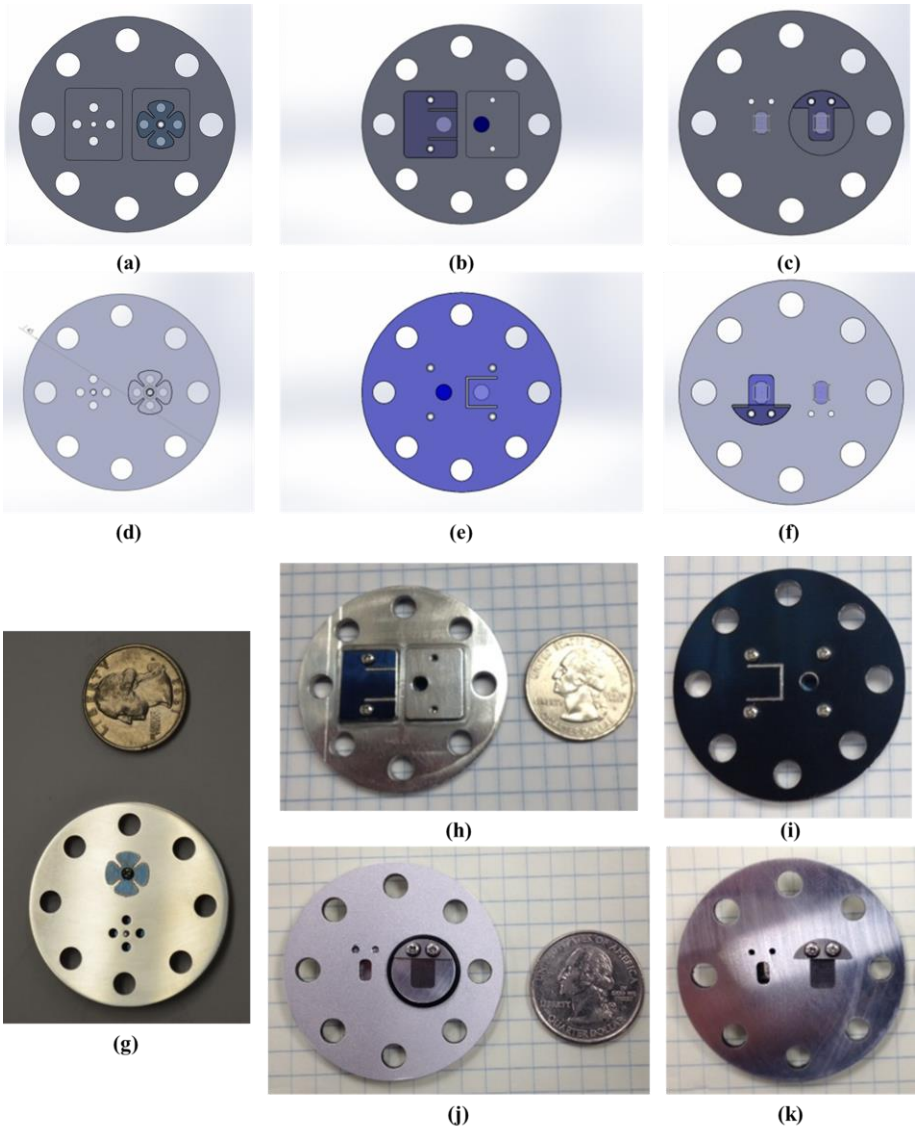

Figure 5-9. (a, g) Outlet valve and valve seat for four-leaf seat, (b,h) outlet valve and valve seat for laser-cut cantilever reed valve, (c,j) outlet valve and valve seat for chemically etched cantilever reed valve, (d) four-leaf inlet valve, (e,i) laser-cut cantilever reed inlet valve and (f,k) chemically etched cantilever reed inlet valve

The second valve design was simplified to increase the maximum valve deflection (but resonant frequency was decreased) and align the valves to the orifices. This valve was cut from 0.005" (127 µm) thick spring steel and has dimensions of 6 mm x 5 mm x 0.127 mm (L x W x t). The calculated resonant frequency for this 2nd design is 2.9 kHz and the maximum deflection (with 100 N/m load per unit length) is 90.4 µm. The orifices are 7/64" (2.77 mm) holes offset 3 mm

from the clamped edge of the valve. While this valve fixed the deflection and alignment issues of the four leaf valve design, the oxidation caused by the laser cutting beam on the edges of the structure resulted in valves that did not sit flush on the valve seat. This affected the metal on metal seal between the valve and valve seat which had a significant effect on the pressure and flow output of the piezohydraulic pump.

The last valve design (Figure 5-9c,f,j,k) had similar dimensions as the 2nd valve design. However, these valves were chemically etched from 0.004" and 0.0002" (50 μm) thick steel. The dimensions are 6.5 mm x 5 mm x 0.101 or 0.05 mm (L x W x t). The calculated resonant frequencies for this 3rd and final design are 2 kHz (0.1 mm thick) and 1 kHz (0.05 mm thick) and the maximum deflection (with 100 N/m load per unit length) are 240 μm (0.1 mm thick) and 1945 μm (0.05 mm thick). The orifices are 2.5 mm x 4 mm slots offset 2 mm from the clamped edge of the valve. While this design gives the smallest resonant frequencies in vacuum, the effective flow areas are much higher than the first two designs. This ensures that there is minimal energy loss in the opening of the valves and the acceleration of fluid through the orifices.

Housing

The last component that will be covered is the piezohydraulic pump housing. From the above discussion, we know that the stiffness of the pump housing can affect the power transmission of the piezoelectric stack to the fluid in the pumping chamber. The housing typically must be at least an order of magnitude more stiff than the stiffness of the actuator [103]. The pump housing in this study consists of an end cap and the housing (Figure 5-10). The end cap is screwed to the hosing with #0-40 machine screws. The end cap is made of 4 mm thick aluminum. The pump housing is also made of aluminum. Typically, the housing should also serve as a heat sink for the piezoelectric actuator. When operated at high frequency, heat generated by the piezoelectric must

be dissipated. The housing in this research was not designed to be a hit sink. Future iterations of this device should utilize the housing as a heat sink.

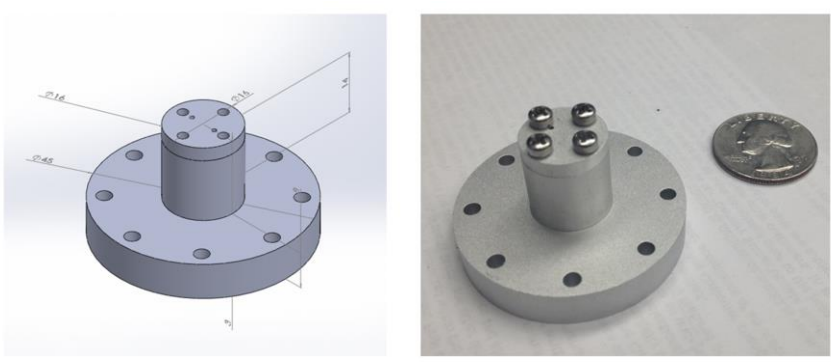

(a) (b)

Figure 5-10. (a) Computer aided design (CAD) model of the pump housing and end cap and (b) finished assembly of the housing and end cap

Figure 5-11 shows the final piezohydraulic pump assemblies used in this study. Figure 5-10a shows the final assembled pump that is designed for the smaller piezoelectric stacks (NAC2011, AE0203D16, and Pst150/3.5x3.5). Figure 5-11b shows the final assembled piezohydraulic pump that is intended to house the EPCOS and NAC2013 piezoelectric stacks. The smaller pump weighs approximately 150g while the larger piezohydraulic pump weighs 190g. Both of these designs constitute the smallest (non-MEMs) piezoelectric pumps designed to provide useful mechanical work. Before the pumps were mechanically tested, a three-dimensional multi-physics model was developed in COMSOL Multiphysics to more accurately predict the pressure and flow outputs of the fabricated piezoelectric pumps. A static analysis predicted the stroke volume at different pump chamber loading conditions (to simulate bias pressure) for different diaphragm-stiffener combinations. This was then translated to predict the amount of stroke work the pumps could output. A dynamic simulation calculating the frequency response and electrical impedance of the pump was also carried out.

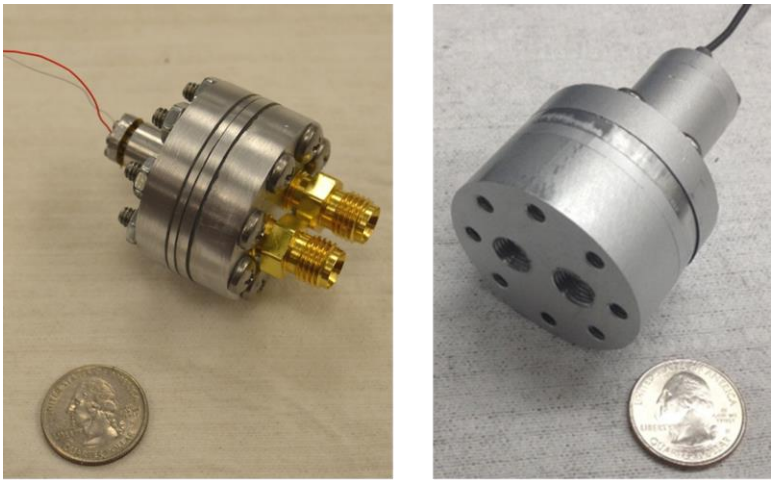

(a) (b)

Figure 5-11. (a) Piezoelectric pump designed to hold NAC2011, AE0203D16, and Pst150/3.5x3.5 piezoelectric stacks, and (b) pump designed to hold the EPCOS and NAC2013 piezoelectric stacks

5.2Three-Dimensional Piezoelectric Hydraulic Pump Model

The theoretical analysis and calculation up to this point (as seen in section 5.1 and 4.1) have been one dimensional approximations to predict piezohydraulic flow rate and pressure output. A three dimensional multi-physics finite element model was developed to accurately predict the theoretical stroke work and diaphragm stresses in the piezohydraulic pump. Two models were created on COMSOL Multiphysics® (COMSOL Multiphysics 4.2, Los Angeles CA). The first model simulates the Pst150/3.5x3.5 piezohydraulic pump while the second model simulates the EPCOS piezohydraulic pump. Both these piezoelectric stacks represent the highest energy density actuators used in this research with volumes under 0.25 cm^3 and 1.5 cm^3 respectively. The computer aided design pump components (Figure 5-12a) were imported into COMSOL Multiphysics® software and meshed (Figure 5-12b). The piezoelectric devices module was used and the aluminum and steel parts were modeled as linear elastic materials.

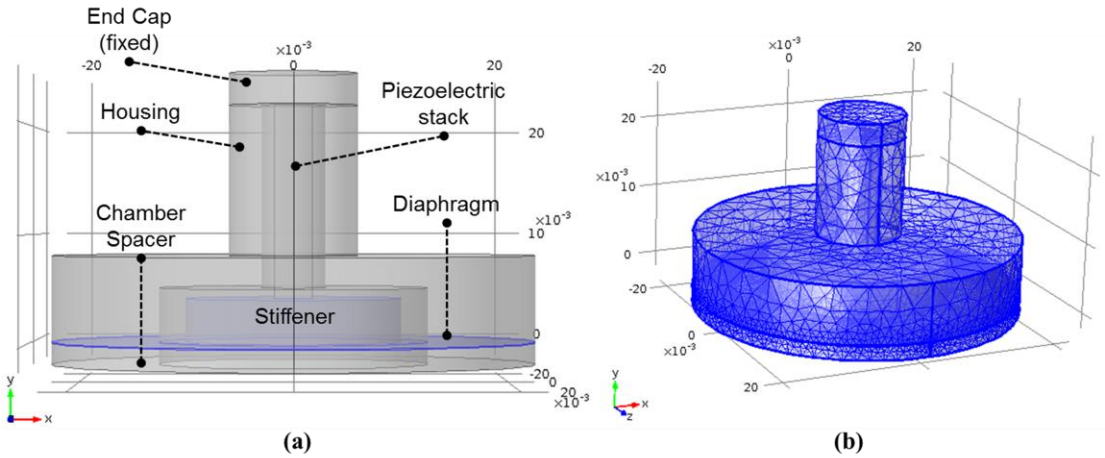

Figure 5-12. (a) Components of the 3D piezohydraulic pump multiphysics model and (b) meshed piezohydraulic pump

The pump model consists of an aluminum end cap, housing and chamber spacer. The stiffener and diaphragm are made of steel AISI 4340. The components are modeled as isotropic materials and are taken to be in contact and form a union. The piezoelectric stacks, Pst150/3.5x3.5 and EPCOS, are modeled as monolithic piezoelectric devices with thickness of 18 mm and 30 mm respectively. The compliance at constant electric field, piezoelectric coupling coefficient, and electric permittivity matrices for the Pst150/3.5x3.5 stack are shown in equations 5-20 to5-22.

$$s_{ij}^{E}=\begin{bmatrix} 1.5 & -0.5 & -0.5 & 0 & 0 & 0 \\ -0.5 & 1.5 & 0 & 0 & 0 & 0 \\ -0.5 & 0 & 1.8 & 0 & 0 & 0 \\ 0 & 0 & 0 & 3.4 & 0 & 0 \\ 0 & 0 & 0 & 0 & 3.4 & 0 \\ 0 & 0 & 0 & 0 & 0 & 3.4 \end{bmatrix} \times 10^{-11}\,\frac{1}{\text{Pa}} \qquad (5\text{-}20)$$

$$d_{mj}=\begin{bmatrix} 0 & 0 & 0 & 0 & 930 & 0 \\ 0 & 0 & 0 & 930 & 0 & 0 \\ -287 & -287 & 640 & 0 & 0 & 0 \end{bmatrix} \times 10^{-12}\,\frac{\text{C}}{\text{N}}, \qquad (5\text{-}21)$$

$$\varepsilon_{mk}^{T}=\begin{bmatrix} 5000 & 0 & 0 \\ 0 & 5000 & 0 \\ 0 & 0 & 5400 \end{bmatrix} \qquad (5\text{-}22)$$

Similarly, the compliance at constant electric field, piezoelectric coupling coefficient, and electric permittivity matrices for the EPCOS stack are shown in equations 5-23 to5-25.

$$s_{ij}^{E}=\begin{bmatrix} 1.3 & -0.4 & -0.4 & 0 & 0 & 0 \\ -0.4 & 1.3 & 0 & 0 & 0 & 0 \\ -0.4 & 0 & 2.5 & 0 & 0 & 0 \\ 0 & 0 & 0 & 3.4 & 0 & 0 \\ 0 & 0 & 0 & 0 & 3.4 & 0 \\ 0 & 0 & 0 & 0 & 0 & 3.4 \end{bmatrix} \times 10^{-11} \frac{1}{\text{Pa}} \qquad (5\text{-}23)$$

$$d_{mj}=\begin{bmatrix} 0 & 0 & 0 & 0 & 590 & 0 \\ 0 & 0 & 0 & 590 & 0 & 0 \\ -175 & -175 & 714 & 0 & 0 & 0 \end{bmatrix} \times 10^{-12} \frac{\text{C}}{\text{N}}, \qquad (5\text{-}24)$$

$$\varepsilon_{mk}^{T}=\begin{bmatrix} 657 & 0 & 0 \\ 0 & 657 & 0 \\ 0 & 0 & 903 \end{bmatrix} \qquad (5\text{-}25)$$

The end of the end cap and the bottom of the chamber spacer are taken as fixed boundary conditions. All other boundaries are taken to be free. The top of the piezoelectric stack (touching the end cap) is designated as an electrical terminal where the voltage to the device is applied. The bottom of the piezoelectric stack was designated as the electrical ground. A zero charge boundary condition is applied to the sides of the piezoelectric stack. A pressure load on the face of the diaphragm (on the side of the chamber spacer) was applied to simulate the load from an external bias pressure. Two types of analysis were carried out. First, the diameter of the stiffener relative to the diameter of the inner chamber spacer diameter was varied to investigate the effect of this dimension on pump stroke volume and the stress on the diaphragm. The effect of bias pressure on the pump stroke volume for these different stiffener dimensions is also investigated. From this study, the theoretical pump load line (pressure versus flow rate) can be extrapolated. This plot gives the entire range of pump performance from the stall pressure to the maximum

stroke volume in the unloaded condition. It also allows us to calculate the maximum stroke work that can be achieved from the piezohydraulic pump.

Static Analysis – Stroke Volume and Diaphragm Stress

A static electric field of 2 MV/m was applied across the piezoelectric actuator (for both simulations). A bias pressure of 344 kPa (50 psi) was applied to the diaphragm and the inner part of the chamber spacer. A parametric sweep of different stiffener diameters was carried out on both the EPCOS and Pst150/3.5x3.5 piezoelectric pump models. The diaphragm displacement profile and the diaphragm stresses along the diaphragm length were plotted for all stiffener geometries.

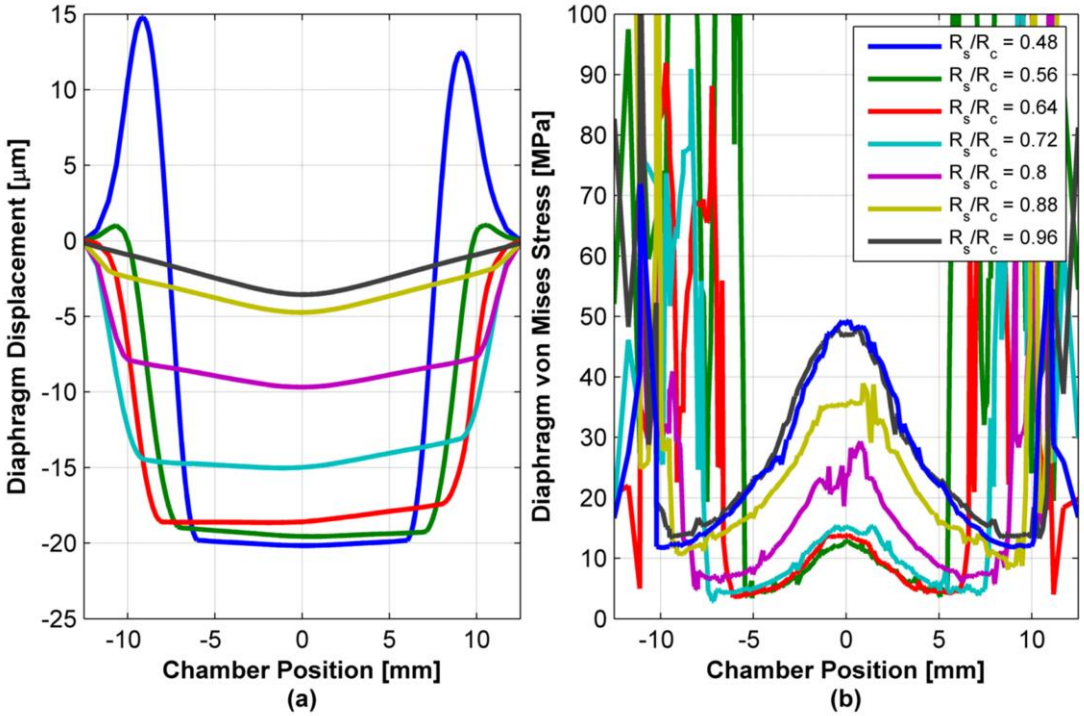

Figure 5-13.(a) Pst150/3.5x3.5 pump diaphragm displacement profile with a 50 psi pressure load and (b) stresses along the diaphragm length

Figure 5-13a shows the displacement of the Pst150/3.5x3.5 pump diaphragm along the length of the diaphragm. In this plot, a negative displacement corresponds to a net displacement

into the pumping chamber (stroke volume out of the pump) and a positive displacement represents an undesired deformation in the opposite direction of the piezoelectric strain. As can be seen in Figure 5-13a, the stiffener provides a relatively even diaphragm deformation to increase the effective stroke volume. The maximum deflection is 20 μm, which approximates the free displacement of this actuator (23 μm from Equation 4-4), and occurs when a small diameter (R_s/R_c = 0.48) stiffener is used. The maximum diaphragm displacement decreases nonlinearly with increasing stiffener size. However, while decreasing the stiffener diameter increases the maximum achievable diaphragm displacement, it also results in a volumetrically inefficient pump. Decreasing the stiffener diameter also decreases the overall stiffness of the diaphragm-stiffener structure. Thus, when a bias pressure is introduced in the pumping chamber (which is often the case) the diaphragm deforms into pump housing and decreases the effective stroke volume. In summary, the stiffener diameter should be small enough to allow the actuator displacement to approach its free displacement but it should also be large enough to prevent diaphragm deformation into the pump housing. The stiffener also affects the stresses on the pump diaphragm.

Figure 5-13b shows the von Mises stresses along the length of the diaphragm for the various stiffener sizes. Similar to the displacement profile, there is an optimal stiffener size that results in minimal diaphragm stress along the diaphragm length. The largest stress values occur at the diaphragm clamped edges (12.5 mm and -12.5 mm) and at the outer circumferential edge of the stiffener. These values, which are greater than 100 MPa, are not realistic and are an artifact of the clamping and fixed conditions at these edges. For stiffener radii that are above 80% of the pumping chamber diameter, the maximum stress at the center of the diaphragm increases. Smaller stiffener diameters result in smaller stresses in the diaphragm up to a point. If the

stiffener diameter becomes too small (as seen when R_s/R_c = 0.48), the diaphragm stresses increase as a result of the large deformation in the diaphragm. The maximum diaphragm stresses measured are about 40 MPa for stiffeners greater than 96% of the chamber diameter and less than 50% the chamber diameter. From this analysis it can be seen that a stiffener radius to pump chamber radius of 0.64 gives the best diaphragm displacement and the smallest stresses along the diaphragm length when a 50 psi bias pressure is applied to the pumping chamber.

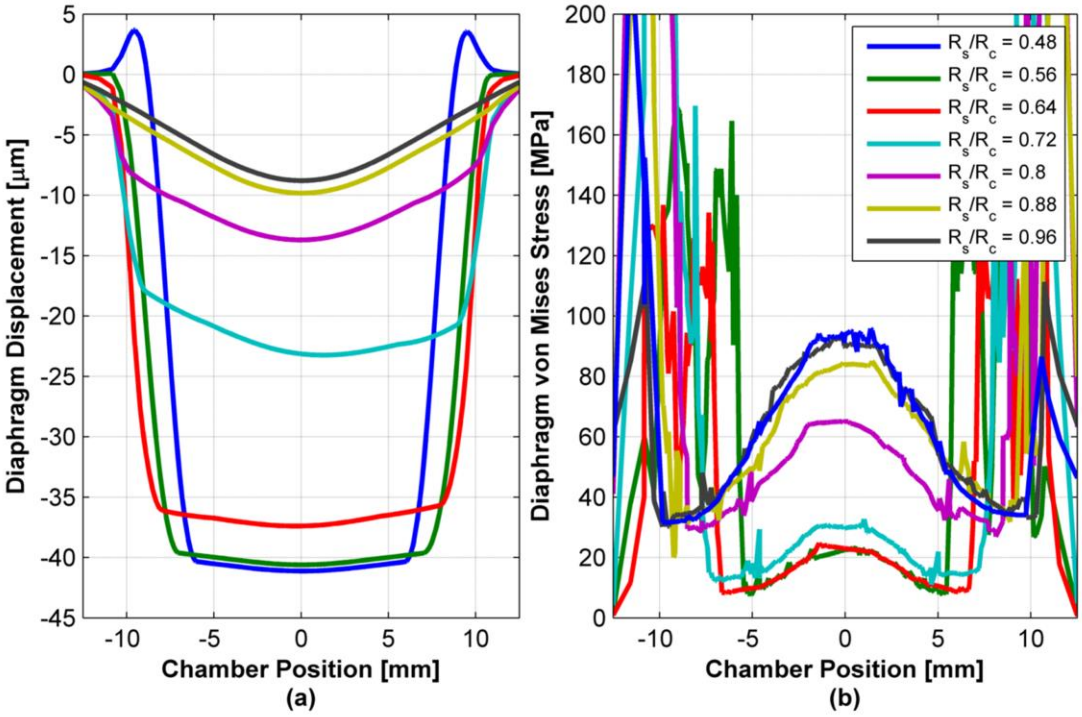

Figure 5-14. (a) EPCOS pump diaphragm displacement profile with a 50 psi pressure load and (b) stresses along the diaphragm length

Figure 5-14a and 5-14b show the same diaphragm displacement and von Mises stress profiles for the EPCOS piezoelectric stack pump. The trends measured in the Pst150/3.5x3.5 model are valid for this model as well but the displacement values and stress values differ. The largest net displacement of the pump is 41 µm and occurs for a stiffener diameter that is 48% of the chamber diameter. However, similar to the Pst150/3.5x3.5 model, the diaphragm von Mises

stress is large at the center, 95 MPa, because of the large diaphragm deformation. There is also some diaphragm deformation into the pump housing. The best diaphragm displacement, 37 µm, and diaphragm stress (21 MPa) profiles occur when the stiffener radius is 64% of the chamber radius. Using these static models, the theoretical stroke volume of the pump could be calculated by integrating the diaphragm displacement profile. Various bias pressures ranging from 0 MPa to 1 MPa (140 psi) were applied to the pump diaphragm and the stroke volume of the diaphragm was calculated when a 2 MV/m electric field was applied to the piezoelectric stack.

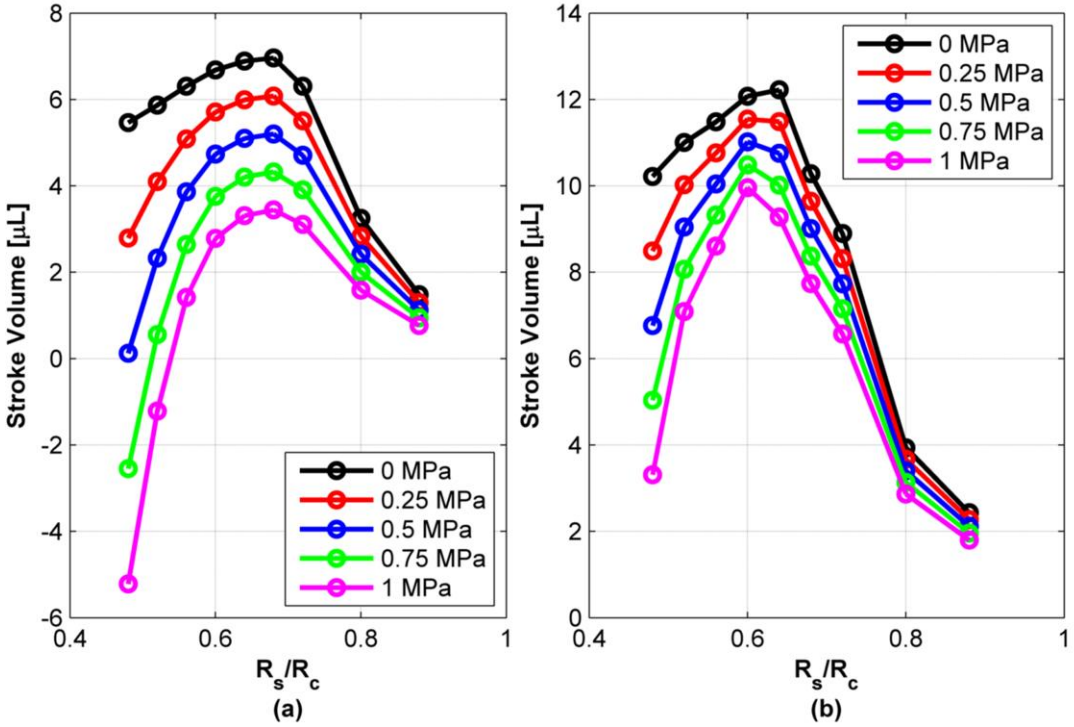

Figure 5-15. (a) Calculated stroke volume of the Pst150/3.5x3.5 pump at various bias pressures and stiffener radius to chamber radius ratios and (b) calculated stroke volume of the EPCOS pump at various bias pressures and stiffener radius to chamber radius ratios

Figure 5-15a shows the effective stroke volume of the Pst150/3.5x3.5 pump and Figure 5-15b shows the effective stroke volume of the EPOS pump as a function of the stiffener to chamber radius ratio at various bias pressures. The stoke volume is calculated by taking the surface integral of the diaphragm displacement and subtracting the volume loss associated with

applying a pressure to the diaphragm. Thus, a negative stroke volume indicates that the volume loss is greater than the stroke volume. The maximum stroke volume, 7 µL (Pst150) and 12 µL (EPCOS), occurs when there is no bias pressure and when the stiffener diameter is 64% (16 mm) of the chamber diameter. The stroke volume decreases dramatically for stiffener diameters greater than 16mm. This volume loss is associated with an increase in the effective stiffness of the diaphragm-stiffener structure. The stroke volume also decreases with decreasing stiffener diameter. This change in stroke volume is increased when the pressure applied to the chamber is increased and can be seen by the downward shift in the curves. The volume loss for stiffener diameters less than 16 mm is associated with the diaphragm deformation into the pump housing. Since the piezoelectric pump does require a bias pressure to provide a preload to the piezoelectric stack, ensure adequate pump chamber refilling, and prevent cavitation within the hydraulic system. Since the final design with utilize a 16 mm diameter stiffener and the bias pressure will be between 0.25 MPa (36 psi) to 0.75 MPa (108 psi), the stroke volume of the Pst150/3.5x3.5 pump will range from 4 µL to 6 µL and from 10 µL to 11 µL for the EPCOS pump. This type of static analysis could also be used to predict the stroke work from the pump.

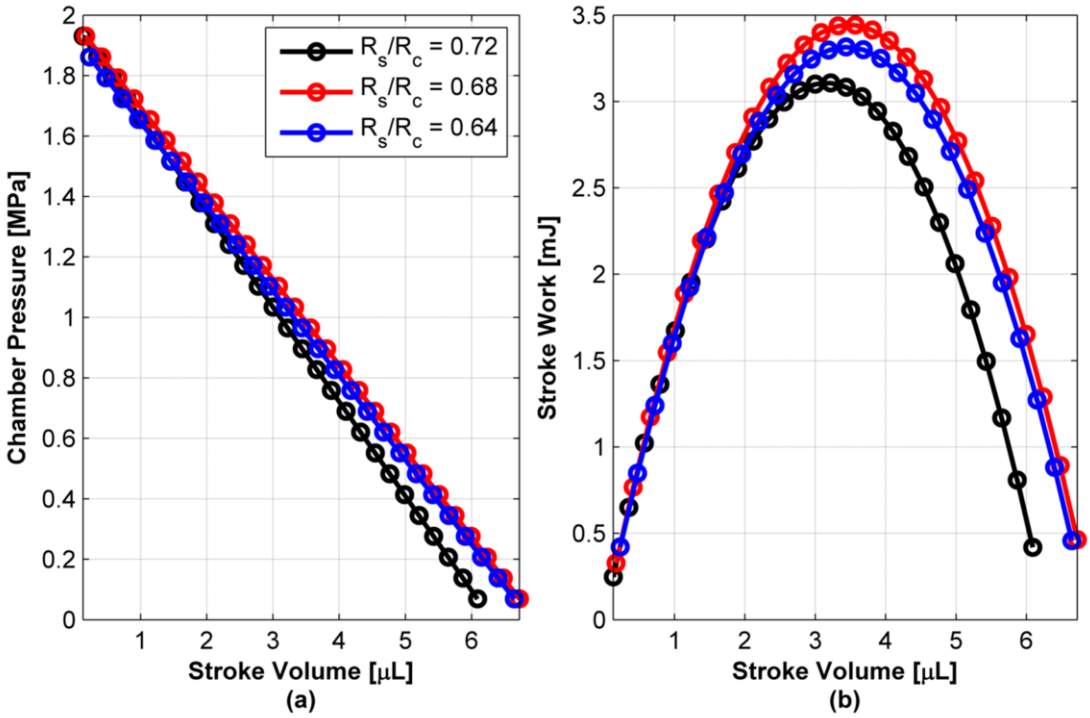

Figure 5-16. (a) Pst150/3.5x3.5 piezoelectric pump load line for various stiffener diameters and (b) stroke work versus stroke volume

Figure 5-16 shows the load line for the Pst150/3.5x3.5 piezoelectric pump and stroke work versus stroke volume. Three stiffener radii (closest to the 64% optimal stiffener size) were used in this model. Figure 5-16a shows the maximum operating pressure and stroke volume outputs for the pump. For stiffener diaphragms 64-72% of the chamber radius (16-18 mm), the maximum pressure output, called the stall pressure, is 1.9 MPa (275.5 psi) and occurs when there is no net stroke volume out of the pump. The maximum stroke volume occurs when there is no external pressure on the pump diaphragm and ranges from 6 µL to 7 µL, as confirmed by Figure 5-15a. The product of the chamber pressure and stroke volume gives the pump stroke work, which is shown in Figure 5-15b. The stroke work varies parabolically with stroke volume and has a maximum value of 3.5 mJ (for a 16 mm diameter stiffener) at 3.5 µL (or half the maximum stroke volume). This represents an impedance matched condition and the optimal operating point

of the piezoelectric pump in terms of work output. Thus, assuming quasi-static behavior, the piezoelectric pump can achieve a power output of 3.5 W at 1 kHz operation.

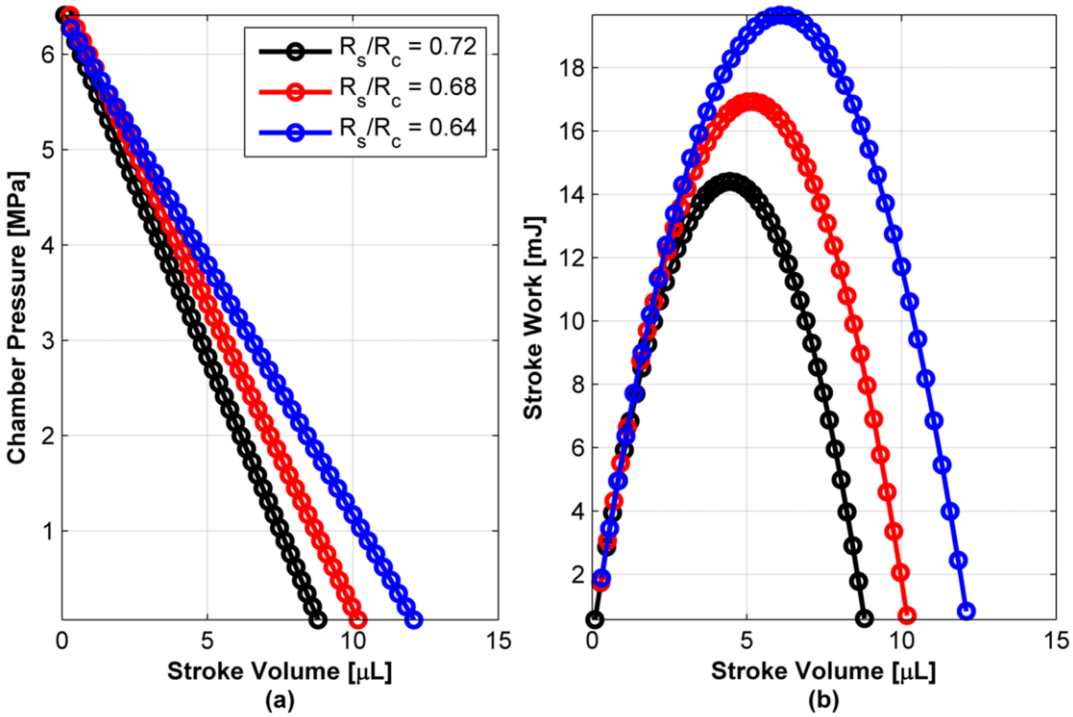

Figure 5-17. (a) EPCOS piezoelectric pump load line for various stiffener diameters and (b) stroke work versus stroke volume

Figure 5-17 shows the load line for the EPCOS piezoelectric pump and stroke work versus stroke volume. Similar to the Pst150/3.5x3.5 model, three stiffener diameters (64-72% of the chamber size) were used in this model. For stiffener diameters between 16-18 mm, the stall pressure is 6.5 MPa (942 psi). The unloaded stroke volume for these stiffener sizes ranges from 8.8-12 µL. The stroke work, shown in Figure 5-17b, varies parabolically with stroke volume and has a maximum value of 14 W, 17 W, and 19 W for the 16, 17, and 18 mm stiffener diameters respectively. The maximum work output occurs at half the maximum stroke volume and also represents an impedance matched condition. Assuming quasi-static behavior, the EPCOS piezoelectric pump utilizing a 16 mm diameter stiffener can achieve a power output of 19 W at 1

kHz operation. While the quasi-static assumption is accurate for frequency ranges up to about 250 Hz, it does not hold above this frequency bandwidth. This is because there are three frequency dependent phenomena that can affect the performance of the piezohydraulic pump. These phenomena include:

1. The mechanical resonances of the reed valves (discussed in the previous sections)
2. The electromechanical resonance frequencies of the piezohydraulic pump
3. The resonance frequencies of the hydraulic fluid in the system

The valve resonance was discussed in the previous section of this chapter. When a mechanical oscillation, like an oscillating pressure, is applied on the valve, the structure oscillates more readily at the resonant frequency. There is also a resonant frequency associated with the piezoelectric actuator and mechanical structure which it is attached to, known as an electromechanical resonance. This electromechanical resonance occurs under an electrical excitation and causes a mechanical vibration and change in the electrical impedance of the piezoelectric structure. There are also resonances associated with the oscillation of fluid in the hydraulic circuit attached to the piezohydraulic pump. As will be seen later in this chapter, this fluidic resonance can have a significant impact on the performance of the pump. First, we will predict the eletromechanical resonance frequencies of the piezohydraulic pump.

Dynamic Analysis – Piezohydraulic Pump Electromechanical Resonance

A frequency domain study step in COMSOL was added to find the resonance frequency of the piezohydraulic pump structure. A 1 kV/m electric field was applied to the piezohydraulic pump (both Pst150/3.5x3.5 and EPCOS) and the frequency sweep ranged from 1 Hz to 35 kHz. The stiffener radius to chamber radius ratio was also varied from 48% to 88%. The resonance of a piezoelectric actuator bonded to an external structure is typically measured by measuring the

electrical impedance of the piezoelectric material. Generally, at low frequencies, the piezoelectric impedance decreases with increasing frequency like a capacitor. However, at a specific frequency, called the resonance, the impedance drops dramatically. This sharp drop in impedance is associated with a large current drawn from the power supply and a large mechanical displacement from the piezoelectric actuator and its attached structure. There is also an anti-resonance associated with piezoelectric structures. This frequency occurs when the electrical impedance of the piezoelectric actuator increases dramatically. At this frequency, there is minimal current draw from the power supply and there is a small displacement in the actuator and structure. The resonance and anti-resonance pair represent the piezoelectric structure's point of maximal and minimal power consumption.

Figure 5-18 show the impedance spectrum for the piezohydraulic pumps for different stiffener radius to chamber radius ratios. The resonance frequencies for the various permutations are defined as occurring at the first dramatic drop in the impedance plot. Figure 5-18a shows the impedance plots for the Pst150/3.5x3.5 piezohydraulic pump and Figure 5-18b shows the impedance spectrum for the EPCOS piezoelectric pump. The lowest resonant frequency for both types of pumps occurs when the stiffener diaphragm is 64% of the chamber radius. As seen previously, this size of stiffener corresponds to the ratio that results in the least stiff configuration. Larger diameter stiffeners increase the resonance frequency of the pump because of the increased overall stiffness of the diaphragm-stiffener structure. Smaller diameter stiffeners (below 64% stiffener and chamber ratio) also result in larger resonance frequencies which are attributed to the decrease in mass of the entire structure. Thus, from the static and dynamic analysis of the PPst150/3.5x3.5 and EPCOS piezohydraulic pump, the optimal stiffener radius to chamber radius is 0.64 or the stiffener radius should be 64% of the radius of the chamber spacer

to increase pump stroke volume, prevent large diaphragm stresses, increase stroke work, and decrease the resonant frequency value.

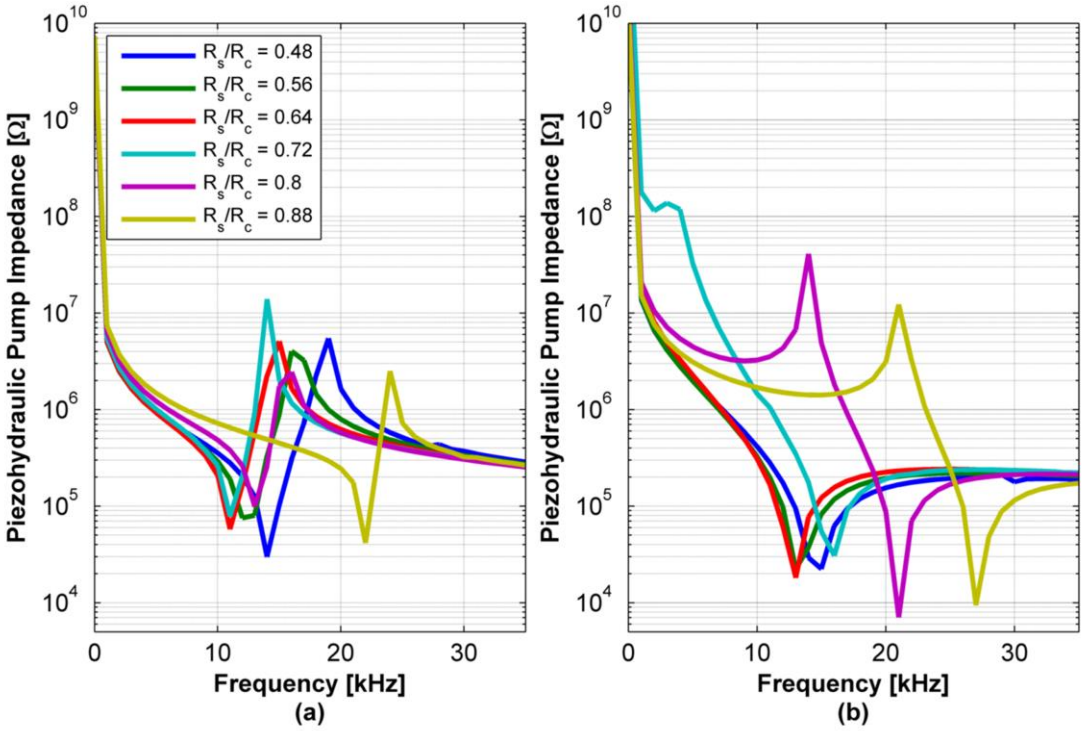

Figure 5-18. (a) Impedance versus frequency curves for Pst150/3.5x3.5 pump with different stiffener radius to chamber radius ratio and (b) impedance versus frequency curves for EPCOS pump with different stiffener radius to chamber radius ratio

Piezohydraulic Pump Impedance Testing

Figure 5-19 shows the experimental setup to measure the impedance of the EPCOS different piezoelectric pump. The piezoelectric stack was attached to a 1Ω resistor which was connected in series to the piezoelectric actuator. A dynamic signal analyzer (Stanford SR785 DSA, Palo Alto CA) was used to measure the impedance of the piezohydraulic pump. The signal analyzer applied a small sinusoidal voltage (5 VPP) to the resistor-piezoelectric circuit. Impedance, which is defined as the voltage applied to the stack divided by the current through the stack ($\frac{V_{stack}}{I_{stack}}$), was measured by measuring the voltage across the piezoelectric stack and dividing by the voltage across the 1Ω resistor (gives current directly). The frequency was swept from 1 kHz to 20 kHz

(2047 data points). The stiffener radii were changed (12 mm, 16 mm, and 19 mm) to verify the resonance values seen in Figure 5-18a and 5-18b. The phase difference between the current and voltage through and across the piezoelectric stack was also measured.

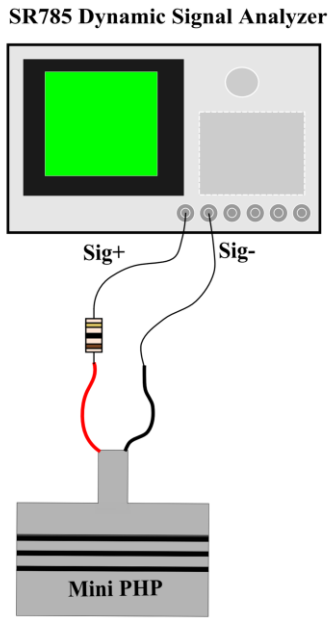

Figure 5-19. Piezoelectric pump impedance measurement experimental setup

Figure 5-20a and 5-20b show the impedance and phase plots, respectively, for the EPCOS piezoelectric pump using different stiffener sizes. Figure 5-20a shows the logarithm of the impedance ($20 \log_{10} Z_{php}$) in units of dB. At resonance, the electrical impedance of the pump drops off dramatically. This resonance point occurs at 13.95 kHz for the 12 mm stiffener (15 kHz in model), 11.75 kHz for a 16 mm stiffener (13 kHz in the model), and 12.7 kHz for the 18.75 mm stiffener (16 kHz in the model for 19mm stiffener). These points represent the points where the piezoelectric actuator draws the largest amount of current. It also the point of the largest piezoelectric actuator displacement. The phase of the piezohydraulic pump is shown in Figure 5-20b. The phase is defined as the phase difference between the voltage applied to the piezoelectric stack and the current going through the actuator. At low frequencies the phase difference is 90

degrees, which corresponds to a capacitive load. At resonance, the phase difference approaches a more positive value, which indicates it becomes electrically resistive. Thus, while a higher mechanical displacement can be achieved by operating the pump at resonance, it also corresponds to the highest power dissipation.

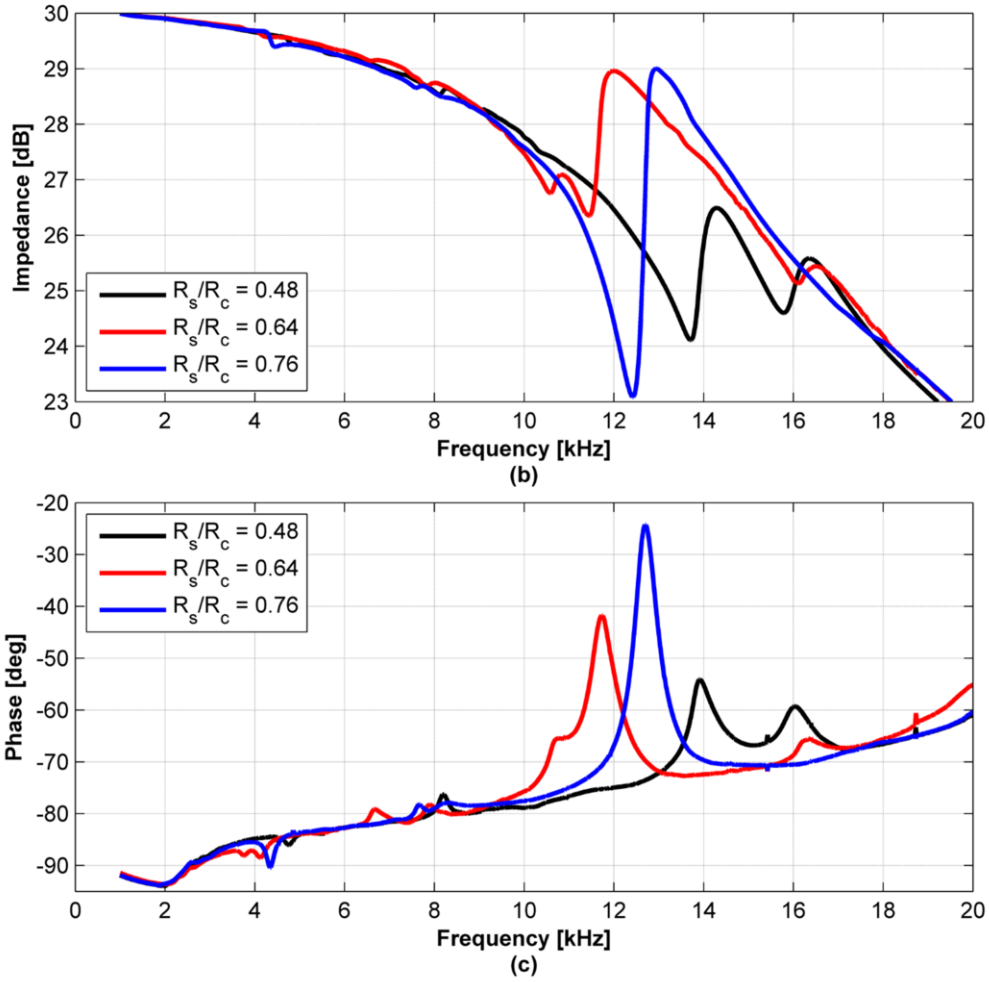

Figure 5-20. (a) Impedance versus frequency curves for EPCOS pump with different stiffener radius to chamber radius ratio and (b) phase versus frequency curves

Reed Valve Model and Testing

In addition to the 3D piezohydraulic model described above, a two-dimensional model of the reed valve flap was constructed to predict the valve losses. The 2D model was constructed in COMSOL using the fluid-stricture interaction module (Figure 5-21a). The valve was modeled as

a two dimensional linear elastic steel cantilever beam (6.5 mm x 0.1 mm) clamped at one end. A fluid domain was constructed around the beam and consisted of an inlet channel (5 mm wide) and outlet channel. It is important to note that the reed valve has a very small gap between the unclamped edge of the cantilever valve and the inlet channel. This is because the fluid domain must be continuous within the model. A pressure is applied to the inlet boundary condition and to the outlet boundary condition. Flow rate through the valve was calculated by taking the line integral of the y-component of the fluid velocity and multiplying this integral by the inlet channel width (2.5 mm). Various pressure differentials (outlet pressure subtracted from inlet pressure), ranging from 7 kPa (1 psi) to 139 kPa (20 psi) were applied across the cantilever valve. Three different fluids were used: Dexron VI automatic transmission fluid (dynamic viscosity: 24 mPas), SAE10 oil (dynamic viscosity: 65 mPas) and water (dynamic viscosity: 1 mPas).

Figure 5-21b shows the results for the two-dimensional valve model for three working fluids with different viscosities. As can be seen, the flow rate increases parabollically with an increase in pressure differential across the valve. This is not surprising, since from equation 5-18, we know that the flow rate and pressure differential have a $Q_{valve}^2 \propto \Delta P$ dependency. Because the density, ρ, is proportional to the dynamic viscosity, fluids with more viscosity tend to resist flow more readily than those with lower viscosities. Thus, because water is less viscous than both Dexron VI and SAE10 oil, the highest flow rate that can be achieved with a 68 kPa (10 psi) pressure differential is 0.075 cm^3/s, 0.19 cm^3/s, and 0.42 cm^3/s for SAE10 oil, Dexron VI ATF and water respectively. The results of this model show that automatic transmission fluid or some water based transmission fluid can effectively transfer work from the piezoelectric transducer to the load. Fluids that have fluid viscosities close to water would offer a superior choice over

mineral oil fluids in terms of minimizing the pressure drop across the valve structure for a given flow rate. Since we anticipate mean piezohydraulic pump flow rates well above 0.5 cm^3/s we need a valve design and working fluid that minimize pressure losses during the pumps open flow operation. These plots can be experimentally verified by providing fluid flow through the reed valve structure and measuring the resulting pressure drop across the valve.

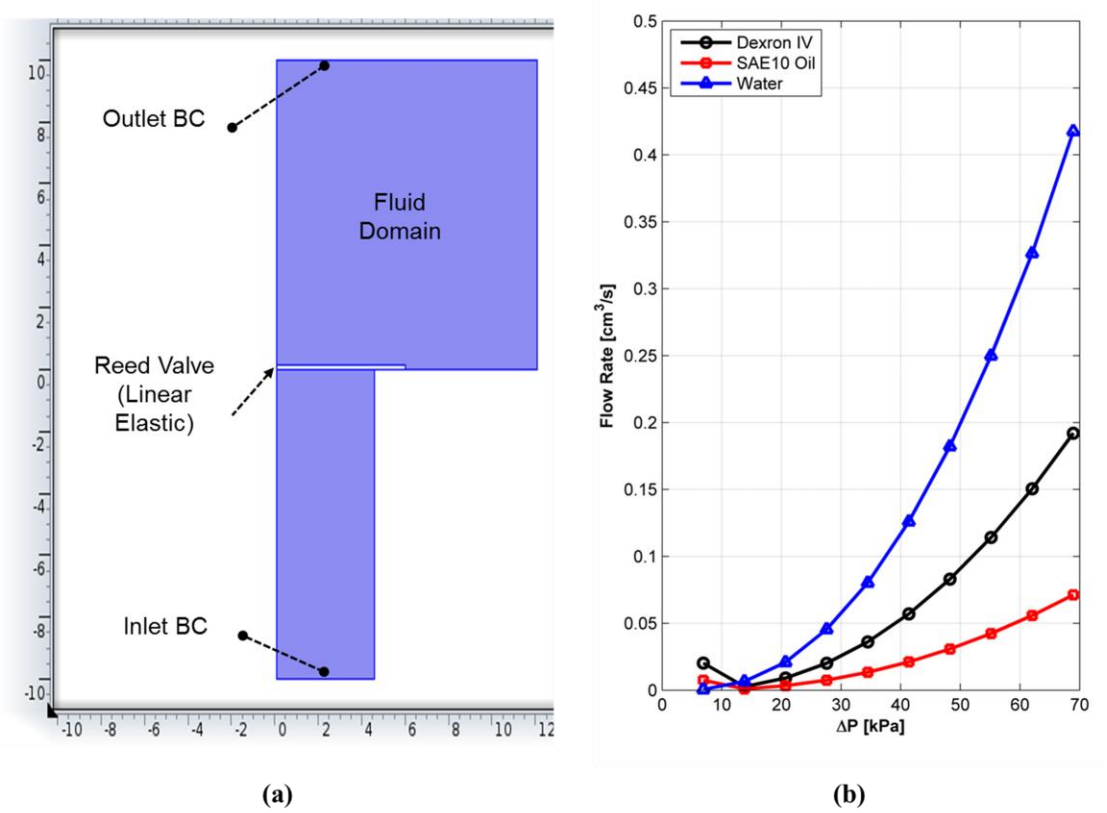

Figure 5-21. (a) Two-dimensional COMSOL fluid-structure interaction model of a simple cantilever reed valve (b) flow rate versus pressure differential across the valve for various fluids (Dexron IV, SAE10 Oil, and water)

5.3 Piezohydraulic Pump Prototype Testing and Results

Initial Pump Prototypes

The initial prototypes were designed after a Kinetic Ceramics large volume flow pump (PHP2). This design utilized a stiffener with a radius 80% the size of the chamber radius. It is important to note that while the initial data is for a 20 mm diameter stiffener, the final design utilized a 16

mm diameter stiffener to optimize the amount of work performed on the working fluid. Initial prototype pumps were installed and connected to a hydraulic circuit. The hydraulic circuit (shown in Figure 5-22) consists of a couple of static 4-20mA pressure transducers (Wika Instrument Corp., A-10) to measure the inlet and outlet pressure. A positive displacement turbine totalizer (Omega Engineering Inc., FPD1102B) is used to measure the flow rate out of the pump and a pincher valve is used to modulate the resistance of the outlet branch. The totalizer counts the volume that has passed through the device and flow rate is measured by using a stop watch and counting the amount of volume that has passed over a set amount of time. A 40m L diaphragm-style hydraulic accumulator (Hawe Hydraulics Inc., AC-40) was used to pressurize the hydraulic circuit. The pump was attached to high pressure braided wire-reinforced Buna-N rubber hydraulic hoses. Automatic transmission fluid (Dexron IV) was used as the working fluid. A sinusoidal electric field was applied to the piezoelectric actuator. An oscilloscope provided the sinusoidal waveform to a voltage amplifier. Initial tests (that involved the NAC2011 and AE0203D16 piezoelectric stacks) utilized a low bandwidth high voltage amplifier (Trek, Model 50/750), as seen in Figure 5-22a. For higher bandwidth pump operation (>100 Hz), a high bandwidth low voltage switching amplifier (PiezoDrive Inc., PDX200b) was used to ensure the current drawn was sufficient for full actuation (Figure 5-20b).

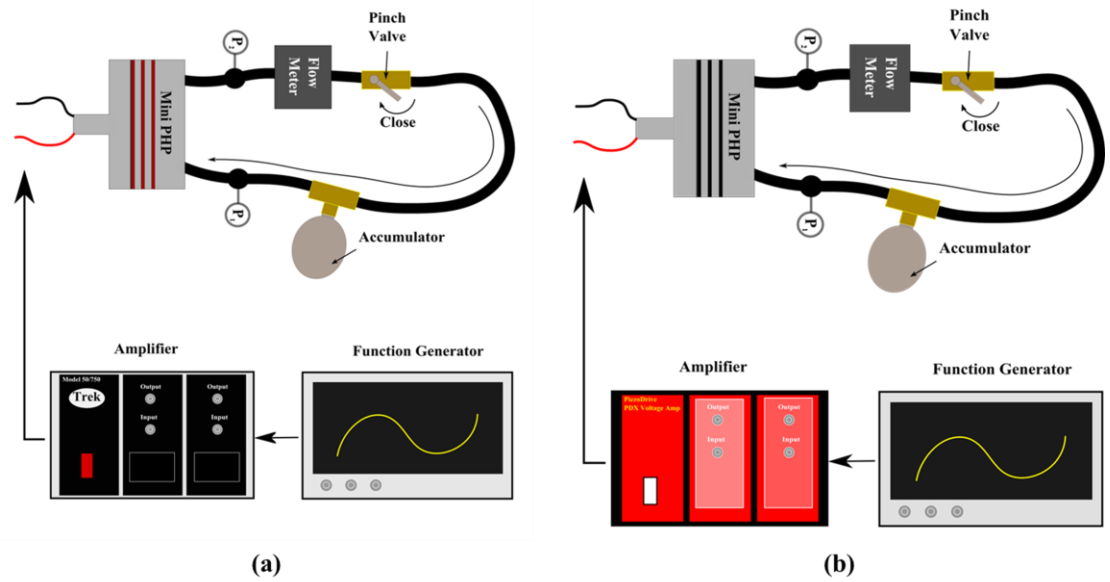

Figure 5-22. (a) Hydraulic setup used to measure the flow rate and pressure from the piezohydraulic pump driven by the Trek Model 50/750 voltage amplifier and (b) driven by the PDX 200b switching amplifier

In an effort to develop the smallest piezohydraulic pump in the field, the first iterations of the miniature piezohydraulic pump utilized the NAC2011 and AE0203D16 piezoelectric stacks. These stacks have volumes of 0.08 cm^3 and 0.12 cm^3 respectively and represent the smallest piezoelectric actuators used in piezohydraulic pumps that can perform useful mechanical work. The pumps utilized a 5/8" (15.85 mm) diameter stiffener and the 0.005" thick four-leaf reed valves. The NAC2011 stack was driven with sinusoidal electric fields from 0-3 MV/m at frequencies ranging from 5 Hz to 75 Hz. Similarly, the AE0203D16 stack was driven with a sinusoidal electric field ranging from 0-1.5 MV/m at the same frequency range. The pinch valve was left open to allow for open flow conditions. Lastly, a 20 psi bias pressure was applied to the hydraulic circuit.

Figure 5-23a shows the open flow low rate versus actuation frequency of small stack piezohydraulic pumps. For both pumps, the flow rate increases linearly with frequency, which indicates the pumps are within the quasi-static regime of operation. The NAC2011 stack pump

reach a maximum flow of 16.5 mL/min at 70 Hz and the AE0203D16 pump reached a flow of 17 mL/min at 70 Hz. The amplifiers could not operate the pumps above 150 Hz frequency since the current drawn from the amplifier resulted in voltage sag. The stiffener diameter was varied to experimentally measure the dependence of stroke volume, or flow rate in this case, on the stiffener radius to chamber radius ratio. Stiffeners of different sizes (1/2", 5/8", and ¾" or 12.5 mm, 15.85 mm, and 19 mm diameter) were epoxied to three separate diaphragms (Figure 5-5d). The AE0203D16 piezoelectric stack was used in this experiment and was driven at 60 Hz at maximum electric fields ranging from 0.5-1.5 MV/m. Flow rates were measured by counting the amount of volume passing the totalizer and using a manual stopwatch to record the time elapsed. Three different flow rate readings were taken for each stiffener radius to chamber radius ratio and averaged. The error bars represent the standard deviation of each measurement.

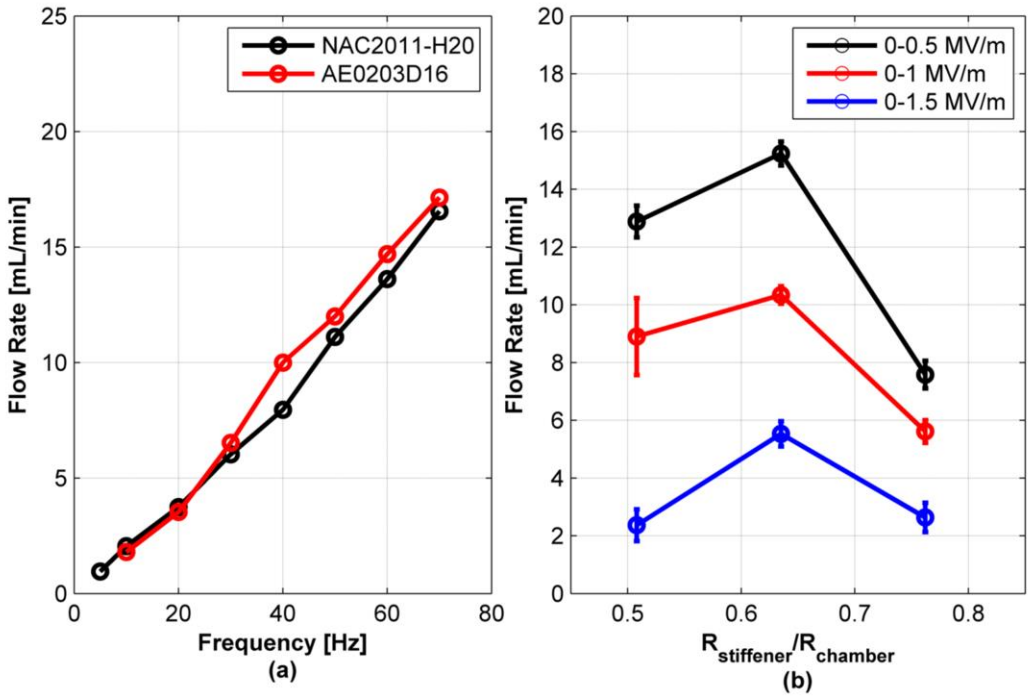

Figure 5-23. (a) Initial low frequency flow rate measurements for the NAC2011 and AE0203D16 piezoelectric stack pumps and (b) the dependence of piezoelectric pump flow rate on the stiffener and chamber diameter

Figure 5-23b shows the piezohydraulic pump flow rate dependence on the stiffener to pump chamber radius ratio. As can be seen, the highest flow rate for all ranges of electric fields occurs when utilizing a 5/8" (15.875 mm) diameter stiffener, which is close to the predicted value of 64% of the chamber diameter. When the stiffener size is increased, there is a large drop in flow rate due to the fact that the stiffened diaphragm-stiffener structure limits the piezoelectric stack strain. The drop in flow rate when the stiffener size is decreased is a result of the diaphragm deformation into the housing of the pump. This flow rate falls off more gradually and was predicted in Figure 5-15. If the bias pressure were increased, the volume loss would be much greater for smaller diameter stiffeners.

From the two-dimensional reed valve model above, it was shown that the reed valves could be major contributors of power transmission loss. While they can be operated at high frequencies (due to their large bandwidth compared to check valves), they require large cracking pressures. To experimentally verify if the valves restrict the power (flow or pressure output) output of the pump at low frequencies, the reed valve (0.005" thick 4-leaf valves) were compared to commercially available check valves. The pump utilized the 5/8" diameter (15.875 mm) stiffener, AE0203D16 stack, and Trek Model 50/750 high voltage amplifier. The actuation frequency ranged from 50 Hz to 250 Hz.

Figure 5-24 shows the flow rate versus frequency for the piezohydraulic pumps using the 0.005" four-leaf reed valves and check valves. For frequencies below 150 Hz, the flow rate for all permutations of valves and electric fields, the flow rate increases approximately linearly with actuation frequency. This indicates that there are no frequency dependent phenomena that affect the pumps flow rate performance. The relative magnitudes of the flow rate are very different for the pump using the check valves and the pump using the reed valves. For instance, when a 0- 1.5

MV/m electric field is applied, the check valve pump achieves a flow rate of 94.6 mL/min at 150 Hz. However, reed valve pump only achieves a 62.2 mL/min flow rate with the same electric field and operation frequency. The 31% difference in flow rate performance can be attributed to the losses across the valves. For a 0-1.25 MV/m electric field the flow rate for the percent difference in the check valve and reed valve flow rates is 42%. For a 0-1 MV/m electric field the flow rate for the percent difference in the check valve and reed valve flow rates is 72%. Thus, the 0.005" thick reed valves limit the stroke volume and reduce the flow rate that can be achieved. The non-constant percentage difference between the check valve and reed valve flow rates indicates that the valve response is very dependent on the force and strain output of the piezoelectric stack. Reed valve response can be increased by either decreasing the stiffness of the valves (make them thinner) or increasing the size of the stack so that the force or strain produced by the actuator increases the valve response. The non-linear flow rate response at frequencies higher than 150 Hz is a result of the limited bandwidth of the Trek Model 50/750 high voltage amplifier. At this point in the research, a low voltage (0-200V) high bandwidth switching amplifier was purchased to increase the operation frequency of the piezohydraulic pumps. In addition, 0.004" thick reed valves and larger area stack (Pst150/3.5x3.5) were used to increase the valve response and increase flow output.

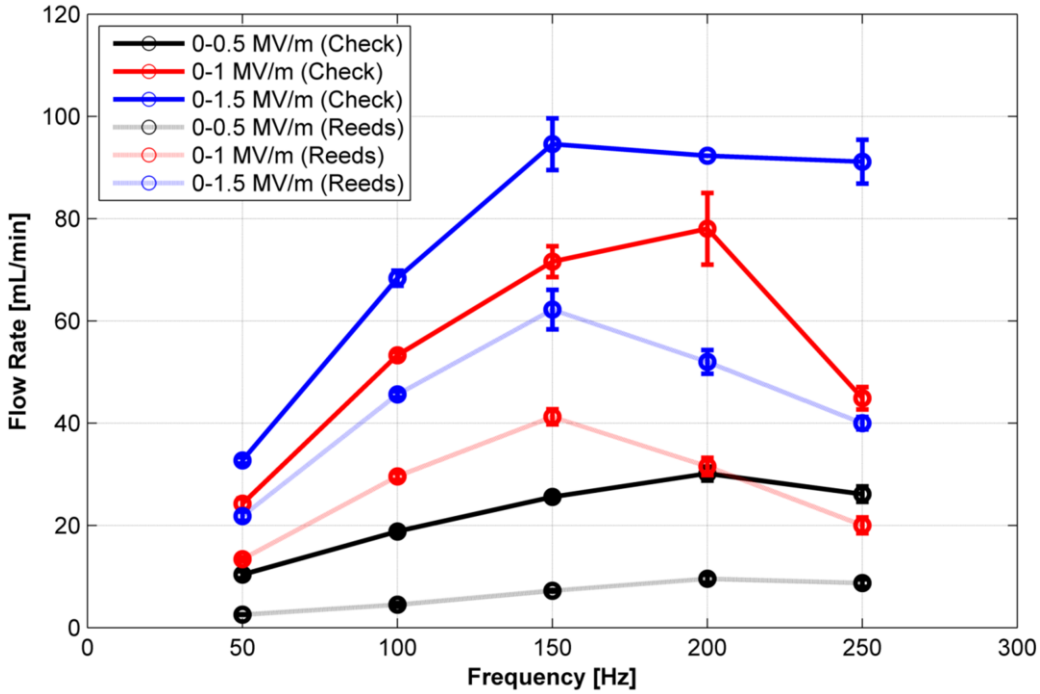

Figure 5-24. Flow rate versus frequency for piezoelectric pump utilizing AE0203D16 piezoelectric stack and the 0.005" thick 4-leaf reed valve (light lines) and check valves (darker lines)

The following tests show the flow rate versus frequency plots of the Pst150/3.5x3.5 and EPCOS piezoelectric pumps. Sinusoidal electric fields were applied with the PDX200b switching amplifier and hydraulic circuits were pressurized to 275 kPa (50psi) bias pressure. The Pst150/3.5x3.5 pump, which utilized the four-leaf reed valve, was swept from 100 Hz to 2 kHz operation frequency (100 Hz steps) at maximal electric fields of 0.5, 1, and 1.5 MV/m. Operation frequencies higher than 2 kHz were not achievable because of the capacitance of the piezoelectric stack and current drawn above 2 kHz. Similarly, the EPCOS piezohydraulic pump, which utilized the chemically etched reed valve, was swept from 50 Hz to 700 Hz (at 50 Hz steps) at maximal electric fields of 0.5, 1, and 1.5 MV/m. Operation frequencies higher than 700 Hz were not achievable because of the larger capacitance of the piezoelectric stack and current drawn above 700 Hz.

Figure 5-25a shows the frequency dependent flow rate of the Pst150/3.5x3.5 piezoelectric pump. At frequencies below 300 Hz, for all electric field strengths, the flow rate increases linearly with frequency. This represents the pumps quasi-static regime in which no frequency dependent phenomena are present. At 400 Hz, each of the curves hits a local maximum, with the largest flow rate measuring 186 mL/min with a 0-1.5 MV/m electric field. The flow rate then drops to a local minimum at 800 Hz which measures 72 mL/min with a 0-1.5 MV/m electric field. The flow rate again increases to 138 mL/min to a second local maximum flow rate at 1.2 kHz. After this second local maximum the flow rate decreases linearly with an increase in frequency. One important observation is that the flow rate does not scale linearly with electric field. Theoretically, the displacement, and consequently the flow rate, should scale linearly with applied electric field. While the 0-1.5 MV/m and 0-1 MV/m scale almost linearly, the 0-0.5 MV/m and 1 MV/m traces do not scale linearly. For instance, at 300 Hz, the flow rates for each electric field (0.5, 1, and 1.5 MV/m) are 17.6, 84, and 138 mL/min. The flow rate at 0-1.5 MV/m is approximately 1.5 times the flow rate at 1 MV/m. However, the flow rate for a 0-0.5 MV/m electric field is more than 4.5 times smaller than the flow rate at twice the electric field (0-1 MV/m). This nonlinear scaling indicates there is some compliance within the pump and that a minimum electric field is necessary to overcome this loss. Overall, the nonlinear dependence of the flow rate on frequency indicates some frequency dependent phenomena in the system. In fact, other researchers have seen similar phenomena, which are attributed to the resonance frequency of the fluid in the hydraulic system and acoustic reflections in the piping.

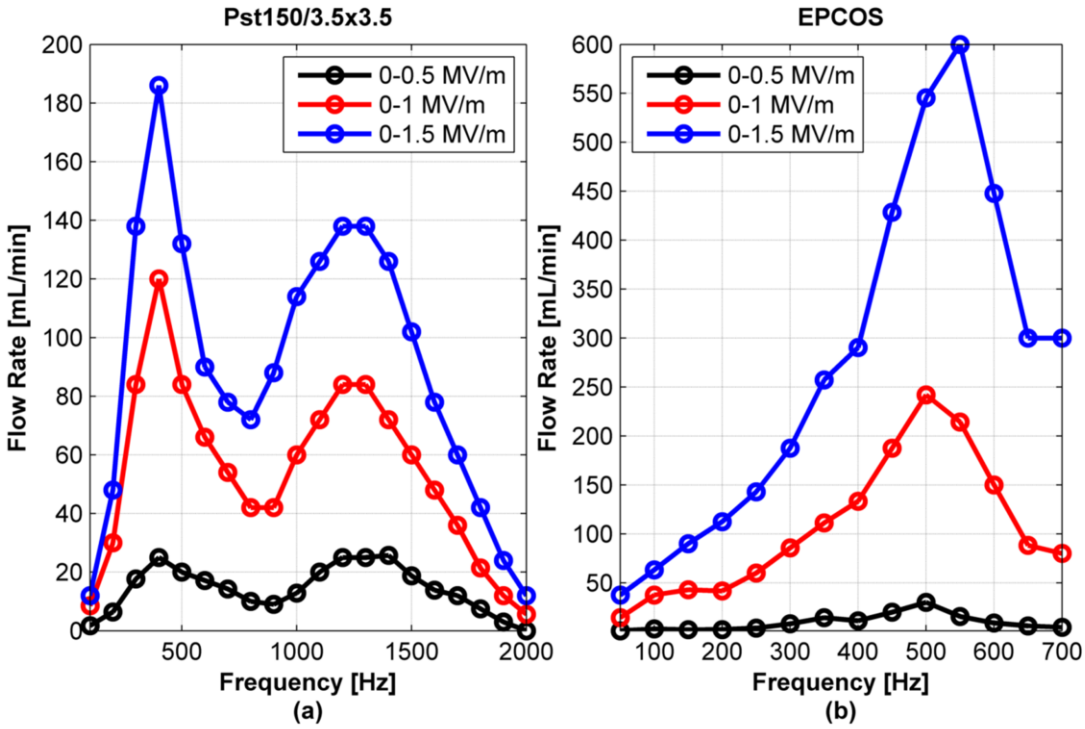

Figure 5-25. (a) Nonlinear flow rate versus frequency plot for the piezoelectric pump utilizing the Pst150 stack and 0.004" 4 leaf reed valves and (b) nonlinear flow rate versus frequency plot for the piezoelectric pump utilizing the EPCOS stack and 0.004" chemically etched reed valve

Figure 5-25b shows the frequency dependent flow rate of the EPCOS piezoelectric pump. Similar to the Pst150/3.5x3.5 pump, the EPCOS pump flow rate increases linearly with increasing frequency below 300 Hz when a 0-1.5 MV/m electric field is applied. Interestingly, the flow rate is not linear within the 50 Hz to 300 Hz range for the 0-1 MV/m and 0.5 MV/m traces. Peak flow rate for all electric fields occur at 500 Hz, which is close to the 400 Hz resonance for the Pst150/3.5x3.5 piezoelectric pump. A 600 mL/min flow rate is achieved at 500 Hz. Flow rate then decreases sharply at frequencies greater than 500 Hz. The nonlinear electric field scaling is also observed in this experiment. Thus from Figure 5-25, the flow rate performance of the pump is highly dependent on the dynamics of the fluid in the piping system. In this case, when the piezoelectric is actuated at the resonance frequency of the fluid in the

system the volumetric efficiency of the pump also increases and results in higher flow. While the unrestricted flow rate is an important characteristic of the piezohydraulic pump, the stall pressure, or the maximum achievable pressure output, is also important.

Figure 5-26 shows the differential stall pressure for the three types of pumps (AE0203D16, Pst150, and EPCOS) in time. At approximately 4 seconds in the plot, the pincher valve is fully closed which causes a spike in the pressure output of the pump. Theoretically, the stall pressure is related to the blocking force and the size of the pump chamber diameter. Specifically, the pump stall pressure, assuming the fluid is incompressible, should be equal to the blocking force divided by the chamber area. Thus, the theoretical stall pressures should be 407 kPa, 1600 kPa, and 5000 kPa for the AE0203D16, Pst150/3.5x3.5, and EPCOS piezoelectric pumps respectively. The measured stall pressures are 17 kPa, 85 kPa, and 275 kPa for the AE0203D16, Pst150/3.5x3.5, and EPCOS piezoelectric pumps respectively. These measured stall pressures are 18-23 times smaller than the theoretical values. Since the valves have changed across tests, the cause of the limited stall pressures is related to some compliance within the housing or the pumping chamber. In fact, the height of the pumping chamber, which was 2 mm for all the experiments described, is too large. Because the bulk modulus of the working fluid can be as small as 10% of the manufacturers reported value [103], the stiffness of the fluid can have a significant effect on the pressure output of the pump. From equation 5-6, decreasing the height of the chamber can linearly increase the pressure output of the pump. However, this is limited by the space needed to clamp the inlet valve and machinability tolerances. Ensuring that there is no internal leakage within the housing is also important. To optimize the final pump, the chamber height of the pump was reduced to 0.1mm tall. The valve seat was machined to give enough clearance for the inlet valve.

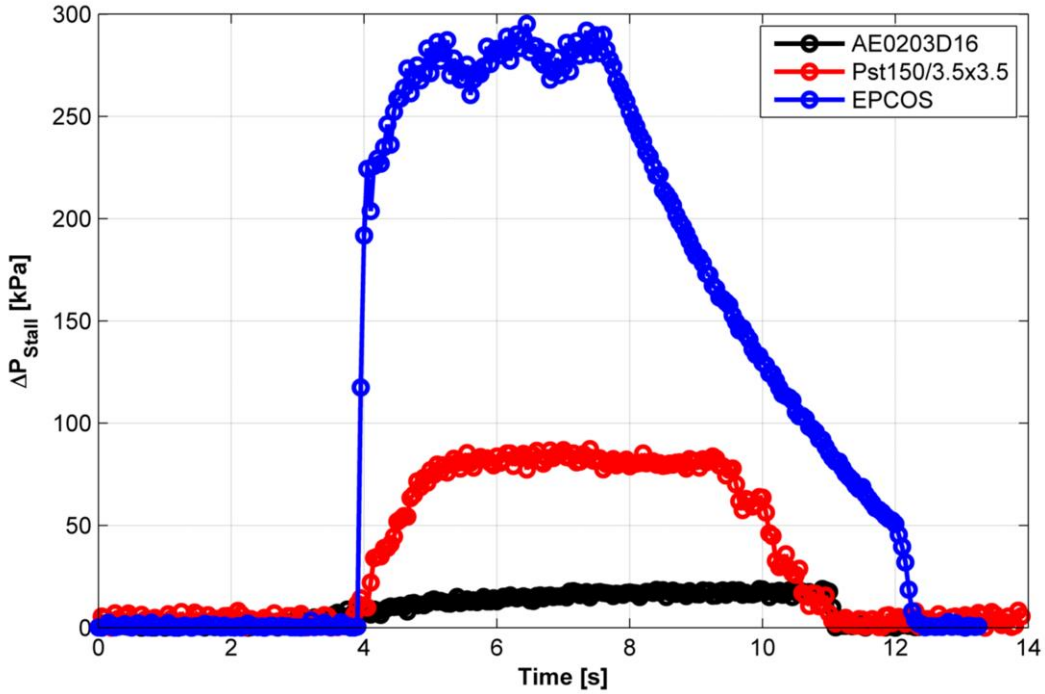

Figure 5-26. Different stall pressures measured for the AE0203D16 (black), Pst150/3.5x3.5 (red) and EPCOS (blue) piezoelectric stack pumps utilizing a 2 mm tall chamber spacer

Final Pump Prototypes

The final prototypes have taken into considerations the observations from the previous sections. The following changes were made in the final design to improve the volumetric performance and pressure output for both the Pst150/3.5x3.5 and the EPCOS piezoelectric pumps.

1. The chamber size was reduced to 0.4mm to increase the effective stiffness of the fluid. Chamber sizes that are smaller can restrict the flow of fluid through the chamber.
2. The working transmission fluid used was changed to Hydrolubric 123B, a synthetic water additive that has a larger bulk modulus and lower viscosity than Dexron VI ATF.
3. 15.875 mm (5/8”) diameter stiffener is used to increase the effective stroke volume of the pump.

In order to mimic the hydraulic impedance seen when using the piezoelectric pump as an actuator in the ventricular assist deriver, the pump flow rate, pressure and power output were

measured by attaching the pump to a single rod hydraulic cylinder. The measurement system (shown in figure 5-27) contains four pressure sensors (two are not shown in the schematic); two mean pressure sensors (Wika Instrument Corp., A-10) at the inlet and outlet and two dynamic pressure sensors (PCB Piezotronics Inc., 106B) at the inlet and outlet. Hydraulic cylinder rod displacement was measured with an LVDT sensor (Omega Engineering; LD620). Flow rate was calculated by taking the velocity of the rod and multiplying it with the effective area of the hydraulic cylinder piston. A data acquisition card (National Instruments, USB-6218 BNC) converted the analog signals for data collection on a computer. A piston-spring accumulator was used to pressurize the hydraulic system. The low voltage switching amplifier (PiezoDrive Inc., PDX200b) provided the sinusoidal electric field to the piezoelectric stack.

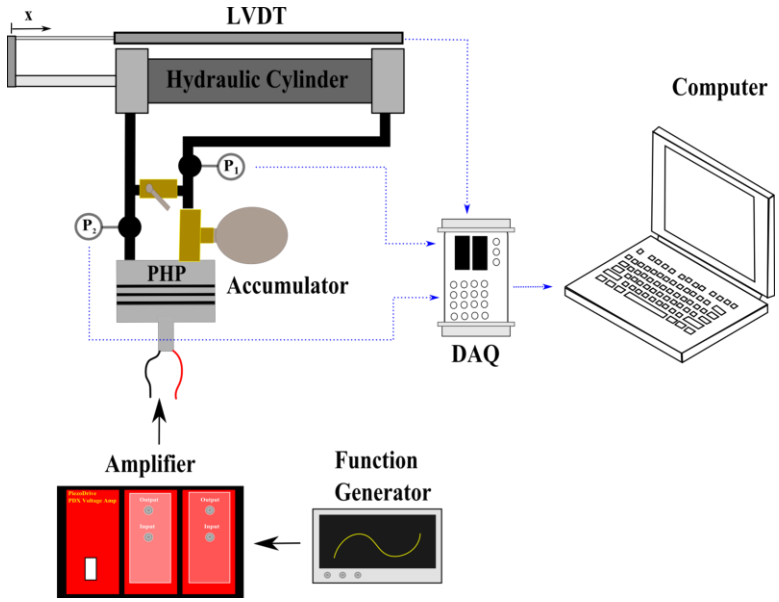

Figure 5-27. Experimental setup of final piezohydraulic pump design utilizing Hydrolubric 123B, a 0.4 mm tall chamber, and a 16 mm diameter stiffener

Figure 5-28a shows the measured flow rate versus bias pressure for the EPCOS piezoelectric pump operated at 300 Hz with a 0-160 V sinusoidal applied voltage. The bias pressure was varied between 10-90 psi (68.9 kPa-620.5 kPa) in10 psi increments. Flow rate increases with

increasing bias pressure in the system up to a point. At 80 psi bias pressure (551.6 kPa) the maximum flow rate measured was 200 mL/min. It is important to note that this was not a measure of the free flow but the flow with 50 psi pressure differential across the pump. From the data, increasing bias pressure helps piezoelectric pump filling by providing a return force when the piezoelectric actuator is de-energized. However, above 90 psi, the total stroke volume of the pump decreases, most likely from deformation in the diaphragm. Thus an optimal bias pressure exists that gives the best volumetrically efficient design point.

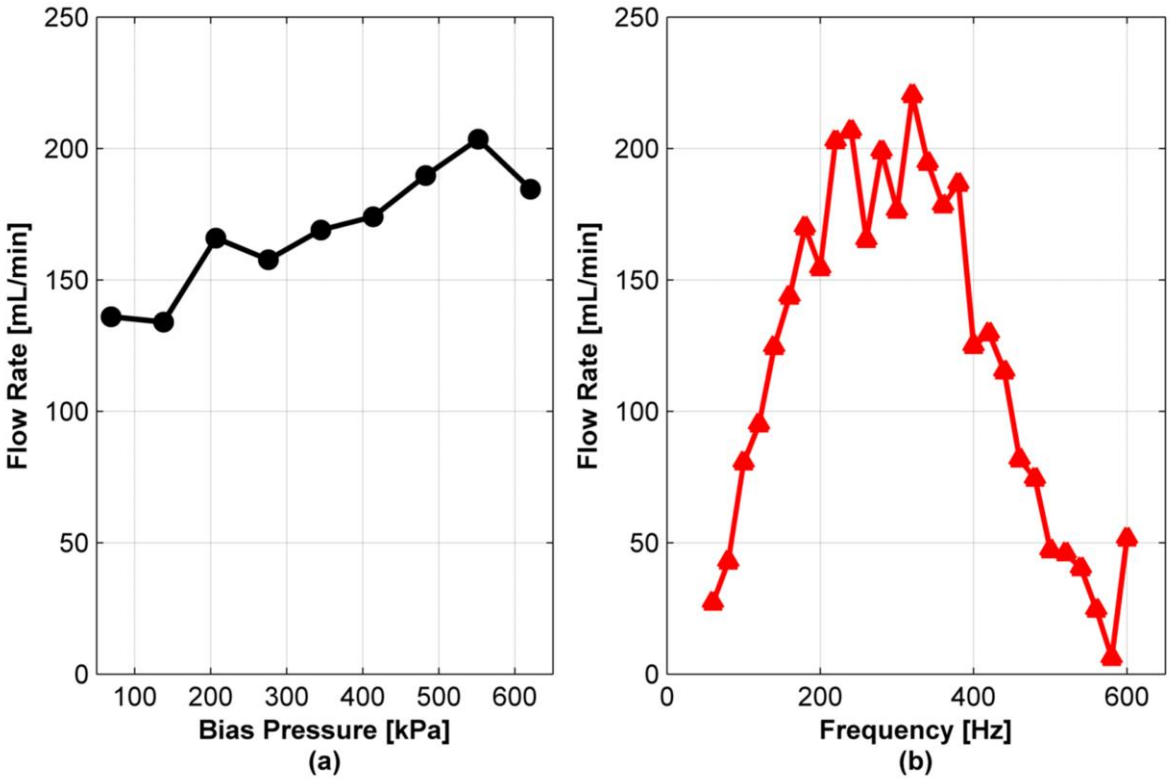

Figure 5-28. (a) The effect of bias pressure on the flow rate output of the EPCOS piezoelectric pump (driven at 160 V and 300 Hz) and (b) flow rate as a function of frequency (driven at 160 V)

Figure 5-28b shows the flow rate frequency sweep plot of the EPCOS piezoelectric pump driven with a 0-160V sinusoidal voltage and an 80 psi bias pressure in the hydraulic system. All flow rates are flow rates with a piezoelectric pump differential of 40 psi. Between an operational frequencies of 80-180 Hz, the flow rate increases almost linearly with frequency. However,

above 200 Hz, some frequency-dependent flow rate phenomena, similar to that seen in Figure 5-25, were observed for this setup as well. Maximum flow occurs at 320 Hz, 220 mL/min, but falls off between 340 Hz and 580 Hz. The minimum flow output of 6 mL/min occurs at 580 Hz. It is important to note that the flow rate frequency response is dependent on the hydraulic circuit attached to the piezoelectric pump. These line dynamics affect the pump flow rate in two different ways. First, the inertia of the fluid within the external piping adds a resonance to the system which is much lower than the piezohydraulic pump resonance and smaller than the reed valve resonance. Second, the reflection of acoustic waves also affects the inlet and outlet valve dynamics and can lead to some flow rate maxima and minima as a function of frequency. Thus, this hydraulic resonance and acoustic reflections can be used to increase pump volumetric efficiency. However, this non-linear behavior is generally undesirable since it is dependent on geometries outside the design of a piezohydraulic pump.

Figure 5-29 shows the piezoelectric stack voltage, current, and power delivered by the low voltage switching amplifier when the piezohydraulic pump is driven at 330 Hz. The voltage, shown in black on Figure 5-29a, oscillates between 0 V and 160V. The current, shown in red, leads the voltage by 72˚ and oscillates between -0.8 A and 0.8 A. The negative current corresponds to current that is returned from the piezoelectric actuator to the amplifier. This represents reactive power which can theoretically be recycled if the appropriate electronic driver was designed. The instantaneous power delivered, which is the product of the stack voltage and current delivered, is plotted on Figure 5-29b. The power output oscillates between -60 W and 72 W. Similar to the current, the positive instantaneous power represents the power delivered to the piezoelectric stack from the amplifier and the negative values represent the power returned from the actuator. The total consumed power output can be approximated by taking the root-mean-

square (RMS) value of the voltage and multiplying it by the RMS value of the current. Using this methodology, the average electrical power for an EPCOS piezoelectric pump operated at 330 Hz is 43 W. Knowing the electrical power input, the efficiency of the pump can be measured by measuring the mechanical power output of the pump.

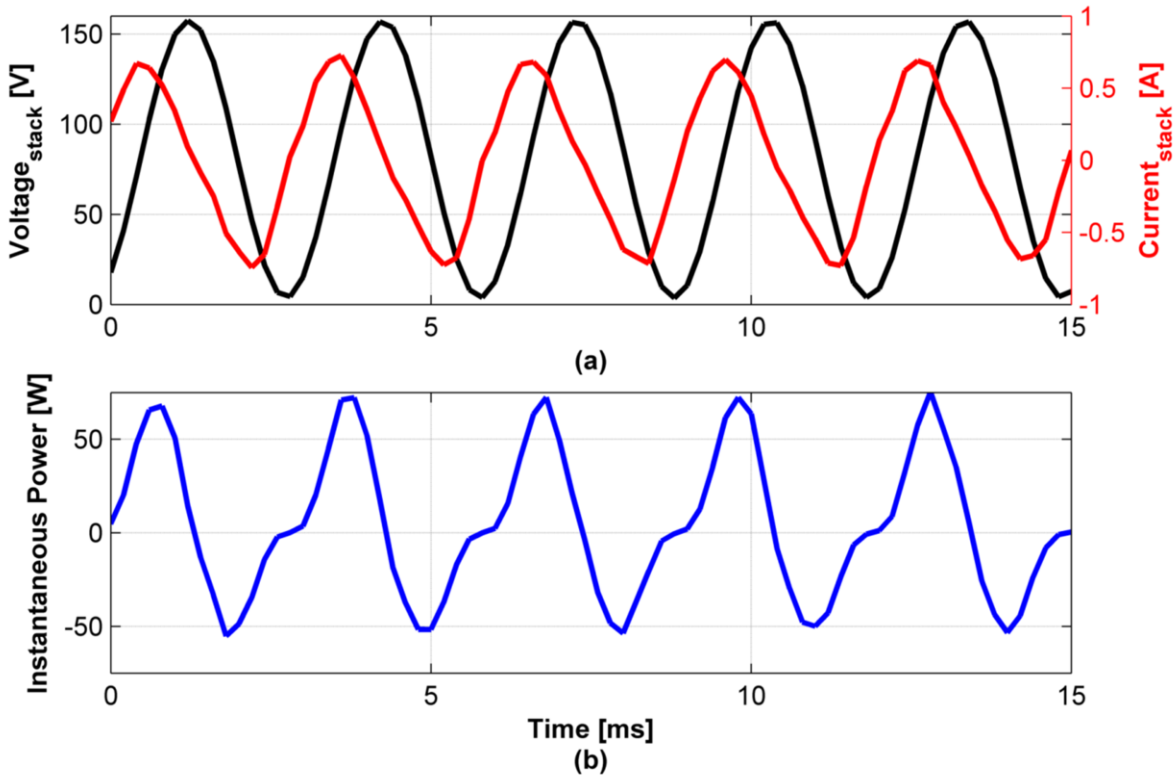

Figure 5-29. (a) Voltage and current delivered to piezoelectric stack and the (b) instantaneous power delivered to and returned by the stack actuator

The mechanical power output was measured by attaching a compression spring to the hydraulic cylinder rod in the experimental setup shown in Figure 5-27. When the pump is turned on, the rod retracts to compress the spring. The variable load allows the pump to experience an increasingly higher load at the outlet. Mechanical power is calculated by taking the product of the differential pressure across the pump (outlet pressure minus inlet pressure) and flow rate (hydraulic cylinder rod velocity multiplied by hydraulic cylinder piston area). The pressure differential across the EPCOS pump and the mechanical power output as a function of flow rate

are shown in Figure 5-30a. The bias pressure in the hydraulic system was 80 psi and the pump was operated at 330 Hz. The pressure difference across the pump, ΔP, decreases linearly for increasing flow rate. At no flow, stall condition, the maximum ΔP is 700 kPa (101.5 psi). This is 2.5 times the stall pressure recorded when a 2 mm tall piezoelectric pump chamber was used. Theoretically, the five-fold decrease in chamber size should increase the stall pressure by the same factor. However, there is another source of compliance in the pump or hydraulic setup. Figure 5-30a also shows the mechanical power output versus flow rate. The maximum power output recorded is 1.6 W and occurs at approximately half the stall pressure and measures 250 mL/min. This represents an impedance matched condition and it is within the range of power needed to drive a ventricular assist device. Theoretically, the maximum flow output, with no ΔP for this pump is 500 mL/min.

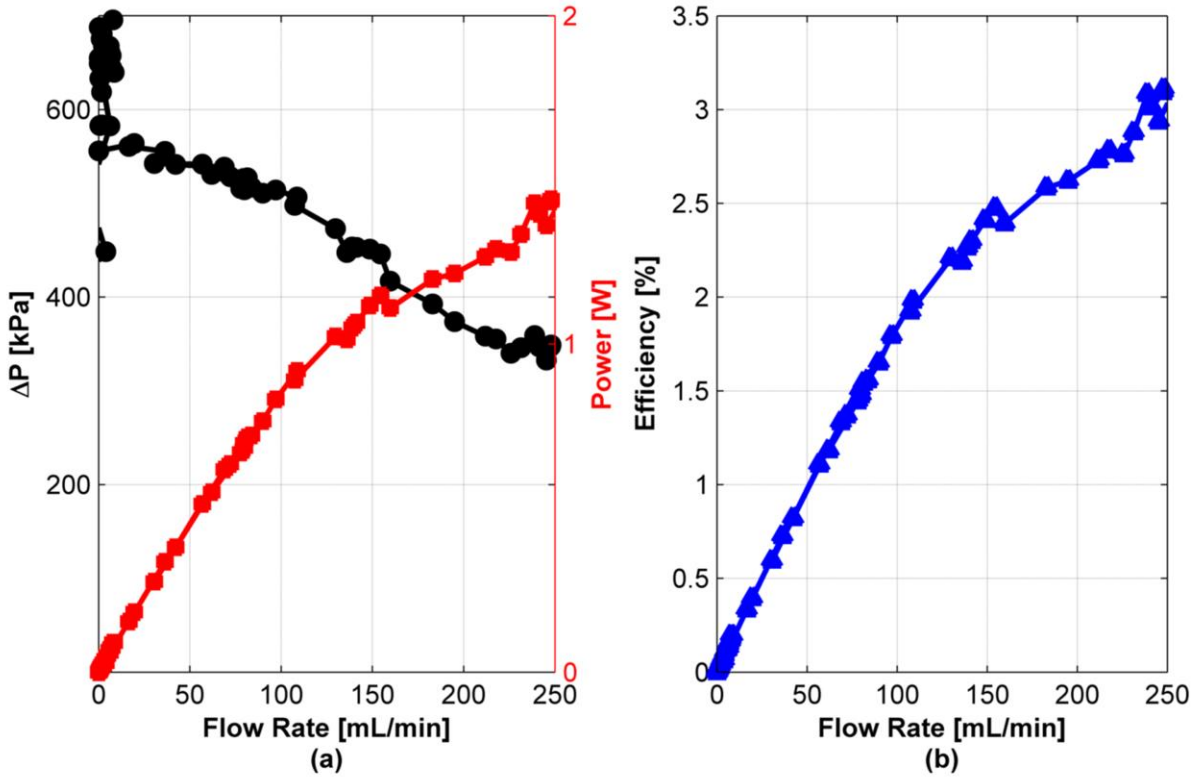

Figure 5-30. (a) Pressure differential versus flow rate and power output versus flow rate for the EPCOS piezoelectric pump and (b) efficiency versus flow rate

Figure 5-30b shows the efficiency of the pump versus flow rate. The efficiency is defined as the ratio of the mechanical work output to the electrical power input. The maximum efficiency for this pump is 3% and occurs at 250 mL/min. The high end of efficiency, hydraulic power output over electrical input power for continuous flow ventricular assist devices is 15%. However, most blood pumps operate at overall efficiencies around 10% (40-80% motor efficiencies). Thus the currently design miniature piezoelectric pump is about three to four times less efficient than commercially available blood pumps. While there still needs to be improvement, the potential for using piezohydraulic technology is promising since this pump has yet to be optimized.

5.4Summary

This chapter detailed the development of a piezohydraulic pump specifically designed to drive a pediatric ventricular assist device. An updated 1D model was used to get initial sizing of the pump components that would be impedance matched to the flow and pressure outputs needed by a pediatric blood pump. It was decided that a piezoelectric pump chamber size of 25-30 mm was necessary to output 25 kPa pressure and 3 L/min from the entire driver system. In modeling and testing two piezoelectric pumps, we noticed that various pump components had a significant impact on the output of the device. The stiffener diameter relative to the chamber diameter played a crucial role in determining the volumetric efficiency of the pump. Using COMSOL Multiphysics and conducting several experiments, it was clear that using a stiffener with 60-64% the diameter of the chamber size increased the stroke volume of the pump. The pump chamber also had a drastic effect on the pressure output of the piezoelectric pump. Using a small height increases the effective stiffness of the fluid in the chamber and leads to a better impedance matched device. The use of a lower viscosity fluid coupled with a small height chamber and appropriate stiffener yielded a, 8 W/kg piezoelectric pump. Nonetheless, while frequency

leveraging can lead to high power output per unit size, the high frequency oscillation of the piezoelectric also causes frequency-dependent phenomena to affect pump flow rate. These are a few considerations to take into account when using piezohydraulic pumps in all applications. The net chapter focuses on using the EPCOS piezoelectric pump to drive a pediatric blood pump.

Chapter 6: Pediatric Blood Pump Design and Piezohydraulic Driver

This chapter discusses the design of a piezohydraulic actuated pulsatile ventricular assist device driver. The design and development of a pediatric blood pump, also called a ventricular assist device, is first presented. The blood pump presented in this chapter, unlike traditional pneumatically actuated devices, has been designed to take the hydraulic input from the compact piezohydraulic pump designed in Chapter 5. The sizing, component design, and fabrication are covered in detail. A simple lumped element model of the blood pump and driver is developed to predict the performance of the entire system given a specific flow and pressure output. Lastly, an in vitro test setup is developed to test the performance of the entire system as a left ventricular assist device. The results from this chapter confirm that piezohydraulic power transmission can be a superior approach to traditional electromagnetic technology.

6.1 Pulsatile Blood Pump Design

In Chapter 5, we introduced the system level components of a ventricular assist device system. Chapter 5 focused on the design of an energy converter using piezohydraulic frequency rectification to power a ventricular assist device. In this chapter, we will focus on the design of a human interface (Figure 6-1) that effectively transfers the power from the energy converter, a piezohydraulic pump in this research, to the load (human circulation in this study). The human interface in mechanical circulatory support systems consist of the mechanical components that convert the mechanical energy produced by the energy converter to useful fluidic power for the human circulation. The human interface for mechanical circulatory support systems is known as the blood pump. For the remainder of this chapter and dissertation, the human interface will be identified as the blood pump. Because the development of pulsatile blood pumps dates back to

the 1970's, the design of a pediatric blood pump that can transmit the power from a piezohydraulic pump will not deviate from the current state of the art.

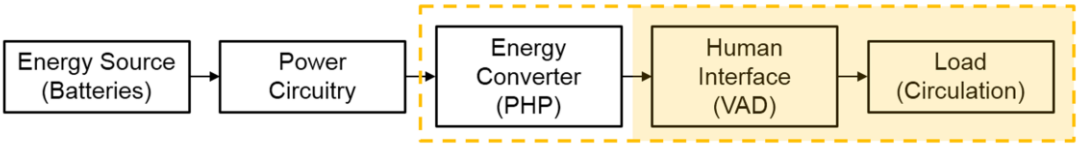

Figure 6-1. The system level components that make up a MCS system (the highlighted boxes indicate the topic of this chapter)

As discussed in chapter 2, the design of the first clinically used pulsatile blood pump was the Pierce-Donachy blood pump [106], [107]. The design was derived from various prototypes that ultimately paved the way for what is now considered the gold standard of pulsatile blood pump designs. Figure 6-2 shows the first four pulsatile blood pump designs from Donachy *et al.* (1979). The dashed lines indicate the movement of the sac during systolic pressurization with a pneumatic source. All designs consist of a smooth sac that holds the blood, pneumatic drive port, and inlet and outlet port to connect to the cannula, and inlet and outlet valves to ensure unidirectional flow through the blood pump. The valves used were either ball-in-cage valves or tilting-disc valves. The first design (Figure 6-2a) consisted of a blood sac that was tethered at the inlet and outlet ports. The design exhibited poor washout at the apex of the pump which corresponded to a thrombus formation at the location.

The second blood pump design (Figure 6-2b) consisted of the segmented polyurethane blood sac tethered on one side in the longitudinal direction to the ports. The sac was tethered by a ring that attached to the polycarbonate outer casing of the pump with glue. Similar to the first design, there was poor washout and low fluid velocity at the apex of the blood sac which resulted in thrombus formation in animal studies. Washout was improved by using the tilting disc valves but the thrombus formation was still significant. Thrombus formation was also observed in the

areas where the blood sac was glued to the ring, indicating a change in the chemistry of the blood sac. The third design (Figure 6-2c) utilized a transversely tethered sac with a transversely tethered diaphragm serving as the barrier between the pneumatic chamber and blood. The diaphragm prevented contamination between the pneumatic chamber and blood. Washout at the apex was improved but the stresses on the diaphragm lead to component failure that precluded the clinical use of this design. The final design, shown in Figure 6-2d, utilized the intermediate diaphragm with a blood sac tethered at the ports (not glues to the polycarbonate housing). The ports were angled to limit the contact of the deforming blood sac and valves. This blood pump design was successfully implanted for 651 days in calves (the longest support for all four blood pump designs). Three important features of blood pump design were elucidated during the Donachy study.

1. Blood sac washout and fluid velocity are crucial in preventing thrombus formation
2. Adhering the blood sac to the housing can undesirably alter chemistry of the sac
3. Utilizing an intermediate diaphragm lowers the stress imposed on the blood sac

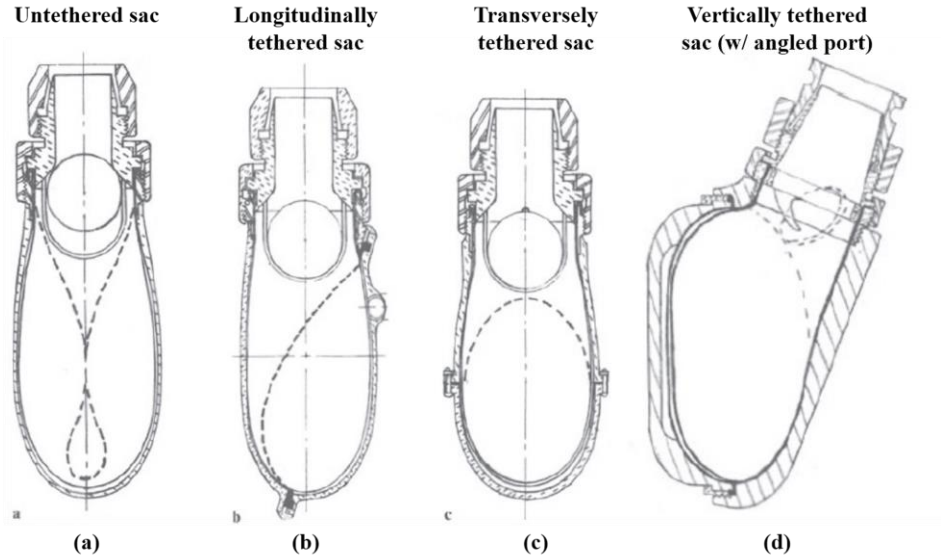

Figure 6-2. Adult pulsatile blood pump designs in which the (a) blood sac is tethered near the valves, (b) longitudinally tethered, (c) transversely tethered, and (d) an angled port

The angled port design is the design utilized by many researches and by Thoratec Corporation's Pneumatic Ventricular Assist Device (PVAD ®). Figure 6-3 shows the components of the Thoratec PVAD®. As mentioned previously, the angled port blood pump consists of a polycarbonate pneumatic chamber housing and blood sac housing. The PVAD® also contains a smooth and seamless segmented polyurethane blood sac. A polyurethane diaphragm separates the pneumatic chamber with the blood sac and tilting-disc valves, called Bjork-Shiley valves, are used for the inlet and outlet valve. The valves consist of a Teflon concave disc that are supported with titanium structure. Titanium cannula connecters are connected to the inlet and outlet ports. The blood pump is designed to provide a 65 mL stroke volume and operate between 40-100 beats per minute (BPM) for adult patients. Pneumatic power is supplied via a large electro-pneumatic driver. In this dissertation, we are concerned with the design of a smaller blood pump to be used for children. Thus, the design can be scaled down to fit the stroke volume and pressure output needs of a pediatric patient. However, before scaling down, the effect of pump scaling on blood pump fluid dynamics must be considered. Fortunately, researchers at Pennsylvania State University have studied the fluid mechanics of scaled-down blood pumps.

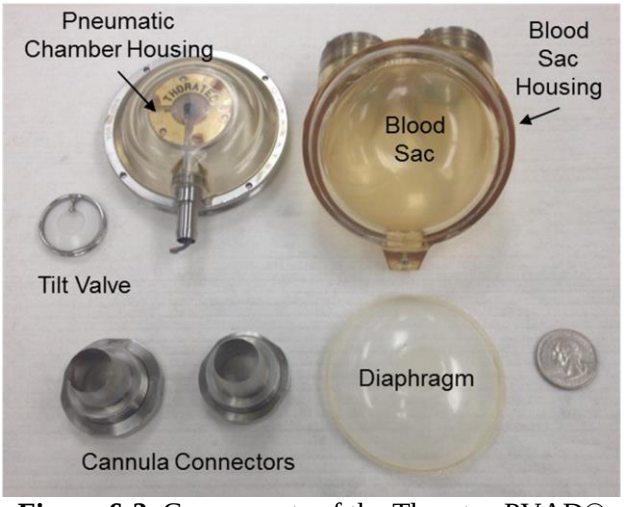

Figure 6-3. Components of the Thoratec PVAD®

Blood Pump Scaling

As mentioned in Chapter 2, the design of pediatric ventricular assist device followed a few decades after the development of adult systems. The first attempts to design a pulsatile ventricular assist device was made by Daily *et al.* (1996) [108]. In this study, the 70 mL stroke volume Pierce-Donachy blood pump was geometrically scaled down to have a stroke volume of 11 mL (from 70 mL). While the wall thickness, diameter and height were scaled proportionally to the cubed root of volume ratios, the inlet and outlet diameters of the blood pump were undersized to accommodate the small cannulas need for the pediatric population. The frequency of thrombus formation in the down-scaled blood pump during animal in vivo studies was much greater than for the adult sized blood pumps. Thus, while the pediatric blood pumps retained geometric similarity to the adult pumps (except for the inlet and outlet diameters) and used the same materials, the smaller blood pumps failed more frequently.

Daily *et al*. attributed the thrombus event discrepancy to the different fluid dynamics attributed to the mean flow rate and inlet and outlet valve geometry of the small blood pumps. They found that the smaller mean flow though smaller blood pumps results in fluid flow characterized by low Reynolds's number (ratio of inertial forces to viscous flow). This low Reynold's number flow affects the ability for inlet diastolic flow to washout the inner walls of the blood sac. The undersized valves (6 mm diameter) contributed to pressure loss, and energy loss, across the inlet and outlet ports. This has a two-fold effect. First, energy loss at the inlets can potentiate blood cell damage and clot formation. Second, the pressure loss at the valve sites can also reduce the momentum of inlet flow during diastole, which reduces washout within the blood chamber.

Bachmann *et al*. (2000) studied the fluid dynamics of a down-scaled Pierce-Donachy blood pump in more detail. They indicate that the blood pump dimensions that are most important, shown in Figure 6-4, are the chamber radius (R), inlet and outlet diameter (do, di), and height (h). Thus, in order design a small blood pump, the dimensions can be scaled down from an adult blood pump as follows:

$$\left(\frac{SV_{adult}}{SV_{pediatric}}\right)^{1/3} = \frac{d_{o,adult}}{d_{o,pediatric}} = \frac{d_{i,adult}}{d_{i,pediatric}} = \frac{R_{adult}}{R_{pediatric}} \qquad (6\text{-}1)$$

Where SV is the stroke volume, $d_o$is the outlet diameter, d_i is the inlet diameter, and R is the blood chamber radius. It is important to note that the outlet and inlet dimensions are size much smaller than the scaling law. This is because the vessels of children are much smaller than the adult vessels and necessitate smaller cannula. Thus, assuming that the dimensions can be scaled appropriately, with the inlet and outlet dimensions scaled more aggressively, Bachmann set out to find out which features were most important in maintaining the anti-thrombogenic nature of the blood pump.

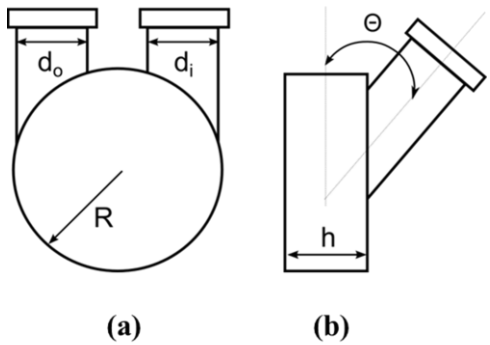

Figure 6-4. Pulsatile blood pump characteristic dimensions

Bachmann *et al*. discovered that the fluid dynamic dimensionless parameters, Reynolds number and Strouhal number, were important indicators of pump thrombus formation. The Reynolds number is defined as the ratio of inertial forces to viscous forces in fluid flow. Fluid flow

dominated by viscous forces is characterized by low Reynolds number and can transition to laminar flow. Conversely, fluid flow characterized by inertial forces corresponds to large Reynolds number and can lead to turbulent flow. In the case of blood pumps, large Reynolds numbers are desirable to ensure blood is washed out during ventricular filling and ejection. The Strouhal number is an important parameter that describes unsteady oscillating flows. It is the relative importance of inertial forces to convective forces in unsteady fluid flow. For high Strouhal numbers (>1) fluid flow is dominated by inertial forces, which is seen in normal ventricular flow patterns. The dimensionless parameters are described by equations 6-2.

$$\mathrm{Re}= \frac{UL}{\upsilon}, \quad \mathrm{St}= \frac{UT}{L} \qquad (6\text{-}2)$$

Where U is the characteristic flow velocity, L is the characteristic length, υ is the kinematic viscosity, and T is the characteristic flow cycle time. Taking L to be d_i, the flow rate $Q= SV \cdot f$, where f is the heart rate/pumping frequency, and the flow velocity to be $U= \frac{4Q}{\pi d_i^2}$. Assuming we only pay attention to diastolic filling, which is about half the cardiac cycle, the flow rate is typically twice the mean flow rate Q. Then the Reynolds and Strouhal numbers become:

$$\mathrm{Re}= \frac{8}{\pi\upsilon}\frac{f \cdot SV}{d_i}, \quad \mathrm{St}= \frac{4}{\pi}\frac{SV}{d_i^3} \qquad (6\text{-}3)$$

For geometrically scaled blood pumps, the Strouhal numbers should remain constant. Equations 6-3 are used to compare the predicted fluid mechanics of the blood pump designed in this dissertation with other commercially available blood pumps. The blood pump designed in this dissertation is a scaled down version of the 65 mL stroke volume Thoratec PVAD®. It is important to note that the blood pump design was deliberately scaled down from a clinically used adult blood pump in order to prevent unwanted fluid mechanic phenomena from the addition of

new components or design considerations. The goal is to keep the blood contacting surfaces and geometries the same and simply change the driving mechanism of the device.

Blood Pump Components

The blood pump designed for this study was designed to take the piezohydraulic pump output and convert it to useful circulatory work for pediatric patients. Specifically, the population of children that this study targets are pediatric patients between the ages of 1-9 years old with average weights between 6-25 kg. Patients this size, regardless of gender, typically need between 1-3 L/min of cardiac output to aid their failing hearts [109]. In addition, the pumping rates of pulsatile blood pumps are limited to a range between 40-125 BPM. Below 40 BPM, the low flows increase the incidence of thrombogenic events. For pumping rates above 125 BPM, the fluid shear stresses result in blood hemolysis. Thus, the stroke volume for the blood pump in this study was chosen to be 25 mL. With this stroke volume the mean flow rates of 1-3 L/min can be achieved within the allowable pumping rates.

Because we want the blood contacting surfaces and blood pump geometry to be similar to clinically used adult blood pumps, we used the scaling relation shown in Equation 6-1. The linear dimensions of the inlet and outlet diameter and pump chamber radius were measured for the Thoratec 65 mL adult PVAD®. The dimensions and scaling for the 25 mL pump, which will be called the UCLA 25mL Pediatric PiezoVAD, is shown on Equation 6-4. It is important to note that the inlet and outlet diameters of the PiezoVAD are the same and are 19 mm in diameter. This is because the inlet valve of the Thoratec PVAD® are used in this design to prevent the new design of a valve, which may complicate the fluid dynamics of the pump.

$$\left(\frac{65\text{ mL}}{25\text{ mL}}\right)^{1/3} = 1.38 = \frac{19\text{ mm}}{13.8\text{ mm}}(d_o) = \frac{24\text{ mm}}{17.4\text{ mm}}(d_i) = \frac{41.5\text{ mm}}{30\text{ mm}}(R) \qquad (6\text{-}4)$$

Figure 6-5 shows the computer aided design of the UCLA 25 mL Pediatric PiezoVAD. The front end of the blood pump consist of components seen in clinical pulsatile adult pumps and other pediatric pulsatile ventricular assist devices. The front end consists of a front housing which is the portion of the blood chamber and connects the angled ports with cannula connectors. The ports are angled at a 30˚ angle from the vertical axis. The polymeric diaphragm and blood sac are not shown in this rendering. The inner diameter of the blood chamber is 50 mm. The back end of the pump contains the actuator section. Unlike the pneumatically actuated blood pumps, this pump utilizes a small hydraulic actuator and a pusher plate to eject blood from the blood chamber in the front end. The pusher plate has a 38 mm diameter. A ventricular assist back housing connects attaches the hydraulic cylinder to the front housing. Within the hydraulic cylinder, a 6 mm diameter rod and 15.9 mm diameter piston convert the hydraulic power from the miniature piezohydraulic pump to mechanical stroke work for the circulation. The hydraulic cylinder also has a 12.5 mm stroke length. Schematic drawings are shown in Appendix B.

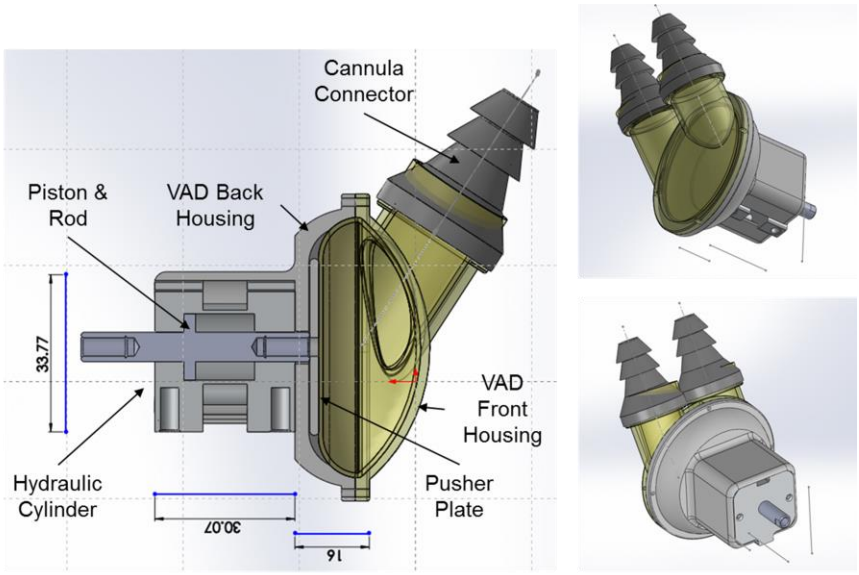

Figure 6-5. (a) Side view of computer aided design of UCLA 25mL Pediatric PiezoVAD and (b) isometric front and back views

A prototype blood pump was fabricated using three dimensional (3D) printing from Solid Concepts Inc. The parts, shown in Figure 6-6, were fabricated using an additive process known as PolyJet printing in which a UV curable polymer is printed in 16 micron layers to create three dimensional assemblies. The back housing, also called the hydraulic cylinder mount in Figure 6-6, and the pusher plate were printed from a white photopolymer. The front housing and cannula connectors are printed from an amber-clear photopolymer to allow for some transparency into the assist device. The blood pump diaphragm was also printed using the PolyJet process and was fabricated from a black rubber-like Shore 50 elastomer. The hydraulic cylinder (Clippard Minimatic, AF-TDD-10-1/2) was a double-rod double-acting 5/8" bore cylinder with 1/4" diameter rod. The 19 mm diameter inlet tilting disc valves used in the Thoratec PVAD® were used as the outlet and inlet valves for this pump. O-rings were used to prevent flow around the valves.

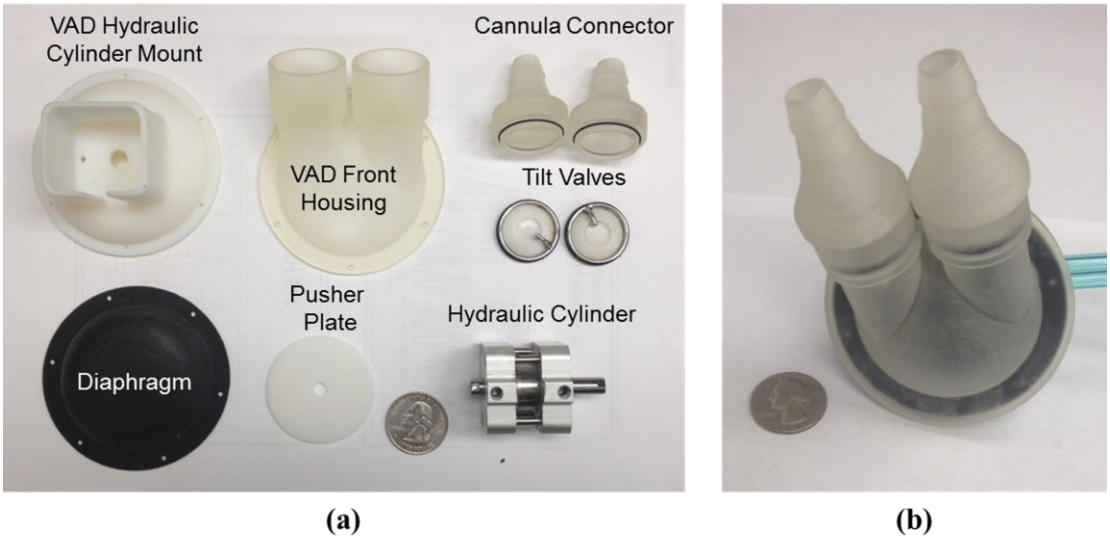

Figure 6-6. (a) 3D printed fabricated parts for the UCLA 25 mL Pediatric PiezoVAD and (b) the fully constructed blood pump prototype

The blood pump was fabricated (Figure 6-6b) by attaching the hydraulic cylinder to the VAD hydraulic cylinder mount with #4-40 screws. The pusher plate was screwed on to the hydraulic

cylinder rod. The elastomeric diaphragm was fixed to the pusher plate with cyanoacrylate and the edges were fixed to the VAD back housing/cylinder mount. The VAD front housing was attached to the back housing by using silicone adhesive. Similarly, the cannula connectors were fixed to the angled port ends with silicone adhesive to prevent leakage. It is important to note that blood sacs were not used in this initial prototype because there was difficulty in fabricating smooth and uniformly thick sacs (which will be discussed later in this chapter).

Once the critical dimensions for the blood pump were fixed, the Reynolds and Strouhal numbers were predicted using Equation 6-3. While this is a predicted number, and is no indication of the actual measured ratios, the calculation can be compared to the predicted values for the adult blood pump it was scaled from (Thoratec PVAD®) and other similar pediatric blood pumps. Using Equation 6-3 and assuming the pumping rate for the blood pumps were 70 BPM and the kinematic viscosity of blood is 3.77 cS, the calculated Reynolds and Strouhal numbers are shown in Table 6-1. From Table 6-1, the calculated Reynolds number for the smaller pediatric blood pumps indicates that flow in these devices are dominated by viscous flow more than in the adult sized blood pumps. The Reynolds number for the UCLA 25 mL blood pump falls in line with the numbers seen in clinically used pediatric blood pumps. The biggest potential advantage of the UCLA blood pump is the calculated Strouhal number.

Table 6-1. Predicted Reynolds and Strouhal Numbers

Blood Pump	Re	St
Thoratec PVAD® (Adult)	2134	6.0
Berlin Heart 12cc Pediatric VAD	785	8.8
Penn State 15cc Pediatric VAD	1567	45.3
UCLA 25mL Pediatric PiezoVAD	1037	4.6

From Bachmann *et al*. the Strouhal number for healthy ventricles, regardless of size and age, ranges from 4-7. While the Penn State 15cc PVAD and the Berlin Heart VAD are out of the normal range, the UCLA 25 mL PiezoVAD falls within range. This has to do with the fact that the inlet and outlet ports are not undersized. In fact they are slightly oversized from the predicted geometric scaling derived from Equation 6-4. This may pose a problem when the ports need to be adapted to fit much smaller cannula (6-12 mm diameter cannula). While the geometric dimensions of the blood pump are important in predicting fluid mechanics, the valve orientations are also crucial in ensuring thrombus formation in the pump during in vivo studies are prevented.

Figure 6-7 shows the orientation references to the horizontal axis of the inlet and outlet valves in the UCLA 25 mL PiezoVAD. Roszelle, Deutsch, and Manning studied the role of tilting disc inlet and outlet valve orientation on the flow field generated during ventricular assist device filling and blood ejection [110]. Using a transparent acrylic model of the blood pump and two-dimensional particle image velocimetry, they showed that when the inlet valve was oriented 15-30˚ from the horizontal axis of the inlet port, the flow jet into the blood pump chamber resulted in greater washout. For this reason, the inlet valve of the UCLA 25 mL PiezoVAD was 20˚ from the horizontal (Figure 6-7a). Similarly, Roszelle *et al*. demonstrated that an outlet valve oriented 15-30˚ from the horizontal axis of the outlet port can increase the shear stress and washout in the outlet cannula. As a result, the outlet valve of the UCLA 25 mL PiezoVAD (Figure 6-7b) was oriented 15˚ from the horizontal of the outlet port. Thus, the geometry of the blood pump, specifically the inlet and outlet diameters, and the valve orientations are important in ensuring that there is adequate shear stress and washout within the blood pump. The blood contacting interface of the device is also important.

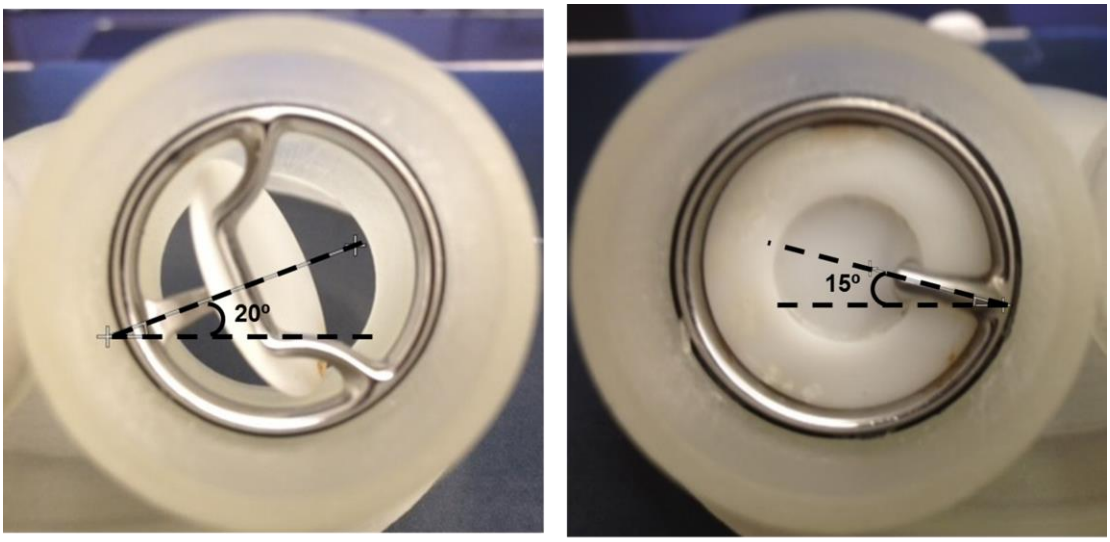

Figure 6-7. (a) Orientation angle of the blood pump inlet valve and (b) orientation of the outlet valve (blood chamber is facing up)

Arguably the most important component to the pulsatile blood pump design is the blood sac. This is the component that is in constant contact with the blood and undergoes cyclical stress during compression. The blood sac not only needs to be able to withstand cyclical compression (long fatigue life) it also needs to be biocompatible with the blood and its constituents. The inner lining of the sac also needs to be smooth to prevent stagnation of flow and blood clot accumulation. These three requirements make the fabrication of a blood sac crucial to its use in pulsatile blood pumps. The requirements are increasing stringent for pediatric blood pumps because of the lower flow fields though the device.

Research on the biocompatibility of materials in ventricular assist devices is abundant [111], [112]. Specifically, the use of polyurethanes for blood sac bladders in left ventricular assist devices is well documented. The blood sacs in this study were fabricated using a casting-mold process shown in Figure 6-8. A smooth hollow ceramic form was fabricated into the shape of the blood sac. A silicone rubber mold was then made by placing the ceramic form into a

container and pouring the liquid silicone into the container while holding the form in place. The silicone solution was allowed to cure for 24 hours and the resulting silicone mold was parted along the circumference of the ceramic form. The ceramic form was removed.

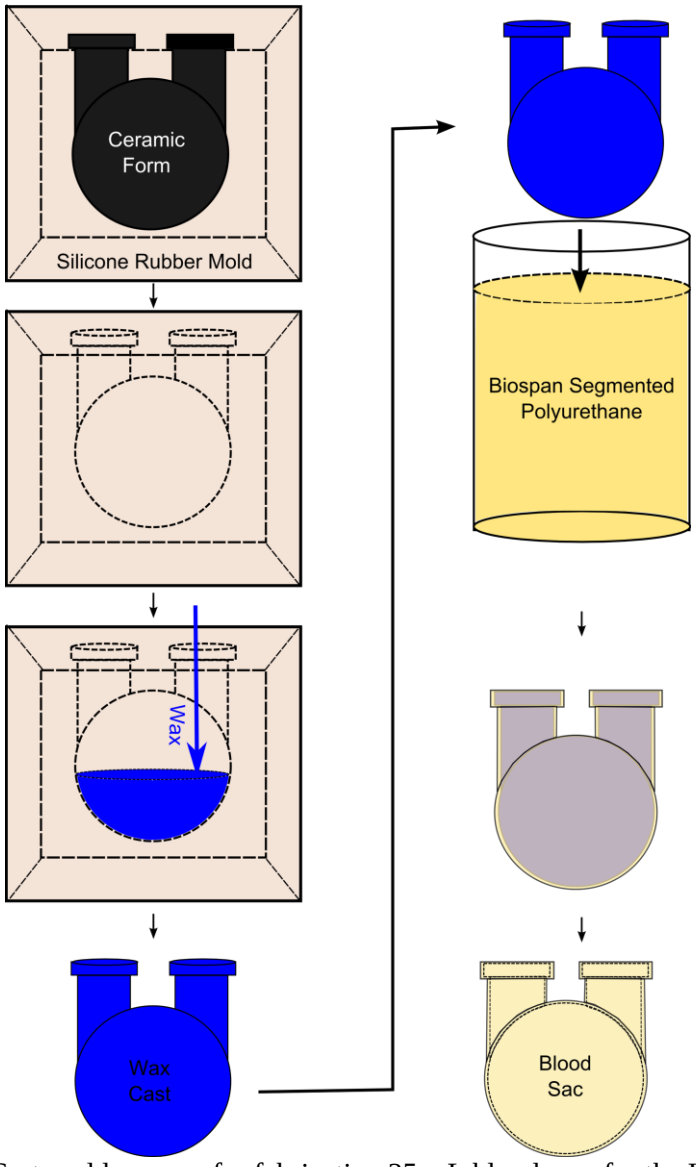

Figure 6-8. Cast-mold process for fabricating 25 mL blood sacs for the UCLA 25 mL PiezoVAD

To fabricate the blood sac, melted casting wax (heated above 200˚ F) was poured into the silicone rubber mold and allowed to cool once filled. The wax casts were then removed from the mold for dip coating. The wax casts were dip coated in a solution of Biospan® segmented

polyurethane (Royal DSM) heated at 105˚ F. The coated wax cast was then heated in an oven at 180˚ F for 1 hour to cure the layer of Biospan®. The dipping and oven curing process was repeated a total of seven times. The wax casts were then melted out in 250˚ F oil bath and the blood sacs were cleaned to remove excess oil. Figure 6-9a shows the ceramic form used to make the silicone mold and the resulting wax casts. Figure 6-9b shows one of the fabricated blood sacs. Unfortunately, none of the blood sacs that were fabricated were useable because of the uneven surface finishes on the inner part of the blood sac. A better controlled dip coating setup is needed to ensure the blood sac has a uniform thickness and smooth inner lining.

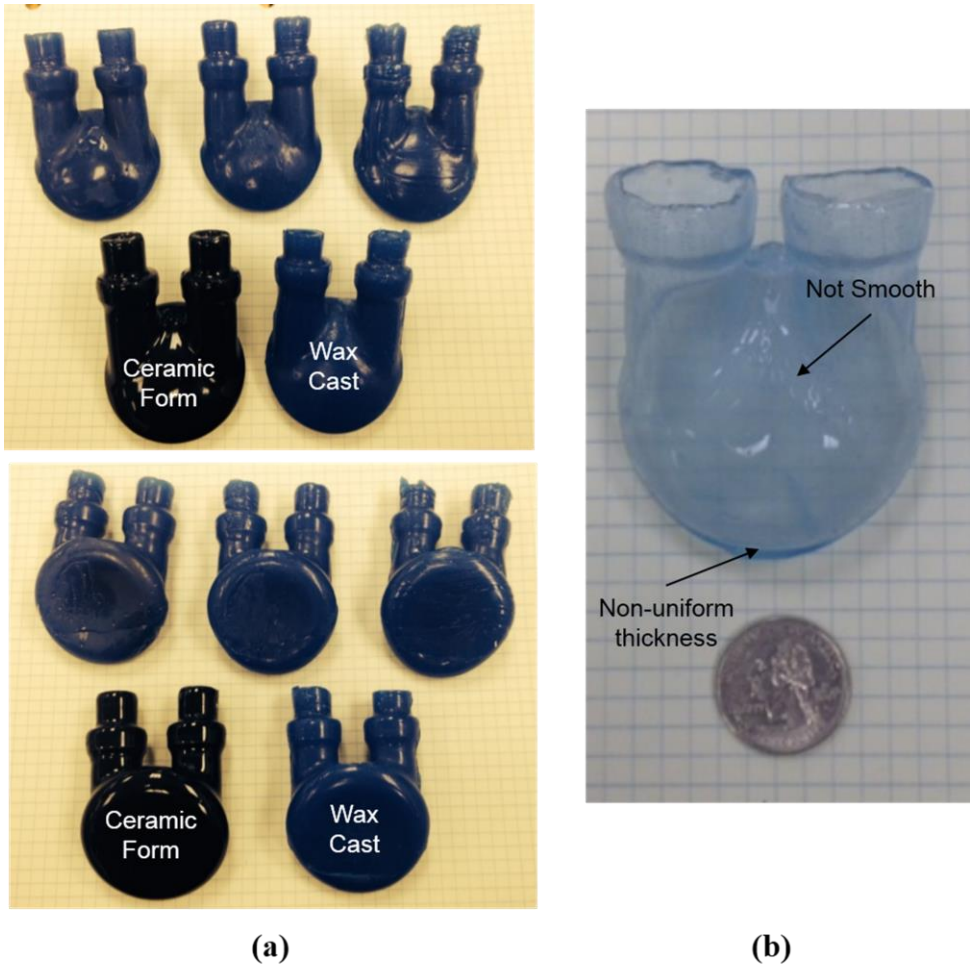

Figure 6-9. (a) Blood pump wax casts and (d) fabricated segmented polyurethane blood sac

6.2 Piezoelectric Hydraulic Ventricular Assist Device Driver Design

The design of the ventricular assist device driver is similar to the driver design from Chapter 4 (Figure 4-4a). The driver consists of a piezoelectric pump, the EPCOS piezohydraulic pump from Chapter 5, an accumulator, a 4-way directional solenoid valve, and a hydraulic cylinder which is attached to a blood pump (Figure 6-10). Plastic high pressure fluid lines were used to connect the piezohydraulic pump to the 4-way valve and blood pump. The design of the blood pump was detailed above. As mentioned previously, the blood pump was designed to output a 25 mL stroke volume. In order to predict the stroke output of the blood pump hydraulic cylinder for a given piezoelectric pump flow rate and pressure output, the entire driver system was modeled on Simscape^{TM}, which allows the modeling of multi-domain physical systems. The model, shown in Figure 6-10, combines a hydraulic and mechanical domain to simulate the displacement of a hydraulic cylinder for a given input flow rate.

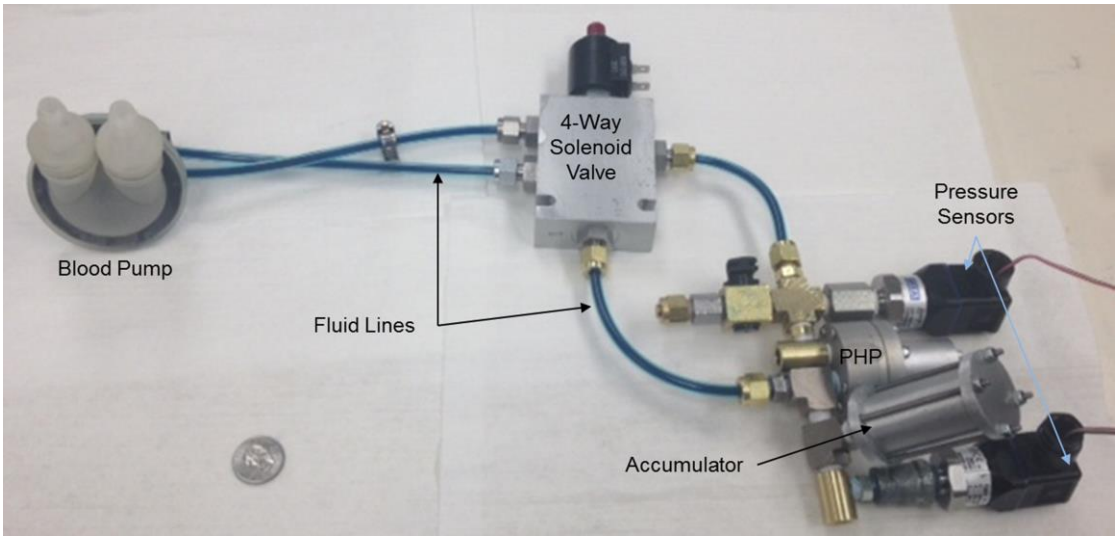

Figure 6-10. Piezoelectric Hydraulic Ventricular Assist Device Driver

The VAD driver is modeled as a system that contains a hydraulic motor that is driven by an ideal angular velocity source. These two components combine to represent an ideal flow source

which represents the piezohydraulic pump. A 4-way spool valve represents the 4-way directional solenoid valve in the driver setup. The position of the spool simulates the applied voltage to a solenoid valve. The 4-way valve is connected to a double-acting hydraulic cylinder, which represents the double–acting double-rod hydraulic cylinder attached to the blood pump. The effective piston area of the hydraulic cylinder is 1.66 cm^2 with a 1.27 cm stroke. A 50 g mass and 0.1 N/m spring was connected to the output shaft of the hydraulic cylinder in the model. The mass simulates the fluid mass in the blood pump chamber and the translational spring represents the compliance of the fluid within the blood pump. Different output flow rates were delivered from the hydraulic motor component. The frequency of 4-way valve switching simulates the stroke rate of the VAD driver. The duty cycle mimics the amount of time the blood pump is actively ejecting blood (systole) and refilling (diastole). For a VAD stroke rate of 60 beats per minute (BPM), the valve switches from the off stat, which is associated with blood ejection, to the on state, pump refilling every 500 ms. The hydraulic cylinder rod stroke was predicted for various pump flow outputs. The model predicts resultant VAD stroke volume at various VAD stroke rates for a given piezohydraulic pump flow rate input. This will show us the minimum flow rate needed to ensure the full stroke of the blood pump is achieved at different stroke rates. The results of this model are compared to the in-vitro tests that will described in the next section.

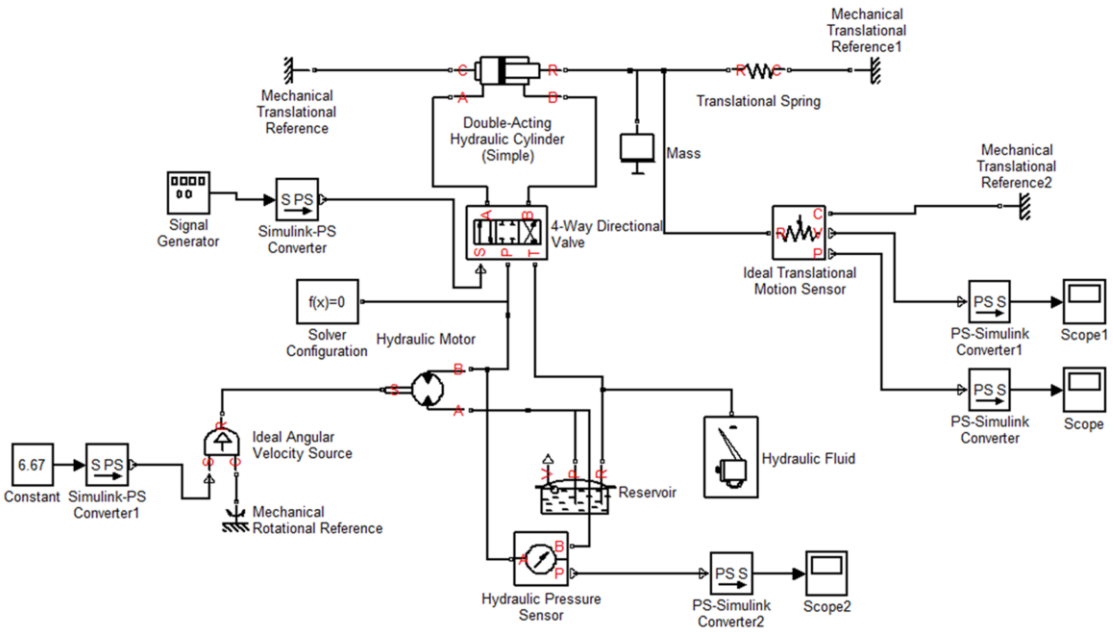

Figure 6-11. Simscape 1D model of a hydraulic cylinder driver that represents the piezohydraulic pediatric VAD driver

6.3 *In-vitro* Testing and Results

In conjunction with the 1D Simscape™ model developed for the VAD driver, the actual driver was built (Figure 6-10) and tested to measure how well the EPCOS piezoelectric pump could provide the necessary flow rate and pressure. The driver was attached to an in vitro mock circulation which mimics the systemic circulation of a pediatric patient. The driver hydraulic circuit was pressurized to 80 psi. The piezoelectric stack in the piezohydraulic pump was excited with a sinusoidal voltage ranging from 0-160V. The 25 mL stroke volume blood pump is attached to two compliance chambers. At the blood pump inlet, a large reservoir is attached to represent the left atrium. The systemic arterial compliance is represented by a compliance chamber attached at the outlet of the blood pump. A clamp was placed between the atrial reservoir and arterial compliance chamber to mimic the arterial vascular resistance. Arterial pressure and atrial pressure were recorded with pressure transducers (Utah Medical; Deltran). Ultrasonic flow probes and flow meter (Transonic Systems Inc., ME12PXL) measured

instantaneous flow rate directly from the outlet of the blood pump. Mean flow was determined from integrating the instantaneous flow measurements over time.

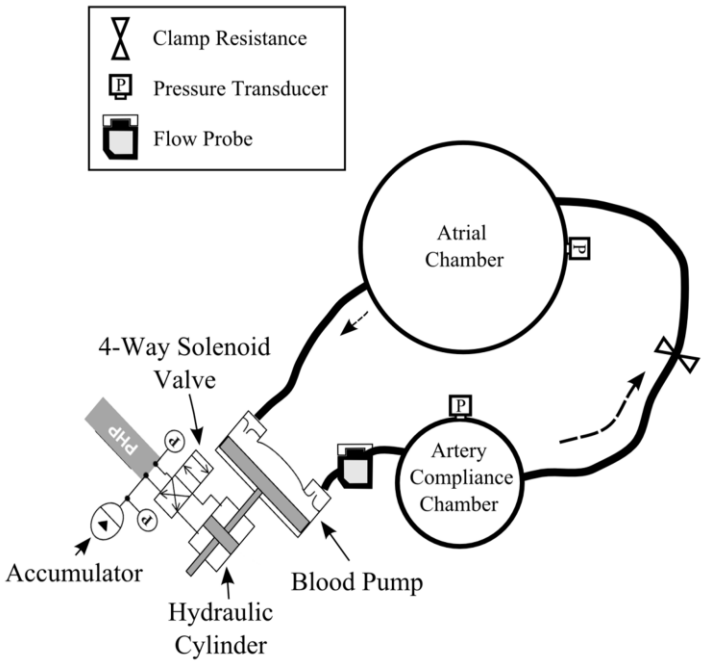

Figure 6-12. In vitro mock circulation used to test the piezohydraulic driver

The first test involved finding the best operational frequency of the piezohydraulic pump. In this test, the 4-way solenoid valve was not switched at various stroke rates. The driver was controlled to only provide fluid ejection from the blood pump (ie. the piezohydraulic pump was used to provide hydraulic cylinder rod extension and 25 mL stroke volume ejection). The instantaneous flow rate from the blood pump was recorded for various piezohydraulic pump operational frequencies. The frequency at which the highest instantaneous VAD flow rate was achieved represented the frequency at which the piezohydraulic pump delivered the best flow rate to the blood pump. Because the external piping has changed for this setup compared to the setup in Figure 5-27, optimal operational frequency has changed as well.

Figure 6-13 shows the instantaneous VAD flow rate versus piezohydraulic pump frequency. Between 100-200 Hz, the instantaneous flow rate increases linearly with increasing

frequency. The maximum Instantaneous flow rate occurs at a 250 Hz operational frequency. This is lower than the 330 Hz maximum piezohydraulic pump flow rate measured in Chapter 5 (Figure 5-28b). The VAD flow rate decreases for frequencies higher than 250 Hz, with the sharpest drop in flow rate performance between 400-450 Hz. Thus the best operation frequency for this driver design is at 250 Hz. It is important to note that the length of the hydraulic lines connecting the piezohydraulic pump to the blood pump can be increased to take advantage of acoustic reflections that may increase volumetric efficiencies and operational frequency. While this may easily boost performance, the resulting vibrations in the system may not be beneficial to patients using this system.

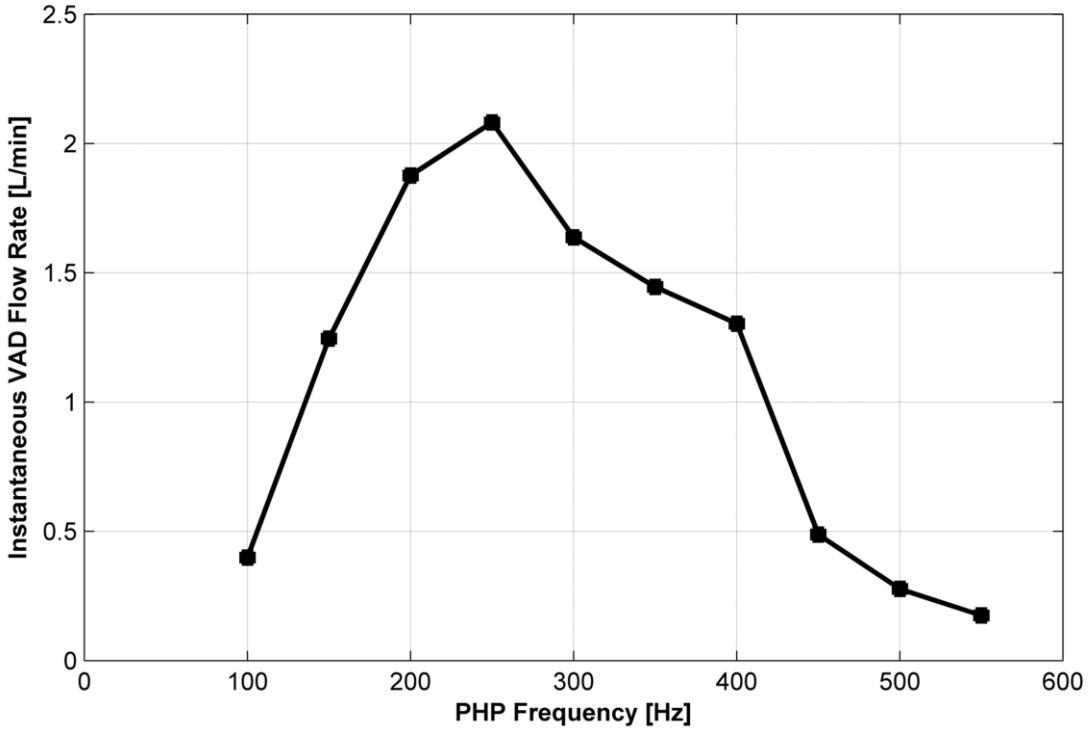

Figure 6-13. Instantaneous VAD flow rate recorded at the outlet of the blood pump as a function of various piezohydraulic pump operational frequencies

Once the operational frequency of the piezohydraulic pump was chosen, the ventricular assist device driver was tested at various stroke rates. In this case, the 4-way solenoid valve was

switched to provide blood pump fluid ejection for half the cycle and blood pump refilling for the other half of the cycle. The frequency of this solenoid valve switching is known as the stroke rate and it simulates the heart rate of a natural heart. The stroke rate was varied between 30-100 beats per minute (BPM) in 5 BPM increments. During operation, the piezohydraulic pump pressure differential was recorded. The resulting arterial pressure and VAD flow rate in the mock circulation were also recorded. Mean VAD flow rate was also measured by averaging the instantaneous flow rate measured by the ultrasonic flow meter.

Figure 6-14 shows the in vitro waveforms for the ventricular assist device driver and the mock circulation for the driver operating in 40 BPM stroke rate. During blood pump refilling, highlighted in blue, the pusher plate in the VAD is retracted from a fully extended position to allow fluid to enter the blood pump. The piezohydraulic pressure needed to retract the pusher plate is 15 psi. This retraction in the VAD pusher plate causes the arterial pressure to decrease from 90 mm Hg to 60 mm Hg. There is also leakage flow that goes through the outlet valve of the blood pump during blood pump refilling. During blood pump fluid ejection, highlighted in red, the 4-way valve switches the direction of the piezohydraulic pump flow rate to cause pusher plate extension. The piezohydraulic pump pressure needed to achieve blood ejection is 30-35 psi, which is higher than the pressure needed to refill the blood pump. This is because the blood pump diaphragm and valves represent a larger load to the piezohydraulic pump than the simple retraction of the pusher plate. The pusher plate extension causes the arterial pressure to increase from 60-90 mm Hg and the VAD flow rate to increase from 0-2 L/min. These waveforms represent physiological outputs that can assist a pediatric circulation.

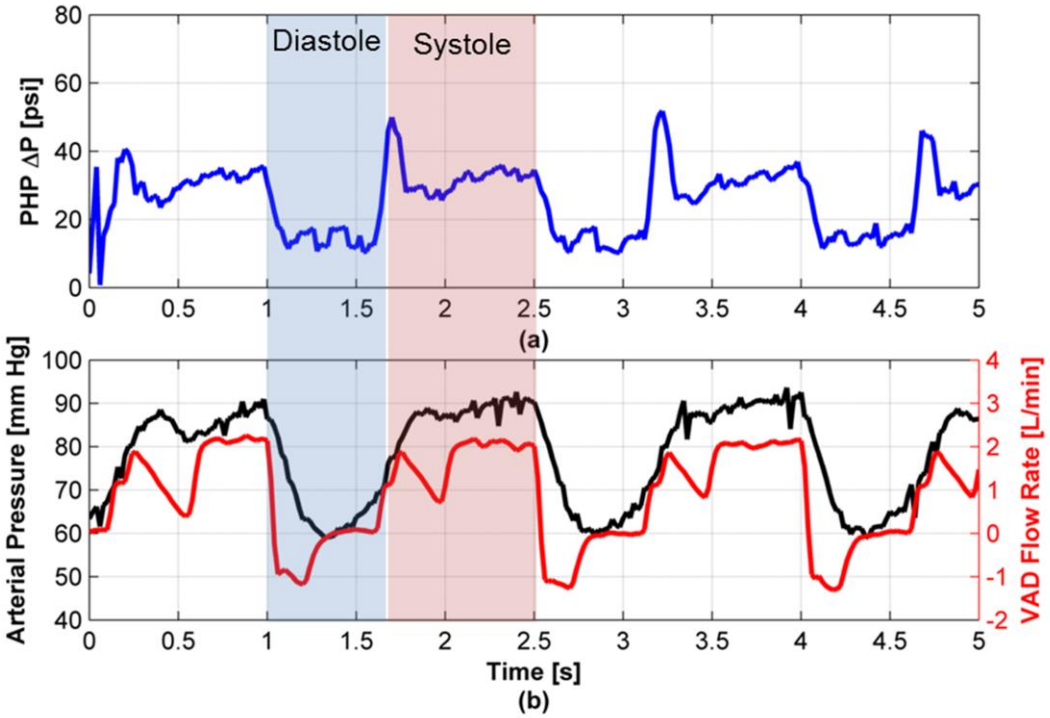

Figure 6-14. (a) Pressure differential across the piezohydraulic pump during the in vitro test and (b) the resulting arterial pressure waveforms and VAD flow rates at 40 BPM stroke rate

Figure 6-15 shows the in vitro waveforms for the ventricular assist device driver and the mock circulation for the driver operating in 80 BPM stroke rate. Similar to the 40 BPM waveforms, the pressure needed to refill the blood pump (35 psi) is smaller than the pressure needed to eject fluid from the blood pump (45 psi). In this case, the 4-way valve is switching twice as fast as the 40 BPM case. This means that there is less time to eject and refill per cycle. This explains why the arterial pressure oscillates between 75 mm Hg and 55 mm Hg instead of 60 mm Hg and 90 mm Hg as seen in Figure 6-14b. The smaller amount of volume per stroke results in a smaller pressure output in the mock circulation. The flow rate from the EPCOS piezohydraulic pump is not large enough to supply the volume needed to achieve a full stroke. This issue is more clearly elucidated in Figure 6-16.

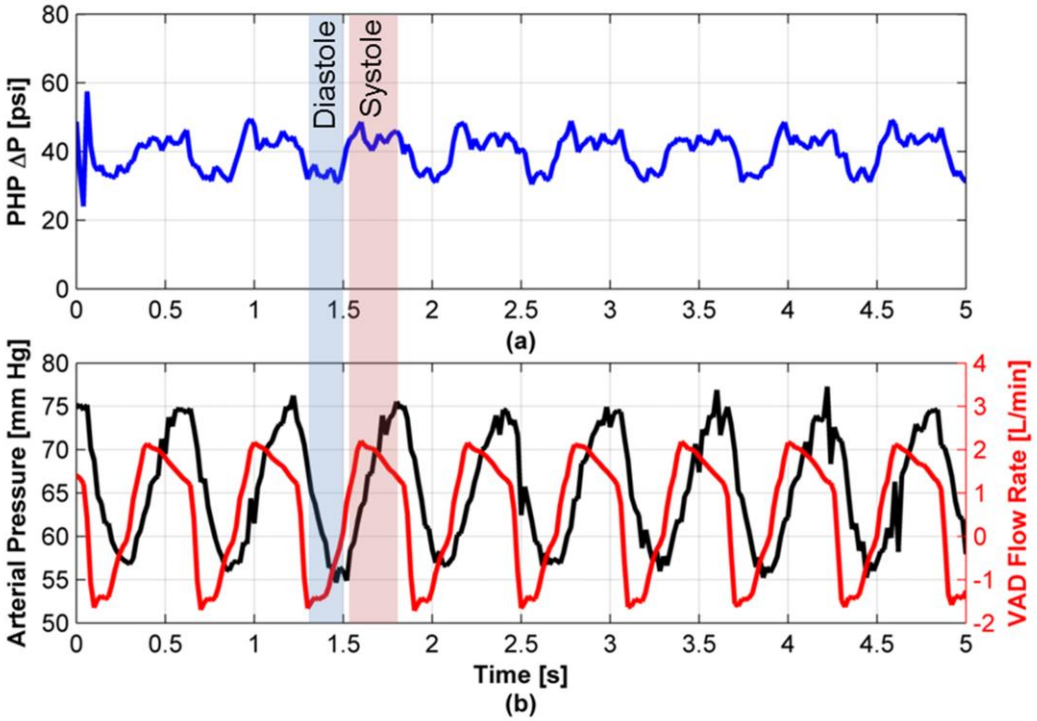

Figure 6-15. (a) Pressure differential across the piezohydraulic pump during the in vitro test and (b) the resulting arterial pressure waveforms and VAD flow rates at 80 BPM stroke rate

Figure 6-16 shows the average flow rate through the mock circulation for various VAD driver stroke rates. The green line represents the ideal flow rate versus stoke rate relationship in which full stroke is achieved. The blue line represents the progress to date. Ideally, the average flow rate for a pulsatile blood pump is the product of the stroke rate and stroke volume (mean flow is proportional to stroke rate). This assumes the full stroke can be achieved at various stroke rates. Unfortunately, for stroke rates above 35 BPM, the EPCOS piezohydraulic pump cannot supply sufficient flow rate to achieve the mean flow necessary to achieve a full blood pump stroke volume. In fact, as the stroke rate increases, the resulting stroke volume of the blood pumps decreased, leading to a decrease in the mean flow seen in the mock circulation.

In order to predict the flow rate that is being output by the piezohydraulic pump in this driver configuration, the experimental data was compared to the Simscape™ model shown in

Figure 6-11. In the model, the flow rate from the ideal flow source was varied from 3 cc/s (mL/s) to 5 cc/s. The mean VAD flow rate was calculated by taking the stroke of the hydraulic cylinder in the model and multiplying it by an area of 19.685 cm^2. From the model, we can see that flow rates larger than 5 cc/s are needed to achieve the full stroke above stroke rates of 65 BPM. It also shows that the current piezohydraulic pump is outputting a flow rate less than 3 cc/s (180 mL/min). Even though we can achieve a 250 mL/min (4.167 cc/s) with the setup in Figure 5-27, it does not translate to this driver setup. Nonetheless, the potential for this technology in mechanical circulatory support is promising. The piezohydraulic pump can still be optimized in terms of efficiency and flow rate and pressure output. Utilizing the frequency dynamics of the hydraulic circuit can bring this technology closer to use in ventricular assist device systems.

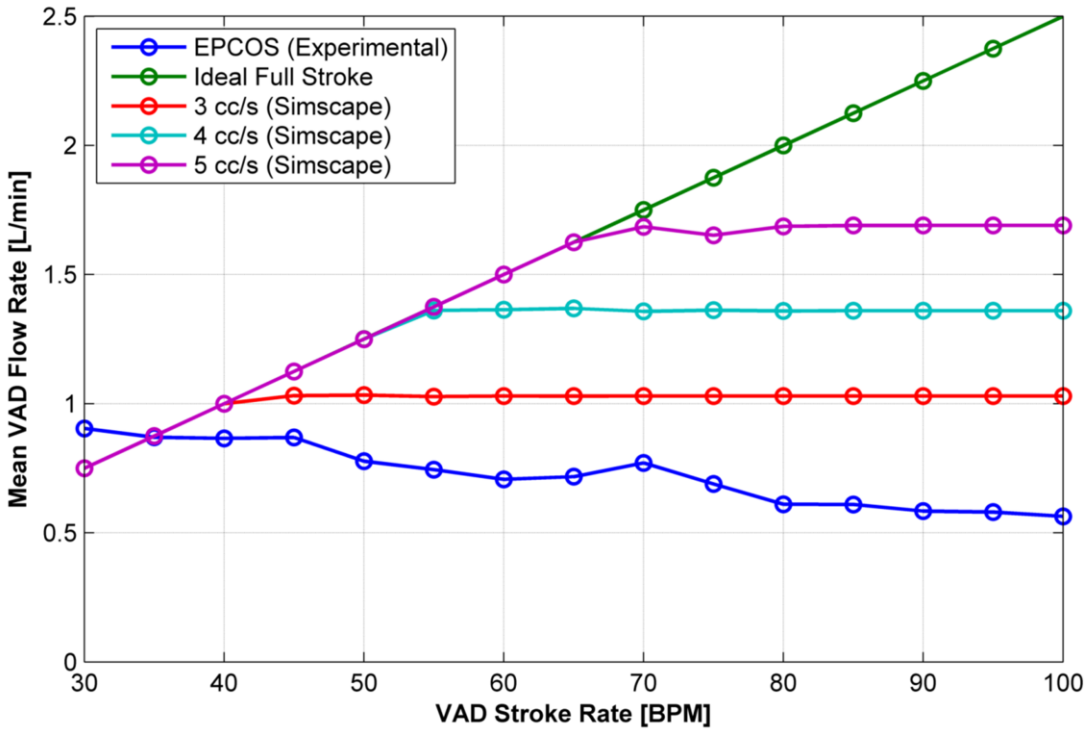

Figure 6-16. Average VAD flow rate from the piezohydraulic driven blood pump (experimental) and the predicted performance (Simscape™)

6.4 Summary

In this chapter, the design of a hydraulically actuated blood pump was presented. The fluid mechanics of pump scaling were presented to ensure that the flow characteristics of the newly designed blood pump were not altered. The design and in vitro testing of the ventricular assist device driver was also presented. The driver was able to output physiological pressure and flow rates. However, the flow rate of the piezohydraulic pump still needs to be improved to allow operation at stroke rates up to 100 BPM.

Chapter 7: Fontan Mechanical Circulatory Support Research

In this chapter other mechanical circulatory support research projects are covered. This particular chapter discusses the use of a commercially available left ventricular assist device, the Sushine C-Pulse, in applications for pediatric Fontan circulations. While Fontan palliation in the form of the total cavopulmonary connection has improved the management of congenital single ventricle physiology, long-term outcomes for patients with this disease are suboptimal due to the lack of two functional ventricles. Researchers have shown that ventricular assist devices (VADs) can normalize Fontan hemodynamics. To minimize blood contacting surfaces of the VAD, we evaluated the use of an external compression device (C-Pulse Heart Assist System, Sunshine Heart Inc.) as a Fontan assist device. A mock circulation was developed to mimic the hemodynamics of a hypertensive Fontan circulation in a pediatric patient. The Sunshine C-Pulse compression cuff was coupled with polymeric valves and a compressible tube to provide non-blood contacting pulsatile flow through the Fontan circulation. The effect of the number, one or two, and placement of valves, before or after the compression cuff, on inferior vena cava pressure (IVCP) was studied. In addition, the effect of device inflation volume and compression rate on maintaining low IVCP was investigated. With one valve located before the cuff, the device was unable to maintain an IVCP below 15.5 mm Hg. With two valves, the C-Pulse was able to maintain IVCP as low as 8.5 mm Hg. The C-Pulse provided pulsatile flow and pressure through the pulmonary branch of the mock circulation with a pulse pressure of 16 mm Hg and 180 mL/min additional flow above un-assisted flow. C-pulse compression reduced IVCP below 12 mm Hg with 13cc inflation volume and compression rates above 105 BPM. This application of an external compression device combined with two valves has potential for use as an artificial right ventricle by maintaining low IVCP and providing pulsatile flow through the lungs.

7.1 Fontan Physiology Background

Fontan palliation is routine in the management of the pathology associated with congenital single ventricle physiology. The current adaptation of the Fontan procedure [1], the total cavopulmonary connection (TCPC), involves bypassing the right atrium and directly connecting the superior vena cava (SVC) and inferior vena cava (IVC) to the pulmonary arteries (PA). This creates a circulation in which the pulmonary and systemic branches are connected in series and are supported by a single ventricle. Unfortunately, the TCPC is prone to eventual failure characterized by deterioration in single ventricle function, central venous hypertension, and decreased ventricular preload. Without a dedicated right ventricle, low systemic venous pressure cannot be maintained [2]. These hemodynamic abnormalities are deleterious to the liver, lungs, and the systemic ventricle and can result in organ failure [3], [4]. Many Fontan patients with failing single ventricles require heart transplantation. Researchers have hypothesized that the use of a mechanical circulatory assist device could prevent, or alter the course of, a hypertensive Fontan circulation [5].

Mechanical circulatory support devices, including pulsatile and continuous flow ventricular assist devices (VADs), have been studied for use as bridge-to-transplantation (BTT) in Fontan patients with suboptimal hemodynamics. Chu *et al.* and Mackling *et al.* have successfully implanted the Berlin Heart EXCOR Pediatric VAD as a BTT for patients with hypoplastic left heart syndrome who have been palliated with the Glenn Shunt [6], [7]. Continuous flow blood pumps have successfully maintained low IVC pressure in sheep animal models mimicking the Fontan circulation [5], [8]. While these devices have shown promise as BTT, they pose additional problems to Fontan patients. Pulsatile VADs require percutaneous cannulae, valves, and a large diameter pneumatic driveline that collectively increase patient risk

of infection and thrombosis [9]. Continuous flow pumps, including those designed specifically for Fontan patients [10], [11], are associated with increased bleeding [12], blood cavitation, and suction when used on the venous side of the circulation [13]–[15]. To circumvent these problems, researchers have used skeletal muscles, namely the latissimus dorsi, to provide non-blood contacting pulsatile Fontan assistance via compression of the right atria or a vascular graft [16]–[18]. Nevertheless, studies on this type of support are limited and the use of skeletal muscle is constrained by muscle fatigue [19]. Devices that reduce risk of infection, thrombosis, and are fatigue resistant may result in improved Fontan patient outcomes.

One device that can potentially reduce the risk of thrombosis while mimicking the external compression provided by a skeletal muscle is the Sunshine C-Pulse Heart Assist System (Sunshine Heart, Eden Prairie, MN). The Sunshine C-Pulse, designed to treat patients with NYHA Class III and ambulatory Class IV heart failure, is an extra-aortic counter-pulsation compression device used to unload the failing left ventricle [20]. The device consists of a counter-pulsation balloon, cuff, and pneumatic drive console coupled with ECG leads. In adult heart failure patients, it functions to increase coronary blood flow during aortic compression and reduces afterload during aortic decompression. This combination yields an increase in cardiac output and a decrease in ventricular wall stress [21]. The C-Pulse can be implanted via a mini-thoracotomy or mini-sternotomy, which may allow for shorter implantation time and shorter hospital stays. Since the device is extravascular, stroke and clotting risks are potentially reduced [22]. The advantages of a cuff-based device for heart failure patients may be applied to patients with hypertensive Fontan circulations. Extra-vascular cuff compression may lead to decreased IVC and PA pressures while simultaneously reducing adverse outcomes seen with traditional VADs.

We hypothesize that the Sunshine C-Pulse and similar non-blood contacting, cuff-based compression devices can effectively address concerns associated with current mechanical circulatory support devices while improving hemodynamics in Fontan patients with venous hypertension. In order to optimize the Sunshine C-Pulse for use in a hypertensive Fontan, it is hypothesized that the external compression cuff must be coupled with two valves to maintain low IVC pressure. A valve located after the compression site prevents retrograde flow upon cuff decompression, and a valve located before the compression site prevents retrograde flow upon cuff compression. We performed proof-of-principle bench testing to determine the number of valves needed for effective Fontan assistance with compression devices, and to demonstrate that the C-pulse device could function as a Fontan assist device.

7.2 Fontan Assist Materials and Methods

Device Description

The Sunshine C-Pulse Heart Assist System is comprised of an extra-aortic compression balloon, cuff, and pneumatic drive console. The compression balloon and cuff provide "thumb-printing" external compression with the balloon inflated via a percutaneous gas line connected to a pneumatic drive console. The compression balloon offers a programmable stroke volume ranging between 4-20 mL [21]. In order to use the Sunshine C-pulse compression balloon and cuff as a Fontan assist device on the venous side of the circulation, valves and compressible tube were used to aid flow through the pulmonary circulation.

The proof-of-concept Fontan assist device consists of the Sunshine C-Pulse Heart Assist System coupled with polyurethane tri-leaflet valves and a compressible tube. The compressible tube has a 19 mm inner diameter and a 25 mm outer diameter. The polymeric tri-leaflet valves, which provide unidirectional flow through the Fontan circuit, are obtained from the disposable

Abiomed BVS5000 (Abiomed Inc., Danvers, Massachusetts). The valves and tube used in this study are not representative of the final assist device. In a clinical setting, vascular grafts and transcatheter valves can be used. The effect of the number of valves and the placement of the valves relative to the compression device on vena cava pressure and flow were investigated. For the purposes of this study, the TCPC Fontan configuration was not used since it was difficult to provide non-retrograde flow in both the IVC and SVC with one device [23]. Instead, we envision the SVC attached to the IVC in end-to-side fashion (IVC-SVC junction), with both subsequently connected to the main pulmonary artery (MPA) (Figure 7-1). Before the Fontan assist was tested, a mock circulation mimicking a hypertensive Fontan circulation was constructed.

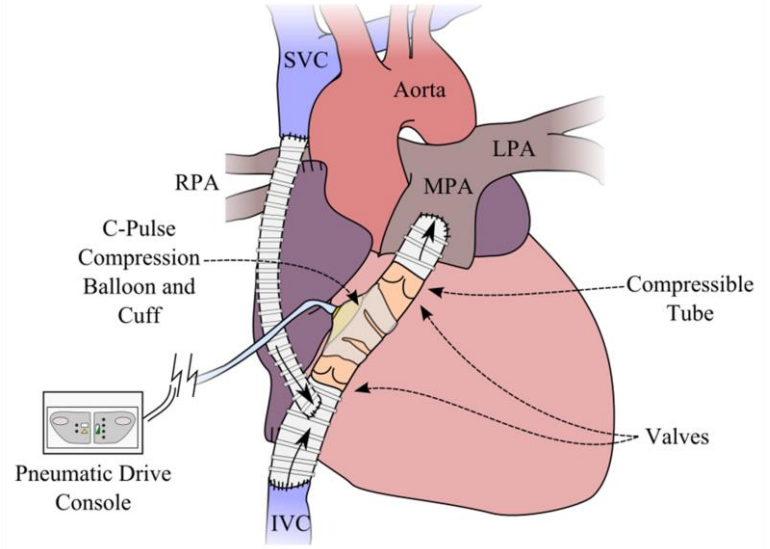

Figure 7-1. Anatomical configuration of an updated Fontan connection consisting of a non-blood contacting C-Pulse compression cuff (Sunshine Heart Inc.), polymeric valves, and compressible tube. MPA, LPA SVC, RPA, RA, IVC refer to main pulmonary artery, left pulmonary artery, superior vena cava, right pulmonary artery, right atrium, and inferior vena cava respectively

Mock Circulation

A bench-top circulation was constructed to mimic hypertensive Fontan hemodynamics of a pediatric patient. Similar to previous mock circulations: a pulsatile blood pump was used to

represent the single ventricle, compliance chambers were fabricated to mimic arterial and venous compliance, and tube clamps were used to simulate vascular resistance (Figure 7-2) [24]–[26]. The single ventricle was modeled by using a pulsatile blood pump (Pulsatile Blood Pump 1421, Harvard Apparatus) with a 4-30 mL stroke volume, and 20-200 BPM stroke rate. Arterial and venous compliances were simulated by using air tight acrylic chambers (1.2 L for the arterial, and 10 L for the venous). Compliance was determined by adjusting the height of the fluid column and the amount of entrapped gas. The atrium was represented by a 1L reservoir that was open to air to facilitate venous return. Vascular resistance was determined by the diameter of the tubes connecting the compliance chambers (3/8" for systemic arterial, pulmonary arterial/venous, and ½" for systemic venous) and tube clamps for fine adjustment of resistance. Pressures were recorded with medical pressure transducers (Utah Medical; Deltran). Ultrasonic flow probes and a flow meter (Transonic Systems Inc., ME12PXL) measured instantaneous flow rate at the various branches in the circulation.

Table 7-1. Comparison of Hypertensive Fontan Mock Circulation to Clinical Data

Property	Pediatric Non-Fontan (Clinical)	Pediatric Hypertensive Fontan (Clinical)	Mock Circulation
MAP (mmHg)	81	82	87
CI (L/min/m^2)	4.4	2.5	2.5*
IVCP (mmHg)	4.3	17.1	21.5

* Assuming a 1 m^2 body surface area (BSA), MAP – Mean Arterial Pressure, CI – Cardiac Index, IVCP – Inferior Vena Cava Pressure

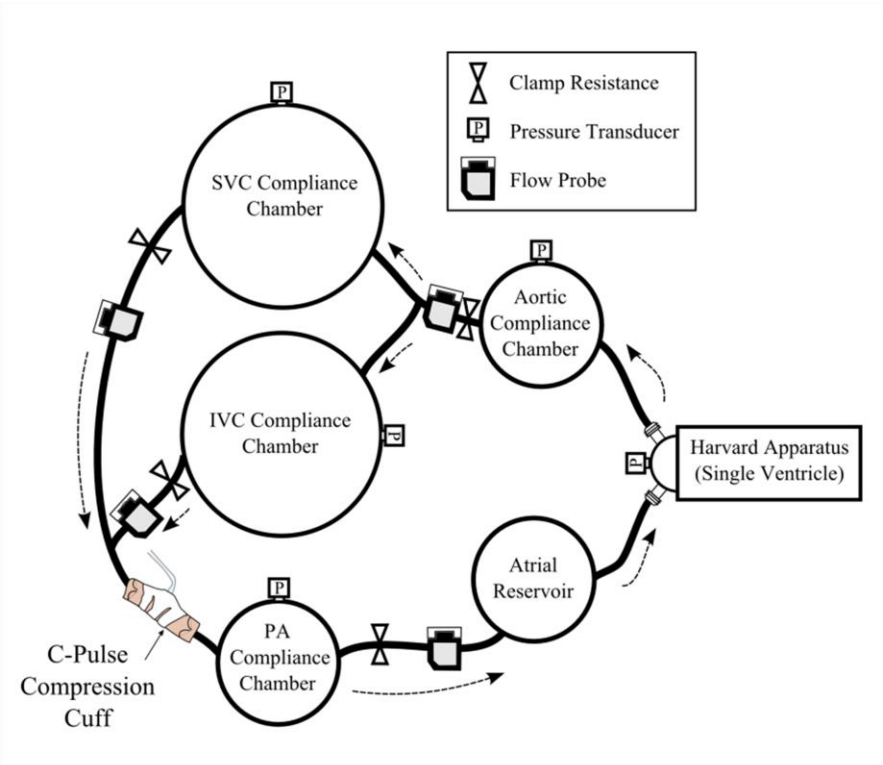

Figure 7-2. Bench-top circulation representing a hypertensive Fontan circulation with the C-Pulse compression cuff (Sunshine Heart Inc.) SVC, IVC, and PA refer to superior vena cava, inferior vena cava, and pulmonary artery respectively

Experimental Procedure

The mock circulation mimicking an unassisted Fontan was tested to accurately model the hemodynamics of the hypertensive Fontan physiology. The Harvard apparatus pump was set to run at 100 beats per minute (BPM) with a 25 mL stroke volume to get a 2.5 L/min cardiac output. The Fontan junction was represented by connecting the IVC, SVC, and pulmonary artery compliance chamber with a Y-tube adapter. Pressures were measured in all of the compliance chambers. Flow rates were measured in the systemic and pulmonary arterial and venous branches. The assisted Fontan mock circulation was then tested to quantify how well the Sunshine C-Pulse device could reduce pressure in the venous branch and provide pulsatile flow in the pulmonary arterial branch.

For Fontan assist, the Sunshine C-Pulse compression cuff was wrapped around the compressible tube and was placed in between the IVC-SVC junction and the pulmonary artery chamber. Three scenarios were used to test the effectiveness of the number and the placement of the polymeric valves on maintaining low IVC pressure in the mock circulation. The use of one valve, before or after the C-Pulse compression site, and the use of two valves were evaluated. Fontan assist was initiated by compressing the compressible tube with the C-Pulse compression balloon and cuff. The extent of compression was determined by the inflation volume of the compression balloon which is set by the pneumatic drive console. The rate of compression was adjusted by an ECG simulator which triggered the inflation and deflation of the compression balloon. It is important to note that the rate of tube compression is independent of the Harvard apparatus pump stroke rate. Pressures were measured at the IVC chamber and the PA chamber. Flow was measured in between the PA compliance chamber and the atrial reservoir.

7.3 Results and Discussion

Hypertensive Fontan Mock Circulation Results

The mock circulation accurately mimicked the pressure and flow waveforms for a pediatric patient with a hypertensive Fontan circulation, as seen in Figures 7-3A and 7-3B respectively. Aortic pressure (AoP) oscillated between 75-112 mmHg, corresponding to a 37 mmHg pulse pressure and an 87 mmHg mean arterial pressure (MAP). IVC pressure (IVCP) was non-pulsatile and was elevated at 21.5 mmHg. Pulmonary artery pressure (PAP) was also elevated at 20 mmHg. The high venous pressure, represented by the IVC pressure, corresponds to the hypertensive venous state seen clinically in hypertensive Fontan circulations. Mean aortic flow (Ao Flow), in Figure 3B, was 2.5 L/min. IVC and SVC flow were steady at 1.7 L/min and 0.8 L/min respectively. Comparison of the mock circulation and clinical data [27] observed in

pediatric patients with venous congestion is shown in Table 7-1. Thus, the mock circulation approximately matches the hemodynamics of a Fontan patient.

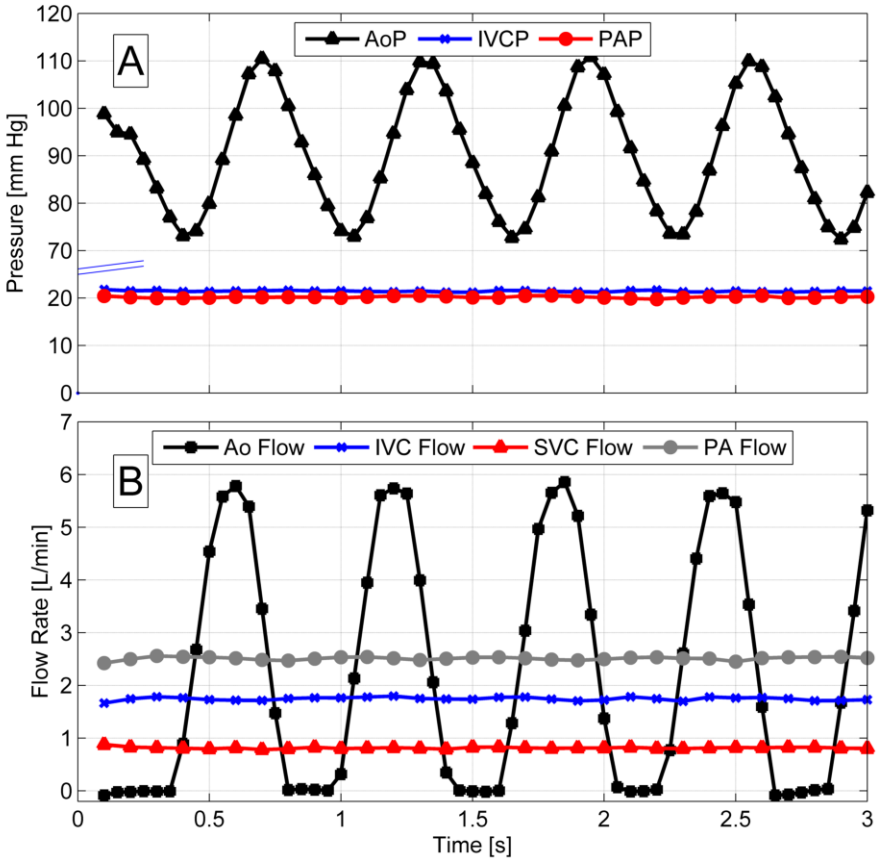

Figure 7-3. (a) Aortic (AoP), inferior vena cava (IVCP), and pulmonary artery (PAP) pressure waveforms and (b) aortic (Ao), inferior vena cava (IVC), superior vena cava (SVC), and pulmonary artery (PA) flow waveforms for the unassisted hypertensive Fontan bench-top circulation

Fontan Assist Results

When the C-Pulse is used as a Fontan assist device with two valves, it was able to mimic the pulsatile nature of the right ventricle and keep IVC pressure as low as 8.5 mmHg (Figure 7-4A to 7-4D). The ECG simulation trigger (Figure 7-4A) pulsed at 125 BPM and triggered the driver to output pressurized gas (Figure 7-4B) to inflate the compression balloon at the end of the T-wave.

The driver then applied vacuum at the QRS complex for balloon deflation. The peak gas driver pressure increases from -5 mmHg to 198 mmHg. This compression causes the instantaneous pulmonary artery flow (PA Flow) to increase from 1.7 L/min to 2.8 L/min (Figure 7-4C). This allows the IVC pressure to remain low at 8.5 mmHg (Figure 7-4D). Thus, when the C-Pulse assists the venous side, oscillatory flow is restored through the lungs and low IVC pressure is maintained.

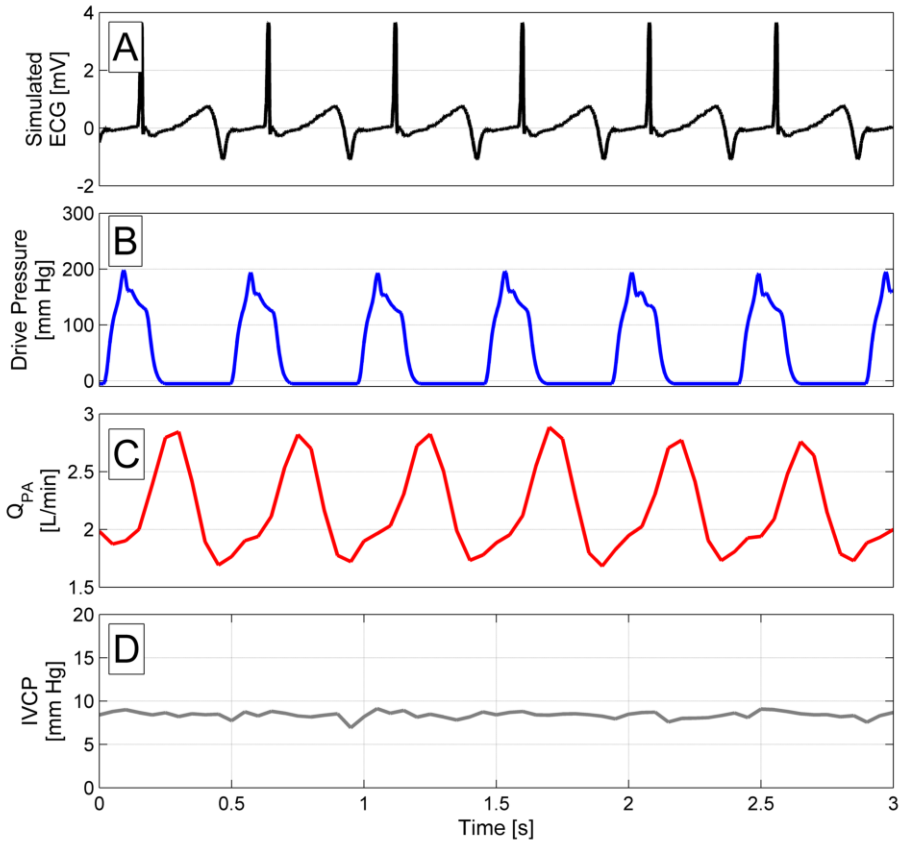

Figure 7-4. (a) Simulated ECG signal used to trigger compression C-pulse Cuff (Sunshine Heart Inc.) inflation, (b) drive pressure of the cuff from the driver, (c) pulmonary artery flow (Q_{PA}) and (d) inferior vena cava pressure (IVCP) during Fontan assistance of a bench-top in vitro mock hypertensive Fontan circulation

Without the use of the C-Pulse and two valves for Fontan assistance, the IVC compliance chamber pressure increases due to a volume shift from the left atrial reservoir to the IVC chamber. In Figure 7-5, the IVC pressure is 12.3 mmHg under Fontan assistance (first 20 seconds) with a 125 BPM compression rate and an 8 cc inflation volume. After Fontan assistance is stopped (20s to 50s), the IVC pressure increases towards a higher steady-state value. With re-initiation of Fontan assistance (50s to 90s), the IVC pressure begins to approach a lower steady-state value. Fontan assistance can be used to shift blood away from the large compliance of the venous circulation. This illustrates that non-blood contacting Fontan assistance can be used to achieve rapid reversal of increased venous pressure in the setting of a failed Fontan.

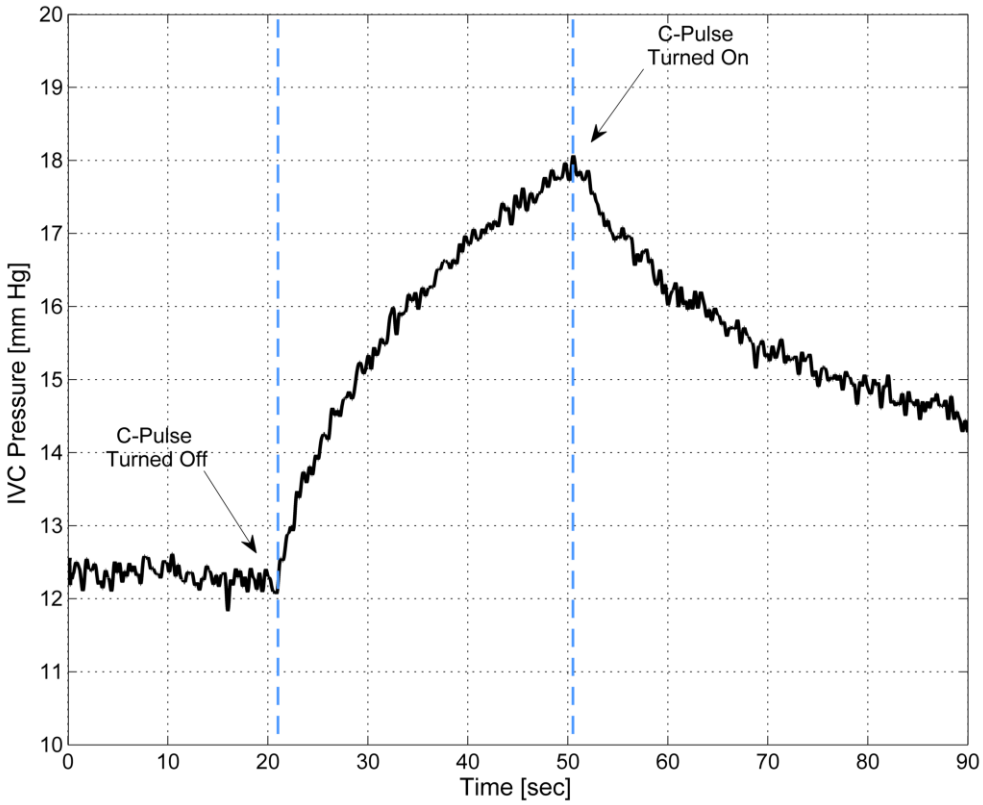

Figure 7-5. Inferior vena cava pressure response when the C-Pulse cuff (Sunshine Heart Inc.) is turned on, turned off, and turned on again

Inferior vena cava pressure can be decreased to values associated with non-hypertensive Fontan patients when the C-Pulse is coupled with two valves and a large inflation volume and high compression rates are used (Figure 7-6). The steady-state IVC pressure is sensitive to the tube compression rate, the number of valves, and the location of the valves (summarized in Table 7-2). Without the use of valves, the IVC pressure increases as a result of vessel occlusion without unidirectional flow. When one valve is placed after the C-Pulse, there was a minimal drop in the IVC pressure from 18 mmHg to 17.5 mmHg. When one valve is placed before the compression device, the IVC pressure drops from 18 mmHg to 15.5 mmHg. When two valves are used and when using an 8 cc balloon inflation volume, the IVC pressure decreases linearly with increasing compression rate from 18.1 mmHg to 11 mmHg. For a 13 cc inflation volume, the IVC pressure decreases linearly from 18.1 mmHg to 8.5 mmHg with increasing compression rate. By increasing the compression rate and the stroke volume (modulated by the inflation volume), the IVC pressure can be decreased by virtue of the volume shift from the vena cava to the left atrial reservoir. Consequentially, the magnitude of IVC pressure reduction is increased as the amount of flow return to the left atrium approaches the cardiac output of the single ventricle.

Table 7-2. Comparison of Assisted and Unassisted Fontan Mock Circulation

	Non-Fontan (Clinical)	Hypertensive Fontan (Mock Circulation)	C-Pulse Assist* (Valve after)	C-Pulse Assist* (Valve before)	C-Pulse Assist* (2 Valves)
IVCP (mmHg)	4.3	21.5	17.5	15.5	8.5

* All Fontan assist listed used 13cc C-Pulse inflation volume, IVCP – Inferior Vena Cava Pressure

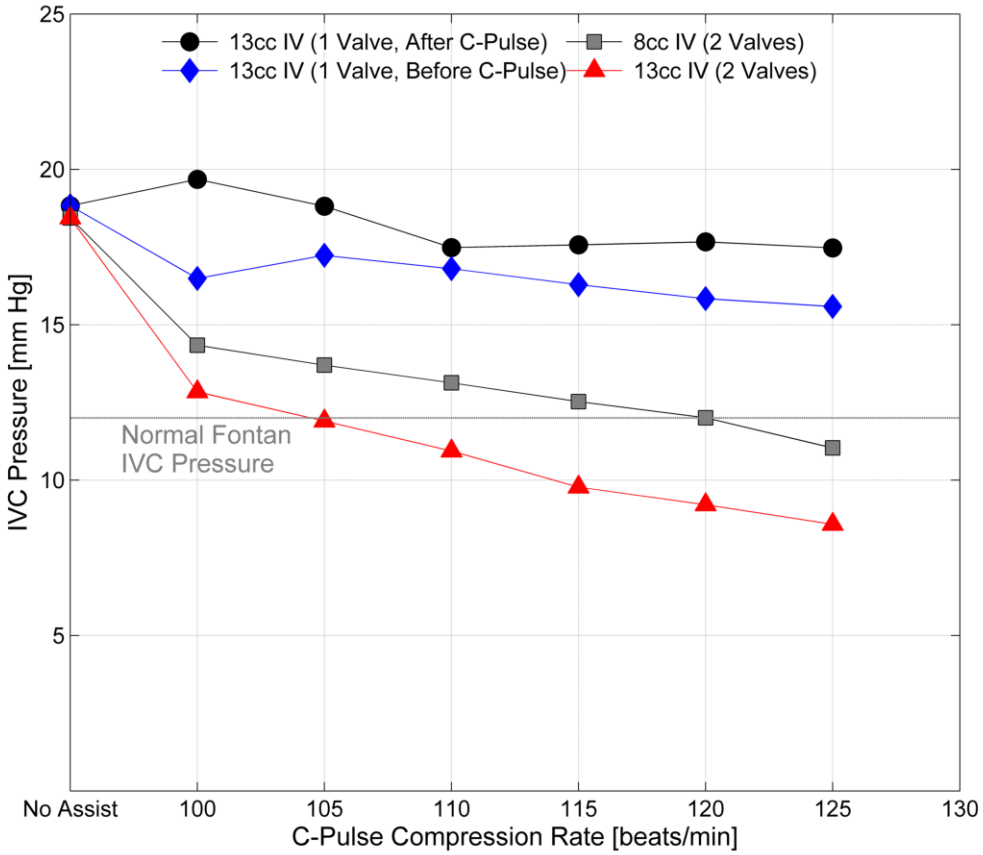

Figure 7-6. Steady state inferior vena cava (IVC) pressure at various C-Pulse compression

Pulmonary artery flow, representative of venous return to the single ventricle, can be increased when the C-Pulse is coupled with two valves and a large inflation volume and high compression rates are used (Figure 7-7). The pulmonary artery flow above the unassisted flow rate, plotted in Figure 7-7, is sensitive to the compression rate of the compressible tube. For increasing compression rates, the flow rate from the venous circulation to the left atrium increases but plateaus above 110 BPM. For an 8 cc inflation volume, 85 mL/min additional flow above the unassisted flow rate can be achieved when actuating the compressible tube at 125 BPM. This additional flow rate is approximately doubled, to 180 mL/min above the unassisted flow rate, when the inflation volume is increased from 8 cc to 13 cc. Additional flow return to

the left atrium plateaus above a compression rate of 110 BPM due to a subsequent increase in back pressure seen by the C-Pulse.

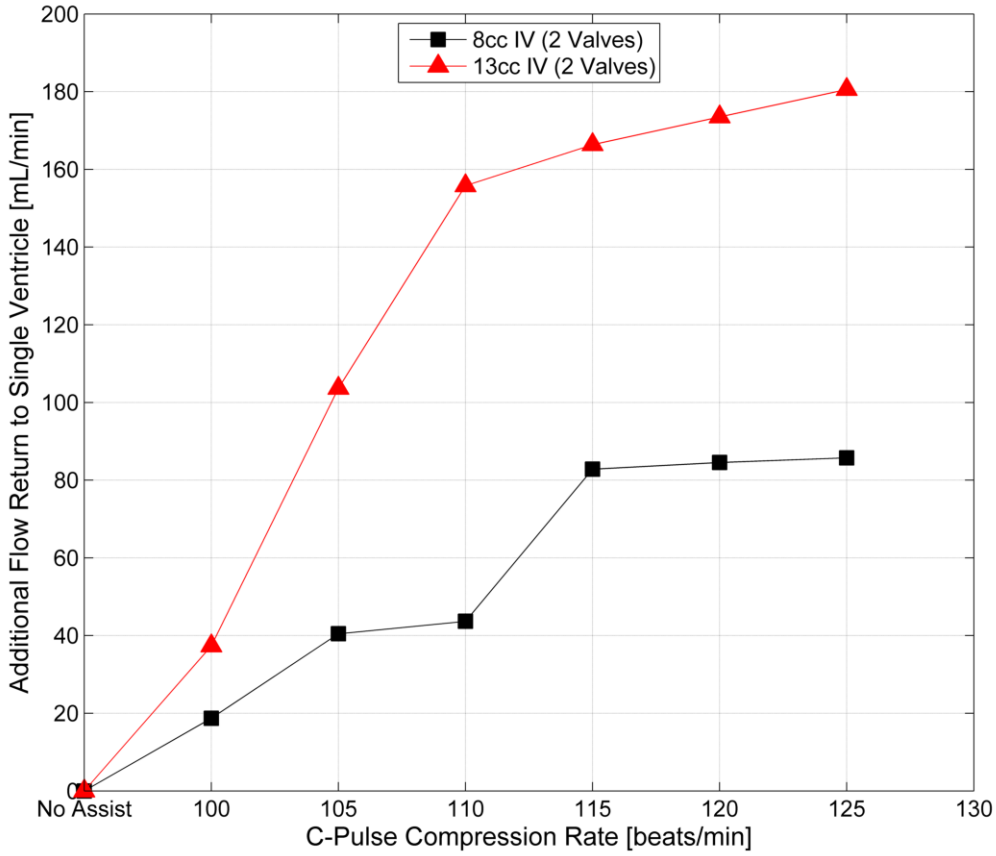

Figure 7-7. Augmented pulmonary artery (PA) flow above the non-assisted flow at various compression rates and for different cuff inflation volume (IV) during Fontan assistance

There exists a need for new technology to serve patients with hypertensive Fontan circulations [5]. Some of the limitations of existing devices include clotting and risk of infection. An external compression device coupled with valves could serve as a safe bridge-to-transplant for these patients. The data shown indicates that the use of external compression cuffs in Fontan applications has the potential to improve quality of life and reduce future risk of heart transplantation in many of these patients.

Using the C-pulse compression balloon and cuff in conjunction with two valves and a compressible tube, adds an artificial right ventricle in series with the single ventricle in Fontan circulations. This device has been shown to successfully "rescue" a failed Fontan circulation in vitro. As seen in the pulsatile waveforms (Figure 7-4C), the pulsatile flow rate in the pulmonary arterial branch mimics a functional right ventricle. While the need for pulsatile flow through the lungs is debated [28], the results from Figure 4 show that the flow and pressure generated by the C-Pulse mimics the flow and pressure of a native right heart. Although most Fontan patients survive with non-pulsatile venous flow to the lungs, it is possible that pulsatile pressure from the C-Pulse may help ensure that additional pulmonary capillaries are recruited, leading to improved pulmonary perfusion and improved pulmonary vascular resistance (PVR) [29].

The Sunshine C-Pulse can potentially reduce central venous pressure by matching the amount of Fontan assistance with single ventricle cardiac output and shifting blood volume from the IVC back to the atrium (Figure 7-5). Because of high venous compliance compared to the systemic and pulmonary compliance, the removal of Fontan assistance shifts the blood volume back to the IVC and SVC. An increase in the single ventricle cardiac output would necessitate a flow match from the right/pulmonary side in order to keep the IVC pressure low (Figures 7-6 and 7-7)**.** By increasing the stroke volume and compression rate of the device, IVC pressure can be reduced and additional flow can be returned to the single ventricle. Ideally, utilizing two valves increases the volumetric efficiency of Fontan assistance (Figure 7-6). If one valve is used, placing it before the compression device can lead to better flow return to the left atrium than if it was placed after the device. A non-valved conduit was deemed to be a non-viable option for the design of our external compression device.

Use of the C-pulse may be clinically advantageous when compared to current VADs. The risk of bleeding and thrombosis is potentially lower than in current VADs because the amount of foreign material contacting the blood, namely the valves and the graft, is less than in other VADs [22]. Because the C-Pulse device is external to the vasculature, access for implantation, maintenance, and removal are potentially simplified. While using two valves in this device may increase the overall risk for thrombosis, the hemodynamic advantages of both valves are clear (Figure 7-6). Incorporation of valves may also lead to increased resistance and potential occlusion in a Fontan circuit. This is detrimental since vessel constriction can further increase elevated PVR in Fontan patients. While the ultimate success of this device will rely on valve longevity, dysfunctional valves can be replaced with transcatheter valves without the need for invasive surgical intervention. A vascular graft, like a GORETEX® vascular graft, can be used as the compressible tube. Further studies need to be carried out to characterize the importance of graft compliance and elasticity. In practice, it would be ideal to wrap the C-pulse cuff around an extracardiac Fontan. Thus, future research should address how the C-Pulse and valves can be placed to benefit patients with existing TCPC and extracardiac Fontans.

Accurately modeling the Fontan circulation on a bench-top is critical for studying hypertensive hemodynamics with the purpose of developing devices that improve outcomes. However, bench-top circulations have various limitations that keep them from accurately mimicking patient hemodynamics. For example, the mechanical pulsatile pump that mimics the left ventricle maintains a constant mean flow regardless of the filling pressure in the atrial reservoir. This is not representative of the Frank-Starling mechanism seen in native hearts. As a result, the mock circulation does not accurately model the complex relationship between cardiac output and venous return. This mechanism can have significant implications on the effectiveness

of this type of assistance [30]. Additionally, the effects of respiration and patient position on vena cava hemodynamics are not taken into account. The flow profiles associated with this type of compression assistance were not studied. Since the local flow profiles and associated shear stresses in the vasculature dictate the risk of thrombosis [31], future studies should take the geometrical anatomy and fluid dynamics of compression into consideration. Lastly, in vivo animal studies with hypertensive Fontan hemodynamics are needed to confirm bench data and to study the durability of grafts under intermittent compression.

7.4 Summary

The Sunshine C-Pulse Heart Assist System can be used as a non-blood contacting Fontan assist device. A bench-top model of a hypertensive Fontan circulation was developed to accurately mimic the systemic and pulmonary flows as well as the pressures of a pediatric patient. In Fontan assistance, the C-Pulse device was able to provide pulsatile pulmonary flow through the lungs when used in conjunction with two valves. In addition, the C-Pulse was able to provide up to 180 mL/min of extra venous return while decompressing the IVC pressure. By using two valves and increasing compression rate and compression balloon inflation volume, the IVC pressure was reduced from 18 mmHg to below 12 mmHg. With a 125 BPM compression rate and 13 cc inflation volume an IVC pressure of 8.5 mmHg was achieved. These results show that the Sunshine C-Pulse should be investigated further as a potential Fontan assist device.

Conclusion

Piezohydraulic pumps offer the potential to miniaturize the drivers for pediatric pulsatile blood pump drivers when operated at high frequencies. This technology has been successfully used in the mechanical and aerospace industry in compact unmanned aerial vehicles and automotive break transmission. In this dissertation a few key contributions to the field of mechanical circulatory support and smart materials have been achieved. First, the first feasibility study utilizing a commercially available piezohydraulic pump from Kinetic Ceramics Inc. was used to drive a clinical FDA approved pulsatile blood pump (Berlin Heart EXCOR). The study, covered in Chapter 4, demonstrated that piezohydraulic pumps, even when impedance mismatched, could lead to drivers the same size as current electro-pneumatic consoles.

Second, the groundwork for developing a compact piezohydraulic pump designed specifically for a pediatric blood pump was presented. The various factors affecting the power transmission from piezoelectric stack to pediatric circulation were detailed. Specifically, the optimal stiffener and chamber dimensions were elucidated. We also demonstrated that the resonance and acoustic reflections in the external hydraulic circuit connected to the piezoelectric pump could be a limiting factor in operating the piezohydraulic pump at high frequencies. The fluidic phenomena however can be beneficial if the hydraulic circuit is designed to operate within a narrow bandwidth. The final product was a 8.1 W/kg pump with a 3.5% efficiency.

This research also described the design of the first piezohydraulically actuated blood pump and the first compact pediatric driver for a 25 mL blood pump. The driver was able to output physiologic pressure ranging between 60-90 mm Hg. It was also able to impart 1 L/min flow rate in a mock circulation mimicking the circulation of a pediatric patient. Improvements with the flow rate need to be explored. However, this dissertation has laid the groundwork for

achieving compact pediatric blood pump drivers to increase the mobility of children waiting bridge-to-transplantation.

Lastly, this dissertation researched the use of a novel non-blood contacting ventricular assist device for use in patients with the Fontan circulation. The results showed that this device could deliver pulsatile blood flow to the pulmonary circulation as well as maintain low inferior vena cava pressure, which are problems that plague these patients. It demonstrates the use of the first minimally invasive device for the Fontan patient population.

APPENDIX A: Piezohydraulic Pump Drawings

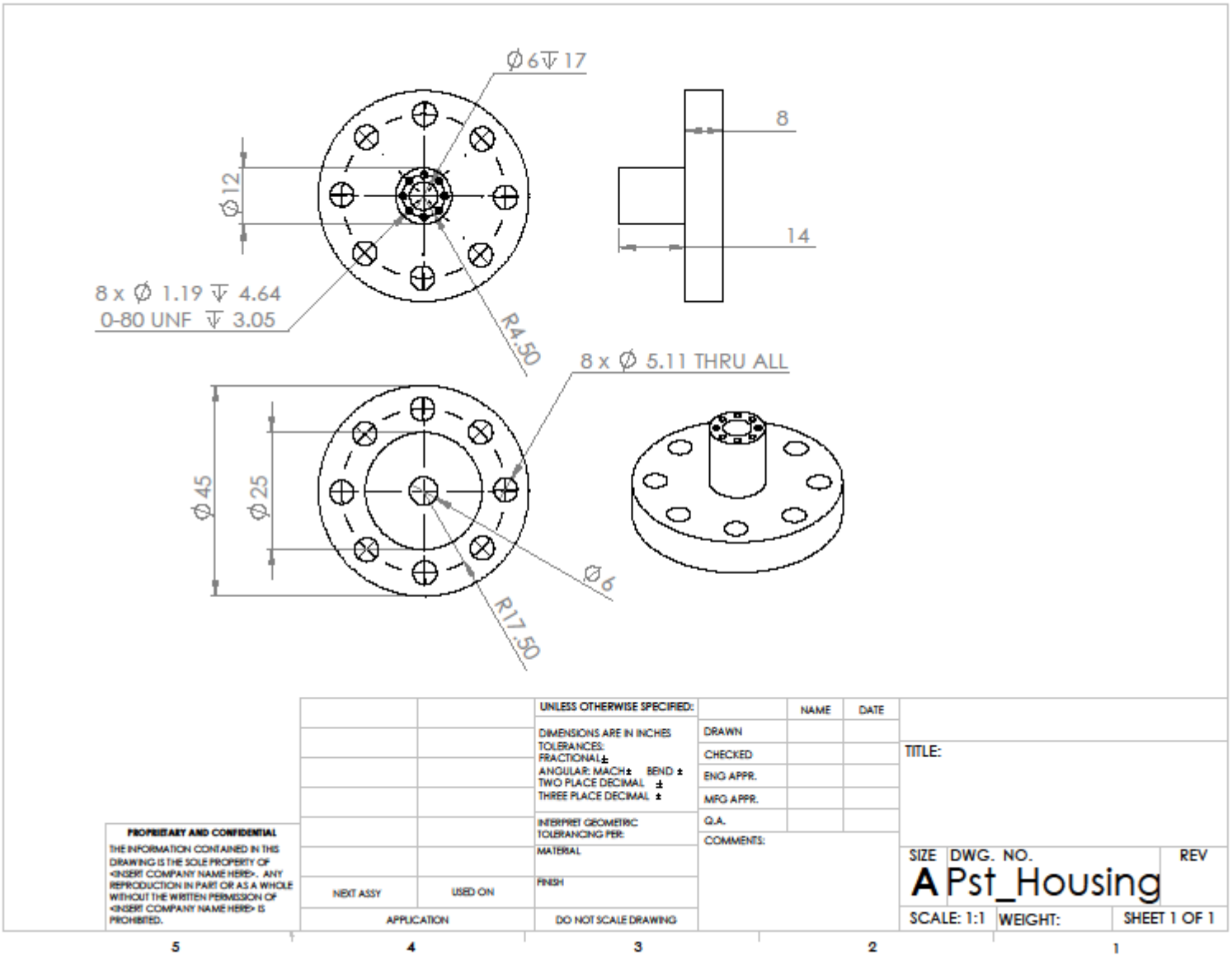

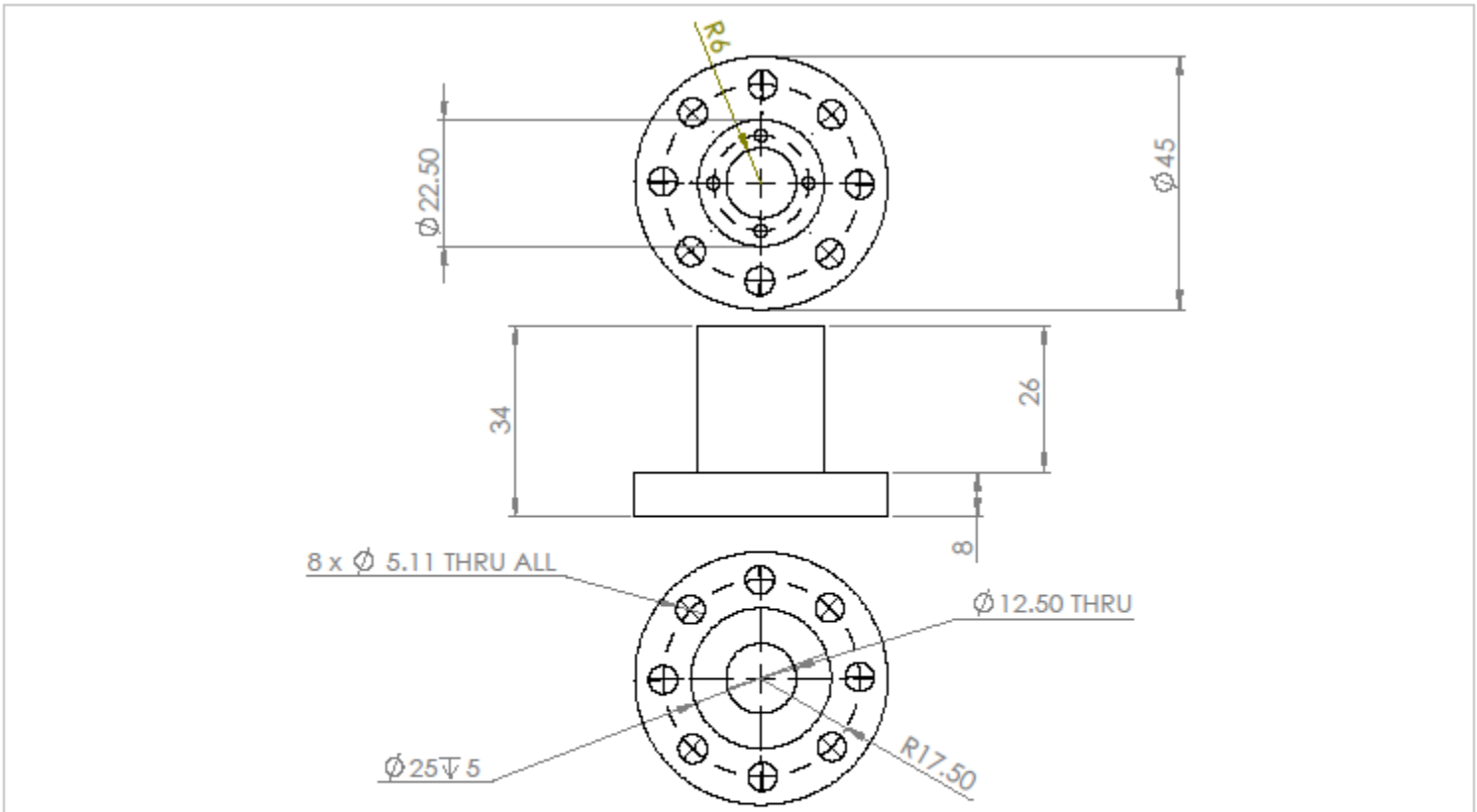

		UNLESS OTHERWISE SPECIFIED:		NAME	DATE
		DIMENSIONS ARE IN INCHES TOLERANCES: FRACTIONAL ± ANGULAR: MACH ± BEND ± TWO PLACE DECIMAL ± THREE PLACE DECIMAL ±	DRAWN		
			CHECKED		
			ENG APPR.		
			MFG APPR.		
		INTERPRET GEOMETRIC TOLERANCING PER:	Q.A.		
		MATERIAL	COMMENTS:		
NEXT ASSY	USED ON	FINISH			
APPLICATION		DO NOT SCALE DRAWING			

PROPRIETARY AND CONFIDENTIAL

THE INFORMATION CONTAINED IN THIS DRAWING IS THE SOLE PROPERTY OF <INSERT COMPANY NAME HERE>. ANY REPRODUCTION IN PART OR AS A WHOLE WITHOUT THE WRITTEN PERMISSION OF <INSERT COMPANY NAME HERE> IS PROHIBITED.

TITLE:

MiniPHPA_Housing_LargerSt

SIZE	DWG. NO.	REV
A		
SCALE: 1:1	WEIGHT:	SHEET 1 OF 1

5 4 3 2 1

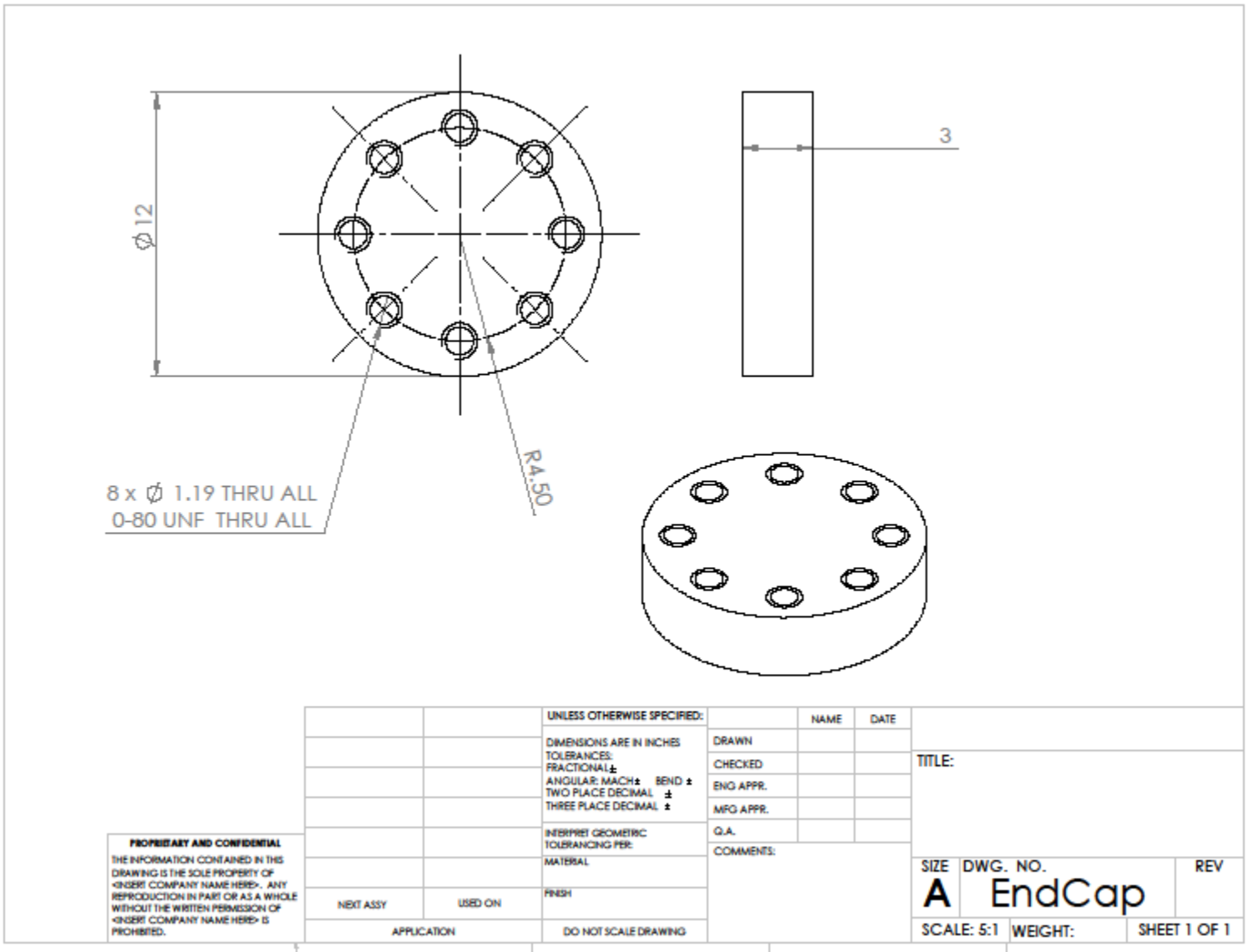

		UNLESS OTHERWISE SPECIFIED:		NAME	DATE
		DIMENSIONS ARE IN INCHES	DRAWN		
		TOLERANCES: FRACTIONAL ±	CHECKED		
		ANGULAR: MACH ± BEND ±	ENG APPR.		
		TWO PLACE DECIMAL ±	MFG APPR.		
		THREE PLACE DECIMAL ±	Q.A.		
		INTERPRET GEOMETRIC TOLERANCING PER:	COMMENTS:		
		MATERIAL			
NEXT ASSY	USED ON	FINISH			
APPLICATION		DO NOT SCALE DRAWING			

TITLE:

SIZE A | DWG. NO. EndCap | REV

SCALE: 5:1 | WEIGHT: | SHEET 1 OF 1

PROPRIETARY AND CONFIDENTIAL

THE INFORMATION CONTAINED IN THIS DRAWING IS THE SOLE PROPERTY OF <INSERT COMPANY NAME HERE>. ANY REPRODUCTION IN PART OR AS A WHOLE WITHOUT THE WRITTEN PERMISSION OF <INSERT COMPANY NAME HERE> IS PROHIBITED.

5 4 3 2 1

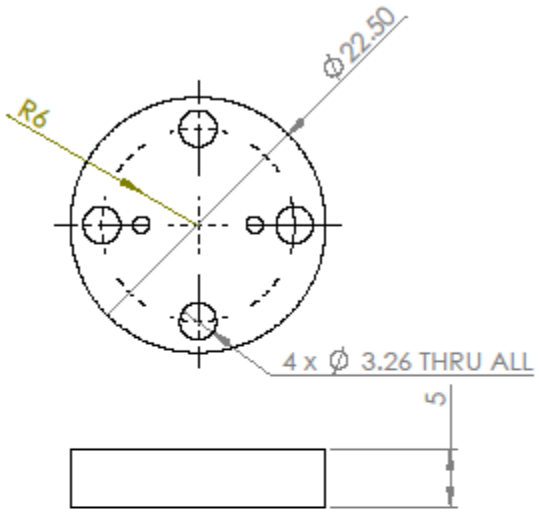

		UNLESS OTHERWISE SPECIFIED:		NAME	DATE
		DIMENSIONS ARE IN INCHES TOLERANCES: FRACTIONAL ± ANGULAR: MACH ± BEND ± TWO PLACE DECIMAL ± THREE PLACE DECIMAL ±	DRAWN		
			CHECKED		
			ENG APPR.		
			MFG APPR.		
		INTERPRET GEOMETRIC TOLERANCING PER:	Q.A.		
		MATERIAL	COMMENTS:		
NEXT ASSY	USED ON	FINISH			
APPLICATION		DO NOT SCALE DRAWING			

PROPRIETARY AND CONFIDENTIAL

THE INFORMATION CONTAINED IN THIS DRAWING IS THE SOLE PROPERTY OF <INSERT COMPANY NAME HERE>. ANY REPRODUCTION IN PART OR AS A WHOLE WITHOUT THE WRITTEN PERMISSION OF <INSERT COMPANY NAME HERE> IS PROHIBITED.

TITLE:

SIZE	DWG. NO.	REV
A	MiniPHPA_EndCap_LargeSto	
SCALE: 2:1	WEIGHT:	SHEET 1 OF 1

5 4 3 2 1

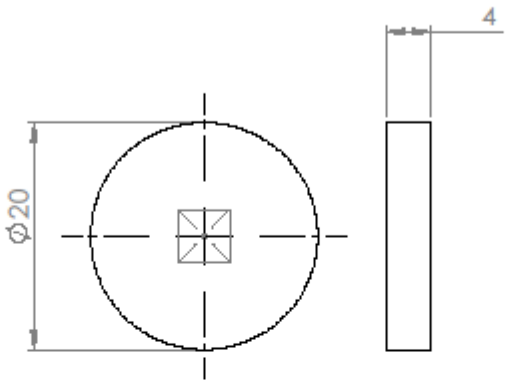

		UNLESS OTHERWISE SPECIFIED:		NAME	DATE
		DIMENSIONS ARE IN INCHES TOLERANCES: FRACTIONAL ± ANGULAR: MACH ± BEND ± TWO PLACE DECIMAL ± THREE PLACE DECIMAL ±	DRAWN		
			CHECKED		
			ENG APPR.		
			MFG APPR.		
		INTERPRET GEOMETRIC TOLERANCING PER:	Q.A.		
		MATERIAL	COMMENTS:		
NEXT ASSY	USED ON	FINISH			
APPLICATION		DO NOT SCALE DRAWING			

PROPRIETARY AND CONFIDENTIAL

THE INFORMATION CONTAINED IN THIS DRAWING IS THE SOLE PROPERTY OF <INSERT COMPANY NAME HERE>. ANY REPRODUCTION IN PART OR AS A WHOLE WITHOUT THE WRITTEN PERMISSION OF <INSERT COMPANY NAME HERE> IS PROHIBITED.

TITLE:

SIZE	DWG. NO.	REV
A	Stiffener_Piston	
SCALE: 2:1	WEIGHT:	SHEET 1 OF 1

5 4 3 2 1

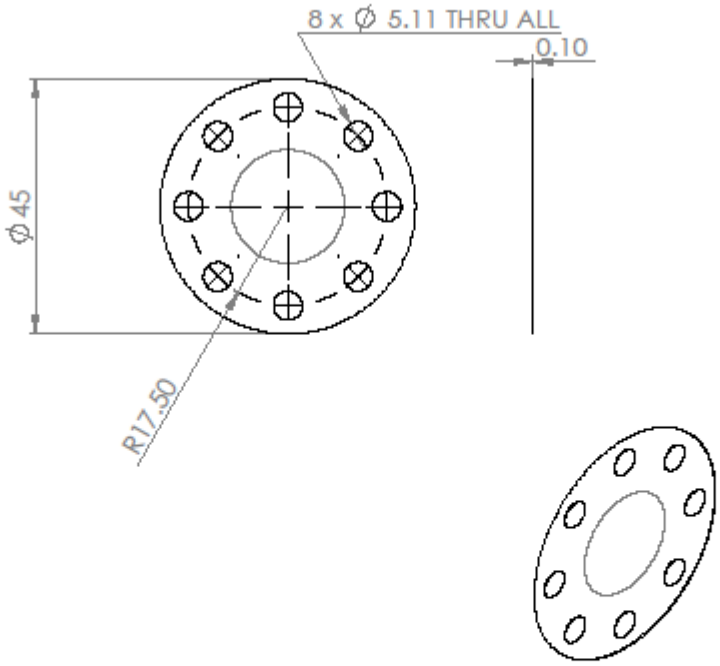

		UNLESS OTHERWISE SPECIFIED:		NAME	DATE
		DIMENSIONS ARE IN INCHES TOLERANCES: FRACTIONAL ± ANGULAR: MACH ± BEND ± TWO PLACE DECIMAL ± THREE PLACE DECIMAL ±	DRAWN		
			CHECKED		
			ENG APPR.		
			MFG APPR.		
			Q.A.		
		INTERPRET GEOMETRIC TOLERANCING PER:	COMMENTS:		
		MATERIAL			
NEXT ASSY	USED ON	FINISH			
APPLICATION		DO NOT SCALE DRAWING			

PROPRIETARY AND CONFIDENTIAL

THE INFORMATION CONTAINED IN THIS DRAWING IS THE SOLE PROPERTY OF <INSERT COMPANY NAME HERE>. ANY REPRODUCTION IN PART OR AS A WHOLE WITHOUT THE WRITTEN PERMISSION OF <INSERT COMPANY NAME HERE> IS PROHIBITED.

TITLE:

SIZE	DWG. NO.	REV
A	Diaphragm	
SCALE: 1:1	WEIGHT:	SHEET 1 OF 1

5 4 3 2 1

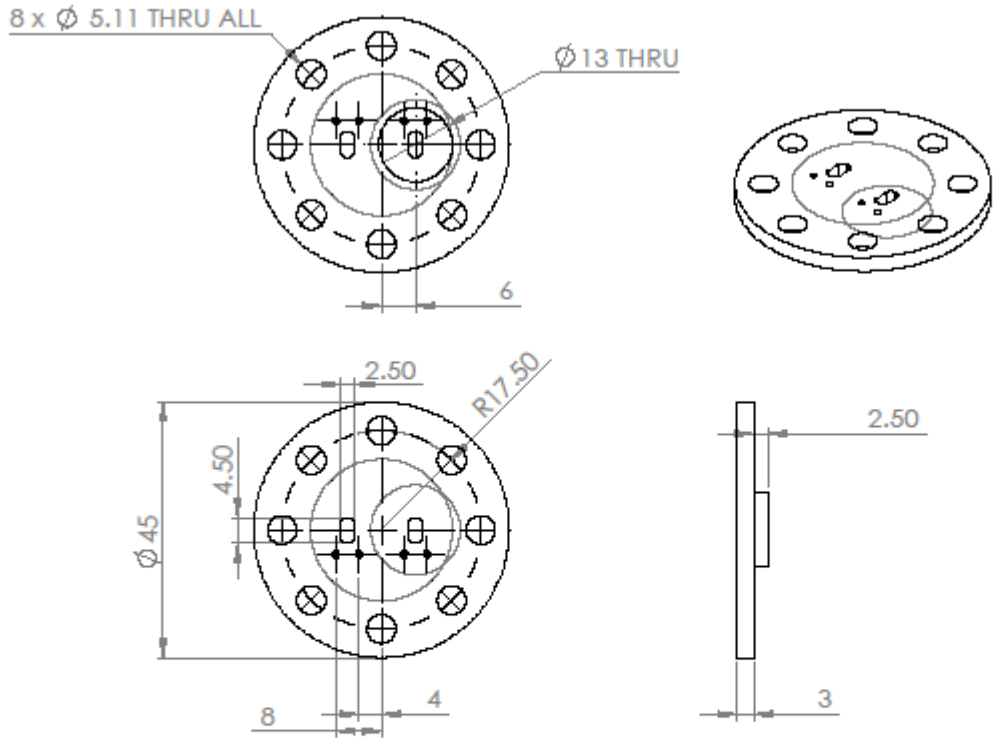

		UNLESS OTHERWISE SPECIFIED:		NAME	DATE
		DIMENSIONS ARE IN INCHES TOLERANCES: FRACTIONAL ± ANGULAR: MACH ± BEND ± TWO PLACE DECIMAL ± THREE PLACE DECIMAL ±	DRAWN		
			CHECKED		
			ENG APPR.		
			MFG APPR.		
		INTERPRET GEOMETRIC TOLERANCING PER:	Q.A.		
		MATERIAL	COMMENTS:		
NEXT ASSY	USED ON	FINISH			
APPLICATION		DO NOT SCALE DRAWING			

PROPRIETARY AND CONFIDENTIAL

THE INFORMATION CONTAINED IN THIS DRAWING IS THE SOLE PROPERTY OF <INSERT COMPANY NAME HERE>. ANY REPRODUCTION IN PART OR AS A WHOLE WITHOUT THE WRITTEN PERMISSION OF <INSERT COMPANY NAME HERE> IS PROHIBITED.

TITLE:

SIZE	DWG. NO.	REV
A	ValveSeat_Final	
SCALE: 1:1	WEIGHT:	SHEET 1 OF 1

5 4 3 2 1

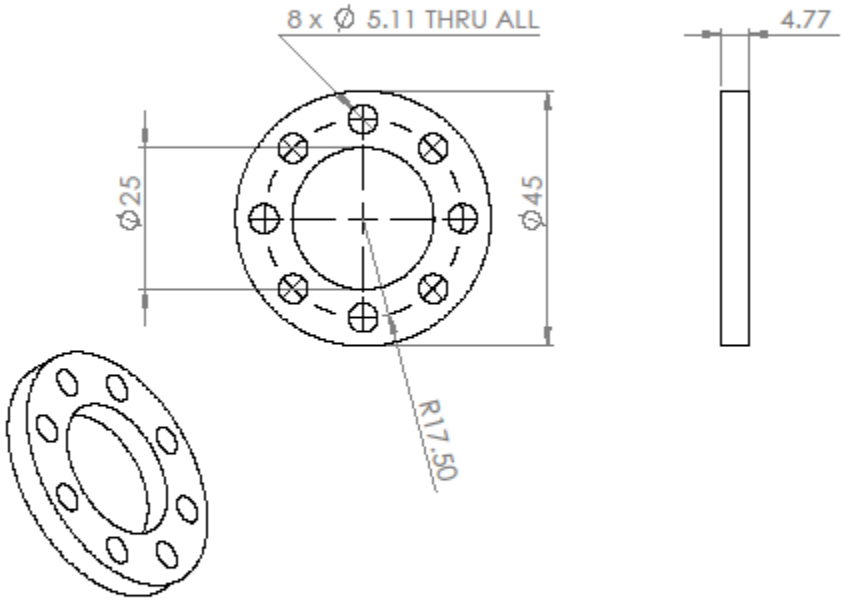

		UNLESS OTHERWISE SPECIFIED:		NAME	DATE
		DIMENSIONS ARE IN INCHES TOLERANCES: FRACTIONAL ± ANGULAR: MACH ± BEND ± TWO PLACE DECIMAL ± THREE PLACE DECIMAL ±	DRAWN		
			CHECKED		
			ENG APPR.		
			MFG APPR.		
		INTERPRET GEOMETRIC TOLERANCING PER:	Q.A.		
		MATERIAL	COMMENTS:		
NEXT ASSY	USED ON	FINISH			
APPLICATION		DO NOT SCALE DRAWING			

PROPRIETARY AND CONFIDENTIAL

THE INFORMATION CONTAINED IN THIS DRAWING IS THE SOLE PROPERTY OF <INSERT COMPANY NAME HERE>. ANY REPRODUCTION IN PART OR AS A WHOLE WITHOUT THE WRITTEN PERMISSION OF <INSERT COMPANY NAME HERE> IS PROHIBITED.

TITLE:

SIZE	DWG. NO.	REV
	ChamberSpacer	
SCALE: 1:1	WEIGHT:	SHEET 1 OF 1

5 4 3 2 1

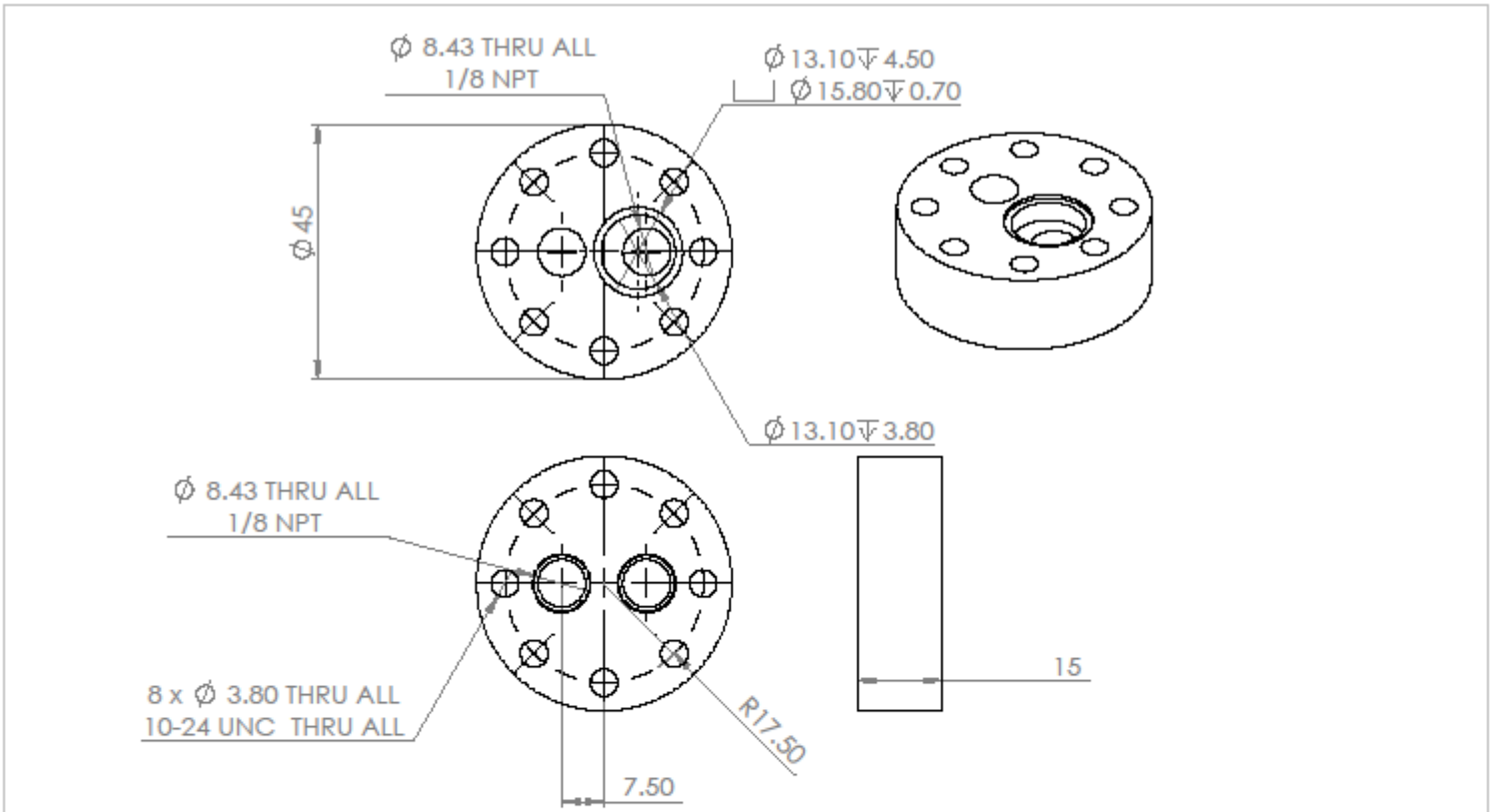

		UNLESS OTHERWISE SPECIFIED:		NAME	DATE
		DIMENSIONS ARE IN INCHES	DRAWN		
		TOLERANCES: FRACTIONAL ±	CHECKED		
		ANGULAR: MACH ± BEND ±	ENG APPR.		
		TWO PLACE DECIMAL ±	MFG APPR.		
		THREE PLACE DECIMAL ±	Q.A.		
		INTERPRET GEOMETRIC TOLERANCING PER:	COMMENTS:		
		MATERIAL			
NEXT ASSY	USED ON	FINISH			
APPLICATION		DO NOT SCALE DRAWING			

PROPRIETARY AND CONFIDENTIAL
THE INFORMATION CONTAINED IN THIS DRAWING IS THE SOLE PROPERTY OF <INSERT COMPANY NAME HERE>. ANY REPRODUCTION IN PART OR AS A WHOLE WITHOUT THE WRITTEN PERMISSION OF <INSERT COMPANY NAME HERE> IS PROHIBITED.

TITLE:

SIZE	DWG. NO.	REV
A	PortEnd	
SCALE: 1:1	WEIGHT:	SHEET 1 OF 1

5 4 3 2 1

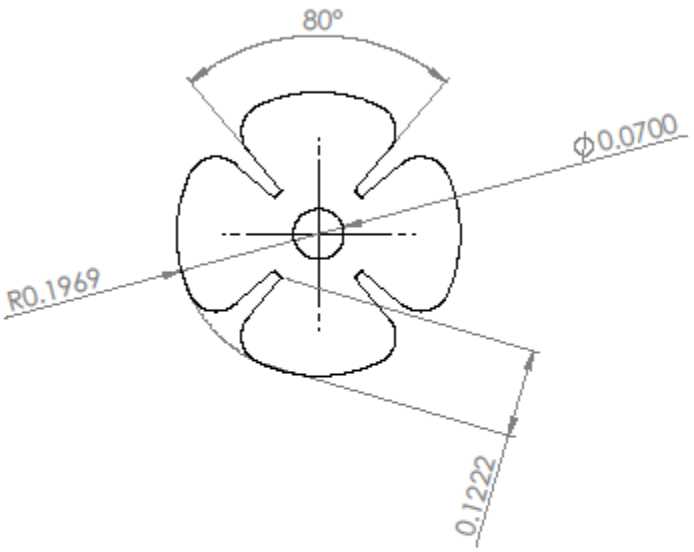

		UNLESS OTHERWISE SPECIFIED:		NAME	DATE
		DIMENSIONS ARE IN INCHES TOLERANCES: FRACTIONAL ± ANGULAR: MACH ± BEND ± TWO PLACE DECIMAL ± THREE PLACE DECIMAL ±	DRAWN		
			CHECKED		
			ENG APPR.		
			MFG APPR.		
		INTERPRET GEOMETRIC TOLERANCING PER:	Q.A.		
		MATERIAL	COMMENTS:		
NEXT ASSY	USED ON	FINISH			
APPLICATION		DO NOT SCALE DRAWING			

PROPRIETARY AND CONFIDENTIAL

THE INFORMATION CONTAINED IN THIS DRAWING IS THE SOLE PROPERTY OF <INSERT COMPANY NAME HERE>. ANY REPRODUCTION IN PART OR AS A WHOLE WITHOUT THE WRITTEN PERMISSION OF <INSERT COMPANY NAME HERE> IS PROHIBITED.

TITLE:

SIZE	DWG. NO.	REV
A	MiniRHP_ValveUpdate	
SCALE: 1:1	WEIGHT:	SHEET 1 OF 1

5 4 3 2 1

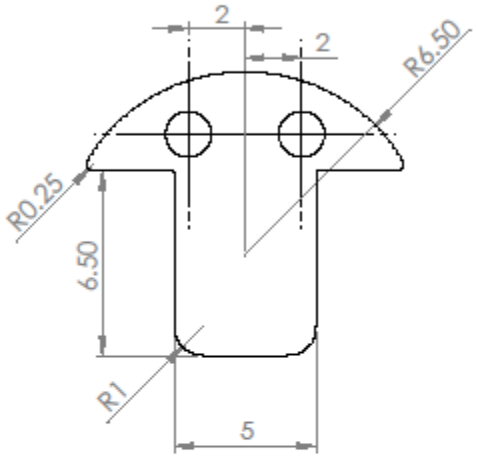

		UNLESS OTHERWISE SPECIFIED:		NAME	DATE
		DIMENSIONS ARE IN INCHES TOLERANCES: FRACTIONAL ± ANGULAR: MACH ± BEND ± TWO PLACE DECIMAL ± THREE PLACE DECIMAL ±	DRAWN		
			CHECKED		
			ENG APPR.		
			MFG APPR.		
			Q.A.		
		INTERPRET GEOMETRIC TOLERANCING PER:	COMMENTS:		
		MATERIAL			
NEXT ASSY	USED ON	FINISH			
APPLICATION		DO NOT SCALE DRAWING			

PROPRIETARY AND CONFIDENTIAL

THE INFORMATION CONTAINED IN THIS DRAWING IS THE SOLE PROPERTY OF <INSERT COMPANY NAME HERE>. ANY REPRODUCTION IN PART OR AS A WHOLE WITHOUT THE WRITTEN PERMISSION OF <INSERT COMPANY NAME HERE> IS PROHIBITED.

TITLE:

SIZE	DWG. NO.	REV
A	Valve	
SCALE: 5:1	WEIGHT:	SHEET 1 OF 1

5 4 3 2 1

APPENDIX B: Blood Pump Drawings

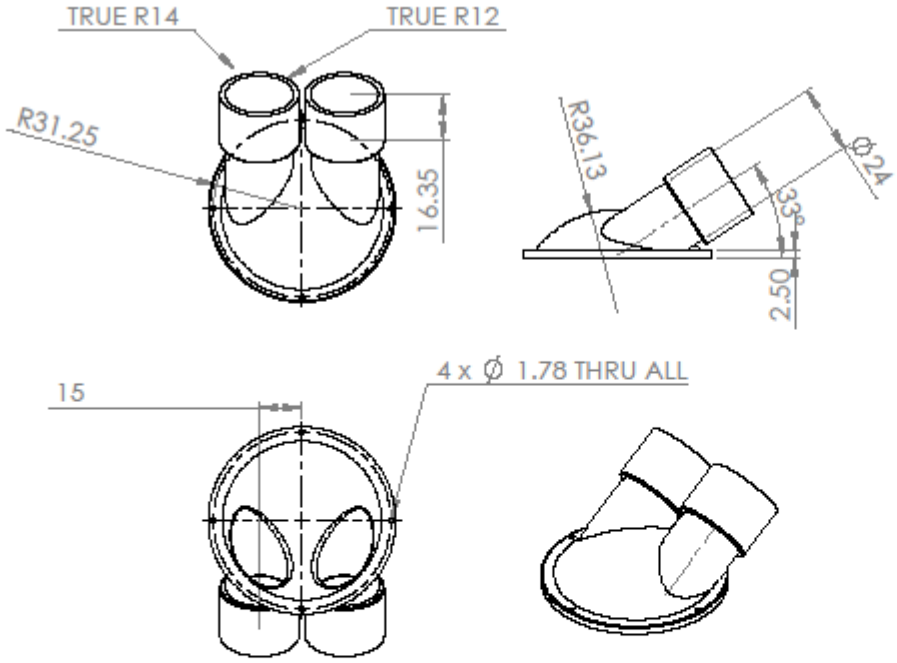

		UNLESS OTHERWISE SPECIFIED:		NAME	DATE
		DIMENSIONS ARE IN INCHES	DRAWN		
		TOLERANCES: FRACTIONAL ±	CHECKED		
		ANGULAR: MACH ± BEND ±	ENG APPR.		
		TWO PLACE DECIMAL ±	MFG APPR.		
		THREE PLACE DECIMAL ±	Q.A.		
		INTERPRET GEOMETRIC TOLERANCING PER:	COMMENTS:		
		MATERIAL			
NEXT ASSY	USED ON	FINISH			
APPLICATION		DO NOT SCALE DRAWING			

PROPRIETARY AND CONFIDENTIAL
THE INFORMATION CONTAINED IN THIS DRAWING IS THE SOLE PROPERTY OF <INSERT COMPANY NAME HERE>. ANY REPRODUCTION IN PART OR AS A WHOLE WITHOUT THE WRITTEN PERMISSION OF <INSERT COMPANY NAME HERE> IS PROHIBITED.

TITLE:

SIZE	DWG. NO.	REV
	Outer_CasingTop	
SCALE: 1:2	WEIGHT:	SHEET 1 OF 1

5 4 3 2 1

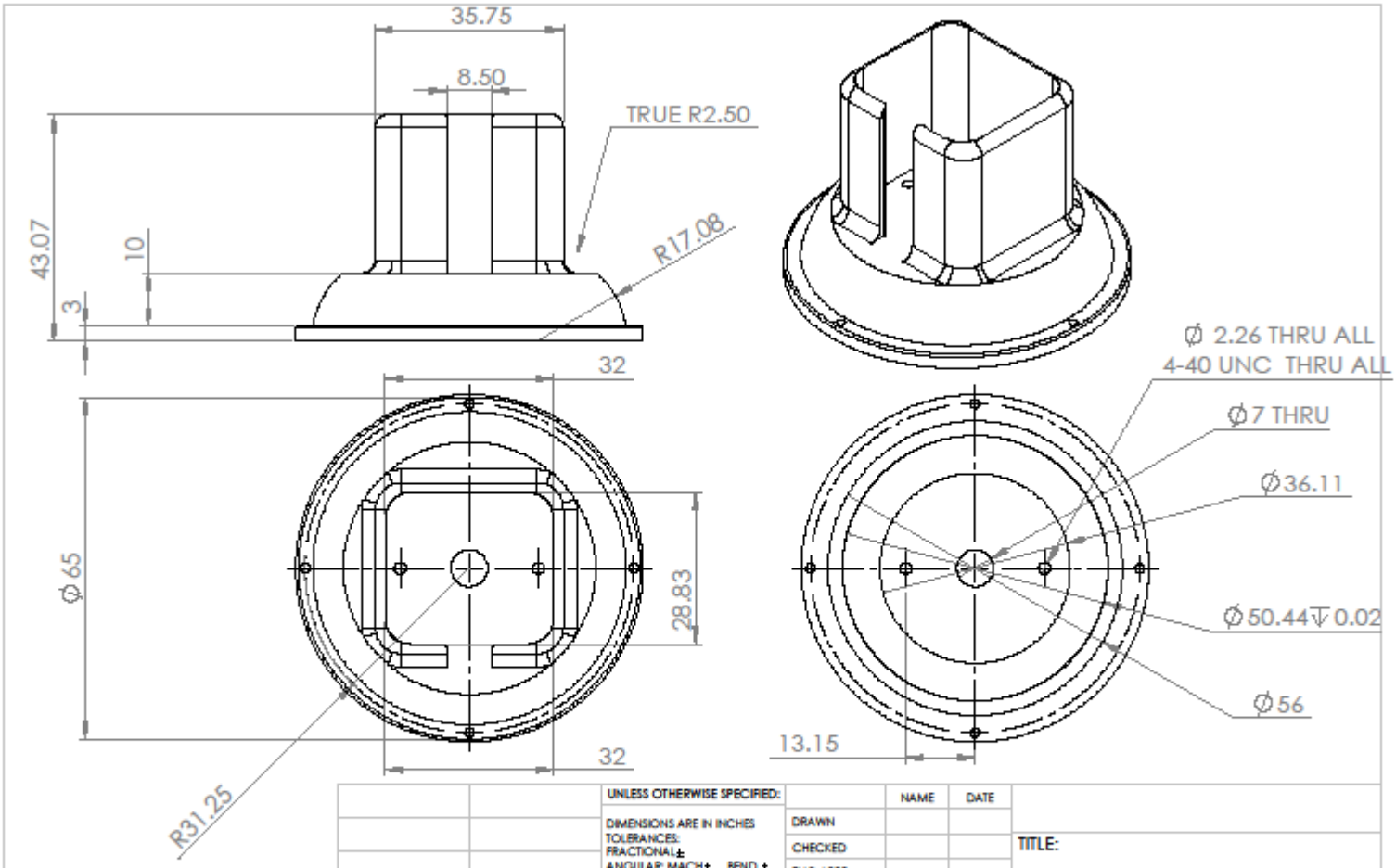

		UNLESS OTHERWISE SPECIFIED:		NAME	DATE
		DIMENSIONS ARE IN INCHES TOLERANCES: FRACTIONAL ± ANGULAR: MACH ± BEND ± TWO PLACE DECIMAL ± THREE PLACE DECIMAL ±	DRAWN		
			CHECKED		
			ENG APPR.		
			MFG APPR.		
			Q.A.		
		INTERPRET GEOMETRIC TOLERANCING PER:	COMMENTS:		
		MATERIAL			
NEXT ASSY	USED ON	FINISH			
APPLICATION		DO NOT SCALE DRAWING			

PROPRIETARY AND CONFIDENTIAL
THE INFORMATION CONTAINED IN THIS DRAWING IS THE SOLE PROPERTY OF <INSERT COMPANY NAME HERE>. ANY REPRODUCTION IN PART OR AS A WHOLE WITHOUT THE WRITTEN PERMISSION OF <INSERT COMPANY NAME HERE> IS PROHIBITED.

TITLE:

Outer_CasingBottom

SIZE	DWG. NO.	REV
A		
SCALE: 1:1	WEIGHT:	SHEET 1 OF 1

5 4 3 2 1

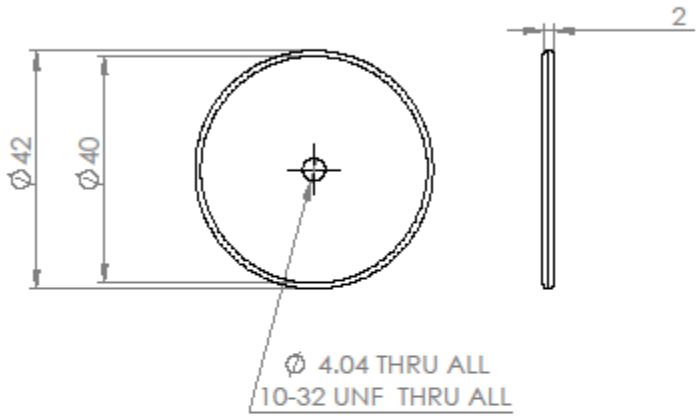

		UNLESS OTHERWISE SPECIFIED:		NAME	DATE
		DIMENSIONS ARE IN INCHES TOLERANCES: FRACTIONAL ± ANGULAR: MACH ± BEND ± TWO PLACE DECIMAL ± THREE PLACE DECIMAL ±	DRAWN		
			CHECKED		
			ENG APPR.		
			MFG APPR.		
			Q.A.		
		INTERPRET GEOMETRIC TOLERANCING PER:	COMMENTS:		
		MATERIAL			
NEXT ASSY	USED ON	FINISH			
APPLICATION		DO NOT SCALE DRAWING			

TITLE:

SIZE	DWG. NO.	REV
A	PusherPlate	
SCALE: 1:1	WEIGHT:	SHEET 1 OF 1

PROPRIETARY AND CONFIDENTIAL

THE INFORMATION CONTAINED IN THIS DRAWING IS THE SOLE PROPERTY OF <INSERT COMPANY NAME HERE>. ANY REPRODUCTION IN PART OR AS A WHOLE WITHOUT THE WRITTEN PERMISSION OF <INSERT COMPANY NAME HERE> IS PROHIBITED.

5 4 3 2 1

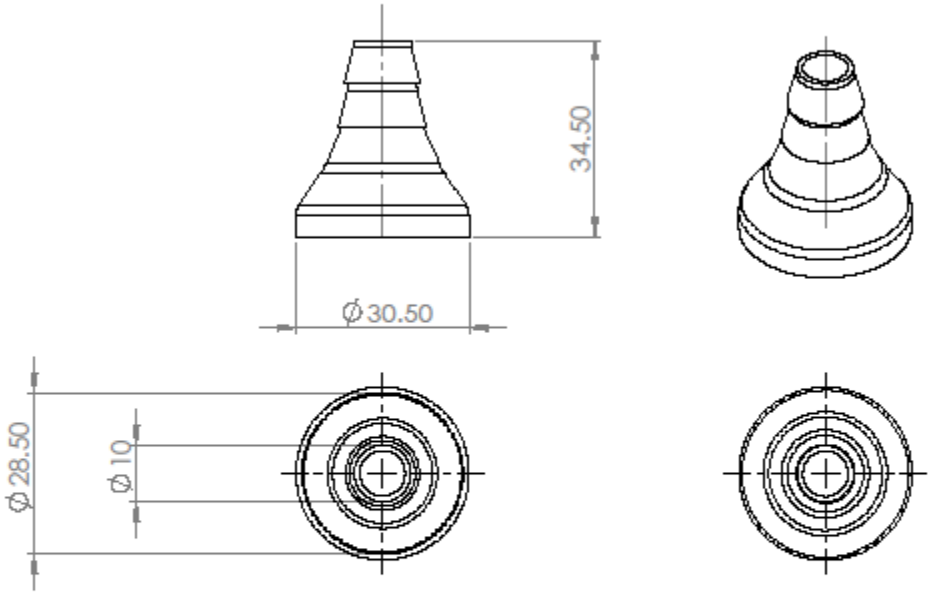

		UNLESS OTHERWISE SPECIFIED:		NAME	DATE
		DIMENSIONS ARE IN INCHES TOLERANCES: FRACTIONAL ± ANGULAR: MACH ± BEND ± TWO PLACE DECIMAL ± THREE PLACE DECIMAL ±	DRAWN		
			CHECKED		
			ENG APPR.		
			MFG APPR.		
		INTERPRET GEOMETRIC TOLERANCING PER:	Q.A.		
		MATERIAL	COMMENTS:		
NEXT ASSY	USED ON	FINISH			
APPLICATION		DO NOT SCALE DRAWING			

PROPRIETARY AND CONFIDENTIAL

THE INFORMATION CONTAINED IN THIS DRAWING IS THE SOLE PROPERTY OF <INSERT COMPANY NAME HERE>. ANY REPRODUCTION IN PART OR AS A WHOLE WITHOUT THE WRITTEN PERMISSION OF <INSERT COMPANY NAME HERE> IS PROHIBITED.

TITLE:

VAD_Cannula_Connectio

SIZE	DWG. NO.	REV
A		
SCALE: 1:1	WEIGHT:	SHEET 1 OF 1

5 4 3 2 1

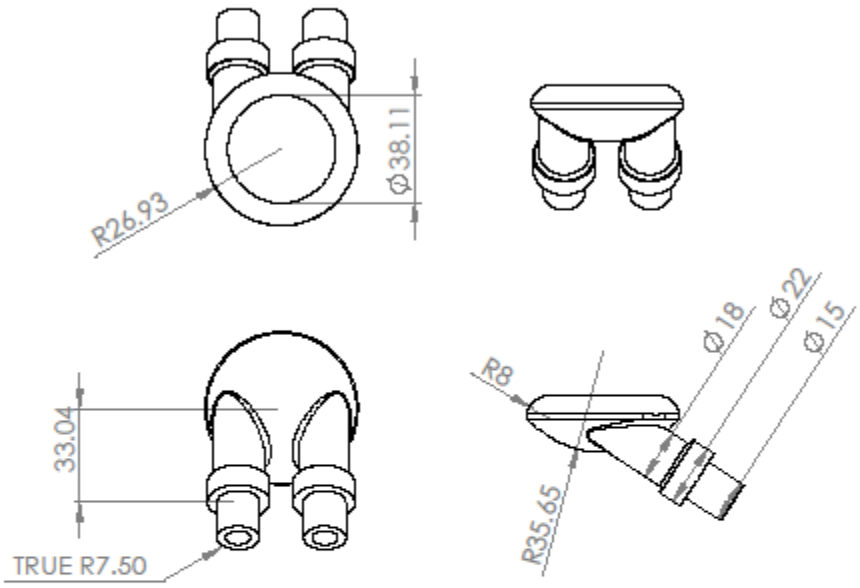

		UNLESS OTHERWISE SPECIFIED:		NAME	DATE
		DIMENSIONS ARE IN INCHES TOLERANCES: FRACTIONAL ± ANGULAR: MACH ± BEND ± TWO PLACE DECIMAL ± THREE PLACE DECIMAL ±	DRAWN		
			CHECKED		
			ENG APPR.		
			MFG APPR.		
		INTERPRET GEOMETRIC TOLERANCING PER:	Q.A.		
		MATERIAL	COMMENTS:		
NEXT ASSY	USED ON	FINISH			
APPLICATION		DO NOT SCALE DRAWING			

PROPRIETARY AND CONFIDENTIAL

THE INFORMATION CONTAINED IN THIS DRAWING IS THE SOLE PROPERTY OF <INSERT COMPANY NAME HERE>. ANY REPRODUCTION IN PART OR AS A WHOLE WITHOUT THE WRITTEN PERMISSION OF <INSERT COMPANY NAME HERE> IS PROHIBITED.

TITLE:

SIZE	DWG. NO.	REV
A	MOLD_PVAD	
SCALE: 1:2	WEIGHT:	SHEET 1 OF 1

5 4 3 2 1

BIBLIOGRAPHY

[1] S. E. Lipshultz, L. A. Sleeper, J. A. Towbin, A. M. Lowe, E. J. Orav, G. F. Cox, P. R. Lurie, K. L. McCoy, M. A. McDonald, J. E. Messere, and S. D. Colan, "The incidence of pediatric cardiomyopathy in two regions of the United States," *N. Engl. J. Med.*, vol. 348, no. 17, pp. 1647–1655, Apr. 2003.

[2] F. Fynn-Thompson and C. Almond, "Pediatric Ventricular Assist Devices," *Pediatr. Cardiol.*, vol. 28, no. 2, pp. 149–155, Jan. 2007.

[3] A. L. Throckmorton and S. G. Chopski, "Pediatric Circulatory Support: Current Strategies and Future Directions. Biventricular and Univentricular Mechanical Assistance," *ASAIO J.*, vol. 54, no. 5, pp. 491–497, Sep. 2008.

[4] J. T. Baldwin, H. S. Borovetz, B. W. Duncan, M. J. Gartner, R. K. Jarvik, W. J. Weiss, and T. R. Hoke, "The national heart, lung, and blood institute pediatric circulatory support program," *Circulation*, vol. 113, no. 1, pp. 147–155, 2006.

[5] J. E. Reedy, M. T. Swartz, D. P. Lohmann, D. A. Moroney, K. J. Vaca, L. R. McBride, and D. G. Pennington, "The importance of patient mobility with ventricular assist device support," *ASAIO J. Am. Soc. Artif. Intern. Organs 1992*, vol. 38, no. 3, pp. M151–153, Sep. 1992.

[6] G. A. Giridharan, T. J. Lee, M. Ising, M. A. Sobieski, S. C. Koenig, L. A. Gray, and M. S. Slaughter, "Miniaturization of Mechanical Circulatory Support Systems," *Artif. Organs*, vol. 36, no. 8, pp. 731–739, 2012.

[7] D. Joyce, L. Joyce, and M. Locke, *Mechanical Circulatory Support: Principles and Applications*, 1st ed. McGraw-Hill Professional, 2011.

[8] K. Uchino, "Piezoelectric ultrasonic motors: overview," *Smart Mater. Struct.*, vol. 7, pp. 273–285, 1998.

[9] T. Galante, J. Frank, J. Bernard, W. Chen, G. A. Lesieutre, and G. H. Koopmann, "Design, Modeling, and Performance of a High Force Piezoelectric Inchworm Motor," *J. Intell. Mater. Syst. Struct.*, vol. 10, no. 12, pp. 962–972, Dec. 1999.

[10] D. J. Leo, *Engineering Analysis of Smart Material Systems*. Wiley, 2007.

[11] B. Koc, A. Dogan, Y. Xu, R. E. Newnham, and K. Uchino, "An Ultrasonic Motor Using a Metal-Ceramic Composite Actuator Generating Torsional Displacement," *Jpn. J. Appl. Phys.*, vol. 37, no. Part 1, No. 10, pp. 5659–5662, Oct. 1998.

[12] S. Cagatay, B. Koc, and K. Uchino, "A 1.6-mm, metal tube ultrasonic motor," *IEEE Trans. Ultrason. Ferroelectr. Freq. Control*, vol. 50, no. 7, pp. 782–786, Jul. 2003.

[13] N. W. Hagood, D. C. Roberts, L. Saggere, K. S. Breuer, K.-S. Chen, J. A. Carretero, H. Li, R. Mlcak, S. W. Pulitzer, M. A. Schmidt, S. M. Spearing, and Y.-H. Su, "Microhydraulic transducer technology for actuation and power generation," *Proc. SPIE*, vol. 3985, no. 1, pp. 680–688, Jun. 2000.

[14] C. O'Neill and J. Burchfield, "Kinetic ceramics piezoelectric hydraulic pumps," presented at the Industrial and Commercial Applications of Smart Structures Technologies 2007, San Diego, California, USA, 2007, p. 65270I–65270I–14.

[15] D. G. Lee, D. D. Shin, and G. P. Carman, "Large flow rate/high frequency microvalve array for high performance actuators," *Sens. Actuators Phys.*, vol. 134, no. 1, pp. 257–263, 2007.

[16] M. L. Loehr, W. F. Kosch, M. Singer, W. S. Pierce, and C. K. Kirby, “The piezoelectric artificial heart,” *Trans. - Am. Soc. Artif. Intern. Organs*, vol. 10, pp. 147–150, 1964.
[17] P. Smiley, C. O’Neill, W. Olander, and J. Creighton, “Development of a Piezoelectric Driver for an Artificial Left Ventricle,” 28-Sep-2010. [Online]. Available: about:blank. [Accessed: 28-Sep-2010].
[18] John F. (Barry) Keane, Donald C. Fyler, and James E. Lock, *Nadas’ Pediatric Cardiology, 2e*, 2nd ed. Saunders, 2006.
[19] W. H. Maisel, *Device therapy in heart failure*. New York: Humana, 2009.
[20] J. F. Keane, Lock, D. C. Fyler, and Nadas, *Nadas’ pediatric cardiology*. Philadelphia: Saunders, 2006.
[21] A. Kantrowitz, “Experimental augmentation of coronary flow by retardation of the arterial pressure pulse,” *Surgery*, vol. 34, no. 4, pp. 678–687, Oct. 1953.
[22] A. Kantrowitz, S. Tjonneland, J. S. Krakauer, S. J. Phillips, P. S. Freed, and A. N. Butner, “Mechanical intraaortic cardiac assistance in cardiogenic shock. Hemodynamic effects,” *Arch. Surg. Chic. Ill 1960*, vol. 97, no. 6, pp. 1000–1004, Dec. 1968.
[23] J. D. Hill, T. G. O’Brien, J. J. Murray, L. Dontigny, M. L. Bramson, J. J. Osborn, and F. Gerbode, “Prolonged extracorporeal oxygenation for acute post-traumatic respiratory failure (shock-lung syndrome). Use of the Bramson membrane lung,” *N. Engl. J. Med.*, vol. 286, no. 12, pp. 629–634, Mar. 1972.
[24] M. E. DeBakey, “Left ventricular bypass pump for cardiac assistance: Clinical experience,” *Am. J. Cardiol.*, vol. 27, no. 1, pp. 3–11, Jan. 1971.
[25] E. A. Rose, A. J. Moskowitz, M. Packer, J. A. Sollano, D. L. Williams, A. R. Tierney, D. F. Heitjan, P. Meier, D. D. Ascheim, R. G. Levitan, A. D. Weinberg, L. W. Stevenson, P. A. Shapiro, R. M. Lazar, J. T. Watson, D. J. Goldstein, and A. C. Gelijns, “The REMATCH trial: rationale, design, and end points. Randomized Evaluation of Mechanical Assistance for the Treatment of Congestive Heart Failure,” *Ann. Thorac. Surg.*, vol. 67, no. 3, pp. 723–730, Mar. 1999.
[26] M. Simon, J. Watson, T. Baldwin, W. R. Wagner, and H. S. Borovetz, “Current and Future Considerations in the Use of Mechanical Circulatory Support Devices,” *Annu. Rev. Biomed. Eng.*, vol. 10, pp. 59–84, Apr. 2008.
[27] D. B. Olsen, “The history of continuous-flow blood pumps,” *Artif. Organs*, vol. 24, no. 6, pp. 401–404, Jun. 2000.
[28] T. J. Myers, K. Robertson, T. Pool, N. Shah, I. Gregoric, and O. H. Frazier, “Continuous flow pumps and total artificial hearts: management issues,” *Ann. Thorac. Surg.*, vol. 75, no. 6 Suppl, pp. S79–85, Jun. 2003.
[29] H. G. Wood, A. L. Throckmorton, A. Untaroiu, and X. Song, “The medical physics of ventricular assist devices,” *Rep. Prog. Phys.*, vol. 68, no. 3, pp. 545–576, Mar. 2005.
[30] X. Song, A. L. Throckmorton, A. Untaroiu, S. Patel, P. E. Allaire, H. G. Wood, and D. B. Olsen, “Axial flow blood pumps,” *ASAIO J. Am. Soc. Artif. Intern. Organs 1992*, vol. 49, no. 4, pp. 355–364, Aug. 2003.
[31] N. T. R. S. (Ntrs), *Development and Testing of a Radial Halbach Magnetic Bearing*. BiblioGov, 2013.
[32] R. John, F. Kamdar, K. Liao, M. Colvin-Adams, A. Boyle, and L. Joyce, “Improved survival and decreasing incidence of adverse events with the HeartMate II left ventricular assist device as bridge-to-transplant therapy,” *Ann. Thorac. Surg.*, vol. 86, no. 4, pp. 1227–1234; discussion 1234–1235, Oct. 2008.

[33] D. V. Amin, J. F. Antaki, P. Litwak, D. Thomas, Z. J. Wu, and M. Watach, "Induction of ventricular collapse by an axial flow blood pump," *ASAIO J. Am. Soc. Artif. Intern. Organs 1992*, vol. 44, no. 5, pp. M685–690, Oct. 1998.
[34] J. T. Baldwin, S. Deutsch, D. B. Geselowitz, and J. M. Tarbell, "LDA measurements of mean velocity and Reynolds stress fields within an artificial heart ventricle," *J. Biomech. Eng.*, vol. 116, no. 2, pp. 190–200, May 1994.
[35] R. B. Medvitz, *Development and Validation of a Computational Fluid Dynamic Methodology for Pulsatile Blood Pump Design and Prediction of Thrombus Potential*. ProQuest, 2008.
[36] M. Behbahani, M. Behr, M. Hormes, U. Steinseifer, D. Arora, O. Coronado, and M. Pasquali, "A review of computational fluid dynamics analysis of blood pumps," *Eur. J. Appl. Math.*, vol. 20, no. 04, pp. 363–397, 2009.
[37] K. H. Fraser, M. E. Taskin, B. P. Griffith, and Z. J. Wu, "The use of computational fluid dynamics in the development of ventricular assist devices," *Med. Eng. Phys.*, vol. 33, no. 3, pp. 263–280, Apr. 2011.
[38] I. J. Karassik, *Pump handbook*. New York: McGraw-Hill, 2001.
[39] E. A. Chen, S. M. Patel-Raman, M. R. Berman, and B. D. Zuckerman, "Food and Drug Administration's Perspectives on Pediatric Cardiac Assist Devices," *ASAIO J.*, vol. 54, no. 2, pp. 147–149, Mar. 2008.
[40] W. J. Weiss, "Pulsatile Pediatric Ventricular Assist Devices," *ASAIO J.*, vol. 51, no. 5, pp. 540–545, Sep. 2005.
[41] P. D. Wearden, V. O. Morell, B. B. Keller, S. A. Webber, H. S. Borovetz, S. F. Badylak, J. R. Boston, R. L. Kormos, M. V. Kameneva, M. Simaan, and others, "The PediaFlow™ pediatric ventricular assist device," 2006, vol. 9, pp. 92–98.
[42] M. Deiwick, A. Hoffmeier, T. D. T. Tjan, T. Krasemann, C. Schmid, and H. H. Scheld, "Heart Failure in Children - Mechanical Assistance," *Thorac. Cardiovasc. Surg.*, vol. 53, pp. S135–S140, Feb. 2005.
[43] M. J. Slepian, Y. Alemu, J. S. Soares, R. G. Smith, S. Einav, and D. Bluestein, "The Syncardia™ total artificial heart: in vivo, in vitro, and computational modeling studies," *J. Biomech.*, vol. 46, no. 2, pp. 266–275, Jan. 2013.
[44] D. J. Farrar, K. E. Buck, J. H. Coulter, and E. J. Kupa, "Portable pneumatic biventricular driver for the Thoratec ventricular assist device," *ASAIO J. Am. Soc. Artif. Intern. Organs 1992*, vol. 43, no. 5, pp. M631–634, Oct. 1997.
[45] T. Nishinaka, Y. Taenaka, E. Tatsumi, H. Ohnishi, A. Homma, K. Shioya, T. Mizuno, T. Tsukiya, S. Mushika, Y. Hashiguchi, A. Suzuki, and S. Kitamura, "Development of a compact portable driver for a pneumatic ventricular assist device," *J. Artif. Organs Off. J. Jpn. Soc. Artif. Organs*, vol. 10, no. 4, pp. 236–239, 2007.
[46] A. J. Sipin, W. J. Fabrey, S. H. Smith, J. D. Doussourd, and D. B. Olsen, "Wearable air supply for pneumatic artificial hearts and ventricular assist devices," *Artif. Organs*, vol. 16, no. 4, pp. 431–438, Aug. 1992.
[47] F. A. Tinker, "United States Patent: 8070455 - Scotch-yoke mechanism for redundant actuation applications," 807045506-Dec-2011.
[48] F. A. Tinker, "United States Patent: 8021422 - Actuating mechanism for pneumatically-driven artificial heart," 802142220-Sep-2011.
[49] O. H. Frazier, "First use of an untethered, vented electric left ventricular assist device for long-term support.," *Circulation*, vol. 89, no. 6, pp. 2908–2914, Jun. 1994.

[50] O. H. Frazier, T. J. Myers, and B. Radovancevic, "The HeartMate left ventricular assist system. Overview and 12-year experience.," *Tex. Heart Inst. J.*, vol. 25, no. 4, pp. 265–271, 1998.
[51] S. M. Mehta, W. E. Pae Jr, G. Rosenberg, A. J. Snyder, W. J. Weiss, J. P. Lewis, D. J. Frank, J. J. Thompson, and W. S. Pierce, "The LionHeart LVD-2000: a completely implanted left ventricular assist device for chronic circulatory support," *Ann. Thorac. Surg.*, vol. 71, no. 3, Supplement 1, pp. S156–S161, Mar. 2001.
[52] R. C. Robbins, M. H. Kown, P. M. Portner, and P. E. Oyer, "The totally implantable Novacor Left Ventricular Assist System," *Ann. Thorac. Surg.*, vol. 71, no. 3, Supplement 1, pp. S162–S165, Mar. 2001.
[53] P. D. Diegel, T. Mussivand, J. W. Holfert, J. T. Juretich, J. A. Miller, G. K. Maclean, Z. Szurmak, J. P. Santerre, K. Rajagopalan, and P. A. Dew, "Electrohydraulic ventricular assist device development," *ASAIO J. Am. Soc. Artif. Intern. Organs 1992*, vol. 38, no. 3, pp. M306–310, Sep. 1992.
[54] T. Mussivand, "Electrohydraulic ventricular assist device," US5704891 A06-Jan-1998.
[55] F. M. Donovan Jr, "Design of a hydraulic analog of the circulatory system for evaluating artificial hearts," *Biomater. Med. Devices Artif. Organs*, vol. 3, no. 4, pp. 439–449, 1975.
[56] Y. Liu, P. Allaire, Y. Wu, H. Wood, and D. Olsen, "Construction of an artificial heart pump performance test system," *Cardiovasc. Eng. Dordr. Neth.*, vol. 6, no. 4, pp. 151–158, Dec. 2006.
[57] S. Vandenberghe, F. Shu, D. K. Arnold, and J. F. Antaki, "A simple, economical, and effective portable paediatric mock circulatory system," *Proc. Inst. Mech. Eng. [H]*, vol. 225, no. 7, pp. 648–656, Jul. 2011.
[58] O. Dur, M. Lara, D. Arnold, S. Vandenberghe, B. B. Keller, C. DeGroff, and K. Pekkan, "Pulsatile In Vitro Simulation of the Pediatric Univentricular Circulation for Evaluation of Cardiopulmonary Assist Scenarios," *Ann Biomed Eng*, vol. 31, pp. 810–22, 2009.
[59] R. S. Figliola, A. Giardini, T. Conover, T. A. Camp, G. Biglino, J. Chiulli, and T.-Y. Hsia, "In Vitro Simulation and Validation of the Circulation with Congenital Heart Defects," *Prog. Pediatr. Cardiol.*, vol. 30, no. 1–2, pp. 71–80, Dec. 2010.
[60] P. A. Iaizzo, *Handbook of Cardiac Anatomy, Physiology, and Devices*, 2nd ed. Humana Press, 2009.
[61] J. A. Dixon and F. G. Spinale, "Large Animal Models of Heart Failure A Critical Link in the Translation of Basic Science to Clinical Practice," *Circ. Heart Fail.*, vol. 2, no. 3, pp. 262–271, May 2009.
[62] S. R. Houser, K. B. Margulies, A. M. Murphy, F. G. Spinale, G. S. Francis, S. D. Prabhu, H. A. Rockman, D. A. Kass, J. D. Molkentin, M. A. Sussman, and W. J. Koch, "Animal Models of Heart Failure A Scientific Statement From the American Heart Association," *Circ. Res.*, vol. 111, no. 1, pp. 131–150, Jun. 2012.
[63] L. APC International, *Piezoelectric ceramics: principles and applications.* Mackeyville, PA: APC International, 2011.
[64] B. Jaffe, W. R. Cook, and H. Jaffe, *Piezoelectric Ceramics*. Techbooks, 1989.
[65] V. Giurgiutiu, Z. A. Chaudhry, and C. A. Rogers, "Stiffness issues in the design of ISA displacement amplification devices: case study of a hydraulic displacement amplifier," *Proc. SPIE*, vol. 2443, no. 1, pp. 105–119, May 1995.
[66] D. J. Leo, *Engineering Analysis of Smart Material Systems*. Wiley, 2007.

[67] K. F. Graff, “A History of Ultrasonics,” in *Physical acoustics*, vol. 15, New York, London: Academic Press, 1981, pp. 1–97.
[68] K. Graff, “Historical highlights in ultrasonics - 2,” in *Frequency Control Symposium and Exposition, 2004. Proceedings of the 2004 IEEE International*, 2004, pp. 5–10.
[69] H. V. Barth, “Ultrasonic Driven Motor,” *IBM Tech. Discl. Bull.*, vol. 16, no. 7, p. 2263, 1973.
[70] T. Sashida and T. Kenjo, *An Introduction to Ultrasonic Motors*. Oxford University Press, USA, 1994.
[71] A. Chaudhuri and N. Wereley, “Compact Hybrid Electrohydraulic Actuators Using Smart Materials: A Review,” *J. Intell. Mater. Syst. Struct.*, Sep. 2011.
[72] C.G. O’Neill and P.C. Smiley, “Piezoelectric Drivers for Fluid Power Control,” in *Proceedings of the National Conference on Fluid Power*, Chicago, IL, 1973, vol. 27, pp. 167–183.
[73] L. D. Mauck and C. S. Lynch, “Piezoelectric Hydraulic Pump Development,” *J. Intell. Mater. Syst. Struct.*, vol. 11, no. 10, pp. 758–764, Oct. 2000.
[74] K. Konishi, T. Yoshimura, K. Hashimoto, and N. Yamamoto, “Hydraulic Actuators Driven by Piezoelectric Elements : 1st Report, Trial Piezoelectric Pump and Its Maximum Power),” *Trans. Jpn. Soc. Mech. Eng. Ser. C*, vol. 59, no. 564, pp. 2477–2484, 1993.
[75] K. Konishi, T. Yoshimura, K. Hashimoto, T. Hamada, and T. Tamura, “Hydraulic Actuators Driven by Piezoelectric Elements : 2nd Report, Enlargement of Piezoelectric Pumps’ Output Power Using Hydraulic Resonance,” *Trans. Jpn. Soc. Mech. Eng. Ser. C*, vol. 60, no. 571, pp. 956–963, 1994.
[76] R. M. Tieck, K. P. Mohanchandra, and G. P. Carman, “<title>Smart material actuators for airfoil morphing applications</title>,” 2004, pp. 235–246.
[77] J. Sirohi and I. Chopra, “Design and Development of a High Pumping Frequency Piezoelectric-Hydraulic Hybrid Actuator,” *J. Intell. Mater. Syst. Struct.*, vol. 14, no. 3, pp. 135–147, Mar. 2003.
[78] J. E. Lindler, E. H. Anderson, M. E. Regelbrugge, and others, “Design and testing of piezoelectric-hydraulic actuators,” *Smart Struct. Mater. 2003*, vol. 5054, pp. 96–107, 2003.
[79] S. John, J. Sirohi, G. Wang, and N. M. Wereley, “Comparison of Piezoelectric, Magnetostrictive, and Electrostrictive Hybrid Hydraulic Actuators,” *J. Intell. Mater. Syst. Struct.*, vol. 18, no. 10, pp. 1035 –1048, Oct. 2007.
[80] A. Chaudhuri and N. M. Wereley, “Experimental Validation of a Hybrid Electrostrictive Hydraulic Actuator Analysis,” *J. Vib. Acoust.*, vol. 132, no. 2, pp. 021006–021006, Mar. 2010.
[81] J. P. Larson and M. J. Dapino, “Reliable, high-frequency miniature valves for smart material electrohydraulic actuators,” *J. Intell. Mater. Syst. Struct.*, vol. 23, no. 7, pp. 805–813, May 2012.
[82] D. G. Lee, D. D. Shin, and G. P. Carman, “Large flow rate/high frequency microvalve array for high performance actuators,” *Sens. Actuators Phys.*, vol. 134, no. 1, pp. 257–263, 2007.
[83] E. G. Chapman, S. L. Herdic, C. A. Keller, and C. S. Lynch, “Development of miniaturized piezo-hydraulic pumps,” pp. 299–310, May 2005.

[84] C. O'Neill and J. Burchfield, "Kinetic ceramics piezoelectric hydraulic pumps," presented at the Industrial and Commercial Applications of Smart Structures Technologies 2007, San Diego, California, USA, 2007, p. 65270I–65270I–14.
[85] A. Doll, M. Wischke, H. J. Schrag, A. Geipel, F. Goldschmidtboeing, and P. Woias, "Characterization of active silicon microvalves with piezoelectric membrane actuators," *Microelectron. Eng.*, vol. 84, no. 5–8, pp. 1202–1206, 2007.
[86] D. G. Lee, S. W. Or, and G. P. Carman, "Design of a Piezoelectric-hydraulic Pump with Active Valves," *J. Intell. Mater. Syst. Struct.*, vol. 15, no. 2, pp. 107–115, Feb. 2004.
[87] J. M. Wen, J. J. Ma, Z. H. Zhang, G. M. Cheng, and J. W. Kan, "The Parameter Design and Experiment of Active Valve with Piezoelectric Pump," *Adv. Mater. Res.*, vol. 305, pp. 320–324, Jul. 2011.
[88] G. W. Kim and K. Wang, "Helmholtz resonance in a piezoelectric–hydraulic pump-based hybrid actuator," *Smart Mater. Struct.*, vol. 20, p. 015010, 2011.
[89] W. S. Oates and C. S. Lynch, "Piezoelectric Hydraulic Pump System Dynamic Model," *J. Intell. Mater. Syst. Struct.*, vol. 12, no. 11, pp. 737–744, Nov. 2001.
[90] K. Nasser and D. J. Leo, "Efficiency of Frequency-Rectified Piezohydraulic andPiezopneumatic Actuation," *J. Intell. Mater. Syst. Struct.*, vol. 11, no. 10, pp. 798–810, Oct. 2000.
[91] A. Ullmann and I. Fono, "The piezoelectric valve-less pump - improved dynamic model," *J. Microelectromechanical Syst.*, vol. 11, no. 6, pp. 655–664, Dec. 2002.
[92] J. Kan, K. Tang, Y. Ren, G. Zhu, and P. Li, "Study on a piezohydraulic pump for linear actuators," *Sens. Actuators Phys.*, vol. 149, no. 2, pp. 331–339, 2009.
[93] S. V. Madihally, *Principles of Biomedical Engineering*, 1st ed. Artech House Publishers, 2010.
[94] K. Uchino, "Piezoelectric actuators 2006," *J. Electroceramics*, vol. 20, no. 3–4, pp. 301–311, Aug. 2008.
[95] L. D. Mauck and C. S. Lynch, "Piezoelectric Hydraulic Pump Development," *J. Intell. Mater. Syst. Struct.*, vol. 11, no. 10, pp. 758–764, Oct. 2000.
[96] G. S. Jeong, C. M. Hwang, K. W. Nam, C. B. Ahn, H. C. Kim, J. J. Lee, J. Choi, H. S. Son, Y. H. Fang, K. H. Son, C. H. Lim, and K. Sun, "Development of a Closed Air Loop Electropneumatic Actuator for Driving a Pneumatic Blood Pump," *Artif. Organs*, vol. 33, no. 8, pp. 657–662, 2009.
[97] L. D. Mauck, W. S. Oates, and C. S. Lynch, "Piezoelectric hydraulic pump performance," presented at the Smart Structures and Materials 2001: Industrial and Commercial Applications of Smart Structures Technologies, Newport Beach, CA, USA, 2001, vol. 4332, pp. 246–253.
[98] M. Karpelson, G.-Y. Wei, and R. J. Wood, "Driving high voltage piezoelectric actuators in microrobotic applications," *Sens. Actuators Phys.*, vol. 176, pp. 78–89, Apr. 2012.
[99] D. K. Lindner, H. Zhu, C. Song, W. Huang, and D. Cheng, "<title>Low input voltage switching amplifiers for piezoelectric actuators</title>," 2002, pp. 282–292.
[100] J. A. Main, D. V. Newton, L. Massengill, and E. Garcia, "Efficient power amplifiers for piezoelectric applications," *Smart Mater. Struct.*, vol. 5, no. 6, p. 766, Dec. 1996.
[101] J. A. Main, "<title>Charge-recovery power amplifier for piezoelectric applications</title>," 1997, pp. 741–746.

[102] S. Vandenberghe, F. Shu, D. K. Arnold, and J. F. Antaki, “A simple, economical, and effective portable paediatric mock circulatory system,” *Proc. Inst. Mech. Eng. [H]*, vol. 225, no. 7, pp. 648–656, Jul. 2011.
[103] I. Chopra and J. Sirohi, “Smart structures theory (cambridge aerospace series),” *CERN Document Server*, 31-Oct-2013. [Online]. Available: https://cds.cern.ch/record/1558716. [Accessed: 31-Mar-2014].
[104] F. Merkle, W. Boettcher, B. Stiller, and R. Hetzer, “Pulsatile mechanical cardiac assistance in pediatric patients with the Berlin heart ventricular assist device,” *J. Extra. Corpor. Technol.*, vol. 35, no. 2, pp. 115–120, Jun. 2003.
[105] M. Elwenspoek and R. J. Wiegerink, *Mechanical microsensors*. Berlin; New York: Springer, 2001.
[106] W. S. Pierce, J. A. Brighton, W. O’Bannon, J. H. Donachy, W. M. Phillips, D. L. Landis, W. J. White, and J. A. Waldhausen, “Complete Left Ventricular Bypass With a Paracorporeal Pump: Design and Evaluation,” *Ann. Surg.*, vol. 180, no. 4, pp. 418–426, Oct. 1974.
[107] J. H. Donachy, D. L. Landis, G. Rosenberg, G. A. Prophet, O. Ferrari, and W. S. Pierce, “Design and Evaluation of a Left Ventricular Assist Device: The Angle Port Pump,” in *Assisted Circulation*, F. U. M.D, Ed. Springer Berlin Heidelberg, 1979, pp. 138–146.
[108] B. B. Daily, T. W. Pettitt, S. P. Sutera, and W. S. Pierce, “Pierce-Donachy pediatric VAD: progress in development,” *Ann. Thorac. Surg.*, vol. 61, no. 1, pp. 437–443, Jan. 1996.
[109] J. M. Connell, T. Khalapyan, J. L. Myers, G. Rosenberg, and W. J. Weiss, “Anatomic fit assessment for the Penn State pediatric ventricular assist device,” *ASAIO J. Am. Soc. Artif. Intern. Organs 1992*, vol. 53, no. 6, pp. 687–691, Dec. 2007.
[110] B. N. Roszelle, S. Deutsch, and K. B. Manning, “A parametric study of valve orientation on the flow patterns of the Penn State pulsatile pediatric ventricular assist device,” *ASAIO J. Am. Soc. Artif. Intern. Organs 1992*, vol. 56, no. 4, pp. 356–363, Aug. 2010.
[111] N. M. K. Lamba, K. A. Woodhouse, and S. L. Cooper, *Polyurethanes in Biomedical Applications*. CRC Press, 1997.
[112] M. Szycher and C. P. Sharma, *Blood Compatible Materials and Devices: Perspectives Towards the 21st Century*. CRC Press, 1990.
[113] M. R. de Leval, P. Kilner, M. Gewillig, and C. Bull, “Total cavopulmonary connection: a logical alternative to atriopulmonary connection for complex Fontan operations. Experimental studies and early clinical experience,” *J. Thorac. Cardiovasc. Surg.*, vol. 96, no. 5, pp. 682–695, Nov. 1988.
[114] S. a. S. Furey, H. a. H. Zieske, and M. N. M. Levy, “The essential function of the right ventricle.,” *Am Heart J*, vol. 107, no. 2, p. 404, Feb. 1984.
[115] M. R. de Leval, “The Fontan circulation: a challenge toWilliam Harvey?,” *Nat. Clin. Pract. Cardiovasc. Med.*, vol. 2, no. 4, 2005.
[116] A. Redington, “The physiology of the Fontan circulation,” *Prog. Pediatr. Cardiol.*, vol. 22, no. 2, pp. 179–186, 2006.
[117] M. D. Rodefeld, J. H. Boyd, C. D. Myers, B. J. LaLone, A. J. Bezruczko, A. W. Potter, and J. W. Brown, “Cavopulmonary assist: circulatory support for the univentricular Fontan circulation,” *Ann. Thorac. Surg.*, vol. 76, no. 6, p. 1911, 2003.
[118] M. W. . Chu, K. Sharma, C. I. Tchervenkov, L. F. Jutras, J. Lavoie, S. D. Shemie, E. Laliberte, C. Calaritis, and R. Cecere, “Berlin Heart ventricular assist device in a child

with hypoplastic left heart syndrome," *Ann. Thorac. Surg.*, vol. 83, no. 3, pp. 1179–1181, 2007.
[119] T. Mackling, T. Shah, V. Dimas, K. Guleserian, M. Sharma, J. Forbess, M. Ardura, J. Gross-Toalson, Y. Lee, J. Journeycake, and A. Barnes, "Management of Single-Ventricle Patients With Berlin Heart EXCOR Ventricular Assist Device: Single-Center Experience," *Artif. Organs*, vol. 36, no. 6, pp. 555–559, 2012.
[120] S. Tsuda, T. Sasaki, K. Maeda, R. K. Riemer, S. H. Reichenbach, and O. Reinhartz, "Recovery during mid-term mechanical support of fontan circulation in sheep," *ASAIO J. Am. Soc. Artif. Intern. Organs 1992*, vol. 55, no. 4, pp. 406–411, Aug. 2009.
[121] A. L. Throckmorton, K. K. Ballman, C. D. Myers, K. N. Litwak, S. H. Frankel, and M. D. Rodefeld, "Mechanical Cavopulmonary Assist for the Univentricular Fontan Circulation Using a Novel Folding Propeller Blood Pump," *ASAIO J.*, vol. 53, no. 6, pp. 734–741, Nov. 2007.
[122] M. D. Rodefeld, B. Coats, T. Fisher, G. A. Giridharan, J. Chen, J. W. Brown, and S. H. Frankel, "Cavopulmonary assist for the univentricular Fontan circulation: von Karman viscous impeller pump," *J. Thorac. Cardiovasc. Surg.*, 2010.
[123] S. J. Ferns, C. El Zein, K. Multani, I. Sajan, S. Subramanian, A. C. Polimenakos, and M. N. Ilbawi, "Is additional pulsatile pulmonary blood flow beneficial to patients with bidirectional Glenn?," *J. Thorac. Cardiovasc. Surg.*, vol. 145, no. 2, pp. 451–454, Feb. 2013.
[124] R. K. Riemer, G. Amir, S. H. Reichenbach, and O. Reinhartz, "Mechanical support of total cavopulmonary connection with an axial flow pump," *J. Thorac. Cardiovasc. Surg.*, vol. 130, no. 2, p. 351, Aug. 2005.
[125] J. C. Chachques, P. Grandjean, A. Serraf, C. Latremouille, V. A. Jebara, O. Ponzio, S. Mihaileanu, S. Chauvaud, I. Bourgeois, and A. Carpentier, "Atrial cardiomyoplasty after Fontan-type procedures," *Circulation*, vol. 82, no. 5 Suppl, pp. IV183–189, Nov. 1990.
[126] A. F. Corno, C. Vergara, C. Subramanian, R. A. Johnson, T. Passerini, A. Veneziani, L. Formaggia, N. Alphonso, A. Quarteroni, and J. C. Jarvis, "Assisted Fontan procedure: animal and in vitro models and computational fluid dynamics study," *Interact. Cardiovasc. Thorac. Surg.*, vol. 10, no. 5, pp. 679–684, Feb. 2010.
[127] B. Voss, F.-U. Sack, W. Saggau, S. Hagl, and R. Lange, "Atrial cardiomyoplasty in a Fontan circulation," *Eur. J. Cardiothorac. Surg.*, vol. 21, no. 5, pp. 780–786, May 2002.
[128] G. N. Askew, V. M. Cox, J. D. Altringham, and D. F. Goldspink, "Mechanical properties of the latissimus dorsi muscle after cyclic training," *J. Appl. Physiol. Bethesda Md 1985*, vol. 93, no. 2, pp. 649–659, Aug. 2002.
[129] V. L. Sales and P. M. McCarthy, "Understanding the C-Pulse Device and Its Potential to Treat Heart Failure," *Curr. Heart Fail. Rep.*, vol. 7, no. 1, pp. 27–34, Feb. 2010.
[130] A. N. Davies, W. S. Peters, T. Su, C. E. Sullivan, T. Perkidides, F. P. Milsom, and G. White, "Extra-ascending aortic versus intra-descending aortic balloon counterpulsation-effect on coronary artery blood flow," *Heart Lung Circ.*, vol. 14, no. 3, pp. 178–186, Sep. 2005.
[131] "Introducing C-Pulse," *http://www.sunshineheart.com*. [Online]. Available: http://www.sunshineheart.com/c-pulse/. [Accessed: 06-May-2013].
[132] F. G. Lacour-Gayet, C. J. Lanning, S. Stoica, R. Wang, B. A. Rech, S. Goldberg, and R. Shandas, "An artificial right ventricle for failing fontan: in vitro and computational study," *Ann. Thorac. Surg.*, vol. 88, no. 1, pp. 170–176, Jul. 2009.

[133] Y. Liu, P. Allaire, Y. Wu, H. Wood, and D. Olsen, “Construction of an artificial heart pump performance test system,” *Cardiovasc. Eng. Dordr. Neth.*, vol. 6, no. 4, pp. 151–158, Dec. 2006.
[134] G. M. Pantalos, C. Ionan, S. C. Koenig, K. J. Gillars, T. Horrell, S. Sahetya, J. Colyer, and L. A. Gray, “Expanded Pediatric Cardiovascular Simulator for Research and Training,” *ASAIO J.*, vol. 56, no. 1, pp. 67–72, Jan. 2010.
[135] R. Buchhorn, D. Bartmus, W. Buhre, and J. Bürsch, “Pathogenetic mechanisms of venous congestion after the Fontan procedure,” *Cardiol. Young*, vol. 11, no. 02, pp. 161–168, 2001.
[136] C. D. Myers, J. H. Boyd, R. G. Presson Jr, P. Vijay, A. C. Coats, J. W. Brown, and M. D. Rodefeld, “Neonatal cavopulmonary assist: pulsatile versus steady-flow pulmonary perfusion,” *Ann. Thorac. Surg.*, vol. 81, no. 1, pp. 257–263, 2006.
[137] R. G. Presson Jr, W. A. Baumgartner Jr, A. J. Peterson, R. W. Glenny, and W. W. Wagner Jr, “Pulmonary capillaries are recruited during pulsatile flow,” *J. Appl. Physiol. Bethesda Md 1985*, vol. 92, no. 3, pp. 1183–1190, Mar. 2002.
[138] D. Mohrman and L. Heller, *Cardiovascular Physiology, Seventh Edition*, 7th ed. McGraw-Hill Professional, 2010.